The University of Hull

Optical Characterisation of Quantum Well Infrared Photodetectors (QWIPs) for Gas Sensing Applications.

being a Thesis submitted for the Degree of

Doctor of Philosophy

in the University of Hull

by

Khue Tian Lai, MEng. (Hull), DipEng. (Singapore)

June, 2004

Abstract

Although much work has been done on $\lambda \sim 5\text{-}12$ μm quantum well infrared photodetectors (QWIPs), the distinctive feature of this project is the use of strain-compensated materials on InP substrates, AlAs (tensile) and InGaAs (compressive), to achieve shorter wavelengths and higher temperature operation. Stepped wells, high thin barriers, and strained layers have been used to achieve $\lambda \sim 2\text{-}5$ μm and also enhanced normal incidence absorption. These structures also give an additional degree of freedom to control the position of the excited states in the QWIPs conduction band. The strain-balancing allows the use of Indium (In) concentrations up to 84% and hence deep wells with a large band offset relative to the outer barrier (which predominantly controls the dark current). The conduction band offset (ΔE_C) for these structures (with respect to the wide InAlAs barrier) is estimated to be ~ 675 meV. In the course of this work, we have also been able to estimate the subband non-parabolicity (m^* and α) from absorption spectra in highly doped quantum wells (QWs).

In this thesis, the main results which I present are on a comparative study of the intersubband absorption in a series of double barrier QW (DBQW) structures grown on GaAs substrates (Chapter 5) and InP substrates (Chapter 6). The background and theory of QWs is given in Chapter 1. In Chapter 2, the experimental procedure is detailed, while the theoretical model to calculate the conduction band profile and energy levels and the comparison of this model with literature values are presented in Chapter 3. Early results are discussed in Chapter 4. Finally, a summary and future work are outlined in Chapter 7.

Acknowledgements

First and foremost, to my first supervisor, Professor S. K. Haywood, I would like to express my heartfelt gratitude for her excellent guidance, encouragement, understanding and advice throughout the project. To my second supervisor, Dr. D. Sands, I would like to thank him for his guidance and support throughout the project.

I would also like to thank Dr. R. Gupta for the many valuable discussions on the theory side of the project.

I am also grateful to Prof. M. Missous, Mr. C. Mitchell, Dr. L. May, Dr. S. I. Rybchenko, Dr. I. Itskevich, Mr. S. Gordon, Mrs. V. Hewer, Mr. G. Robinson, Mr. D. Wright and Mr. E. Thompson for their technical expertise and advice throughout the project. The growth of all samples, Hall and Double-crystal X-ray diffraction measurements were carried out by Prof. M. Missous's group from University of Manchester Institute of Science and Technology (UMIST).

Finally, I would like to thank my brother Khuen Tuck for taking care of my family during my absence and to all former colleagues in Motorola Electronics Pte. Ltd. (Singapore) and Advance Micro Devices (Singapore) Pte. Ltd. for their understanding and assistance during my stay in the company. Last but not least, thanks to friends like Dr. A. Gupta, Mr. Alvin Lim, Dr. Alvin Ong, Mr. Henry Soh, Mr. W. C. Wong, Mr. Aaron Tan, Mr. C. C. Leong and Mr. Andrew Ang for their friendship and moral support. Thank you all for making it possible.

Contents

	Page
Abstract	**2**
Acknowlegements	**3**
Chapter 1 Background and Theory of Quantum Wells	**6**
1.1 Introduction	6
1.2 Detector performance parameters	8
1.3 Overview of Quantum Wells	11
1.3.1 Quantum Well with infinite barriers	14
1.3.2 Intersubband Transitions in Quantum Wells	19
1.3.2.1 Dark Current	21
1.3.2.2 Bound-to-Bound Transitions	23
1.3.2.3 Bound-to-Continuum Transitions	24
1.3.2.4 Bound-to-Quasicontinuum Transitions	25
1.4 N versus P type Quantum Wells	27
1.5 Asymmetric Wells	30
1.6 Absorption Spectra of Intersubband Transitions	33
1.7 Use of Strained Layer Materials in Quantum Wells	34
1.8 Summary	39
References	40
Chapter 2 Experimental Methods	**49**
2.1 Growth-Molecular Beam Epitaxy (MBE)	49
2.2 Sample polishing	52
2.3 Fourier Transform Infrared (FTIR) Absorption Spectroscopy	54
2.4 Photoluminescence (PL) Measurements	56
References	59
Chapter 3 Modelling	**60**
3.1 *k.p* model	60
3.2 Comparison of Model with Literature Values	64
3.2.1 Double barrier quantum wells (DBQWs)	64
3.2.2 *X* valley quantum wells	68
3.2.3 Stepped quantum well	69
3.2.4 P-type quantum wells	71
3.2.5 Summary	73
3.3 Modelling of GaAs based samples	75
3.4 Modelling of InP based samples	77
References	79
Chapter 4 Early Quantum Wells Structure Studies	**81**
4.1 Absorption Setup Test	81
4.2 Photoluminescence Setup Test	86
4.3 Early Samples	88
4.3.1 Conclusions	93
References	93

Chapter 5 GaAs Based Samples **94**
5.1 Initial Characterisation 94
5.2 Absorption 97
5.3 Selection Rules 100
5.4 Conclusions 102
References 102

Chapter 6 InP Based Samples **104**
6.1 Initial Characterisation 104
6.2 Absorption 106
6.2.1 Sample 1561 109
6.2.2 Sample 1563 111
6.2.3 Sample 1554 113
6.2.3.1 Subband Dispersion 117
6.3 Conclusions 122
References 123

Chapter 7 Summary and Future Work **124**
References 127

Appendix A **130**

Appendix B **131**

Appendix C **132**

Appendix D **133**

List of Publications **136**

Chapter 1 Background and Theory of Quantum Wells

1.1 Introduction

Concern about environmental issues has, resulted in stricter legal regulations on pollution emission in almost all industrialised countries. Therefore, to comply with the new laws, measurements of pollutant concentrations in the air will no longer be a laboratory issue, but an industrial one too.

One method of monitoring/detecting environmentally important trace-gas species in ambient air to a sensitivity of several parts in 10^9 (ppb) [1] is laser spectroscopy. This has been a powerful analytic tool in many technical and scientific branches for several decades.

Until ~ 10 years ago, near infrared or visible laser sources (interband semiconductor lasers) were used for these applications. One of the main problems associated with these sources is that to change the emission wavelength a different band gap material is required. In addition, in the infrared region these devices must be based on narrow-gap materials which are known to be unreliable i.e., difficult to grow, process and fabricate as compared to wide band gap materials. Hence, the usefulness of this approach is only limited by the availability of convenient tunable sources. The 3 to 5 μm mid-infrared spectral range is of particular important where many molecules including atmospheric pollutants e.g. CO_2, CO, N_2O, and CH_4 exhibit well resolved fundamental vibrational absorption bands.

The situation changed with the advent of the quantum cascade laser (QCL) also known as the intersubband laser in 1994 [2]. In these devices, photon emission is obtained by making optical transitions between confined energy levels, therefore, the emission wavelength is not controlled by the material bandgap but the layer thicknesses. Hence, using the same heterostructure material system, e.g. InGaAs/InAlAs, a wide spectral range from 3.5 to 19 μm can be covered [3]. Point-to-point atmospheric communications, chemical and gas sensing have been successfully demonstrated using QCLs [4-6]. QCLs have been demonstrated to operate above T>400 K in pulsed mode [7] and continuous wave at 300 K [8] in the mid-infrared range. The most recent reviews on the development and properties of QCLs are given in ref. 3 and ref. 9.

In contrast to emitter technology, there has been little work done to improve the performance (e.g. operating temperature) for detectors based on intersubband transitions. The highest operating temperature reported to date is around 205 K [10]. The use of liquid nitrogen cooled equipment on either the emitter or the detector side makes optical techniques somewhat less appealing for many applications in the field. Hence the goal of this project is to investigate routes to room temperature detection.

Here we propose a detector design based on quantum well (QW) intersubband transitions in the 3-5 μm spectral range capable of operating above 205 K. We hope to develop a robust, compact, and consumable-free system for the sensitive and selective detection/monitoring of atmospheric pollutants. The next section gives an overview of detector performance parameters while an overview of QWs and the various types of intersubband transition are presented in Sec. 1.3. Section 1.4 discusses the differences

between N and P type QWs. The use of asymmetric wells and parameters affecting the absorption spectra of intersubband transitions in QWs are presented in Sec. 1.5 and Sec. 1.6, respectively. Finally, QWs based on strained layer materials are discussed in Sec. 1.7.

1.2 Detector performance parameters

In this section, we briefly discussed the parameters that are commonly used to assess the performance of detectors in general and how these specifically apply to QWIPs.

The responsivity R is defined as the ratio of the output of the detector to its input. The peak responsivity R_p of a QWIP is defined as [11, 12]:

$$R_p = \frac{e}{h\nu}\eta g \quad \text{A/W} \tag{1.2.1}$$

where $h\nu$ is the photon energy, $g \approx 1/Np_c$ is the photoconductive gain (defined as the number of electrons that flow through the external circuit for each mobile carrier that is generated in the sample). Here, N is the number of wells and p_c is the capture probability. The photoconductive gain is also given by $g = \tau_{life}/\tau_{transit}$ where τ_{life} is the photoexcited carrier lifetime and $\tau_{transit}$ is the transit time. The photoconductive gain can be significantly greater than unity [11] which shows that τ_{life} is not limited by $\tau_{transit}$ i.e., the photoexcited carriers make more than one pass through the multiquantum well structure circulating by reinjection at the ohmic contact and can be improved with proper QW design optimisation.

$$\eta = \frac{1}{2}\left(1 - e^{-2\alpha l}\right) \tag{1.2.2}$$

is the unpolarised absorption quantum efficiency (assuming 45^0 waveguide geometry) where α is the absorption coefficient and l is the length of the active region. The factor 2 in the exponential term accounts for the increased absorption due to the reflection off the top metallic contact and the factor of two in the denominator is a result of the quantum mechanical selection rules for n-type QWIPs (see section 1.4), which allow the absorption of radiation polarised along the growth direction (see Fig. 1.2.1).

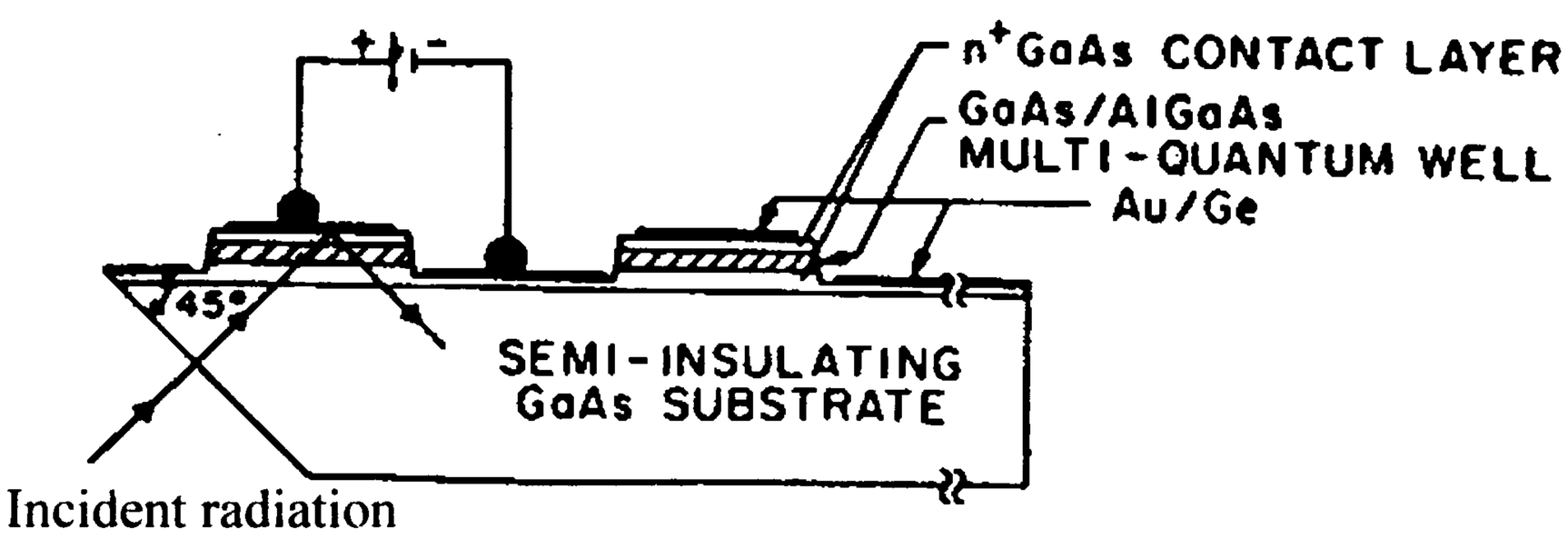

Figure 1.2.1: Cross sectional view of a GaAs/AlGaAs QWIP with a 45^0 polished edge to facilitate absorption and responsivity measurements [13].

From equation (1.2.1), we can see that the responsivity of the device is proportional to the product of η and g. Therefore, the responsivity of the detector increases with η and g.

The principle source of dark current for QWIPs operating at a higher temperature is thermonic emission (see section 1.3.2.1). The presence of high dark

current limits the ability of the device to detect small signals. Conventionally, the minimum detectable signal is taken to be that which would generate a root mean square (rms) output equal to that generated by the noise (i.e., the signal-to-noise ratio is then equal to 1). An indication of the size of the minimum detectable signal is given by the noise equivalent power (NEP). This is defined as the power of sinusoidally modulated monochromatic radiation which would result in the same rms output signal in an ideal noise noise-free detector as the noise signal encountered in the real detector. Assuming that the noise power generated in a detector is proportional to its area A, then the noise current (or voltage) will vary as $A^{1/2}$. Thus we define a unit NEP^* which takes into account the effects of variable bandwidth Δf taken to be 1 Hz and A are:

$$\mathrm{NEP}^* = \frac{NEP}{\sqrt{A\Delta f}} \tag{1.2.3}$$

The reciprocal of this quantity is termed the Detectivity D^*, which is a measure of the ability to distinguish a light signal from the detector noise:

$$D^* = \frac{\sqrt{A\Delta f}}{NEP} \tag{1.2.4}$$

The peak D^* of a QWIP is normally defined as [11, 12]:

$$D_P^* = \frac{R_P\sqrt{A\Delta f}}{\sqrt{4eI_d g\Delta f}} \tag{1.2.5}$$

where R_p is the peak responsivity, and I_d is the dark current.

From equation (1.2.5), we can see that D_p^* depends on R_p and I_d. Therefore, to maximise D^* we have to increase R_p and reduce I_d. To reduce the dark current, one can lower the doping concentration N_d since dark current depends on E_F exponentially [14]. However, this will result in a lower α, and thus a lower η and R. Gunapala *et al* [12] have shown that by reducing N_d, the I_d can be reduced by over two orders of the magnitude without significantly affecting the D^*. In addition, by reducing the bias voltage, the dark current can be further reduced by another order of magnitude again keeping D^* essentially constant. The implies that we can apply a lower bias voltage and use a higher doping level to give a larger α, and thus a higher η and R without affecting the D^*. This apparent doping and bias insensitivity is advantageous to large 2D arrays where bias and doping nonuniformity can have an adverse effect on the performance.

1.3 Overview of Quantum Wells

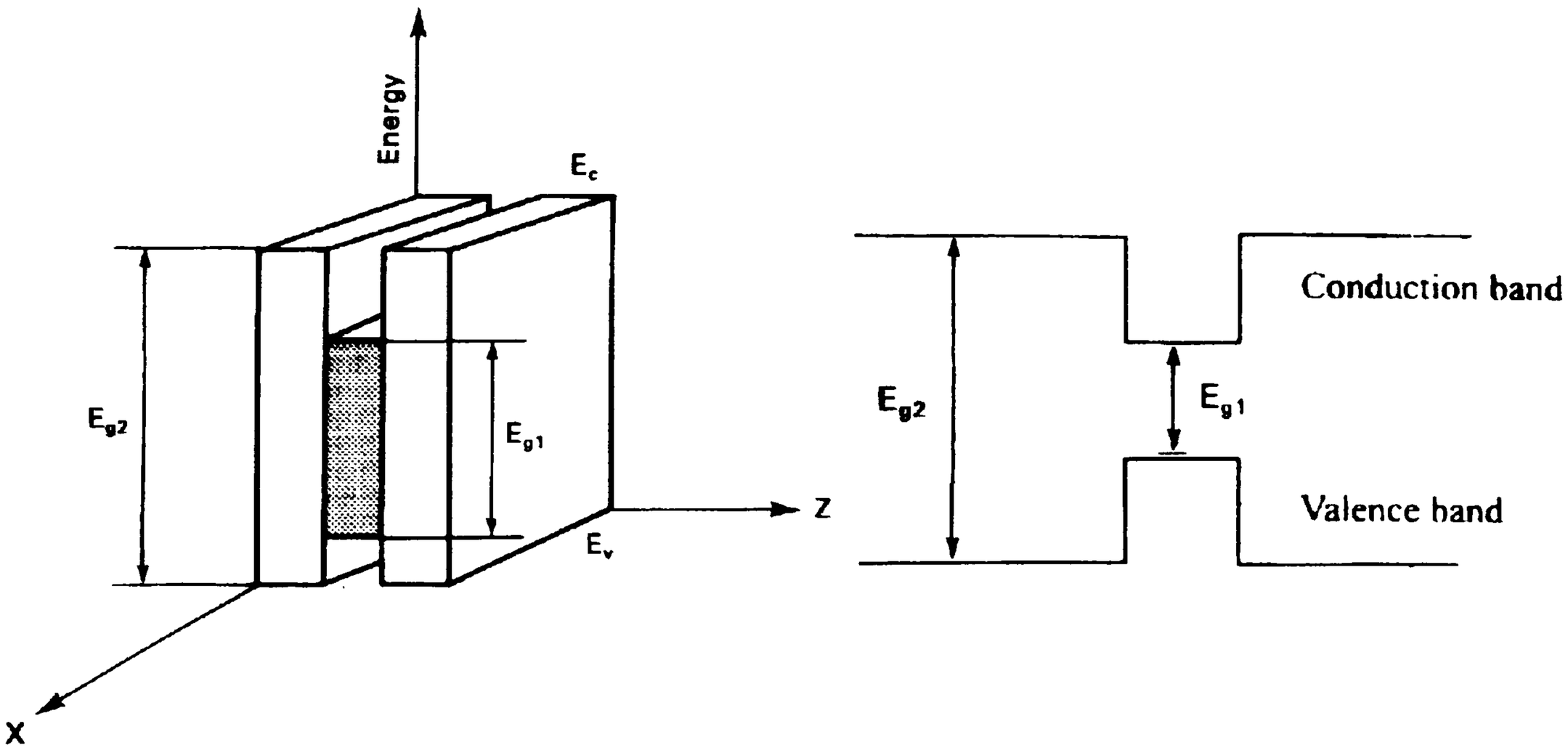

Figure 1.3.1: (a) Quantum well structure where a thin layer of narrow band gap semiconductor (E_{g1}) is sandwiched between two layers of another semiconductors of greater band gap (E_{g2}) and (b) a diagrammatic representation of the resulting energy band structure, showing the discontinuities in both conduction and valence bands.

In any 3-D, bulk semiconductor, electrons within the conduction (E_c) or valence (E_v) bands take on a nearly continuously varying range energies. However, by sandwiching one thin layer, low band gap semiconductor between two layers of another semiconductors of greater band gap a QW is created (see Fig. 1.3.1). The idea is to trap electrons in the lower band gap semiconductor (e.g., Gallium Arsenide (GaAs) which has a band gap energy of 1.42 electron volts (eV)) so that electrons would not be able to transverse the interface or barrier created by the higher band gap semiconductor (e.g., Aluminum Arsenide (AlAs) which has a band gap energy of 2.81 eV). If the GaAs -the actual quantum well-is thin enough, the energy levels of the electrons confined within the well become quantised, that is restricted to discrete well-defined energy levels as shown in Fig. 1.3.2.

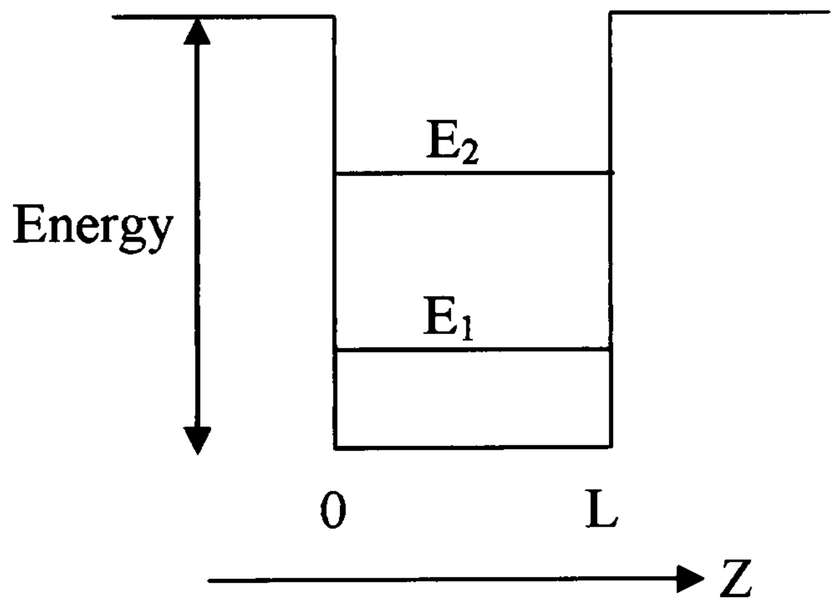

Figure 1.3.2: Conduction band edge profile showing the subband energy levels E_1 and E_2.

Since there is a discontinuity in the conduction and valence band edges in a QW, the carriers are restricted in the z (growth) direction but are essentially unrestricted in the xy plane. The total energy E is related to momentum in the xy plane (K_x or K_y) by the following equation (assuming parabolic bands):

$$E = E_n + \frac{\hbar^2\left(K_x^2 + K_y^2\right)}{2m} \tag{1.3.1}$$

where m is the mass of electron, $\hbar$=h/(2π) is the Planck's constant, E_n is the eigenenergy:

$$E_n = \frac{n^2 h^2}{8mL^2} \qquad n = 1, 2, 3... \tag{1.3.2}$$

where L is the QW width and n is the quantum number. We obtain a set of subbands as shown in Fig. 1.3.3.

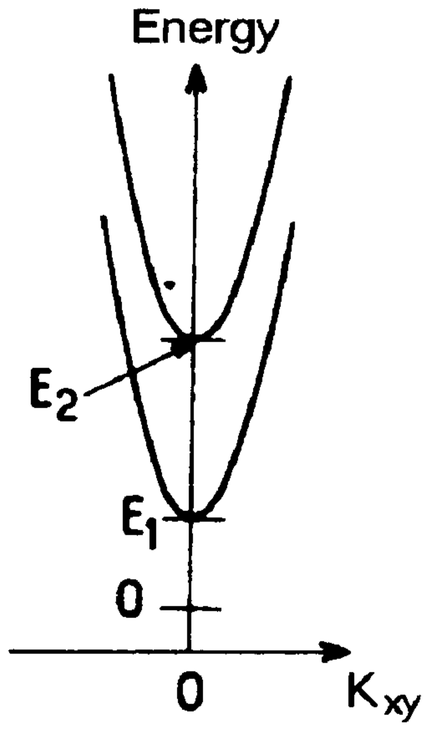

Figure 1.3.3: The quadratic dispersion relation of the E_1 and E_2 subbands with respect to K_{xy}.

The density of states in the K_{xy} plane is given by the 2-D expression $D(E)=m/\pi\hbar^2$ and is independent of E and n. Therefore, for n=1 (the lowest subband) $E_1=h^2/(8mL^2)$, if we arbitrarily put $D(E_1)=1$, then for the next subband (n=2) we have $E_2=4E_1$, and $D(E_2)=2$, and so on, we obtain the 2-D density of states as a function of E as shown in Fig. 1.3.4.

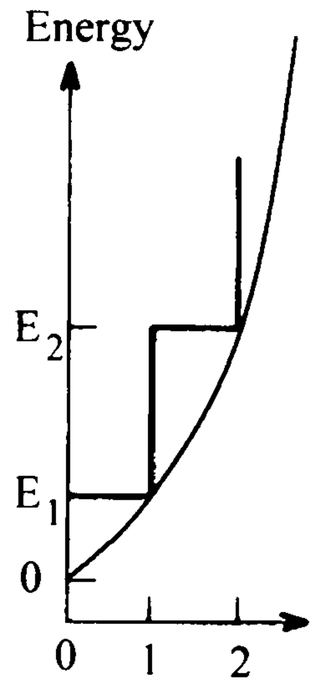

Figure 1.3.4: 2-D density of states as a function of energy. The 3-D density of states is also shown for comparison.

As can be seen from Fig. 1.3.4, the density of states for a given subband is a step function that starts at the appropriate confinement energy. Thus the optical absorption in a QW is a series of steps with one step for each quantum number. Also, it can be seen that if we increase the QW width, a smooth transition to the bulk behaviour can be obtained as the steps become increasing closer together until they merge into the continuous absorption edge of the bulk material. By controlling the physical size and composition of the different semiconductors in a device, researchers can now tune the electronic properties they want.

1.3.1 Quantum Well with infinite barriers

Since the electrons are being confined in the well, the energy levels can be found from solution of the 'particle in a box' problem as shown in the figure below. This simple analytical solution provides a good approximation of the energy levels in an infinite QW (i.e., with infinite high barriers). Hence we will use it to illustrate some basic features of QW energy levels. However, in Chapter 3, we will use a more sophisticated three-band Kane *k.p* model that takes into account the effects of strain

and bulk nonparabolicity to obtain the band structure and energy levels in all the samples used in this thesis.

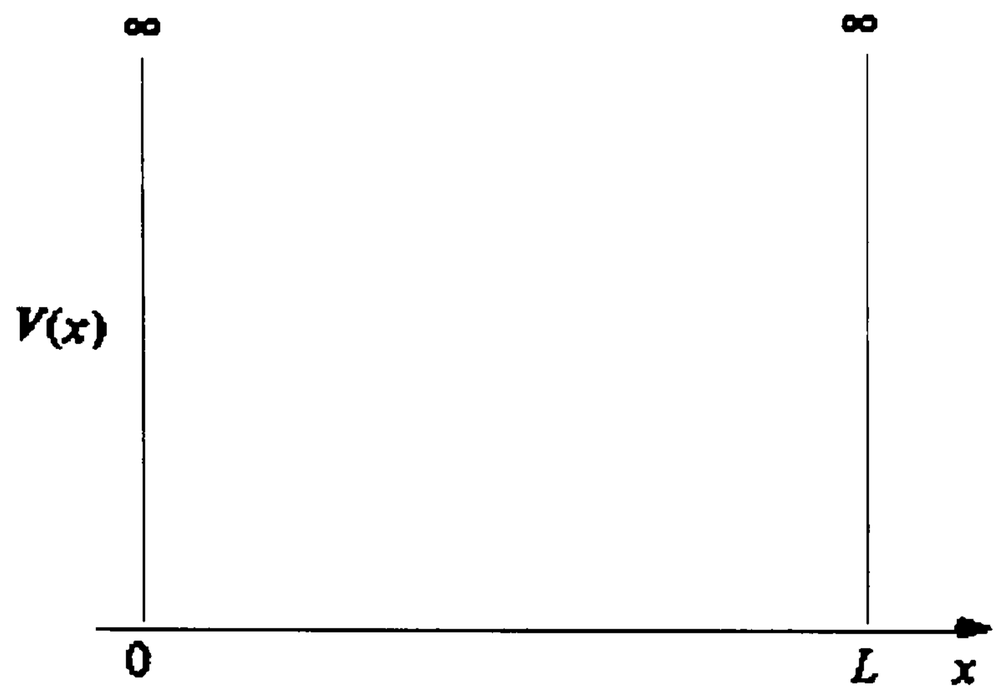

Figure 1.3.1.1: One dimensional potential well of infinite depth.

Consider the particle confined to a one dimensional box of width L. The potential energy (V) inside the box is zero and rises to infinity ∞ at the boundaries, thus confining the particle. If V=0 inside the box, no force acts on it and it will be reflected from the wells.

The time independent Schrödinger equation for the region inside the box is:

$$\frac{\partial^2 \Psi}{\partial X^2} + \frac{2m}{\hbar^2}(E - V)\Psi = 0 \qquad (1.3.1.1)$$

where Ψ=wave function

E=total energy of the system

V=potential energy

and since V=0 then equation (1.3.1.1) becomes:

$$\frac{\partial^2 \Psi}{\partial X^2} + \frac{2m}{\hbar^2}(E)\Psi = 0 \qquad (1.3.1.2)$$

A general solution to this equation can be verified by substitution and it has the form:

$$\Psi = A\sin\frac{\sqrt{2mE}}{\hbar}X + B\cos\frac{\sqrt{2mE}}{\hbar}X \qquad (1.3.1.3)$$

where A and B are constants.

The particle cannot appear outside the box since it would have to possess an infinite amount of energy to do so. Therefore, we have the following conditions:

a) $\Psi=0$ for X<=0

b) $\Psi=0$ for X>=L

To satisfy condition (a), we see that B=0 and for condition (b)

$$\sin\frac{\sqrt{2mE}}{\hbar}L = n\pi \qquad n = 1, 2, 3... \qquad (1.3.1.4)$$

The above equation shows that for this particle, the energy can take discrete values- eigenvalues E_n which is given in equation (1.3.2). The wave function for particle with energy E_n:

$$\Psi_n = A\sin\frac{\sqrt{2mE_n}}{\hbar}X \qquad (1.3.1.5)$$

substituting for E_n gives the eigenfunction

$$\Psi_n = A \sin \frac{n\pi}{L} \mathrm{X} \qquad (1.3.1.6)$$

We can see that Ψ_n is a single valued function of X and is continuous hence $\partial\Psi_n/\partial X$ is also continuous. The integral of $|\Psi_n|^2$ over all space is finite as can be seen by integrating $|\Psi_n|^2\, \partial X$ from X=0 to L (since the particle cannot be outside the box).

$$\begin{aligned} \int_{-\infty}^{+\infty} |\Psi_n|^2 \, \partial X &= \int_0^L |\Psi_n|^2 \, \partial X \\ &= A^2 \int_0^L \sin^2\left(\frac{n\pi X}{L}\right) \partial X \\ &= A^2 \frac{L}{2} \end{aligned} \qquad (1.3.1.7)$$

However, to normalise Ψ we must assign a value to A such that $|\Psi_n|^2$ when integrated from $-\infty$ to $+\infty$ is equal to unity (i.e., the probability of finding a particle at all=1).

Therefore

$$\begin{aligned} \int_{-\infty}^{+\infty} |\Psi_n|^2 \, \partial X &= 1 \\ A^2 \frac{L}{2} &= 1 \\ A &= \sqrt{\frac{2}{L}} \end{aligned} \qquad (1.3.1.8)$$

$$\Psi_n = \sqrt{\frac{2}{L}} \sin \frac{n\pi}{L} \mathrm{X} \qquad (1.3.1.9)$$

Plotting these results gives

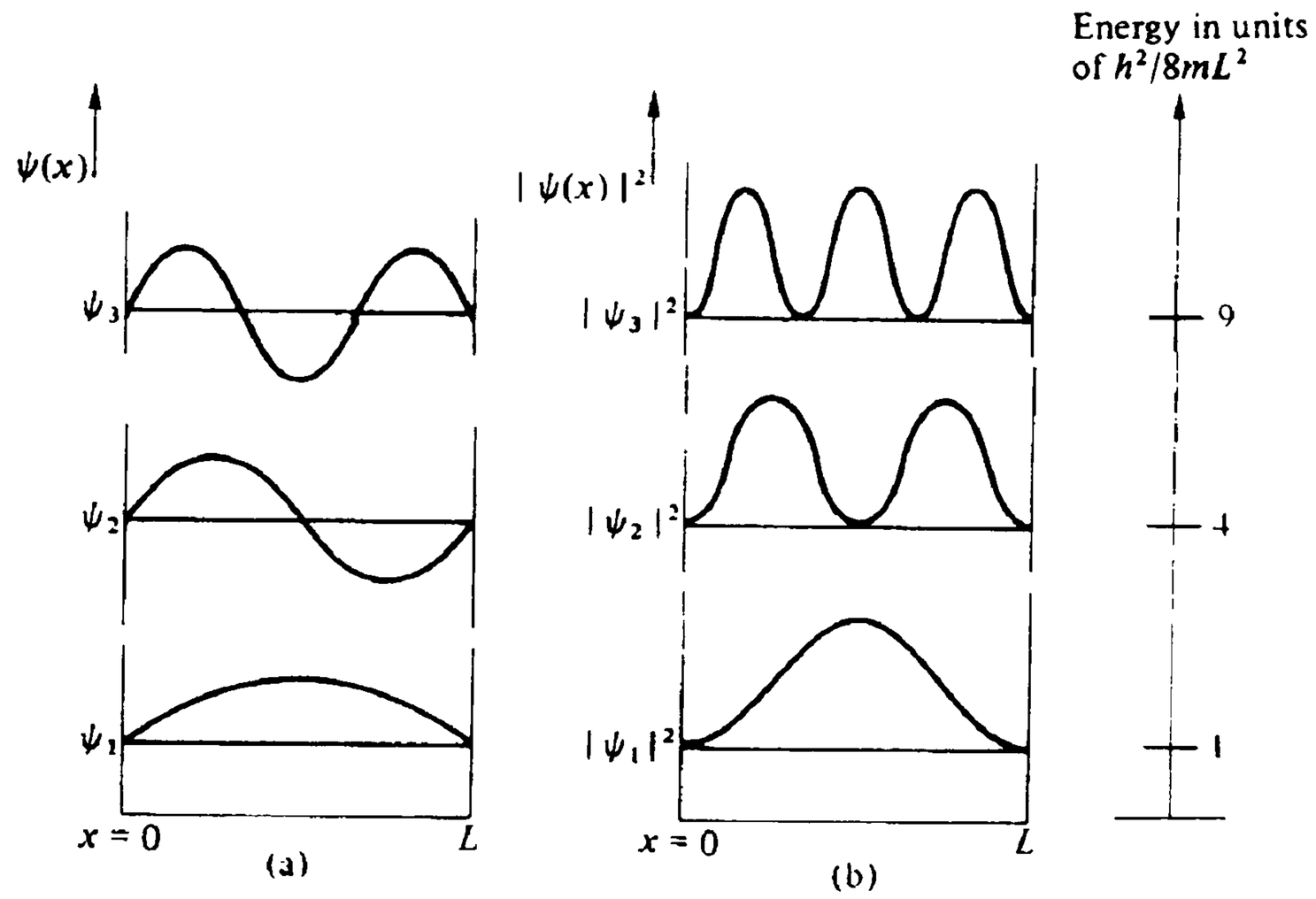

Figure 1.3.1.2: Ground state and the first two excited states of an electron in a potential well: (a) the electron wave functions and (b) the corresponding probability density functions. The energies of these three states are shown on the right.

One point to note is that $|\Psi_n|^2$ at any point (X) in the box is equal to the probability of finding the particle there. As you can see in this example the energy value and wavefunction in the well is dependent on the well width, mass of the electron and the barrier height.

Since electrons are now confined in the thin layers (the well), the whole structure thus can be regarded as a completely new material having properties of neither the well nor the barrier [15-24]. Figure 1.3.1.3 shows the band lineup of a QW of GaAs in $Al_{0.4}Ga_{0.6}As$ where E_1 is the transition in the well.

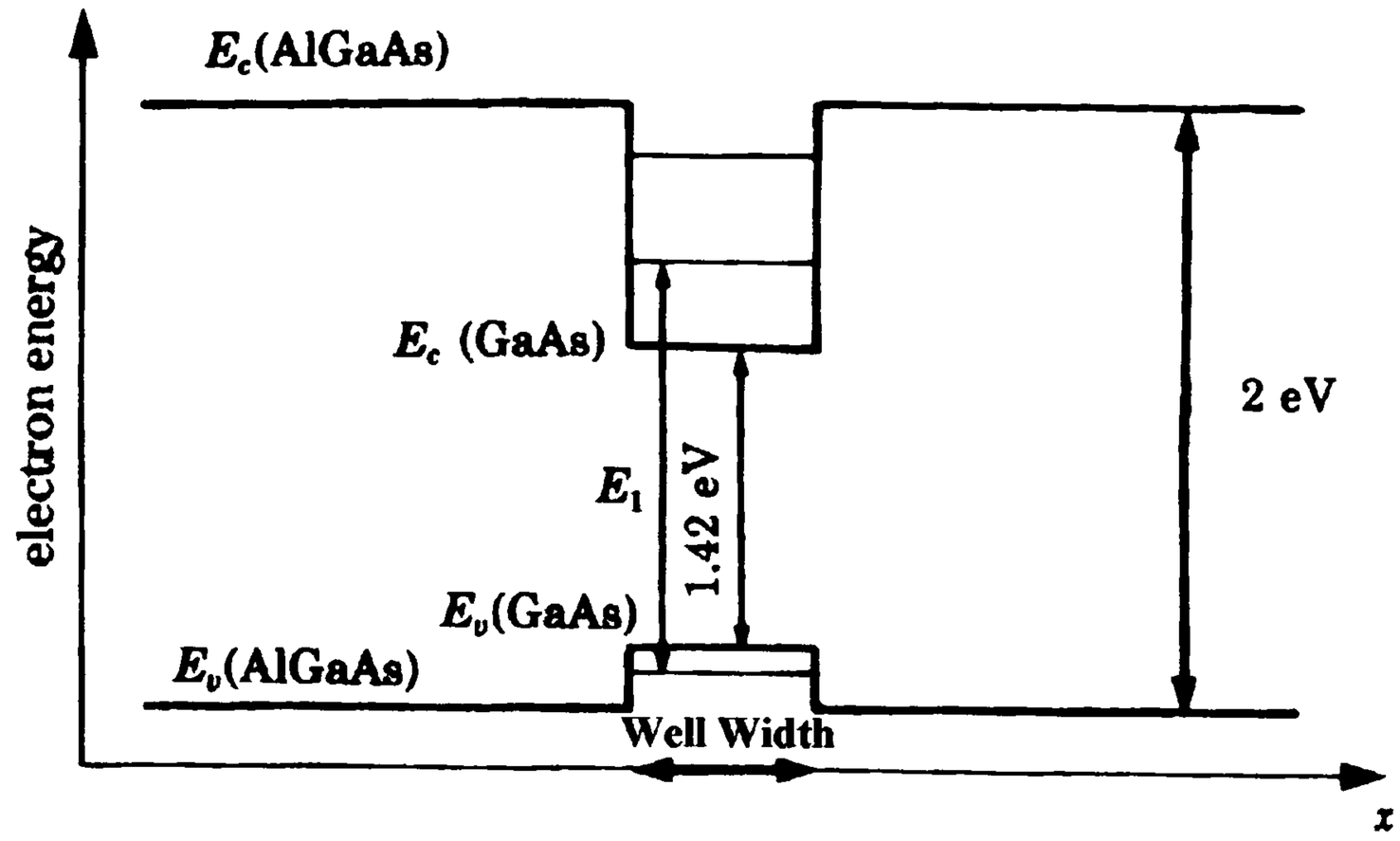

Figure 1.3.1.3: Band structure of a QW of GaAs in $Al_{0.4}Ga_{0.6}As$.

1.3.2 Intersubband transitions in Quantum Wells

Detectors based on intersubband absorption (transition within the same band) not only offer the advantages of long wavelength detection using large band gap materials, but also large oscillator strength, fast response time, and large optical nonlinearities as compared to conventional interband transitions [25-28]. Hence, intersubband optical transitions between quantised electronic levels in the semiconductor QWs are of crucial importance for the implementation of devices such as infrared photodetectors and mid-infrared semiconductor lasers.

A typical conduction band edge and the operation principle of a typical QWIP is shown in Fig. 1.3.2.1.

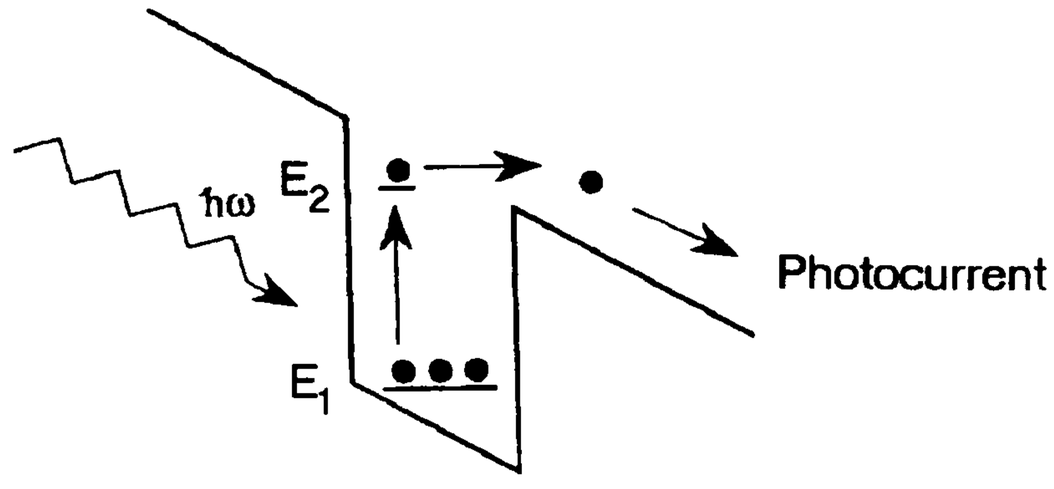

Figure 1.3.2.1: Schematic diagram of a typical conduction band edge of a QW by the application of an applied electric field. The photon ħω causes transitions from the ground state E_1 to the excited state E_2, causing a photocurrent.

The QWs are designed to have two states; ground state E_1 and first excited state E_2. E_2 is located close to the top of the band edge of the barrier so that the photoexcited carriers can easily escape from the QW and give rise to the photocurrent under the effect of the applied field. The energy separation (the intersubband transition energy, E_{ISB}) that corresponds to the wavelength of the light to be detected can be expressed as:

$$E_{ISBT} = E_{n+1} - E_n \tag{1.3.2.1}$$

Substituting n=1 into equation (1.3.2), we have

$$E_{ISBT} = \frac{3}{8}\left(\frac{h^2}{mL^2}\right) \tag{1.3.2.2}$$

It can be seen from the above formula that the E_{ISBT} is inversely proportional to the square of the QW width and effective mass of the carrier in the QW. Hence, the wavelength of the peak response can be engineered by simply varying the QW width in a given material system. Unlike detectors that utilise interband transitions, the QW

of QWIPs must be doped. The Fermi energy level E_F is calculated, assuming an infinite barrier, using the equation below [29]:

$$E_F = \frac{\hbar^2 L_w N_D \pi}{m^*} \qquad (1.3.2.3)$$

where N_D is the three-dimensional electron doping density in the well, L_w is the well width and m^* is the effective mass of electron.

1.3.2.1 Dark Current

In order to use intersubband absorption process to produce an electrical signal and hence optical detection, one has to satisfy the following conditions:

a) The ground state electrons should not produce a high dark current (this is the current that flows through a biased detector in the dark i.e., without any photons striking it). The dark current in a QWIP is typically four to five orders of magnitude higher than in a direct-gap semiconductor with the same band gap and operating at the same temperature [29]. In QWIPs, the dark current originates from three different mechanisms [27, 30, 31] (see Fig. 1.3.2.1.1). They are:

1) Sequential Tunneling - This is due to quantum mechanical tunneling of ground state electrons from well to well through the barriers. This process is independent of temperature and dominates the dark current at very low temperature ($T < 40$ K).

2) Thermally Assisted Tunneling - The ground state electrons are thermally excited and tunnel through the triangular part of the barrier, formed by the applied field, into the continuum. This process occurs between 40 K< T < 70 K.

3) Thermionic Emission - The ground state electrons are thermally excited directly out of the well into the continuum. This process occurs at T > 70 K.

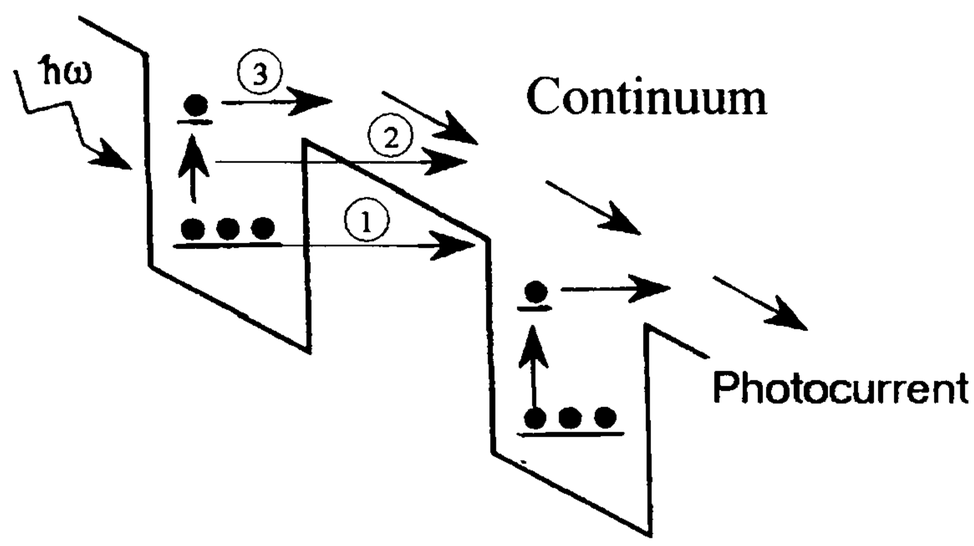

Figure 1.3.2.1.1: Schematic diagram of a typical conduction band edge of a QW under the affect of an applied electric field. The three dark current mechanisms are: 1) sequential tunnelling, 2) thermally assisted tunnelling and 3) thermionic emission.

The major source of dark current for QWIPs operating at a higher temperature is thermonic emission and minimising this is crucial to the commercial success of QWIPs. Hence, a higher barrier height and thicker barrier width should be used in order to improve the detector noise performance [32, 33].

b) It should be possible to extract the excited state electrons from the quantum well so that it can contribute to photocurrent. The excited state electrons

should, therefore, be ideally near the top of the quantum well barrier so that the excited electrons can be extracted with ease by an applied electric field [34, 35].

1.3.2.2 Bound-to-Bound Transitions

Figure 1.3.2.2.1: Conduction band profile of a bound-to-bound transition (a) A schematic of electron wavefunction in the ground state and the excited state. A photon having energy ħω excites an electron in the bound ground state to the bound excited state from where the photoexcited electron tunnel out of the well and thus contributes to the photocurrent as shown in (b).

Figure 1.3.2.2.1 shows a QW containing two bound states. The incident infrared radiation results in an infrared absorption due to the intersubband transition from a bound ground state to the bound excited state where the photoexcited carriers tunnel out of the well as shown above. These photoexcited carriers which escape from the well are then being transported by an electric field in the continuum above the top of the barrier thereby producing a photocurrent. As the excited state is bound, therefore, a higher bias is required to assist the photoexcited carriers to tunnel through the tip of the barrier in order to escape into the continuum. It is well known that if the voltage is too large, unwanted leakage from the ground state may occur leading to higher dark current [11]. This will degrade the performance of the device.

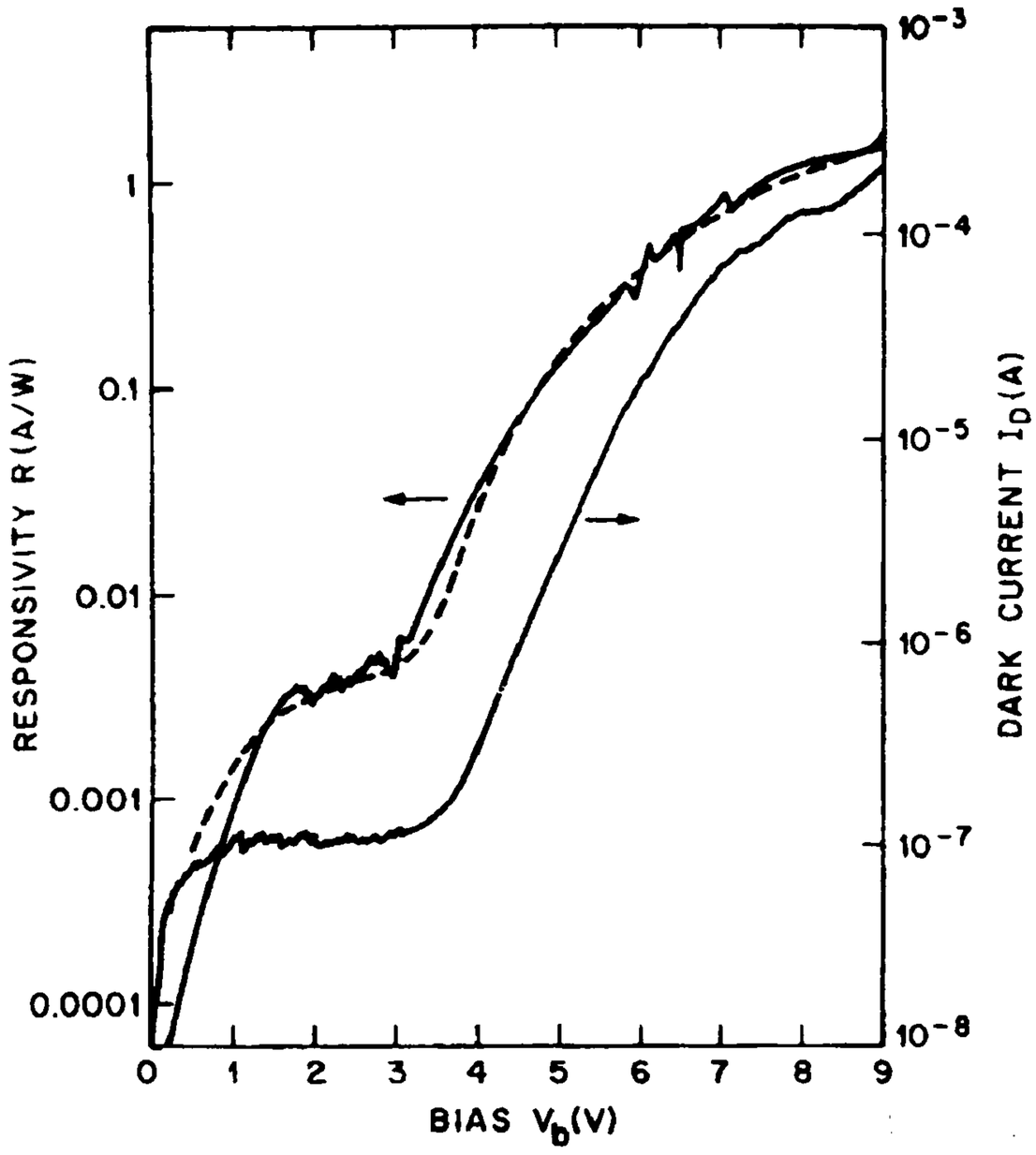

Figure 1.3.2.2.2: Voltage dependence of the dark current and the responsitivity for a bound-to-bound QW. The dashed line is theory [11].

1.3.2.3 Bound-to-Continuum Transitions

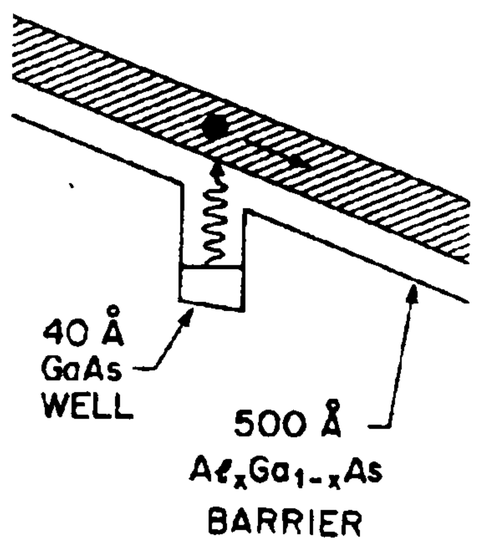

Figure 1.3.2.3.1: Conduction band structure for a bound-to-continuum QW showing the photoexcitation and hot electron transport processes.

Figure 1.3.2.3.1 shows a conduction band profile of a bound-to-continuum QW which is achieved by making the width of the well small enough that the excited state is pushed up into the continuum. This bound-to-continuum design provides improved absorption strength as compared to bound-to-bound QW [36] and

eliminates the need for the photoexcited carriers to tunnel through the barrier so as to escape from the well (meaning a lower bias voltage is required for the photoexcited carriers to efficiently escape from the well thus strongly lowering the dark current). This leads to improve detector performance [37].

However, the spectral bandwidth of the bound-to-continuum QW is much broader than the bound-to-bound QW and this is expected as the excited state is now more delocalised [36-39].

1.3.2.4 Bound-to-Quasicontinuum Transitions

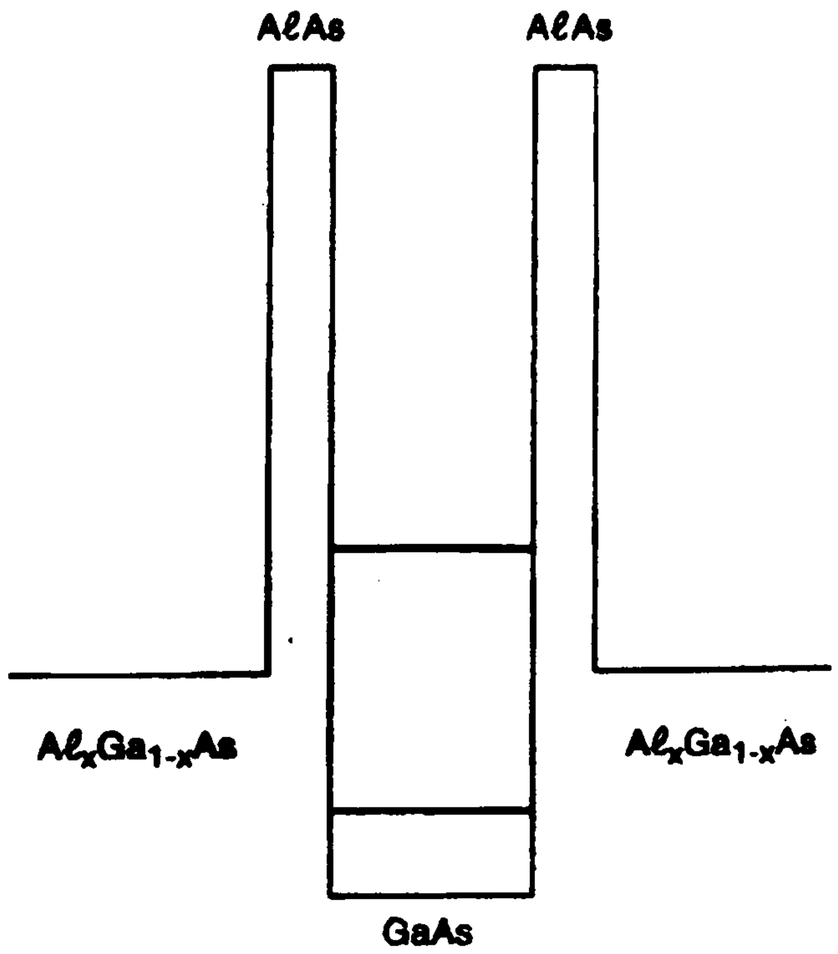

Figure 1.3.2.4.1: Schematic conduction band diagram of a bound-to-quasicontinuum QW.

Figure 1.3.2.4.1 shows a bound-to-quasicontinuum QW [10, 40-52] which is the intermediate between a strongly bound excited state and a weakly bound continuum state. As you can see from the diagram, the excited state is bound by the high barriers (AlAs) but is in the continuum of the lower barriers ($Al_xGa_{1-x}As$). Therefore, we would expect it to have an absorption spectrum of a bound-to-bound

QW (narrow spectral bandwidth) and with the high escape probability of a bound-to-continuum QW [11, 32].

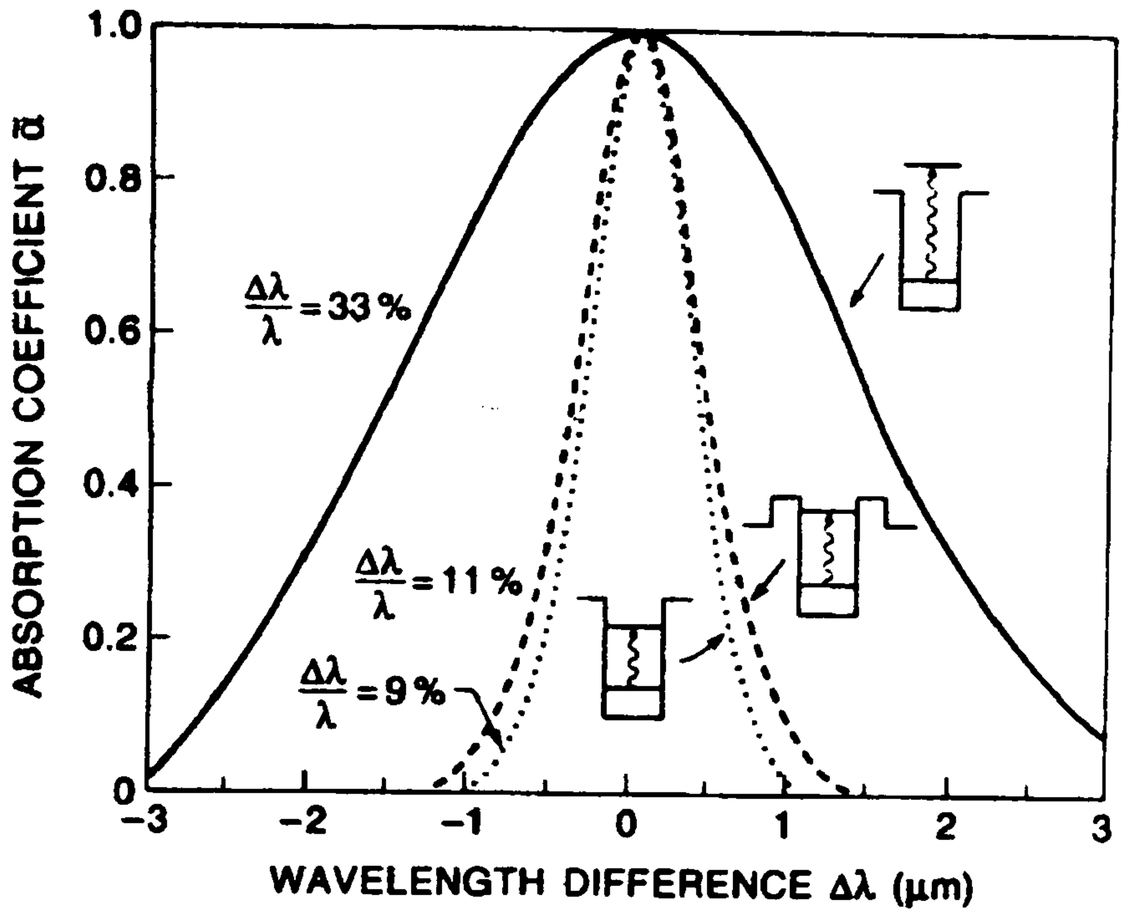

Figure 1.3.2.4.2: Normalised absorption coefficient a for bound-to-bound, bound-to-continuum and bound-to-quasicontinuum QW.

The use of the ultra high thin AlAs barrier results in the excited state being shifted towards higher energies thus allowing a large intersubband energy transition between the ground and the excited state.

As the ground state is confined both by the thin AlAs barriers and by the subsequent the thick $Al_xGa_{1-x}As$ layers, the dark current is, therefore, lowered as compared to QWIPs having the same detection wavelengths and well doping but lacking the AlAs thin barriers [45, 46]. Furthermore, since the excited state is now confined by the ultra thin AlAs barriers, it is only weakly bound. Thus, the photoexcited carriers can easily tunnel out of the well and escape and this causes an increase in detectivity as shown in Fig. 1.3.2.4.3 [11, 32]. Another reason for using thin AlAs barriers is that $Al_xGa_{1-x}As$ is a direct-gap semiconductor for $x<=0.45$ (i.e. Γ band is the lowest energy bandgap), but becomes indirect when $x>0.45$ (i.e. *X* band is

the lowest energy bandgap). This creates an *X* QW in the AlAs layer with $Al_xGa_{1-x}As$ x<=0.45 the barrier. Therefore, the AlAs layer cannot be too thick (more than 22 Å [46]) so that the transit time for the photoexcited carrier is sufficiently fast not to scatter from Γ to *X* states in the *X* QW.

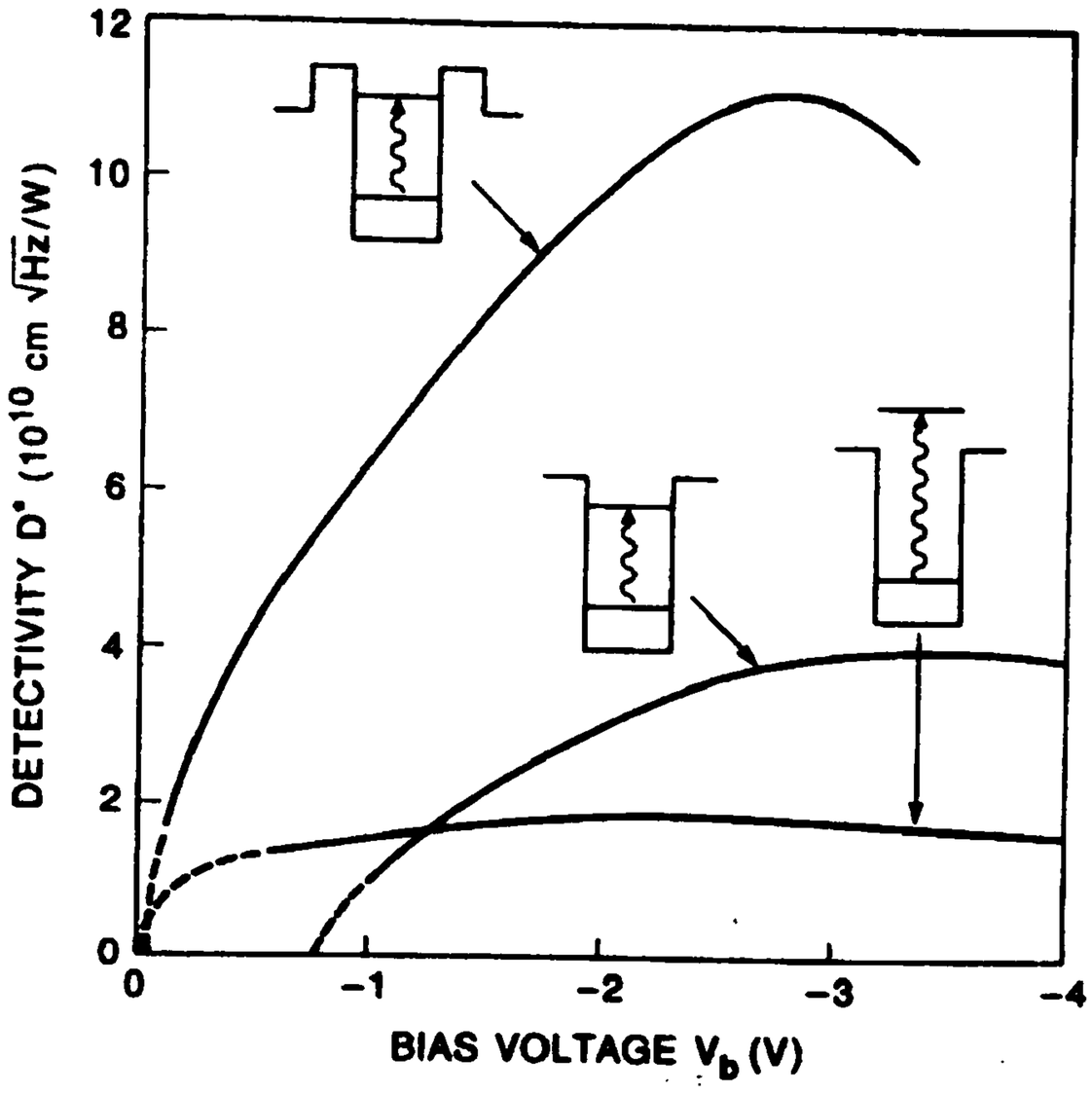

Figure 1.3.2.4.3: Detectivity D^* (at T=77K) vs bias voltage V_b for bound-to-bound, bound-to-continuum, and bound-to-quasicontinuum QW.

1.4 N versus P type Quantum Wells

Detectors based on transitions involving electrons in the conduction band, known as n-type QWIPs, are preferred over those based on holes in the valence band (p-type QWIPs) due to the lighter mass and higher mobility of electrons in the conduction band compared to holes in the valence band. However, one drawback associated with n-type QWIPs is that, only photons with a component of radiating electric field vector perpendicular to the plane of the QW is absorbed. Hence the

angle of incidence with respect to the QW layers must differ from zero [25, 28, 53-55].

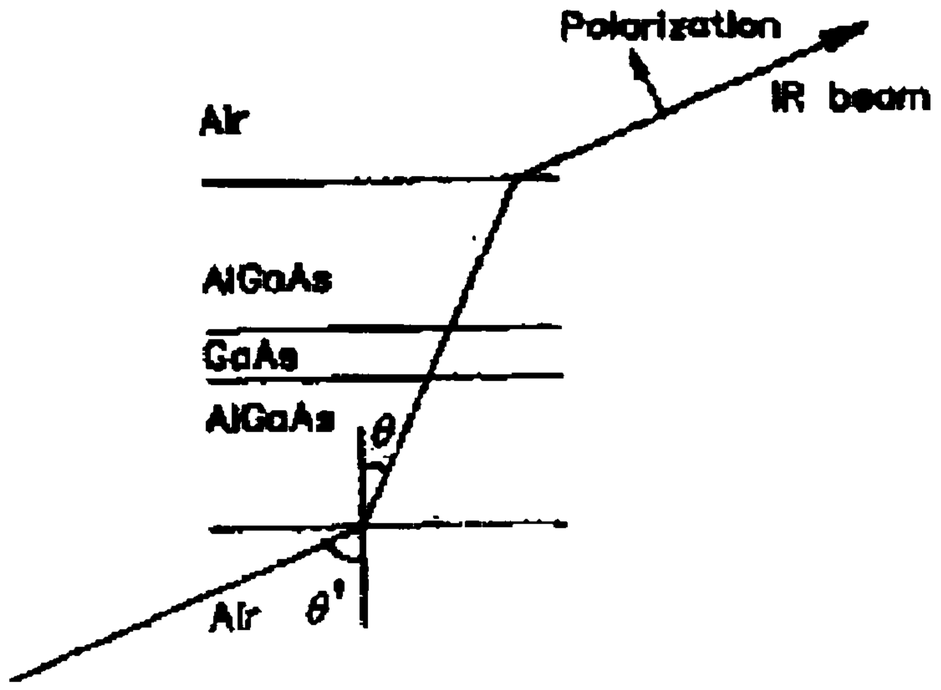

Figure 1.4.1: Sketch showing the angle of the infrared (IR) beam with respect to the QW.

To induce absorption, the sample can be oriented at the Brewster angle (~73^0) to maximise the electric field vector perpendicular to the plane of the QWs. This also reduces reflection loss. This can be shown in the reflection coefficient equation for light with its electric field vector polarised parallel to the plane of incident below

$$r_{\parallel} = \frac{n_t \cos\theta_i - n_i \cos\theta_t}{n_t \cos\theta_i + n_i \cos\theta_t} \tag{1.4.1}$$

where n_t=refractive index of the transmitted media

n_i=refractive index of the incidence media

θ_t=angle of transmission

θ_i=angle of incidence

θ_t and θ_i are related by Snell's law of refraction

$$\frac{\sin\theta_i}{\sin\theta_t} = \frac{n_t}{n_i} \tag{1.4.2}$$

Alternatively, to obtain the necessary optical coupling of radiation into the QW, n-type QWIPs are often fabricated with an optical grating to refract the normally incident radiation so that a component of radiation electric field perpendicular to the plane of the QW is absorbed [56, 57]. This, however, adds to the technical complications of device fabrication and system implementation. P-type QWIPs, do not suffer from this restriction due to the strong mixing of the heavy and light holes. This selection rule is lifted and all polarisations of incident radiation are absorbed [58-60].

Nevertheless, the development of p-type QWIPs has been impeded by their often inferior transport and confinement properties compared to n-type QWIPs. Furthermore, the smaller electron effective mass and the higher mobility typical of the conduction band are also highly desirable to the detector's sensitivity and speed. In addition, due to the different curvatures of dispersion relations for the heavy and light hole states (different effective masses), the absorption spectrum based on the intersubband transition between the heavy and light hole states is broad [61]. Hence the absorption strength [62] and detectivity [32] are significantly smaller than for intersubband transitions in the conduction band.

1.5 Asymmetric Wells

For a simple rectangular QW, we can only vary the well width and the barrier height (composition). In addition, the dipole matrix elements of transitions for odd-to-odd or even-to-even (i.e., 1-3 or 2-4) quantum numbers disappear (meaning these kind of transitions are not allowed) since the envelope functions of these energy states have the same parity due to the symmetry of the well. However, the symmetry of the well can be broken by applying a strong electric field [63] or doping the QW heavily [64]. As mentioned earlier, a high bias can produce relative large leakage current, which will degrade the performance of the device. For the heavily doped case, the large thermionic emission associated with the high doping densities will prevent the operation at higher temperatures. Another approach is to use an asymmetric structure such as a stepped QW as shown in Fig. 1.5.1.

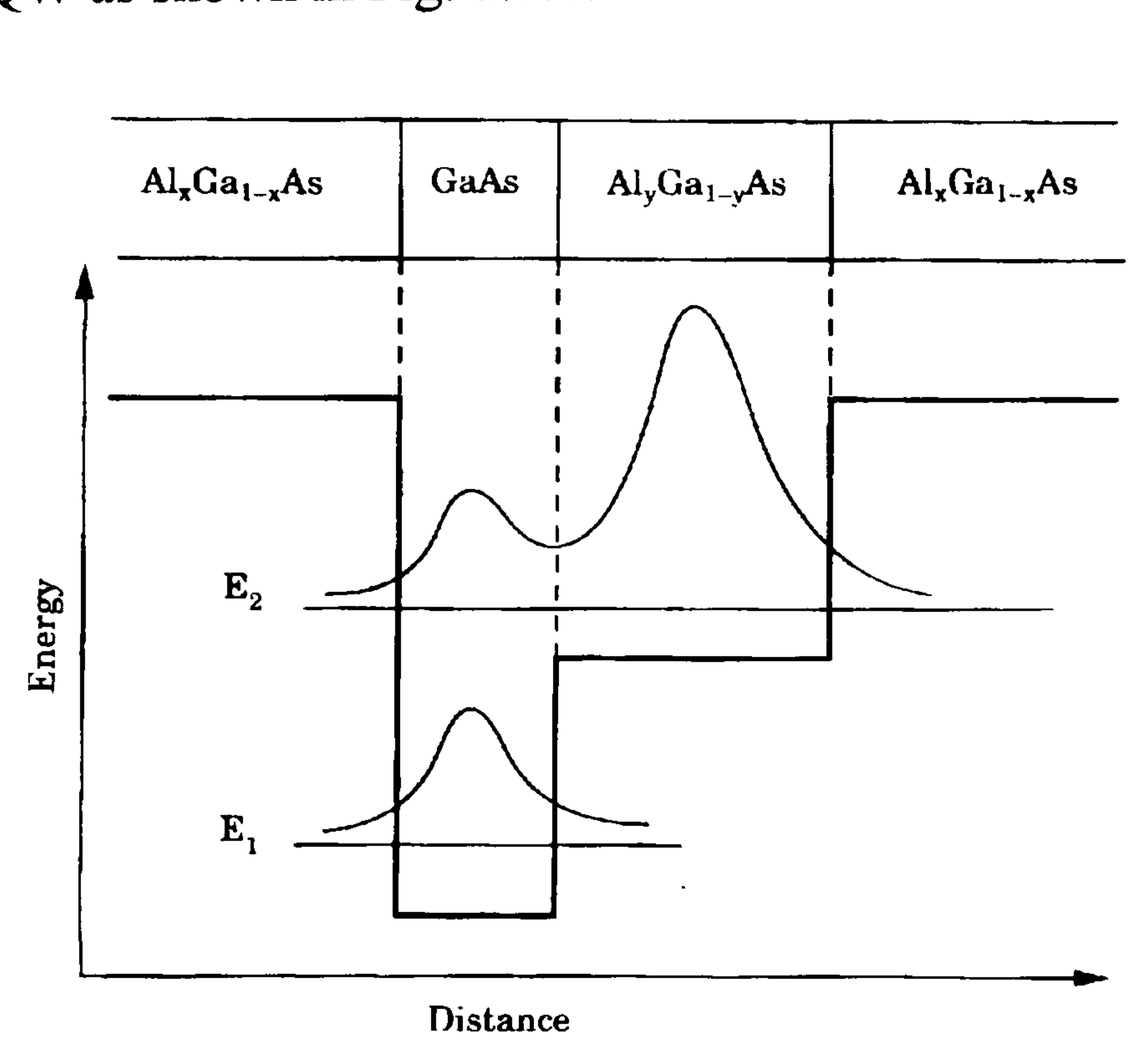

Figure 1.5.1: Conduction band profile of the asymmetric step QW.

The introduction of an additional barrier (step) inside the well results in normally "not allowed" transitions becoming allowed. Furthermore, the transition

energies and related oscillator strengths can now be tuned "independently" by changing the well width, the step width, and the step height. This gives us an advantage over the high electric field and doping induced asymmetry in a simple square well [65-67].

In such a structure as shown in Fig. 1.5.1, the average position of an electron in the quantised level E_2 is shifted in space with respect to the quantised level E_1. This charge displacement is due to a very large transition matrix element between E_1 and E_2 which ensures a very strong coupling of the well with the electromagnetic field. This is due to the fact the wavefunction in the smaller well E_1 can overlap more with the E_2 wavefunction in the wider well as compared to overlap found for a symmetric well of similar dimensions (see Fig. 1.3.1.2).

When the structure in Fig. 1.5.2 is illuminated with infrared photons of energy $\hbar\omega$, electrons can either be excited from E_1 to E_2 the bound-to-bound transition (b) or from E_1 to the delocalised levels (a) above the $Al_xGa_{1-x}As$ barrier (bound-to-continuum transition).

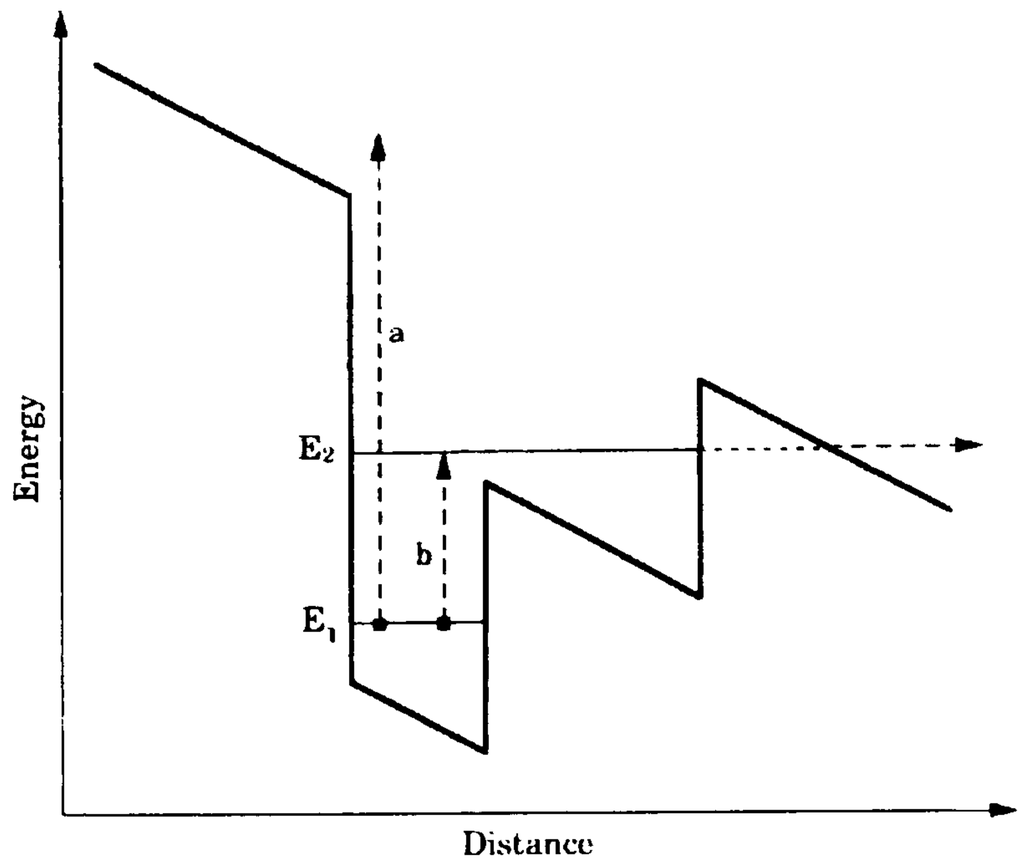

Figure 1.5.2: Modification of the conduction band profile of a step QW by the application of an applied electric field (stark effect [28]).

If an infrared photon excites a bound-to-continuum transition as shown in (a) of Fig. 1.5.2, the photoexcited carrier is then swept by the applied electric field and thus contributes to the photocurrent. If a photon excites a bound-to-bound (b) transition (from E_1 to E_2), the photoexcited carrier can then tunnel from E_2 through the tip of the triangular barrier in presence of the applied electric field where it can then contribute to the photocurrent.

Due to the asymmetry of the structure, the subband level energy spacing of E_1 and E_2 can either be moved closed to or further apart depending on the direction of the applied field. Hence, we can shift to longer (red) or shorter (blue) wavelengths simply by changing the bias direction as shown below [68-72].

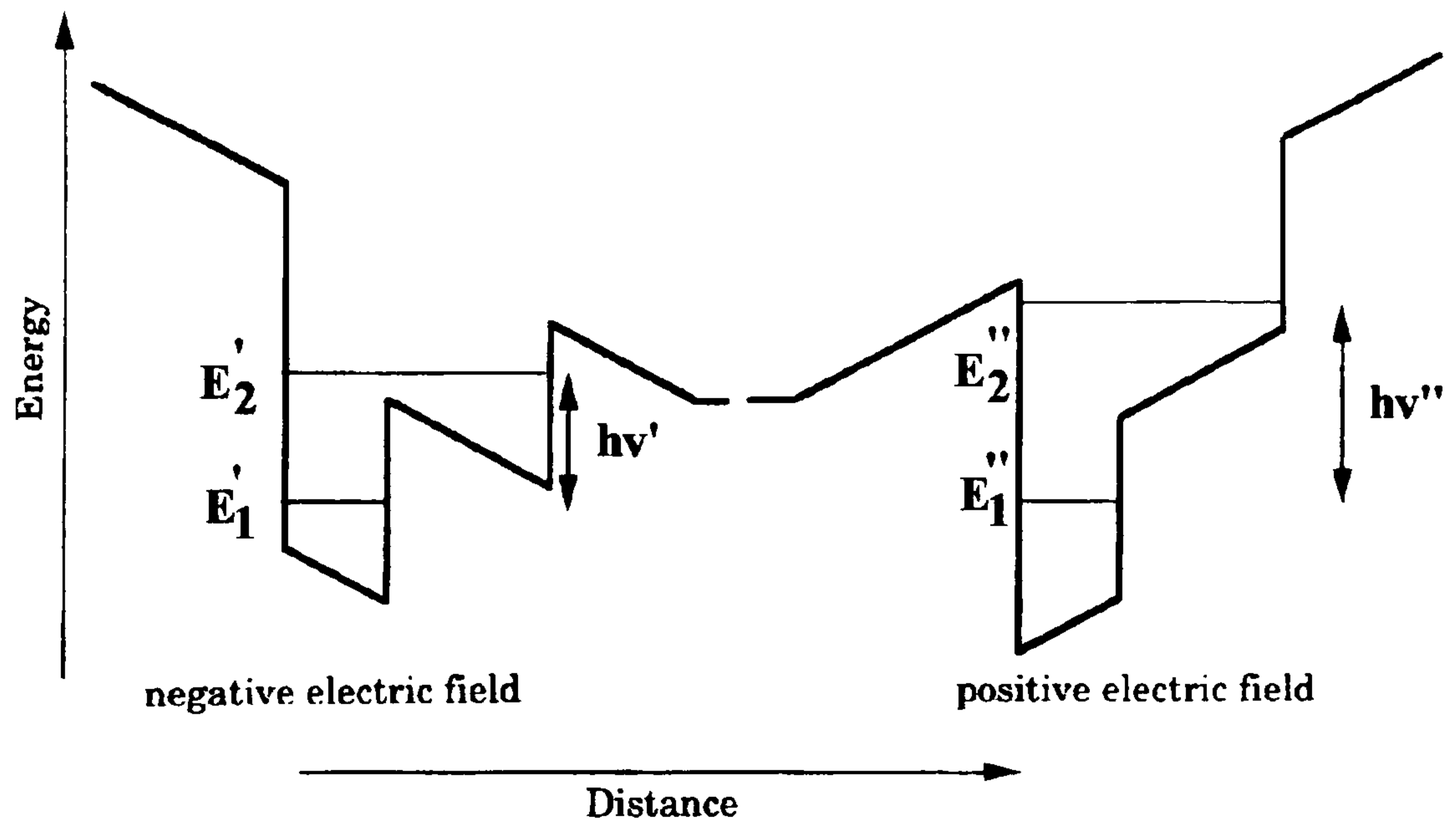

Figure 1.5.3: Effect of stark shift [28] on the conduction band profile. The modifications of the energy level positions and of the optical transitions depend on the polarity of the applied electric field.

Besides showing large Stark shifts due to the optical transitions from the states in the small well to the states in the big well, the oscillator strength which indicates whether a transition is allowed or forbidden is also comparable to that of the symmetric well case. This is due to the fact that the localised wave function in the

small well can overlap appreciably with those in the big well. Hence, large Stark shifts as well as large oscillator strengths can be achieved in asymmetric wells [65, 66, 69].

1.6 Absorption Spectra of Intersubband Transitions

The absorption spectrum can be modelled approximately using a Lorentzian line shape which can be fitted according to the following form:

$$\frac{A}{(w_o - w_p)^2 + \Gamma^2} \tag{1.6.1}$$

where 2Γ is the full width at half maximum (FWHM) of the absorption peak, w_o is the photon energy (eV), w_p is the intersubband transition peak energy (eV). A and Γ are used as fitting parameters. By integrating the area under the absorption curve, we obtain the integrated absorption intensity I_{abs}. The I_{abs} at Brewster angle (~73^0) is given by [25] (Note: for 45^0 waveguide geometry a factor F is included in the numerator which takes into account the internal reflections at each boundary and changes in path the length of a single ray [73]):

$$I_{abs} = N_s W(\frac{e^2 h}{4\varepsilon_0 m_w c})\left(\frac{f}{n_r^2\sqrt{n_r^2+1}}\right) \tag{1.6.2}$$

where f is the oscillator strength defined by [25]:

$$f = (\frac{2m_w\omega}{\hbar})\langle z\rangle^2 \tag{1.6.3}$$

and the dipole matrix element <*z*>

$$\langle z \rangle = L_w \left(\frac{8}{\pi^2}\right)\left[\frac{mn}{\left(m^2 - n^2\right)^2}\right] \tag{1.6.4}$$

where N_s is the two-dimensional electron density per well, W is the number of wells, m_w is the well effective mass, n_r is the refractive index, ω is the transition frequency, L_w is the well width and m and n are integers denoting the initial and final states. From equations (1.6.2) and (1.3.2.3), one can see that there is a trade off between strong absorption intensity and low dark current as the dark current depends exponentially on E_F [14].

1.7 Use of Strained Layer Materials in Quantum Wells

QWIPs based on the lattice matched $GaAs/Al_yGa_{1-y}As$ material system have been widely investigated and high performance, large uniform focal plane arrays (FPAs) for detection in the 6 to 18 μm range have already been demonstrated by many research groups [74-80]. For detection below 6 μm [81] a different material system is needed due to the problems associated with using using high Al content [81, 82]. The direct gap materials, $GaAs/Al_{0.45}Ga_{0.55}As$ grown on GaAs [83] and $In_{0.53}Ga_{0.47}As/In_{0.52}Al_{0.48}As$ lattice-matched to InP [84], have conduction band offsets (ΔE_C) of ~ 350 meV and ~ 500 meV, respectively. The use of a lattice-mismatched (strained-layer) material system is thus necessary since loosening of the lattice matching constraint allows increased flexibility in choosing constituent materials. Among many lattice-mismatched systems, the $In_xGa_{1-x}As/Al_yGa_{1-y}As$ material system

has attracted much attention [82]. However, high crystalline quality lattice-mismatched systems can only be fabricated provided that the layer thicknesses do not exceed strain-dependent critical values [85-88] as strained-layer growth of thin epitaxial films upon substrates with different lattice parameters is known to be sensitive to atomic misfit and film thickness. This limits the indium content and the number of QWs that can be grown without significant material degradation. This mismatch increases with (x) and the strain increases with the number of periods until the material relaxes. Then misfit dislocations are formed in order to relieve the strain energy built into the crystal as a result of the misfit between the epilayer taken as a whole and its substrate. Therefore, knowledge of the critical layer thickness (h_c) (defined as the thickness at which the strain energy density in the film is sufficient to create a fully dense network of dislocations) is a fundamental requirement for growing high quality lattice-mismatched heterostructures. Fig. 1.7.1 shows the concept of h_c and dislocation formation [89].

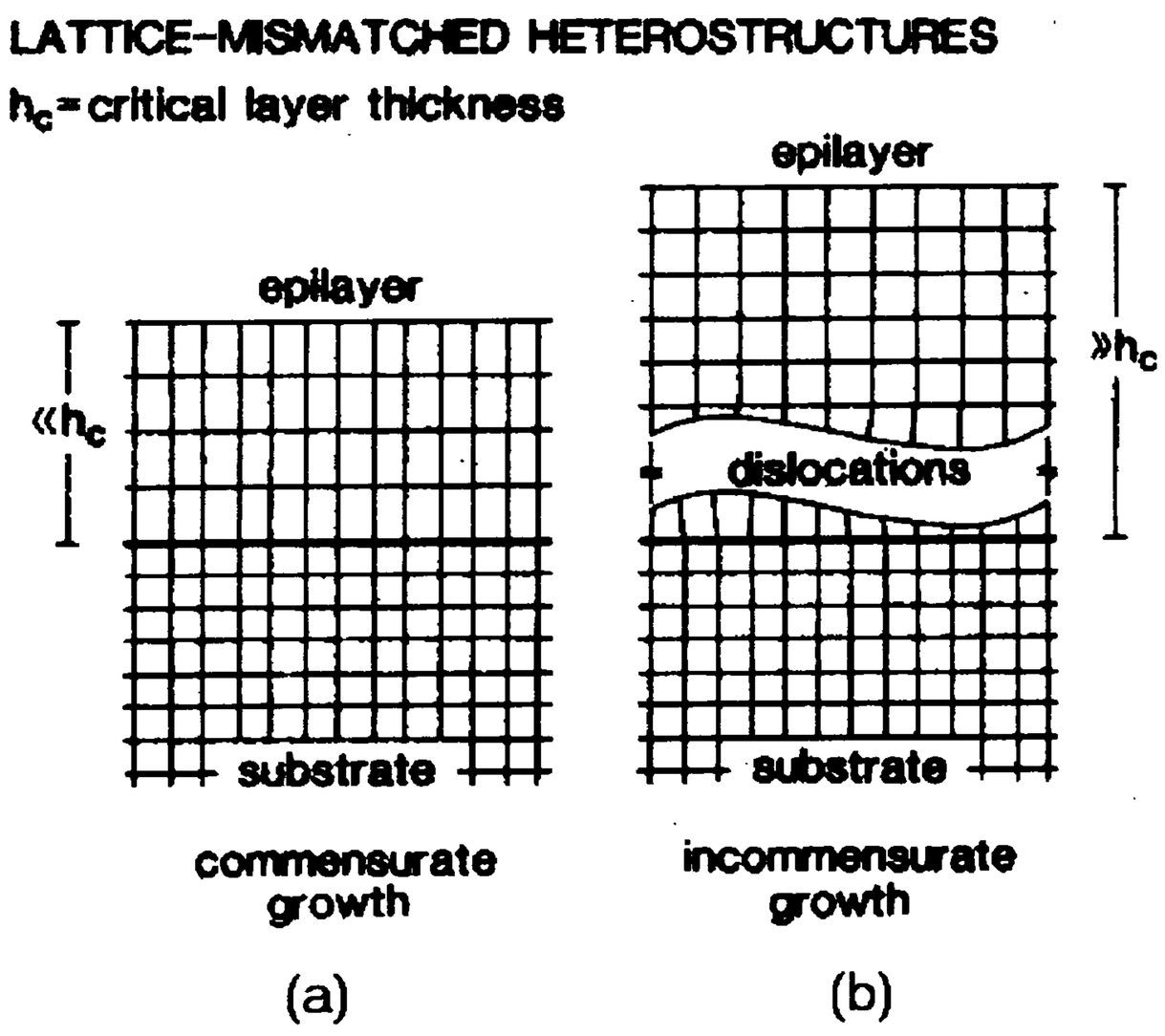

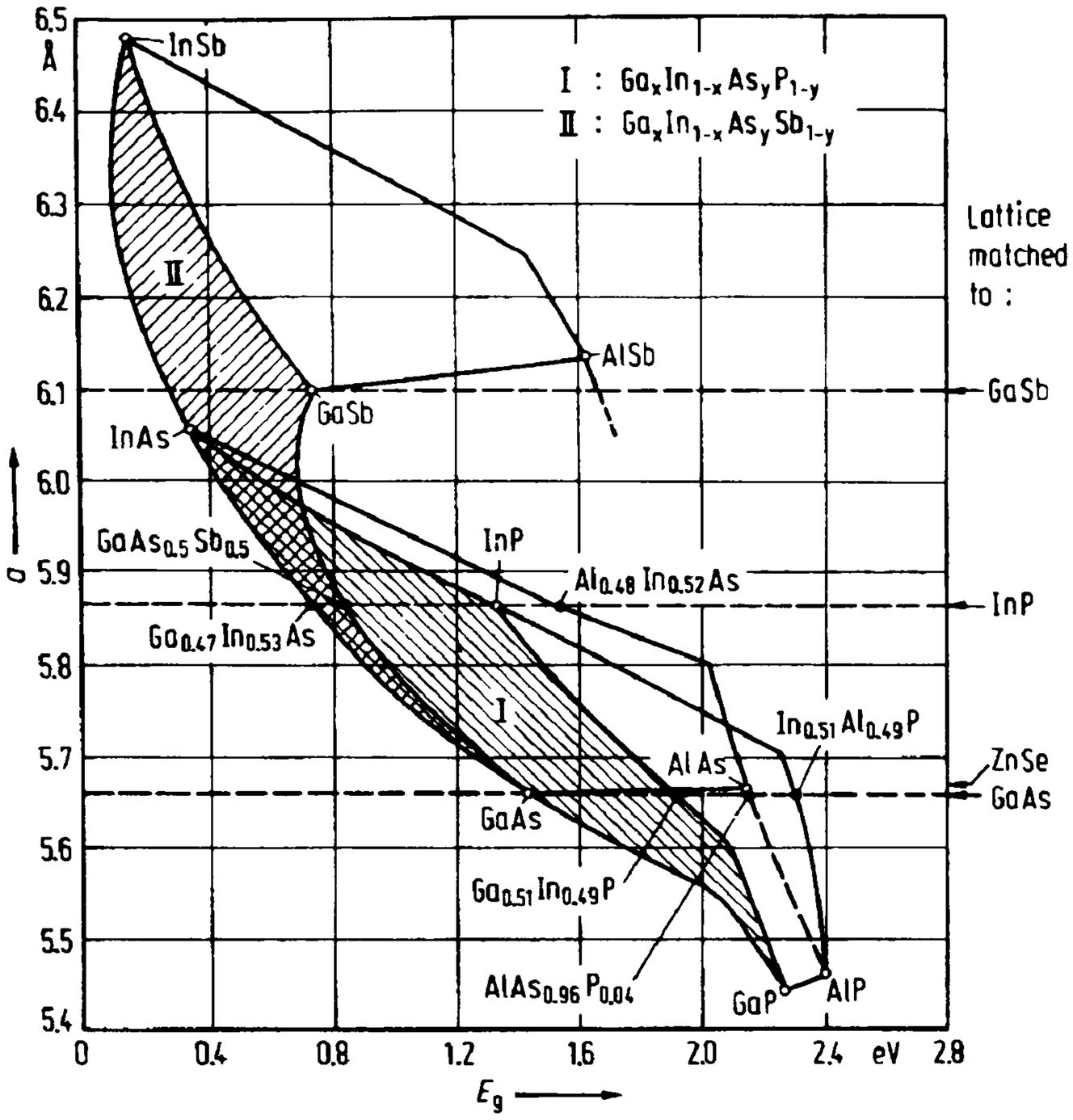

(c)

Figure 1.7.1: High quality lattice-mismatched heterostuctures can be growth from constituent semiconductors differing significantly in their bulk lattice constants provided that the layer thicknesses do not exceed the strain-dependent critical values (a) commensurate growth (b) incommensurate growth when the critical thickness is exceeded [89] and (c) lattice parameter (a) vs energy gap (300 K values) for various III-V compounds and their alloys [90].

There are two theoretical models used to predict h_c which have gained experimental support in recent years; the Matthew and Blakeslee mechanical equilibrium model [86], and the People and Bean energy balance model [88]. The Matthew and Blakeslee mechanical equilibrium model gives the h_c as

$$h_c = \frac{b}{[1+\nu(x)]4\pi f(x)}\left[\ln\left(\frac{h_c}{b}\right)+1\right] \qquad (1.7.1)$$

whereas the People and Bean energy balance model gives the h_c as

$$h_c = \frac{[1-\nu(x)]b}{[1+\nu(x)]\beta 2\pi f(x)^2}\ln\left(\frac{h_c}{b}\right) \qquad (1.7.2)$$

where ν is the Poisson's ratio and f is the lattice mismatch are functions of the In mole fraction x. The lattice mismatch is defined as $(a_{InGaAs} - a_{GaAs})/a_{GaAs}$ and b is the magnitude of the Burgers vector, taken as $a_{InGaAs}/\sqrt{2}$. Fig. 1.7.2 shows the h_c obtained using equations (1.7.1) and (1.7.2).

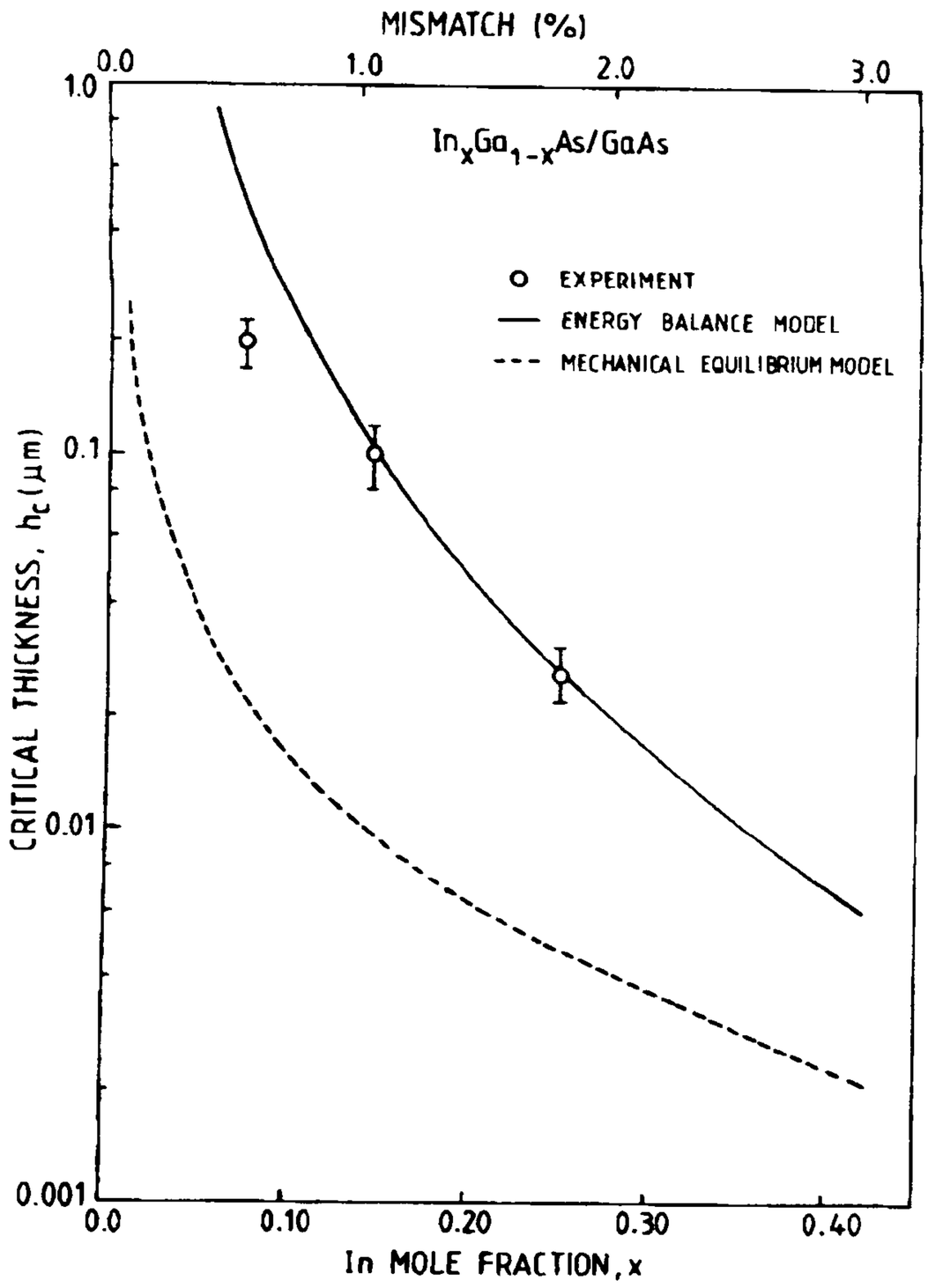

Figure 1.7.2: Experimental and theoretical values of critical thickness vs Indium mole fraction and lattice mismatched for $In_xGa_{1-x}As/GaAs$ single heterostructures. The open circles represent the experimental data, the solid line is the result from People and Bean energy balance model, and the dashed line is the result from Matthew and Blakeslee mechanical equilibrium model [91].

The Matthew and Blakeslee mechanical equilibrium model is the preferred model for several authors probably because it gives a conservative estimate of the h_c [89, 92-96].

In a strained InGaAs layer on GaAs system, the stress is compressive, therefore, holes at the highest valence band maximum are heavy [97]. Figure 1.7.3 shows the strain-induced modification (splitting) of the upper valence bands due to tensile and compressive strain (the direction of size quantisation is in the perpendicular direction [97]).

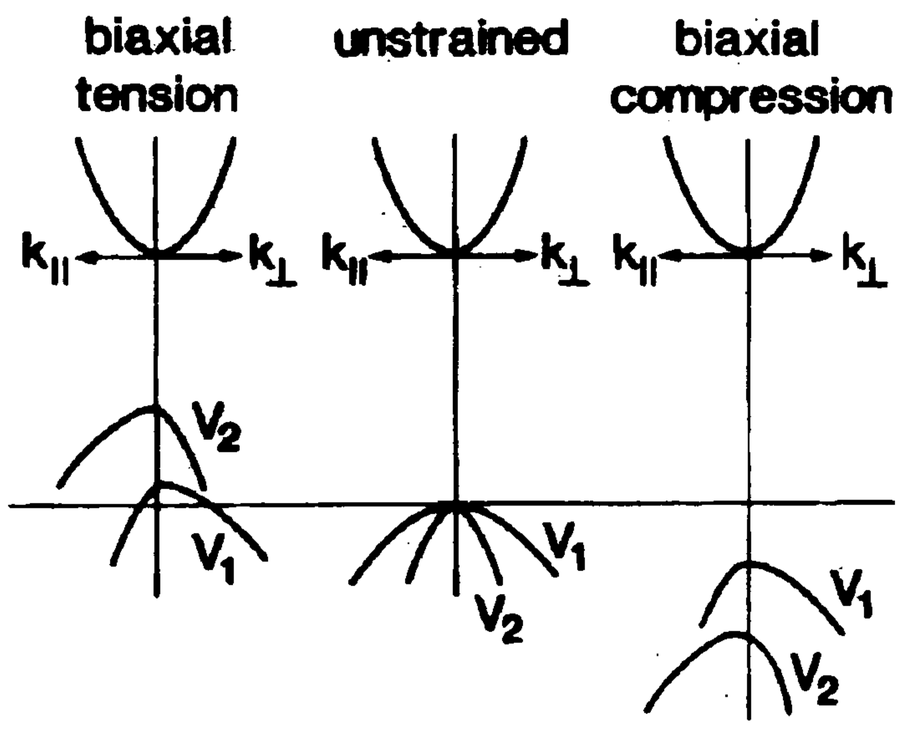

Figure 1.7.3: Band structure of a typical zincblende semiconductor near the Brillouin zone center for the case of no strain, biaxial tensile and compression strain. Note symbols $k_{||}$ and $k_\perp$ refer to wavevectors parallel and perpendicular to the plane of the epitaxial layer and V_1 and V_2 refer to the bulk heavy and light holes, respectively [89].

Another effect of strain is the strain-induced band-gap energy shift. For InGaAs layer on GaAs system, the strain increases the bandgap [82, 89, 97]. These effects must be taken into account for the calculation of the band structure and subband energy levels.

1.8 Summary

As mentioned previously in Sec. 1.2, to maximise the detector detectivity, we have to increase the responsivity and reduce the dark current. The responsivity of the device is proportional to the product of η and g (i.e., the escape probability of the carriers once they have been promoted to the excited level). Depending on the position of the bound levels in the well, there are mainly three types of transitions. In a Bound-to-Bound QWIP, the η is high due to the large oscillator strength caused by the well confined upper state, but the g is low as the photoexcited electrons have to tunnel through the tip of the barrier formed by the applied field in order to escape out of the well. In a Bound-to-Continuum QWIP, the g is large because the excited state is above the barrier, but the η is not as high as the Bound-to-Bound QWIP. In the Bound-to-Quasibound QWIP, the excited state is partially confined in the well, hence, the η and the g of this configuration is in between that of the Bound-to-Bound and Bound-to-Continuum QWIP i.e., the high η of a Bound-to-Bound QW (with a narrow spectral bandwidth) and high g of a Bound-to-Continuum QW can be achieved. A further advantage of using a DBQW is increased flexibility in the design e.g. it provides a means of strain compensation (see Sec. 3.4). Since the detectivity is insensitive to bias and doping and the main source of dark current for QWIPs operating at high temperature is thermionic emission of ground state electrons directly out of the well into the energy continuum, a high barrier height is thus necessary in order to minimise the dark current. In Sec. 3.3 (GaAs) and Sec. 3.4 (InP) we show DBQW structures using lattice mismatched material system designed to increase the barrier height. Hence, by optimising the device structure and the doping density, we can maximise the detectivity and responsivity.

References

1) K. P. Petrov, S. Waltman, E. J. Dlugokencky, M. Arbore, M. M. Fejer, F. K. Tittle and L. W. Hollberg, "*Precise Measurement of Methane in Air using Diode-pumped 3.4-μm Difference-frequency Generation of PPLN*", Applied Physics B, 1997, vol. 64, p. 567-572.

2) J. Faist, F. Capasso, D. L. Sivco, C. Sirtori, A. L. Hutchinson, and A. Y. Cho, "*Quantum Cascade Lasers*", Science, 1994, vol. 264, p. 553-556.

3) F. Capasso, C. Gmachl, R. Paiella, A. Tredicucci, A. L. Hutchinson, D. L. Sivco, J. N. Baillargeon, A. Y. Cho, and H. C. Liu, "*New Frontiers in Quantum Cascade Lasers and Applications*", IEEE Journal on Selected Topics in Quantum Electronics, 2000, vol. 6, p. 931-947.

4) S. Blaser, D. Hofstetter, M. Becker, and J. Faist, "*Free-space Optical Data Link using Peltier-cooled Quantum Cascade Laser*", Electronics Letters, 2001, vol. 37, p. 778-780.

5) A. Kosterev and F. K. Tittel, "*Chemical Sensors Based on Quantum Cascade Lasers*", IEEE Journal of Quantum Electronics, 2002, vol. 38, p. 582-591.

6) A. A. Kosterev, R. F. Curl, F. K. Tittel, C. Gmachl, F. Capasso, D. L. Silvco, J. N. Baillargeon, A. L. Hutchinson, and A. Y. Cho, "*Methane Concentration and Isotopic Composition Measurements with a Mid-infrared Quantum-Cascade Laser*", Optics Letters, 1999, vol. 24, p. 1762-1763.

7) C. Gmachl, A. Tredicucci, F. Capasso, A. L. Hutchinson, D. L. Silvco, A. M. Sergent, T. Mentzel, and A. Y. Cho, "*High Temperature (T≥425K) Pulsed Operation of Quantum Cascade Lasers*", Electronics Letters, 2000, vol. 36, p. 723-725.

8) M. Beck, D. Hofstetter, T. Aellen, J. Faist, U. Oesterle, M. Ilegems, E Gini, and H. Melchior, "*Continuous Wave Operation of a Mid-infrared Semiconductor Laser at Room Temperature*", Science, 2002, vol. 295 p. 301-305.

9) F. Capasso, R. Paiella, R. Martini, R. Colombelli, C. Gmachl, T. L. Myers, M. S. Taubman, R. M. Williams, C. G. Bethea, K. Unterrainer, H. Y. Hwang, D. L. Sivco, A. Y. Cho, A. M. Sergent, H. C. Liu and E. A. Whittaker, "*Quantum Cascade Lasers: Ultrahigh-Speed Operation, Optical Wireless Communication, Narrow Linewidth, and Far-infrared Emission*", IEEE Journal of Quantum Electronics, 2002, vol. 38, p. 511-532.

10) J. H. Lee, J. C. Chiang, S. S. Li, and P. J. Kannam, "*An AlAs/InGaAs/AlAs/InAlAs Double-barrier Quantum Well Infrared Photodetector Operating at 3.4 μm and 205 K*", Applied Physics Letters, 1999, vol. 74, p. 765-767.

11) B. F. Levine, "*Quantum-well Infrared Photodetectors*", Journal of Applied Physics, 1993, vol. 74, p. R1-R81.

12) S. D. Gunapala, B. F. Levine, L. Pfeiffer, and K. West, "*Dependence of the Performance of GaAs/AlGaAs Quantum Well Infrared Photodetectors on Doping and Bias*", Journal of Applied Physics, 1991, vol. 69, p. 6517-6520.

13) G. Hasnain, B. F. Levine, C. G. Bethea, R. A. Logan, J. Walker, and R .J. Malik, "*GaAs/AlGaAs Multiquantum Well Infrared Detector Arrays using Etched Gratings*", Applied Physics Letters, 1989, vol. 54, p. 2515-2517.

14) H. C. Liu, A. G. Steele, M. Buchanan, and Z. R. Wasilewski, "*Dark Current in Quantum Well Infrared Photodetectors*", Journal of Applied Physics, 1993, vol. 73, p. 2029-2031.

15) T. Ando, A. B. Fowler, and F. Stern, "*Electronic Properties of Two-dimensional Systems*", Reviews of Modern Physics, 1982, vol. 54, p. 437-672.

16) J. Wilson, J. F. B. Hawkes, *Optoelectronics-An introduction*, Prentice-Hall, United Kingdom (1989).

17) M. O. Manasreh, *Semiconductors Quantum Wells and Superlattices for Long Wavelength Infrared Detections*, Artech House, Boston (1993).

18) Kenneth S. Krane, *Modern Physics*, John Wiley & Sons, New York (1996).

19) J. E. Zucker, A. Pinczuk, D. S. Chemla, A. Gossard, and W. Wiegmann, "*Delocalised Excitons in Semiconductor Heterostructures* ", Physical Review B, 1984, vol. 29, p. 7065-7068.

20) M. F. H. Schuurmans, and G. W. 't Hooft, "*Simple Calculations of Confinement States in a Quantum Well*", Physical Review B, 1985, vol. 31, p. 8041-8048.

21) L. Esaki, "*A Bird's-eye View on the Evolution of Semiconductor Superlattices and Quantum Wells*", IEEE Journal of Quantum Electronics, 1986, vol. QE-22, p. 1611-1624.

22) G. Bastard, and J. A. Brum, "*Electronic States in Semiconductor Heterostructures*", IEEE Journal of Quantum Electronics, 1986, vol. QE-22, p. 1625-1644.

23) G. Duggan, "*A Critical Review of Heterojunction Band Offsets*", Journal of Vacuum Science Technology B, 1985, vol. 3, p. 1224-1229.

24) W. A. Harrison, "*Elementary Theory of Heterojunction*", Journal of Vacuum Science Technology, 1977, vol. 14, p. 1016-1021.

25) L. C. West, and S. J. Eglash, "*First Observation of an Extremely Large Infrared Transition Within the Conduction Band of a GaAs Quantum Well*", Applied Physics Letters, 1985, vol. 46, p. 1156-1158.

26) Y. Hirayama, J. H. Smet, L. H. Peng, C. G. Fonstad, and E. P. Ippen, "*Feasibility of 1.55 μm Intersubband Photonic Devices Using InGaAs AlAs Pseudomorphic Quantum Well Structures*", Japanese Journal of Applied Physics, 1994, vol. 33, p. 890-895.

27) A. Rogalski, "*Quantum Well Photoconductors in Infrared Detector Technology*", Journal of Applied Physics, 2003, vol. 93, p. 4355-4391.

28) A. Harwit, and J. S. Harris Jr., "*Observation of Stark Shifts in Quantum Well Intersubband Transitions*", Applied Physics Letters, 1987, vol. 50, p. 685-687.

29) M. A. Kinch, and A. Yariv, "*Performance Limitations of GaAs/AlGaAs Infrared Superlattices*", Applied Physics Letters, 1989, vol. 55, p. 2093-2095.

30) S. D. Gunapala, G. Sarusi, J. S. Park, T. L. Lin, and B. F. Levine, "*Infrared Detector Reach New Heights*", Physics World, Dec 1994, p. 35-40.

31) M. Z. Tidrow, "*Device Physics and State-of-the-Art of Quantum Well Infrared Photodetectors and Arrays*", Materials Science & Engineering B, 2000, vol. 74, p. 45-51.

32) B. F. Levine, A. Zussman, S. D. Gunapala, M. T. Asom, J. M. Kuo, and W. S. Hobson, "*Photoexcited Escape Probability, Optical Gain, and Noise in Quantum Well Infrared Photodetectors* ", Journal of Applied Physics, 1992, vol. 72, p. 4429-4443.

33) Steven K. H. Sim, H. C. Liu, A. Shen, M. Gao, Kevin F. Lee, M. Buchanan, Y. Ohno, H. Ohno, and E. H. Li, "*Effect of Barrier Width on the Performance of Quantum Well Infrared Photodetector*", Infrared Physics & Technology, 2001, vol. 42, p. 115-121.

34) A. G. Steele, H. C. Liu, M. Buchanan, and Z. R. Wasilewski, "*Importance of the Upper State Position in the Performance of Quantum Well Intersubband Infrared Detectors*", Applied Physics Letters, 1991, vol. 30, p. 3625-3627.

35) S. D. Gunapala, and S. V. Bandara, "*Significance of the First Excited State Position in Quantum Well Infrared Photodetectors*", Microelectronics Journal, 1999, vol. 30, p. 1057-1065.

36) B. F. Levine, C. G. Bethea, G. Hasnain, J. Walker, and R. J. Malik, "*High Detectivity $D^* = 1.0 \times 10^{10}$ cm $\sqrt{Hz}/W$ GaAs/AlGaAs Multiquantum Well $\lambda = 8.3$ μm Infrared Detectors*", Applied Physics Letters, 1988, vol. 53, p. 296-298.

37) B. F. Levine, C. G. Bethea, G. Hasnain, V. O. Shen, E. Pelve, R. R. Abbott, and S. J. Hsieh, "*High Sensitivity Low Dark Current 10 μm GaAs Quantum Well Infrared Photodetectors*", Applied Physics Letters, 1990, vol. 56, p. 851-853.

38) B. F. Levine, G. Hasnain, C. G. Bethea, and N. Chand, "*Broadband 8–12 μm High-sensitivity GaAs Quantum Well Infrared Photodetector*", Applied Physics Letters, 1989, vol. 54, p. 2704-2706.

39) G. Hasnain, B. F. Levine, D. L. Silvo, and A. Y. Cho, "*Mid-infrared Detectors in the 3-5 μm Band using Bound to Continuum State Absorption in InGaAs/InAlAs Multiquantum Well Structures*", Applied Physics Letters, 1990, vol. 56, p. 770-772.

40) G. Neu, Y. Chen, C. Deparis, and J. Massies, "*Improvement of the Carrier Confinement by Double-Barrier GaAs/AlAs/(Al,Ga)As Quantum Well Structures*", Applied Physics Letters, 1991, vol. 58, p. 2111-2113.

41) H. Schneider, F. Fuchs, B. Dischler, J. D. Ralston and P. Koidl, "*Intersubband Absorption and Infrared Photodetection at 3.5 and 4.2 μm in GaAs Quantum Wells*", Applied Physics Letters, 1991, vol. 58, p. 2234-2236.

42) H. Schneider, P. Koidl, F. Fuchs, B. Dischier, K. Schwarz, and J. D. Ralston, "*Photovoltaic Intersubband Detectors for 3-5 μm using GaAs Quantum Wells Sandwiched Between AlAs Tunnel Barriers*", Semiconductor Science Technology, 1991, vol. 6, p. C120-C123.

43) J. D. Ralston, H. Schneider, D. F. G. Gallagher, K. Kheng, F. Fuchs, P. Bittner, B. Dischler, and P. Koidl, "*Novel Molecular-beam Epitaxially Grown GaAs/AlGaAs Quantum Wells Structures for Infrared Detection and Integrated Optics at 3-5 and 8-12 μm*", Journal of Vacuum Science Technology B, 1992, vol. 10, p. 998-1001.

44) K. L. Tsai, K. H. Chang, C. P. Lee, K. F. Huang, J. S. Huang, and H. R. Chen, "*Two–color Infrared Photodetector using GaAs/AlGaAs and Strained InGaAs/AlGaAs Multiquantum Wells*", Applied Physics Letters, 1993, vol. 62, p. 3504-3506.

45) A. Fiore, E. Rosencher, P. Bois, J. Nagle, and N. Laurent, "*Strained InGaAs/AlGaAs Quantum Well Infrared Detectors at 4.5 μm*", Applied Physics Letters, 1994, vol. 64, p. 478-480.

46) H. C. Liu, P. H. Wilson, M. Lamm, A. G. Steele, Z. R. Wasilewski, J. M. Li, M. Buchanan, and J. G. Simmons, "*Low Dark Current Dual Band Infrared Photodetector Using Thin AlAs Barriers and Γ-X Mixed Intersubband Transition in GaAs Quantum Wells*", Applied Physics Letters, 1994, vol. 64, p.475-477.

47) K. L. Tsai, C. P. Lee, P. C. Chen, J .S. Tsang, C. M. Tsai, and J. C. Fan, "*The Effect of Barrier Structure On The Performance of Double Barrier Quantum Well Infra-red Photodetectors*", Solid-State Electronics, 1996, vol. 39, p. 201-204.

48) H. C. Liu, M. Buchanan, and Z. R. Wasilewski, "*Short wavelength (1-4 μm) Infrared Detectors Using Intersubband Transitions in GaAs-based Quantum Wells*", Journal of Applied Physics, 1998, vol. 83, p. 6178-6181; erratum vol. 91, p. 10230 (2002).

49) W. G. Wu, D. S. Jiang, L. Q. Cui, C .Y. Song, and Y. Zhuang, "*Structural and Photoelectric Studies on Double Barrier Quantum Well Infrared Detectors*", Solid-State Electronics, 1999, vol. 43, p. 723-727.

50) N. Georgiev, T. Dekorsy, F. Eichhorn, M. Helm, M. P. Semtsiv and W. T. Masselink, "*Short-wavelength Intersubband Absorption in Strain Compensated InGaAs/AlAs Quantum Well Structures Grown on InP*", Applied Physics Letters, 2003, vol. 83, p.210-212.

51) E. Luna, A. Guzmán, J. L. Sánchez-Rojas, E. Calleja, and E. Muñoz, "*Modulation-doping in 3-5μm GaAs/AlAs/AlGaAs Double-barrier Quantum-well Infrared Photodetectors: An Alternative to Achieve High Photovoltaic Performance and High Temperature Detection*", Infrared Physics & Technology, 2003, vol. 44, p. 383-390.

52) E. Luna, M. Hopkinson, J. M. Ulloa, A. Guzmán, and E. Muñoz, "*Dilute Nitride Based Double-barrier Quantum-well Infrared Photodetector Operating in the Near Infrared*", Applied Physics Letters, 2003, vol. 83, p. 3111-3113.

53) B. F. Levine, R. J. Malik, J. Walker, K. K. Choi, C. G. Bethea, D. A. Kleinman, and J. M. Vandenberg, "*Strong 8.2 μm Infrared Intersubband Absorption in Doped GaAs/AlAs Quantum Well Waveguides*", Applied Physics Letters, 1987, vol. 50, p. 273-275.

54) L. C. Lew Yan Voon, M. Willatzen, and L. R. Ram-Mohan, "*Can Normal Incidence Absorption be realized with n-doped (001)-grown Direct-gap Quantum Well?*", Journal of Applied Physics, 1995, vol. 78, p. 295-298.

55) H. C. Liu, M. Buchanan, and Z. R. Wasilewski, "*How Good is the Polarization Selection rule for Intersubband Transitions*", Applied Physics Letters, 1998, vol. 72, p. 1682-1684.

56) K. W. Goossen, and S. A. Lyon, "*Grating Enhanced Quantum Well Detector*", Applied Physics Letters, 1985, vol. 47, p. 1257-1259.

57) J. Y. Andersson, L. Lundqvist, and Z. F. Paska, "*Quantum Efficiency Enhancement of AlGaAs/GaAs Quantum Well Infrared Detectors using a Waveguide with a Grating Coupler*", Applied Physics Letters, 1991, vol. 58, p. 2264-2266.

58) B. F. Levine, S. D. Gunapala, J. M. Kuo, S. S. Pei, and S. Hui, "*Normal Incidence Hole Intersubband Absorption Long Wavelength GaAs $Al_xGa_{1-x}As$ Quantum-well Infrared Photodetectors*", Applied Physics Letters, 1991, vol. 59, p. 1864-1866.

59) S. D. Gunapala, B. F. Levine, D. Ritter, R. Hamm, and M. B. Panish, "*InGaAs/InP Hole Intersubband Normal Incidence Quantum Well Infrared Photodetector*", Journal of Applied Physics, 1992, vol. 71, p. 2458-2460.

60) J. Katz, Y. Zhang, and W. I. Wang, "*Normal Incidence Infra-red Absorption from Intersub-band Transitions in P-type GaInAs/AlInAs Quantum Wells*", Electronics Letters, 1992, vol. 28, p. 932-934.

61) H. C. Liu, T. Oogarah, E. Dupont, Z. R. Wasilewski, M. Byloos, M. Buchanan, F. Szmulowicz, J. Ehret, and G. J. Brown, "*P-type Quantum Well Infrared Photodetectors Covering Wide Spectrum*", Electronics Letters, 2002, vol. 38, p. 909-911.

62) J. L. Pan, and C. G. Fonstad, "*Comparison of Hole and Electron Intersubband Absorption Strengths for Quantum Well Infrared Photodetectors*", IEEE Transcations on Electron Devices, 2000, vol. 47, p. 1325-1329.

63) J. P. Pan, L. C. West, S. J. Walker, R. J. Malik, and J. F. Walker, "*Inducing Normally Forbidden Transitions within the Conduction Band of GaAs Quantum Well*", Applied Physics Letters, 1990, vol. 57, p. 366-368.

64) K. Kheng, M. Ramsteiner, H. Schneider, J. D. Ralston, F. Fuchs, and P. Koidl, "*Two-color GaAs/(AlGa)As Quantum Well Infrared Detector with Voltage-tunable Spectral Sensitivity at 3-5 and 8-12 μm*", Applied Physics Letters, 1992, vol. 61, p. 666-668.

65) P. F. Yuh, and K. L. Wang, "*Optical Transitions in a Step Quantum Well*", Journal of Applied Physics, 1989, vol. 65, p. 4377-4381.

66) Y. J. Mii, K. L. Wang, R. P. G. Karunasiri, and P. F. Yuh, "*Observation of Large Oscillator Strengths for Both 1-2 and 1-3 Intersubband Transitions of Step Quantum Well*", Applied Physics Letters, 1990, vol. 56, p. 1046-1048.

67) H. S. Li, Y. W. Chen, K. L. Wang, and D. Y. C. Lie, "*Intersubband Transitions in Pseudomorphic InGaAs/GaAs/AlGaAs Multiple Step Quantum Wells*", Journal of Vacuum Science Technology B, 1993, vol. 11, p. 1840-1843.

68) S. R. Parihar, S. A. Lyon, M. Santos, and M. Shayegan, "*Voltage Tunable Quantum Well Infrared Detector*", Applied Physics letters, 1989, vol. 55, p. 2417-2419.

69) Y. J. Mii, R. P. G. Karunasiri, K. L. Wang, M. Chen, and P. F. Yuh, "*Large Shark Shifts of the Local to Global State Intersubband Transitions in Step Quantum Well*", Applied Physics Letters, 1990, vol. 56, p. 1986-1988.

70) R. P. G. Karunasiri, Y. J. Mii, and K. L. Wang, "*Tunable Infrared Modulator and Swtich using Stark Shift in Step Quantum Wells*", IEEE Electron Device Letters, 1990, vol. 11, p. 277-279.

71) E. Martinet, F. Luc, E. Rosencher, Ph. Bois, and S. Delaitre, *"Electrical Tunability of Infrared Detectors using Compositionally Asymmetric GaAs/AlGaAs Multiquantum Wells*", Applied Physics Letters, 1992, vol. 60, p. 895-897.

72) W. Q. Chen, and T. G. Andersson, "*Intersubband Transitions for Differently Shaped Quantum Wells Under an Applied Electric Field*", Applied Physics Letters, 1992, vol. 60, p. 1591-1593.

73) X. Zhou, P. K. Bhattacharya, G. Hogo, S. C. Hong, and E. Gulari, "*Intersubband Absorption in Strained $In_xGa_{1-x}As/Al_{0.4}Ga_{0.6}As$ ($0 \leq X \leq 0.15$) Multiquantum Wells*", Applied Physics Letters, 1989, vol. 54, p. 855-856.

74) B. F. Levine, C. G. Bethea, K. G. Glogovsky, J. W. Stayt, and R. E. Lelbenguth, "*Long-wavelength 128 X 128 GaAs Quantum Well Infrared Photodetector Arrays*", Semiconductor Science Technology, 1991, vol. 6, p. C114-C119.

75) S. D. Gunapala, J. S. Park, G. Sarusi, T.-L. Lin, J. K. Liu, P. D. Maker, R. E. Muller, C. A. Shott, and T. Hoelter, "*15-μm 128 X 128 $GaAs/Al_xGa_{1-x}As$ Quantum Well Infrared Photodetector Focal Plane Array Camera*", IEEE Transactions on Electron Devices, 1997, vol. 44, p. 45-50.

76) S. D. Gunapala, S. V. Bandara, J. K. Liu, W. Hong, M. Sundaram, P. D. Maker, R. E. Muller, C. A. Shott, and R. Carralejo "*Long-wavelength 640 X 486 GaAs/AlGaAs Quantum Well Infrared Photodetector Snap-shot Camera*", IEEE Transactions on Electron Devices, 1998, vol. 45, p. 1890-1895.

77) S. D. Gunapala, S. V. Bandara, J. K. Liu, E. M. Luong, N. Stetson, C. A. Shott, J. J. Bock, S. B. Rafol, J. M. Mumolo, and M. J. McKelvey, "*Long-wavelength 256 X 256 GaAs/AlGaAs Quantum Well Infrared Photodetector (QWIP) Palm-size Camera*", IEEE Transactions on Electron Devices, 2000, vol. 47, p. 326-332.

78) H. Schneider, M. Walther, C. Schönbein, R. Rehm, J. Fleissner, W. Pletschen, J. Braunstein, P. Koidl, G. Weimann, J. Ziegler, and W. Cabanski, "*QWIP FPAs for High-performance Thermal Imaging*", Physica E, 2000, vol. 7, p. 101-107.

79) A. Goldberg, P. N. Uppal, and M. Winn, "*Detection of Buried Land Mines using a Dual-band LWIR/LWIR QWIP Focal Plane Array*", Infrared Physics & Technology, 2003, vol. 44, p. 427-437.

80) S. D. Gunapala, S. V. Bandara, J. K. Liu, E. M. Luong, S. B. Rafol, J. M. Mumolo, D. Z. Ting, J. J. Bock, M. E. Ressler, M. W. Werner, P. D. Levan, R. Chehayeb, C. A. Kukkonen, M. Levy, P. LeVan, and M. A. Fauci, "*Quantum Well Infrared Photodetector Research and Development at Jet Propulsion Laboratory*", Infrared Physics & Technology, 2001, vol. 42, p. 267-282, and references therein.

81) B. F. Levine, S. D. Gunapala, and R. F. Kopf, "*Photovoltaic GaAs Quantum Well Infrared Detectors at 4.2 μm using Indirect $Al_xGa_{1-x}As$ Barrier*", Applied Physics Letters, 1991, vol. 58, p. 1551-1553.

82) K. K. Choi, S. V. Bandara, S. D. Gunapala, W. K. Liu, and J. M. Fastenau, "*Detection Wavelength of InGaAs/AlGaAs Quantum Wells and Superlattices*", Journal of Applied Physics, 2002, vol. 91, p. 551-564.

83) R. C. Miller, D. A. Kleinman, and A. C. Gossard, "*Energy-gap Discontimuities and Effective Masses for GaAs-$Al_xGa_{1-x}As$ Quantum-well*", Physical Review B, 1984, vol. 29, p. 7085-7087.

84) H. Asai, and Y. Kawamura, "*Intersubband Absorption in $In_{0.53}Ga_{0.47}As/In_{0.52}Al_{0.48}As$ Multiple Quantum Wells*", Physical Review B, 1991, vol. 43, p. 4748-4759.

85) J. H. Vander Merwe, "*Crystal Interfaces Part II. Finite Overgrowths*", Journal of Applied Physics, 1963, vol. 34, p. 123-126.

86) J. W. Matthews, and A. E. Blakeslee, "*Defects in Epitaxial Multilayers* : I. Misfit Dislocations*", Journal of Crystal Growth, 1974, vol. 27, p. 118-6125.

87) G. C. Osbourn, "*Strained-layer Superlattices from Lattice Mismatched Materials*", Journal of Applied Physics, 1982, vol. 53, p. 1586-1589.

88) R. People, and J. C. Bean, "*Calculation of Critical Layer Thickness versus Lattice Mismatch for Ge_xSi_{1-x}/Si Strained-layer Heterostructure*", Applied Physics Letters, 1985, vol. 47, p. 322-324; erratum vol. 55, p. 206 (1986).

89) R. M. Kolbas, N. G. Andersson, W. D. Laidig, Y. K. Sin, Y. C. Lo, K. Y. Hsieh, and Y. J. Yang, "*Strained-layer InGaAs-GaAs-AlGaAs Photopumpled and Current Injection Lasers*", IEEE Journal of Quantum Electronics, 1988, vol. 24, p. 1605-1613.

90) O. Madelung, *Semiconductors: Group IV Elements and III-V Compounds*, Springer, Berlin (1991).

91) P. J. Orders and B. F. Usher, "*Determination of Critical Layer Thickness in $In_xGa_{1-x}As/GaAs$ Heterostructures by X-Ray Diffraction*", Applied Physics Letters, 1987, vol. 50, p. 980-982.

92) I. J. Fritz, S. T. Picraux, L. R. Dawson, T. J. Drummond, W. D. Laidig, and N. G. Anderson, "*Dependence of Critical Layer Thickness on Strain for $In_xGa_{1-x}As/GaAs$ Strained-Layer Superlattices*", Applied Physics Letters, 1985, vol. 46, p. 967-969.

93) T. G. Andersson, Z. G. Chen, V. D. Kulakovskii, A. Uddi, and J. T. Vallin, "*Variation of Critical Layer Thickness with In Content in Strained $In_xGa_{1-x}As$-GaAs Quantum Well Grown on Molecular Beam Epitaxy*", Applied Physics Letters, 1987, vol. 51, p. 752-754.

94) R. L. S Devine, "*Photoluminescence Characterisation of InGaAs/GaAs Quantum Well Structures*", Semiconductor Science Technology, 1988, vol. 3, p1171-1176.

95) H. Temkin, D. G. Gershoni, S. N. G. Chu, J. M. Vandenberg, R. A. Hamm, and M. B. Panish, "*Critical Layer Thickness in Strained $Ga_{1-x}In_xAs/InP$ Quantum Wells*", Applied Physics Letters, 1989, vol. 55, p. 1668-1670.

96) J. C. Dries, M. R. Gokhale, K. J. Thomson, S. R. Forrest, and R. Hull, "*Strained Compensated $In_{1-x}Ga_xAs$ ($x<0.47$) Quantum Well Photodiodes for Extended Wavelength Operation*", Applied Physics Letters, 1998, vol. 73, p. 2263-2265.

97) J. –Y. Marzin, M. N. Charasse, and B. Sermage, "*Optical Investigation of a New Type of Valence-band Configuration in $In_xGa_{1-x}As$-GaAs Strained Superlattices*", Physical Review B, 1985, vol. 31, p. 8298-8301.

Chapter 2 Experimental Methods

2.1 Growth-Molecular Beam Epitaxy (MBE)

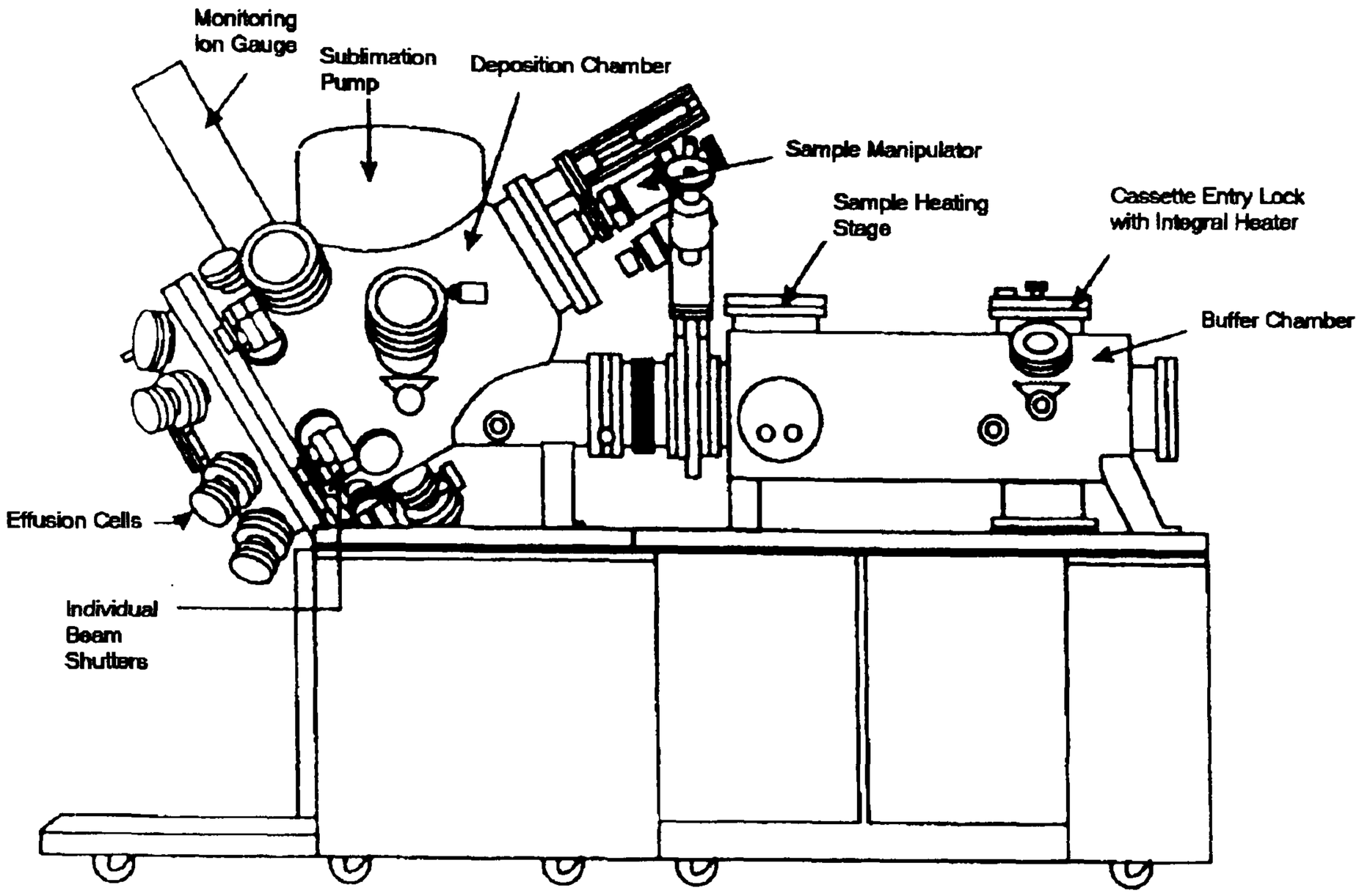

Figure 2.1.1: A schematic diagram of a solid source MBE system for the growth of III-V compounds.

It was the invention of molecular beam epitaxy (MBE) at Bell Labs by Alfred Y. Cho and John Arthur in the late 1960s that finally moved quantum research from the theoretical to the practical realm. At the heart of the MBE machine shown in Fig. 2.1.1 is an ultrahigh-vacuum chamber (UHV), which allows workers to deposit layers of atoms as thin as 0.2 nm on a heated semiconductor substrate where they react to form an epitaxial film. Attached to the vacuum chamber, like spokes on a hub, are a number of Knudsen or effusion cells. Elements such as Gallium, Indium, Arsenide or Aluminum are vaporised in these cells, and the resulting gas phase atoms/molecules are directed towards a substrate. By programming the shutters on each cell and

controlling the temperature, researchers can dictate the thickness of the layers deposited on the substrate, which is in this work Gallium Arsenide (GaAs) or Indium Phosphide (InP) [1-4].

The samples presented here were grown in UMIST (unless otherwise stated) by molecular beam epitaxy on (100) oriented semi-insulating GaAs or InP substrates in a VG Semicon V90H reactor with four inch substrate growth capability. We used near stoichiometric growth conditions [5] at low temperatures (~520 ^{0}C for GaAs and ~420 ^{0}C for InP based DBQWs) to achieve the high optical quality evidenced by efficient room temperature photoluminescence from all the samples. Fig. 2.1.2 and 2.1.3 show the generic epitaxial layer structure of the GaAs and InP based DBQWs samples, respectively and Table 2.1.1 and 2.1.2 list the samples parameters.

	1 x 100 Å GaAs Cap Undoped
MQW x 50	220 Å AlGaAs with Al=0.4 Undoped
	20 Å AlAs Undoped
	L_W Å $In_{(x)}Ga_{(1-x)}As$ with In = x doped N_S
	24 Å GaAs step Undoped (only in 1557)
	20 Å AlAs Undoped
	1 x 1000 Å GaAs Buffer Undoped
	GaAs Semi-insulating substrate

Figure 2.1.2: Generic epitaxial layer structure of the GaAs based DBQWs samples. The samples were grown by MBE at a growth temperature of 520 ^{0}C.

	Sample No.			
Parameters	**1546**	**1547**	**1551**	**1557**
Indium content (x)	0	0.2	0	0.25
QW Thickness (L_w) Å	45	45	45	24+24 (stepped)
Measured Hall QW Sheet Carrier Density (N_S) 10^{11} cm^{-2}	7.65	7.65	38.25	20.40

Table 2.1.1: GaAs based DBQWs samples parameters.

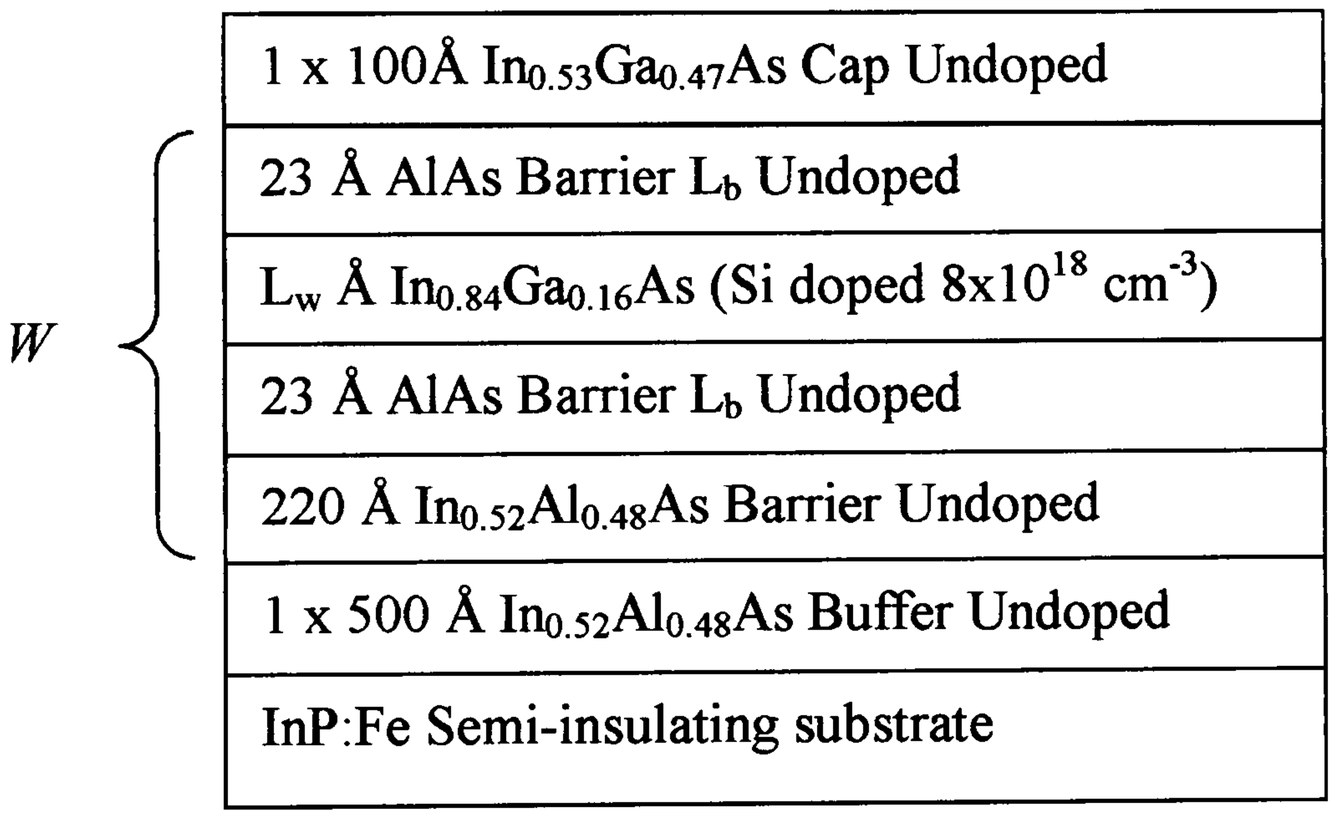

Figure 2.1.3: Generic epitaxial layer structure of the InP based DBQWs samples. The samples were grown by MBE at a growth temperature of 420 ^{0}C.

Parameters	Sample No. 1554	1563	1561
QW Periods (W)	15	15	25
QW Thickness (L_w) Å	80	45	30
Average Net Strain in a Period %	0*	-0.74*	-1.3*
Measured Hall QW Sheet Carrier Density (N_S) 10^{12} cm^{-2}	11	7.0	4.24
Hall Mobility (μ) cm^2/Vsec	2000	1832	269
Fermi Energy as inferred from Hall measurement (E_F) meV	482	444	330

Table 2.1.2: Samples parameters. *These values were obtained using $[(L_w(a_w-a_s)/a_s) + (L_b(a_b-a_s)/a_s)]/(L_w + L_b)$, where a_w, a_b and a_s are the lattice constants for the InGaAs well, AlAs inner barrier and the InP substrate, respectively.

2.2 Sample Polishing

A Multipol2 Metal Research Polisher with Texmet 2000 polishing cloth and 3 micron diamond paste (both from Buehler) was used to polish the back of the samples prior to the absorption measurements in order to reduce scattering. For 45^0 absorption measurements, the samples are then made into waveguide structures of ~ 4 mm wide and 8 mm long by polishing both the edges at 45^0. Figures 2.2.1 and 2.2.2 show the setup for back and 45^0 edge polishing, respectively.

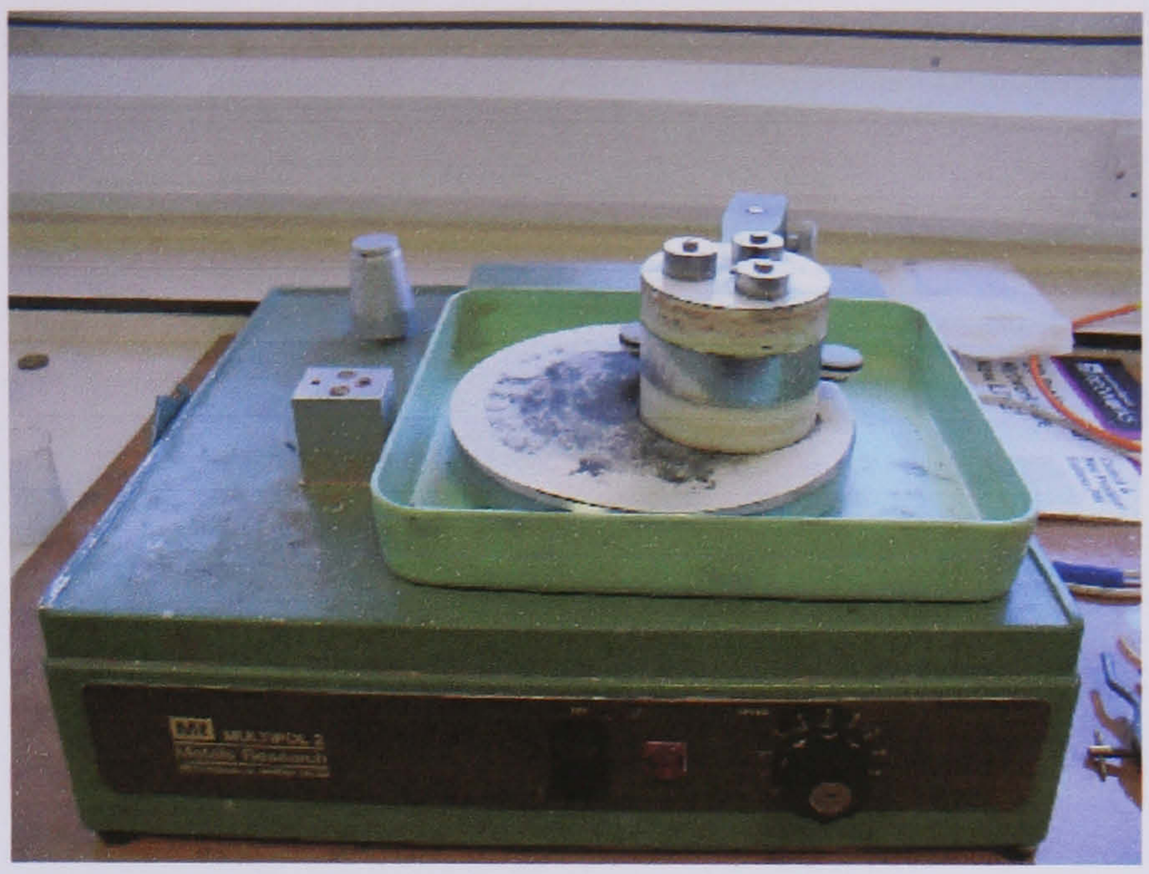

(a)

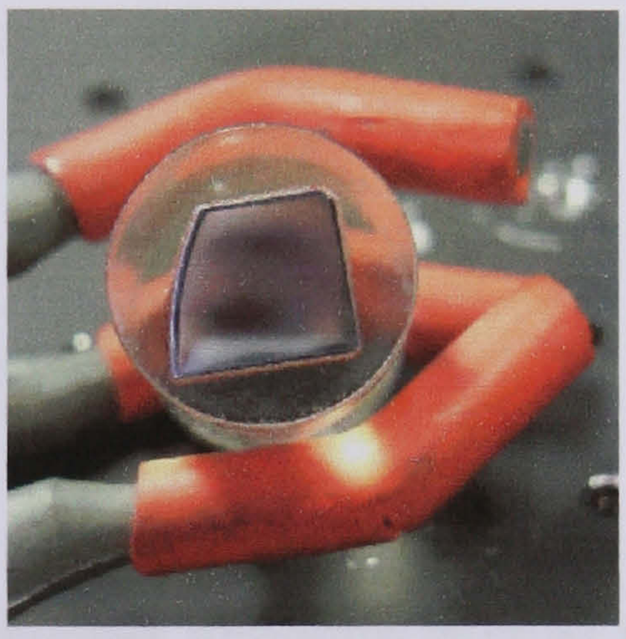

(b)

Figure 2.2.1: Polishing setup for (a) back polishing and (b) result of the back polishing.

(a)

(b)

Figure 2.2.2: Polishing setup for (a) 45^0 edge polishing and (b) result of the 45^0 edge polishing.

2.3 FTIR Absorption Measurements

A Bio-Rad FTS-3000 Fourier transform infrared spectrometer (FTIR) with a ceramic broadband source, a potassium bromide (KBr) beam splitter and a liquid nitrogen cooled mercury cadmium telluride (MCT) detector was used to measure the absorbance of the GaAs and InP based DBQWs samples at 300 K (where absorbance is equal to $-\log[T_{allowed}/T_{forbidden}]$ and T is the transmittance). FTIR is preferred to conventional grating monochromators because of the well known 'multiplex advantage' of the FTIR interferometer, a higher signal-to-noise ratio can be obtained [6]. For spectra containing peaks below 3 μm, additional measurements were made using a tungsten halogen source and a quartz beam splitter to achieve higher resolution (see Appendix A and B for choice of detectors and schematic internal layout of the Bio-rad FTS-3000 FTIR, respectively). A ZnSe wire grid polarizer was

used to resolve the incident IR light into components with electric field vector perpendicular (allowed) or parallel (forbidden) to the plane of the QWs. Light was coupled into the sample using two methods: Brewster angle incidence or 45^0 waveguide geometry to enhance the detection of the intersubband absorption [7-10]. A substrate spectrum was taken under the same conditions as each sample measurement in order to eliminate any background effects. The resolution was chosen to be at 8 cm^{-1} and the scan size equal to 500. Figure 2.3.1 and 2.3.2 show the schematic and experimental setup of the polarisation resolved room temperature intersubband absorption measurement, respectively.

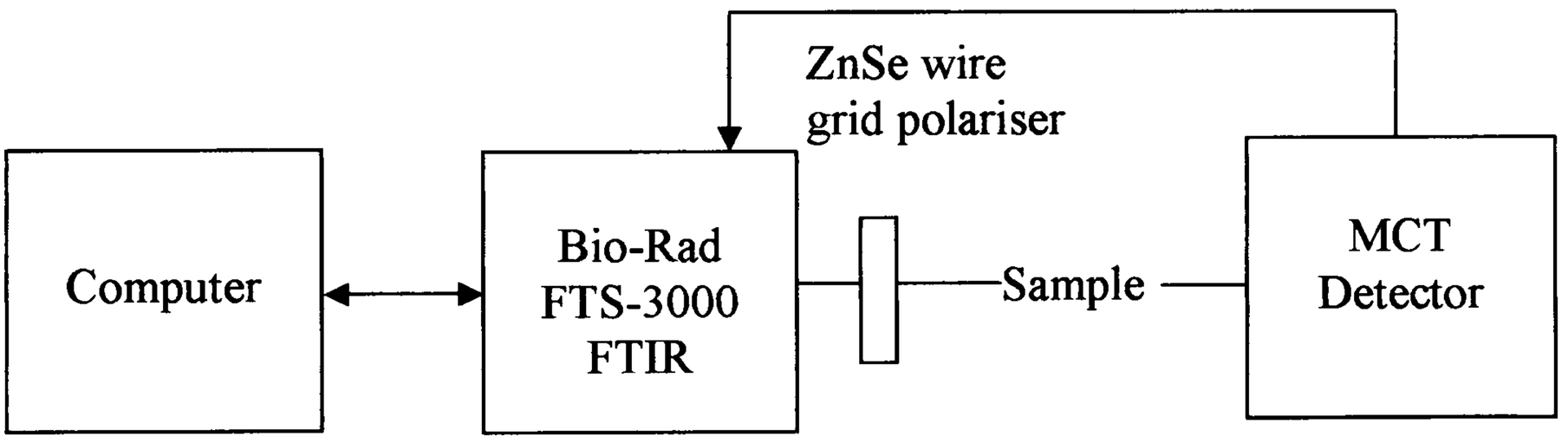

(a)

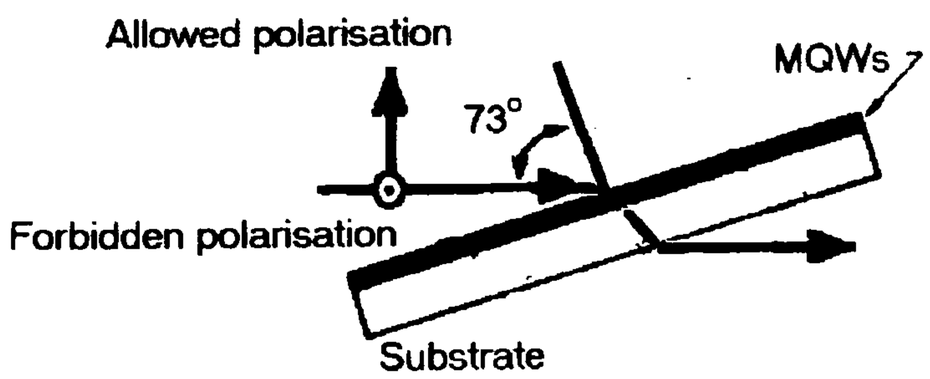

(b)

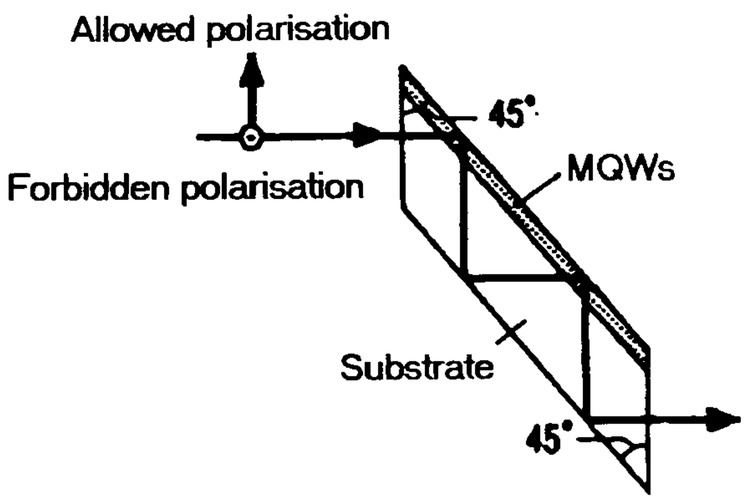

(c)

Figure 2.3.1: (a) The schematic layout of the experimental apparatus for intersubband absorption measurement. Light was coupled into the sample using (b) Brewster angle incidence or (c) 45^0 waveguide geometry.

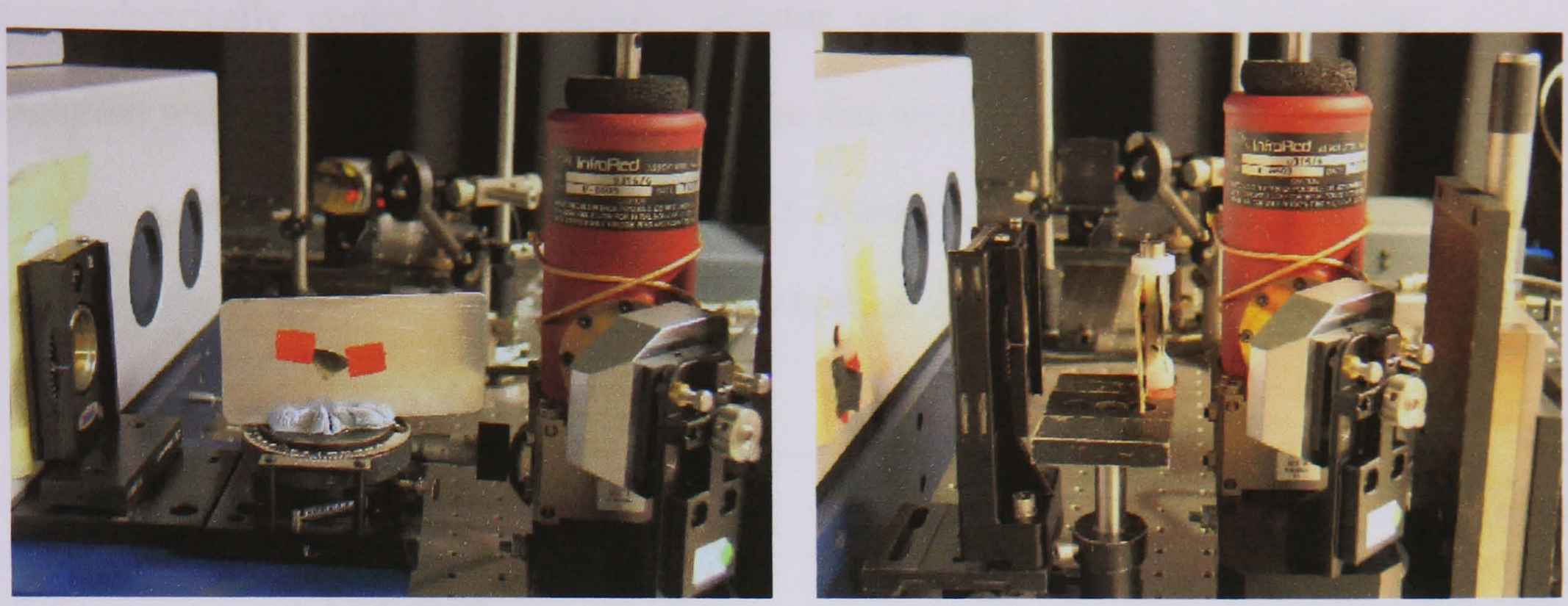

(a) (b)

Figure 2.3.2: The experimental layout of the apparatus for intersubband absorption measurement for (a) Brewster angle geometry and (b) 45^0 waveguide geometry.

2.4 Photoluminescence (PL) Measurements

Photoluminescence (PL) measurement are used to investigate the optical properties of the samples. This technique is widely used for the characterisation of III-V QW heterostructures as it has the advantages of being non-destructive and requiring no sample preparation. For QW structures, the intensity and full width at half maximum (FWHM) of the PL spectrum can extract important information such as layer or interface quality [4, 11, 12]. The position of the PL peaks give the confinement energies.

The PL measurements were obtained using a Ocean optics USB2000 miniature Fiber Optic spectrometer fitted with grating 4 (530-1100 nm) and a high-sensitivity 2048 element linear CCD-array detector (see Fig. 2.4.1). For PL peaks above 1 μm, a Bruker IFS 66/S FTIR with a quartz beam splitter and a

thermoelectrically cooled (TE) InGaAs detector was used (see Fig. 2.4.2). The resolution was chosen to be 32 cm^{-1} and the scan size equal to 7000 (see Appendix C for internal layout of the Bruker IFS 66/S FTIR). A continuous wave 2.6 mW 673 nm diode laser was used as the excitation source for both setups.

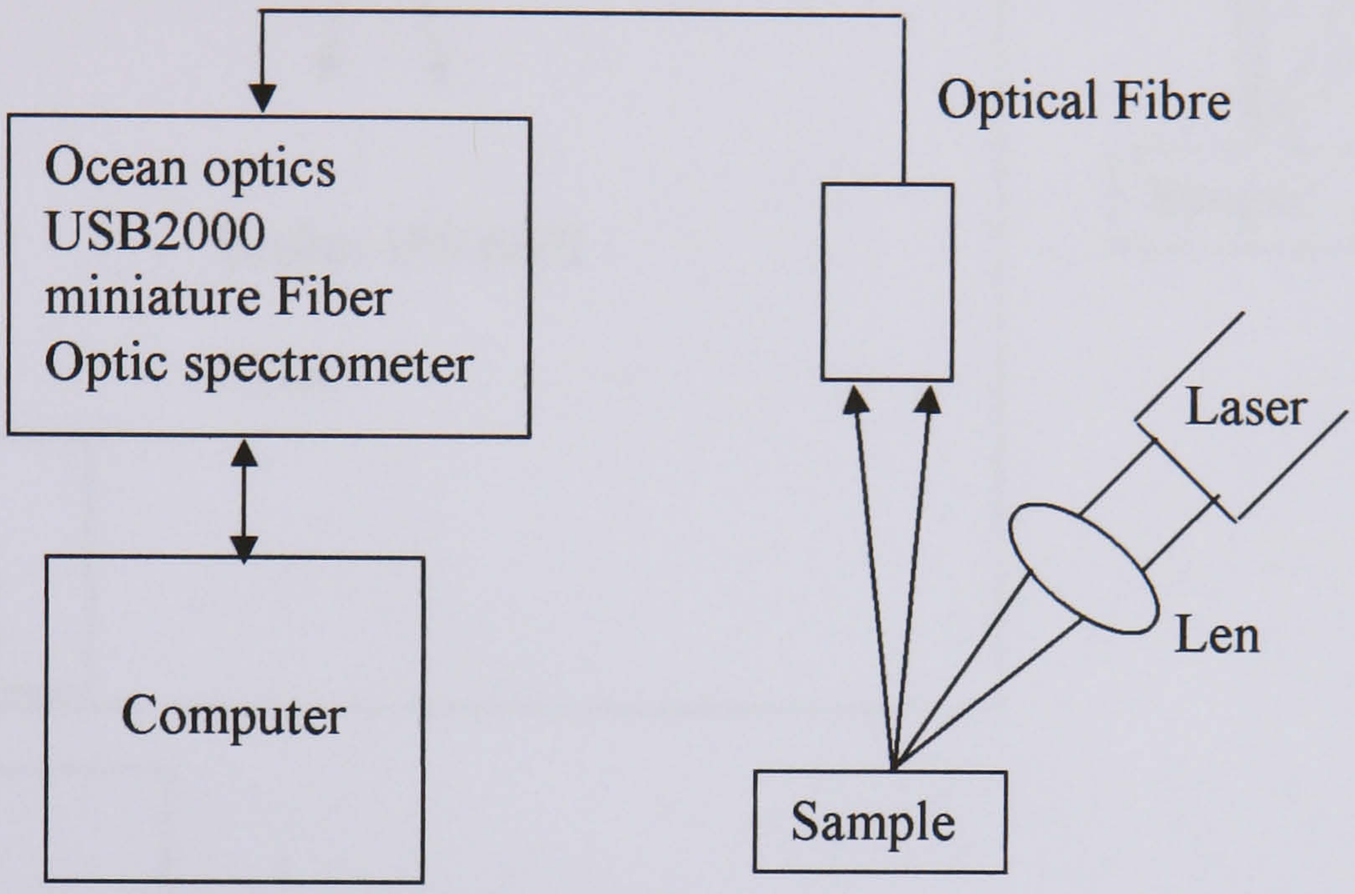

(a)

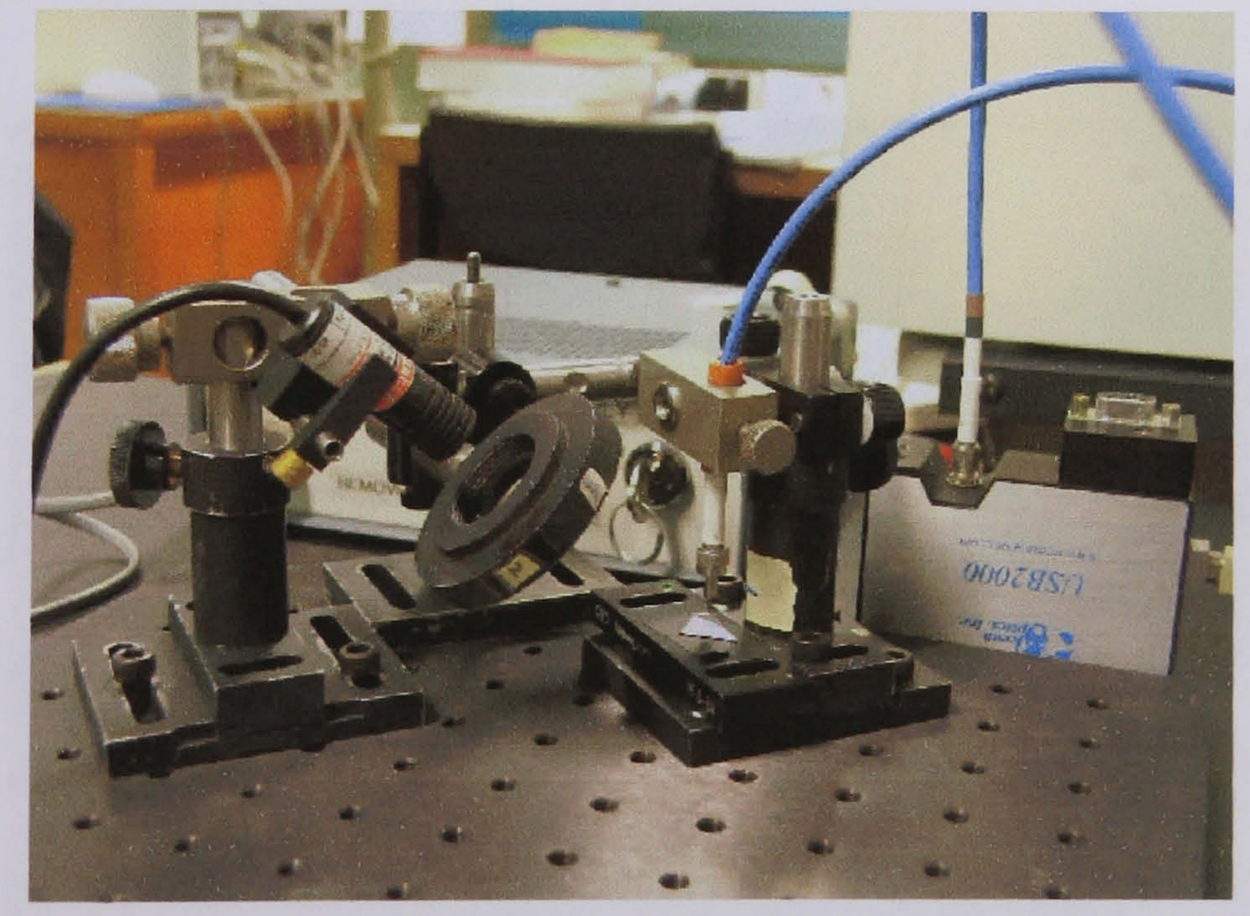

(b)

Figure 2.4.1: The schematic (a) and experimental (b) layout of the photoluminescence system using Ocean optics USB2000 miniature Fiber Optic spectrometer.

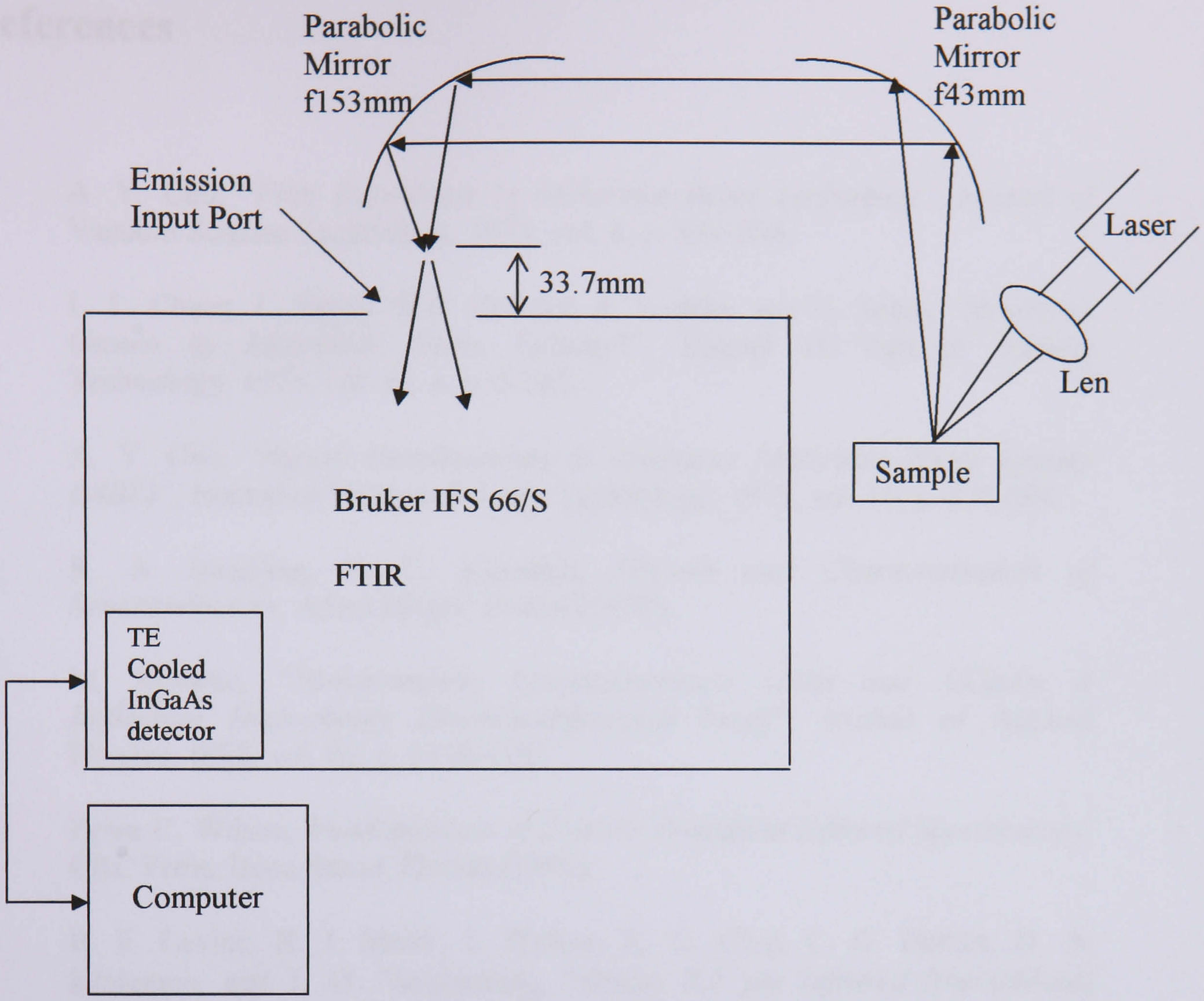

(a)

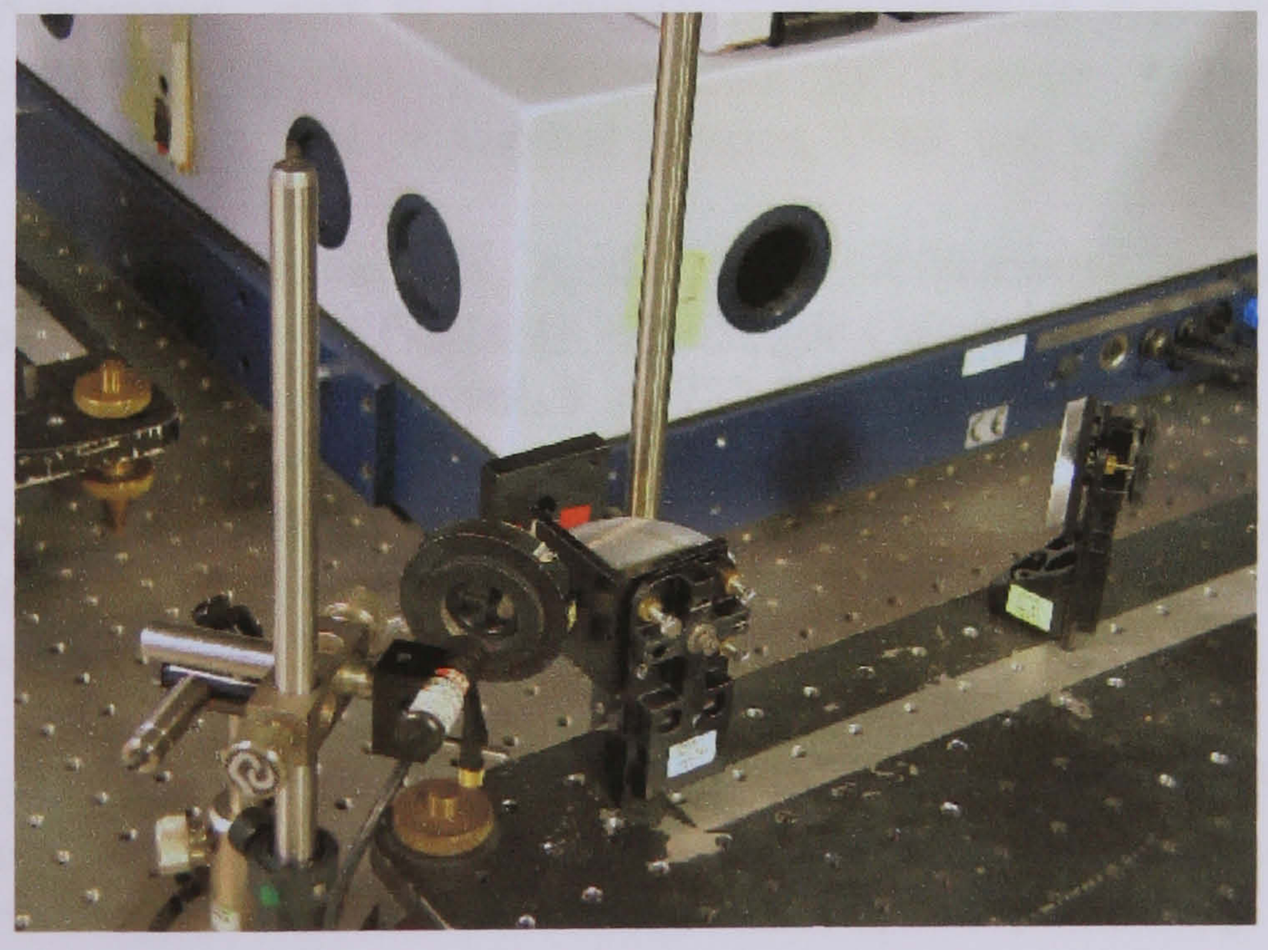

(b)

Figure 2.4.2: The schematic (a) and experimental (b) layout of the photoluminescence system using Bruker IFS 66/S FTIR.

References

1) A. Y. Cho, "*Flim Deposition by Molecular-Beam Techniques*", Journal of Vacuum Science Technology, 1971, vol. 8, p. S31-S38.

2) L. L. Chang, L. Esaki, W.E. Howard, R. Ludeke, and G. Schul, "*Structures Grown by Molecular Beam Epitaxy**", Journal of Vacuum Science Technology, 1973, vol. 10, p. 655-662.

3) A. Y. Cho, "*Recent Developments in structures Molecular Beam Epitaxy (MBE)*", Journal of Vacuum Science Technology, 1979, vol. 16, p. 275-284.

4) R. A. Stradling, P. C. Klipstein, *Growth and Characterisation of Semiconductors*, Adam Hilger, Bristol (1990).

5) M. Missous, "*Stoichiometric Low-temperature GaAs and AlGaAs: A Reflection High-energy Electron-diffraction Study*", Journal of Applied Physics, 1998, vol. 83, p. 6178-6181.

6) Brian C. Wilson, *Fundamentals of Fourier Transform Infrared Spectroscopy*, CRC Press, Boca Raton, Florida (1996).

7) B. F. Levine, R. J. Malik, J. Walker, K. K. Choi, C. G. Bethea, D. A. Kleinman, and J. M. Vandenberg, "*Strong 8.2 μm Infrared Intersubband Absorption in Doped GaAs/AlAs Quantum Well Waveguides*", Applied Physics Letters, 1987, vol. 50, p. 273-275.

8) J. Y. Andersson, and G. Landgren, "*Intersubband Transitions in Single AlGaAs/GaAs Quantum Wells Studied by Fourier Transform Infrared Spectroscopy* ", Journal of Applied Physics, 1988, vol. 64, p. 4123-4127.

9) M. J. Kane, M. T. Emery, N. Apsley, C. R. Whitehouse, and D. Lee, "*Inter-sub-band Absorption in GaAs/AlGaAs Single Quantum Wells*", Semiconductor Science Technology, 1988, vol. 3, p. 722-725.

10) X. Zhou, P. K. Bhattacharya, G. Hogo, S. C. Hong, and E. Gulari, "*Intersubband Absorption in Strained $In_xGa_{1-x}As/Al_{0.4}Ga_{0.6}As$ ($0 \leq X \leq 0.15$) Multiquantum Wells*", Applied Physics Letters, 1989, vol. 54, p. 855-856.

11) C. Weisbuch, R. Dingle, P. M. Petroff, A. C. Gossard, and W. Wiegmann, "*Optical Characterization of Disorder in GaAs- $Ga_{1-x}Al_xAs$ Multi-quantum Well Structures*", Solid State Communications, 1981, vol. 38, p. 709-712.

12) M. Tanaka, H. Sakaki, J. Yoshino, and T. Furuta, "*Photoluminescence and Absorption Linewidth of Extremely Flat GaAs-AlAs Quantum Wells Prepared by Molecular Beam Epitaxy Including Interrupted Deposition for Atomic Layer Smoothing*", Surface Science, 1986, vol. 174, p. 65-70.

Chapter 3 Modelling

3.1 *k.p.* Model

The work and time that goes towards the development of new optoelectronic devices based on QW structure is very high. Therefore, in order to better understand the physical properties of a device, it is important that one can stimulate the expected performance on a computer. They must be tested on a wide range of structures to ensure that they are well behaved. In this work, I have used an existing model [1] developed to deal with up to 3 layers (i.e., a stepped QW with one type of barrier) in the strained InGaAsP material system. I have then modified this model to deal with the InGaAlAs material system. We have compared our model with results from several others in the literature; the energy levels calculated are in good agreement with both experimental and modelled values in the literature.

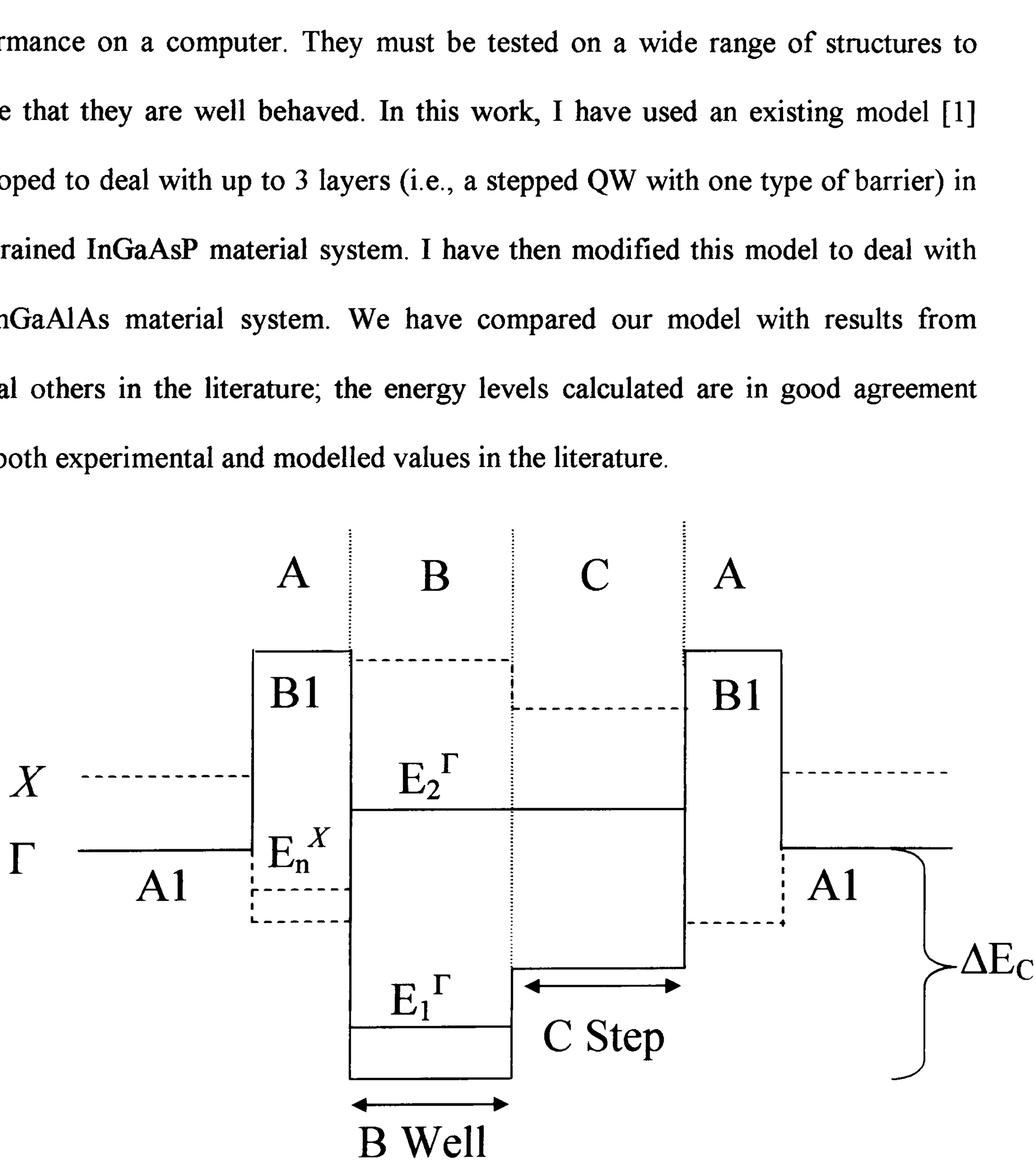

(a)

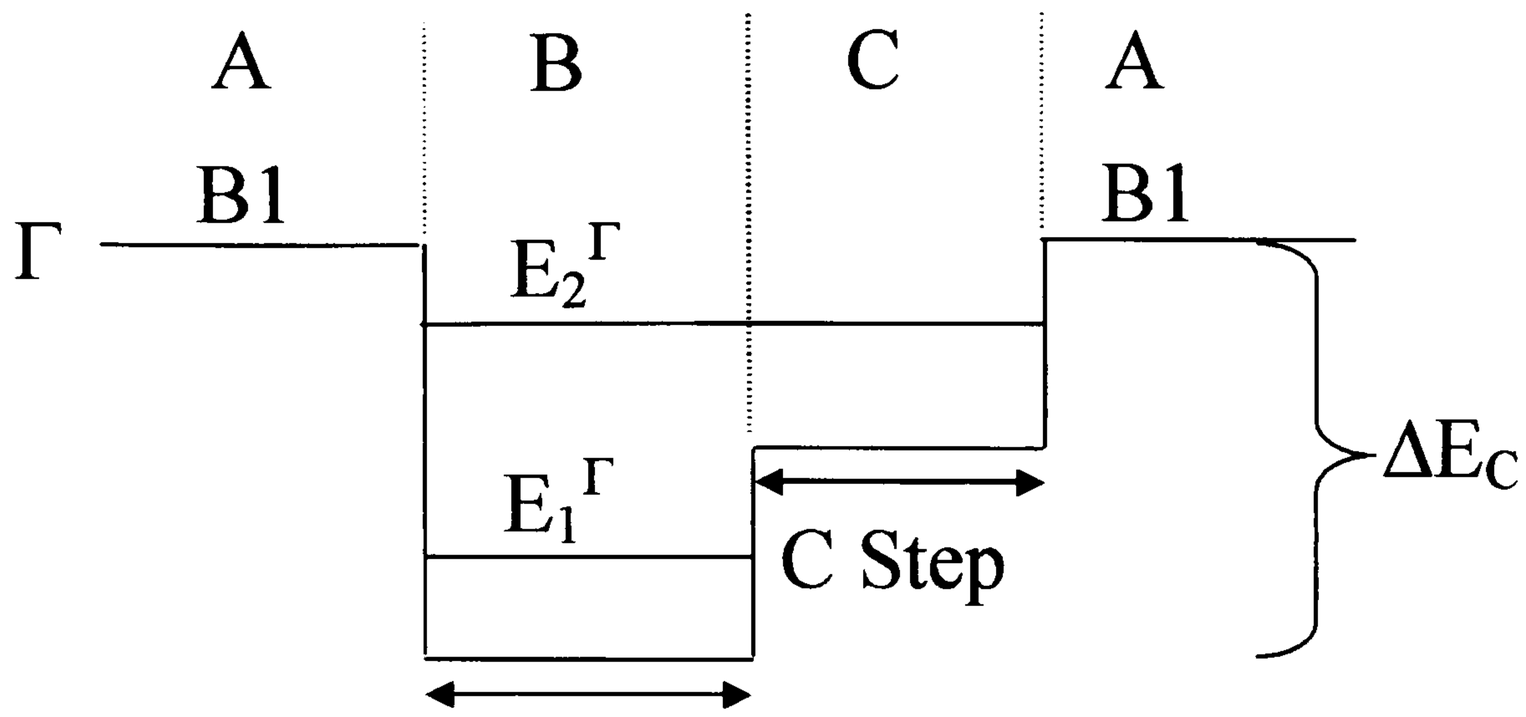

(b)

Figure 3.1.1: Modelled generic Γ (solid line) and *X* (dashed line) conduction band edge profile of (a) proposed QW structure (b) QW structure that the model can deal with.

Modelling of the quantum well subband energy levels was carried out using the envelope function approximation [2] in which the energy states are described using a three-band (electron, light hole, spin split off bands) Kane ***k.p*** model [1] that takes into account the effect of strain and bulk band nonparabolicity (see Appendix D for further details). The band offset ratio ΔE_C:ΔE_V is chosen as an adjustable parameter. For simplicity, the many body effects such as depolarisation [3] and exchange effects [4] are not considered in the current model. The model can only deal with structure shown in Fig. 3.1.1(b) and not Fig. 3.1.1(a) our proposed structure. However, we have shown using a single band model that provided the thin inner barrier (B1 in Fig. 3.3.1(a)) is not reduced below 0.8 nm [5] the position of the gamma (Γ) energy levels in the well are unaffected by the inner barrier thicknesss. This is also confirmed by Tsai *et al.* [6]. The binary materials (B) and ternary (T) alloys used in our model are listed in Table 3.1.1. The material parameters for ternary

alloy with compositions of the form $A_xB_{1-x}C$ are estimated by interpolating the parameters of the binary alloys using:

$$T_{A_xB_{1-x}C} = (x)B_{AC} + (1-x)B_{BC} \tag{3.1.1}$$

Parameters such as spin orbit coupling in ternary alloys, which deviate from the linear relation of equation (3.1.1) can be approximated by the quadratic expression:

$$T_{A_xB_{1-x}C} = (x)B_{AC} + (1-x)B_{BC} + x(1-x)C_{ABC} \tag{3.1.2}$$

where C is known as the bowing parameter.

Parameter	Symbol	Unit	GaAs	InAs	AlAs	InP
Lattice constant	a_o	Å	5.6533[A]	6.0584[B]	5.6611[A]	5.8688[B]
Elastic stiffness constant	C_{11}	10^{11} dyn/cm^2	11.88[A]	8.329[B]	12.02[A]	†
Elastic stiffness constant	C_{12}	10^{11} dyn/cm^2	5.38[A]	4.526[B]	5.70[A]	†
Spin orbit splitting	Delta	eV	0.34[D]	0.38[D]	0.28[D]	†
Shear deformation potential	b	eV	-1.7[A]	-1.8[B]	-1.5[A]	†
Hydrostatic deformation potential	agap	eV	-8.233[D]	-6.08[D]	-8.11[D]	†
Luttinger parameter	g1		6.95[C]	20.40[C]	3.45[C]	†
Luttinger parameter	g2		2.25[C]	8.30[C]	0.68[C]	†
Electron effective mass	m_e/m_o		0.067[C]	0.0239[C]	0.15[C]	†
Static dielectric constants	eperm		13.18[A]	14.6[B]	10.06[A]	†

Parameter	Symbol	Unit	$Al_xGa_{1-x}As$	$In_{1-x}Ga_xAs$	$In_{1-x}Al_xAs$
Heavy Hole effective mass	m_{hh}/m_o		(1/(g1-2*g2))[F]	(1/(g1-2*g2))[F]	(1/(g1-2*g2))[F]
Light Hole effective mass	m_{lh}/m_o		(1/(g1+2*g2))[F]	(1/(g1+2*g2))[F]	(1/(g1+2*g2))[F]
Spin orbit splitting bowing	C(Delta)		0[H]	0.15[H]	0.15[H]
Band gap Energy (300K)	E_g	eV	1.424+1.247x ($0<x<0.45$)[F] 1.424+1.247x+ 1.147$(x-0.45)^2$ ($0.45<x<1.0$)[F] X Energy gap (1.9+0.125x+ 0.143x^2)[G]	(0.324+0.7x+0.4x^2)[E] X Energy gap 2.03+0.25(1-x)[I]	(0.37+1.91x+0.78x^2)[E] X Energy gap (1.8+0.4x)[E]

Table 3.1.1: Material parameters used in the model. †These parameters are not needed in the model.

A) S. Adachi, "*GaAs, AlAs, and $Al_xGa_{1-x}As$: Material Parameters for use in Research and Device Applications*", Journal of Applied Physics, 1985, vol. 58, p. R1-R29.

B) S. Adachi, "*Material Parameters of $In_{1-x}Ga_xAs_yP_{1-y}$ and Related Binaries*", Journal of Applied Physics, 1982, vol. 53, p. 8775-8792.

C) T. Ishikawa, "*Band Lineup and In-plane Effective Mass of InGaAsP on InP Strained-layer Quantum Well*", IEEE Journal of Quantum Electronics, 1994, vol. 30, p. 562-569.

D) J. R. Jensen, J. M. Hvam, and W. Langbein, "*Optical Properties of InAlGaAs Quantum Wells: Influence of Segregation and Band Bowing*", Journal of Applied Physics, 1999, vol. 86, p. 2584-2589.

E) O. Madelung, M. Schulz, W. von der Osten, and U. Rössler, *Landort-Bornstein, Numerical Data and Functional Relationships in Science and Technology, (New Series III)*, vol. 22a, Semiconductors, Springer, Berlin (1987).

F) T. Hiroshima and K. Nishi, "*Quantum-confined Stark Effect in Graded-gap Quantum Wells*", Journal of Applied Physics, 1987, vol. 62, p. 3360-3364.

G) H. C. Casey, Jr. and M. B. Panish, *Heterostructure Lasers Part B: Materials and Operating Characteristics*, Academic Press, New York (1978).

H) M. P. C. M. Krijn, "*Heterostructures Band Offsets and Effective Masses in III-V Quaternary Alloys*", Semiconductor Science Technology, 1991, vol. 6, p. 27-31.

I) The equation is obtained by linearly interpolating between the $E(X_{6c})$ values for $InAs^E$ and $GaAs^E$.

3.2 Comparison of Model with Literature Values

To test the soundness of our model, we used it to calculate the energy levels and band profile of four QWs structures reported in the literature and compared our results with published optical data. ΔE_C:ΔE_V of 0.65:0.35 and 0.7:0.3 are assumed for the Ga(In)As/Al(Ga)As [7-10] and InGaAs/InAlAs [11] heterojunctions, respectively. These ratios are taken to be independent of the indium and aluminum compositions. The results are as shown in the next section. The symbols used are E_c-conduction band edge, E_v-valence band edge, E-Electron, HH-Heavy hole, LH-Light hole and the number after E or HH or LH is the subband index. The E_n^X subband levels in the *X* QW were calculated using an *X* valley effective mass of $m_{e\text{-}x} = 0.4m_0$. $Al_xGa_{1-x}As$ is a direct-gap semiconductor for x<=0.45 (i.e. Γ band is the lowest energy bandgap), but becomes indirect when x>0.45 (i.e. *X* band is the lowest energy bandgap). Therefore, for the AlAs/$Al_{0.4}Ga_{0.6}As$ *X* QW in Sec. 3.2.2, the well is in the AlAs and the barrier is formed by the $Al_{0.4}Ga_{0.6}As$.

3.2.1 Double barrier quantum wells (DBQWs)

Figures 3.2.1.1(a) and 3.2.1.1(b) show the modelled generic conduction band profile of the QW structure reported by Schneider *et al.* [12] and Liu *et al.* [13],

respectively. These were obtained based on transfer matrix method (TMM) using two-band approximation and one band effective mass approximation, respectively. These two QW structures were chosen as they are similar to our proposed structure in term of well/barriers materials and transition energies. Tables 3.2.1.1(a) and 3.2.1.1(b) lists the values of the conduction band edge potential, subbands energies, measured and calculated transition energies obtained by Schneider *et al.* [12], Liu *et al.* [13], and our model, respectively.

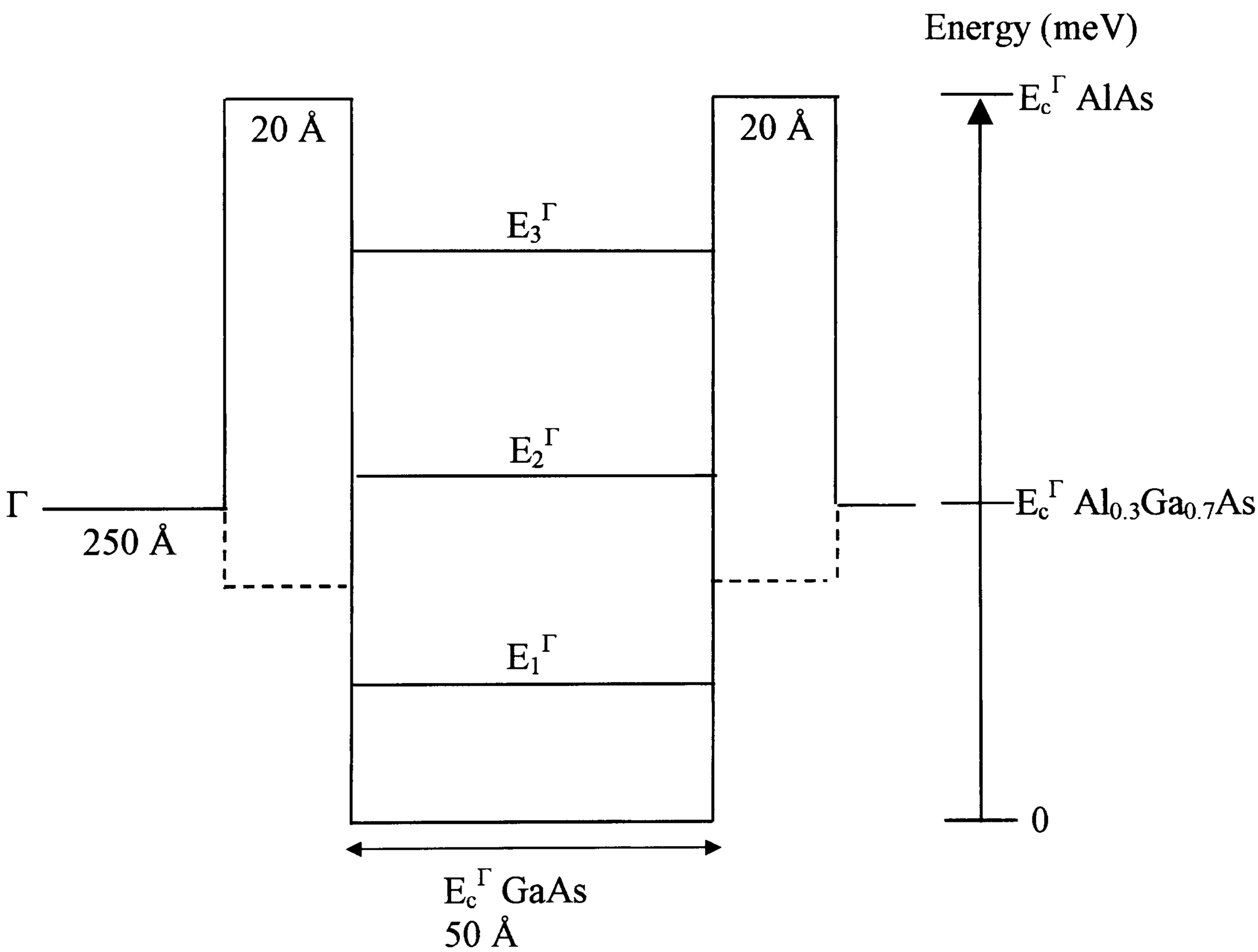

(a)

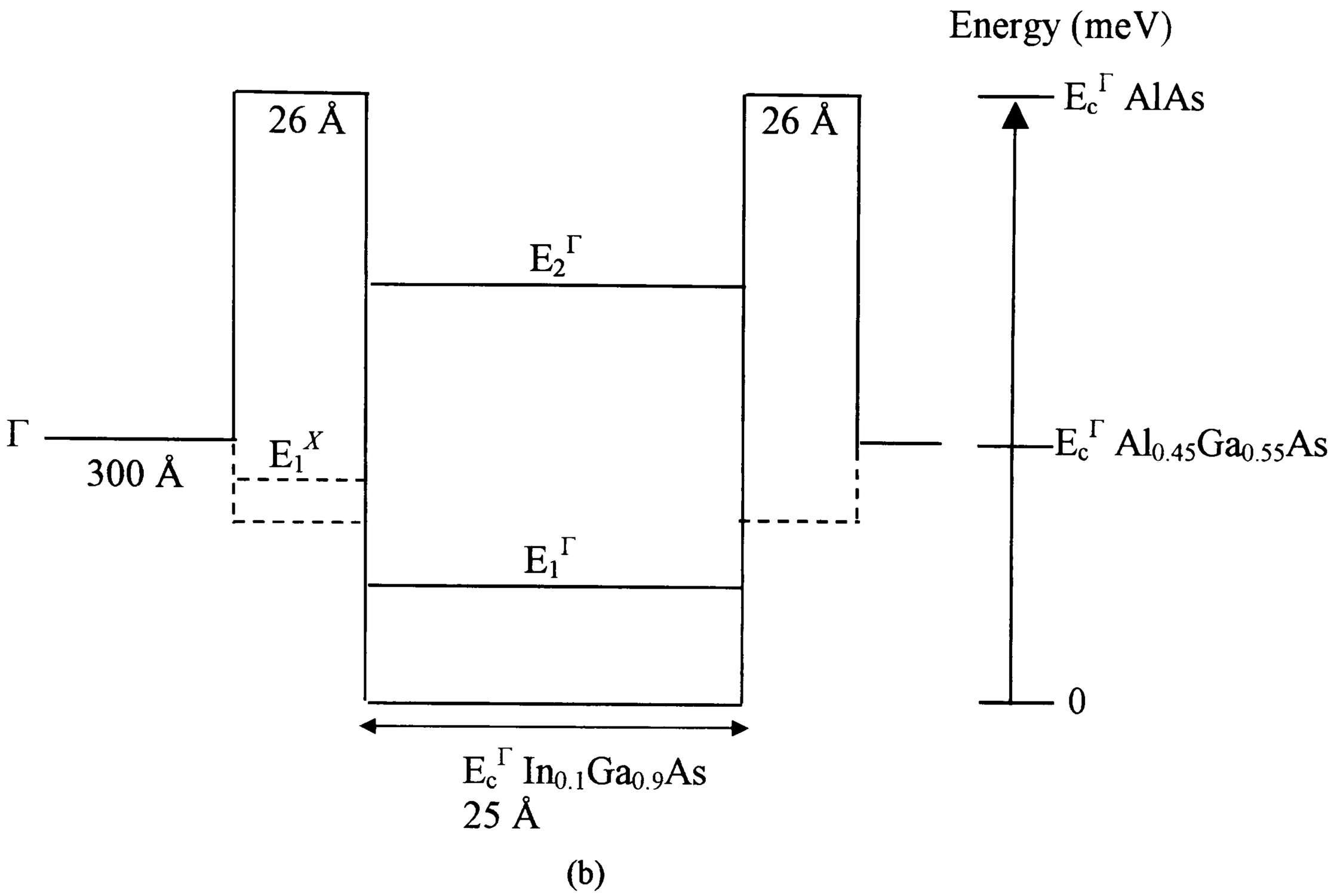

(b)

Figure 3.2.1.1: Schematic Γ (thick line) and *X* (dashed line) conduction band profile of the DBQW structure under study reported by (a) Schneider *et al.* [12] and (b) Liu *et al.* [13].

	Schneider *et al.* [12]	**Our model**
E_1^{Γ} (meV)	118	112
E_2^{Γ} (meV)	414	395
E_3^{Γ} (meV)	790	756
E_c^{Γ} $Al_{0.3}Ga_{0.7}As$ (meV)	250	240
E_c^{Γ} AlAs (meV)	1050	1030
Modelled $E_1^{\Gamma} \rightarrow E_2^{\Gamma}$ transition energy (meV)	296	283
Measured $E_1^{\Gamma} \rightarrow E_2^{\Gamma}$ transition energy (meV)	293	

(a)

	Liu *et al.* [13]	Our model
E_1^{Γ} (meV)	250	280
E_2^{Γ} (meV)	860	870
E_1^{X} (meV)	290	291
E_c^{Γ} $Al_{0.45}Ga_{0.55}As$ (meV)	430	430
E_c^{Γ} AlAs (meV)	1100	1100
Modelled $E_1^{\Gamma} \rightarrow E_2^{\Gamma}$ transition energy (meV)	610	590
Measured $E_1^{\Gamma} \rightarrow E_2^{\Gamma}$ transition energy (meV)	680	
Modelled $E_1^{X} \rightarrow X$ continuum transition energy (meV)	140	139
Measured $E_1^{\Gamma} \rightarrow X$ continuum transition energy (meV)	155	

(b)

Table 3.2.1.1: Comparsion of the modelled conduction band edge potentials, subbands energies of the QW structure obtained by (a) Schneider *et al.* [12] and our model and (b) Liu *et al.* [13] and our model. The measured and calculated transition energies are also shown. All the values shown are with respect to the bottom of the well.

From Tables 3.2.1.1(a) and 3.2.1.1(b), one can see that the values obtained using our model are in good agreement with the theoretical and observed values of Schneider *et al.* [12] and Liu *et al.* [13]. This clearly shows that the model is able to deal with this type of structure.

3.2.2 *X* valley quantum wells

The $E_1^X \rightarrow X$ continuum in ref. [13] was obtained using an *X* band effective mass of $0.4m_0$. This value was chosen as we are able to model the *X* transitions in $AlAs/Al_{0.4}Ga_{0.6}As$ *X* valley QW reported by Katz *et al.* [14]. The conduction band edge profile of $AlAs/Al_{0.4}Ga_{0.6}As$ *X* valley QW obtained by the TMM within the effective-mass approximation is shown in Fig. 3.2.2.1. Table 3.2.2.1 list the values of the conduction band edge potential, subbands energies, measured and calculated transition energies obtained by Katz *et al.* [14] and our model.

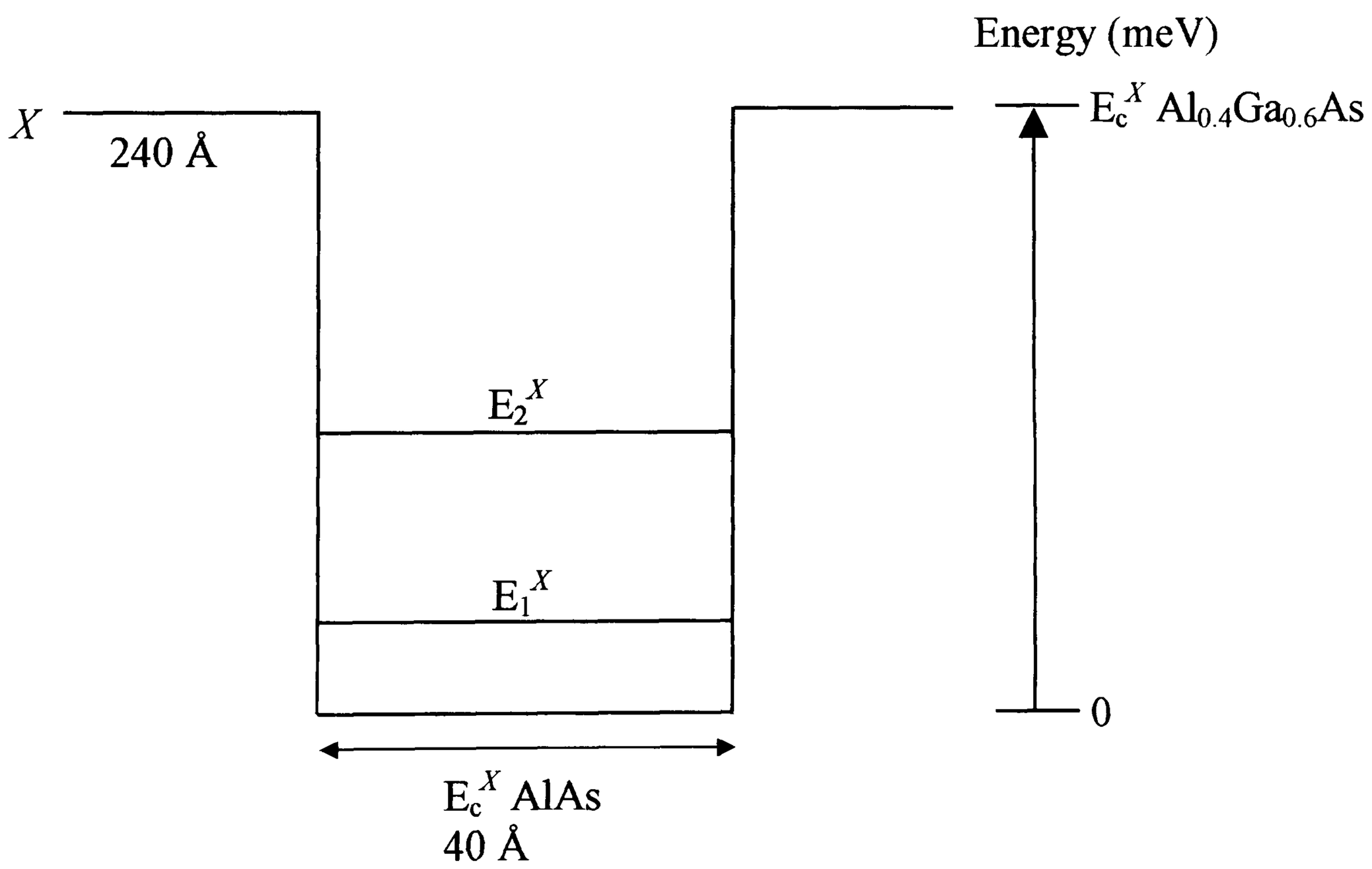

Figure 3.2.2.1: Schematic conduction band profile of $AlAs/Al_{0.4}Ga_{0.6}As$ *X* valley QW reported by Katz *et al.* [14].

	Katz *et al.* [14]	Our model
E_1^X (meV)	23	22
E_2^X (meV)	91	84
E_c^X $Al_{0.4}Ga_{0.6}As$ (eV)	200	191
Modelled $E_1^X \rightarrow E_2^X$ transition energy (meV)	68	62
Measured $E_1^X \rightarrow E_2^X$ transition energy (meV)	73	
Modelled $E_1^X \rightarrow X$ continuum transition energy (meV)	177	169
Measured $E_1^X \rightarrow X$ continuum transition energy (meV)	177	

Table 3.2.2.1: Comparsion of the modelled conduction band edge potentials, subbands energies of the QW structure obtained by Katz *et al.* [14] and our model. The measured and calculated transition energies are also shown. All the values shown are with respect to the bottom of the well.

As can be seen, our calculated values are in good agreement with the values obtained by Katz *et al.* [14].

3.2.3 Stepped quantum well

Figure 3.2.3.1 shows the schematic conduction band profile of stepped $GaAs/Al_{0.18}Ga_{0.82}As/Al_{0.44}Ga_{0.56}As$ QW reported by Mii *et al.* [15]. This structure was chosen as it is similar to some of our proposed structure. The subband energies of the stepped QWs are calculated in this paper using the TMM approach. Table 3.2.3.1 lists the values obtained by both models.

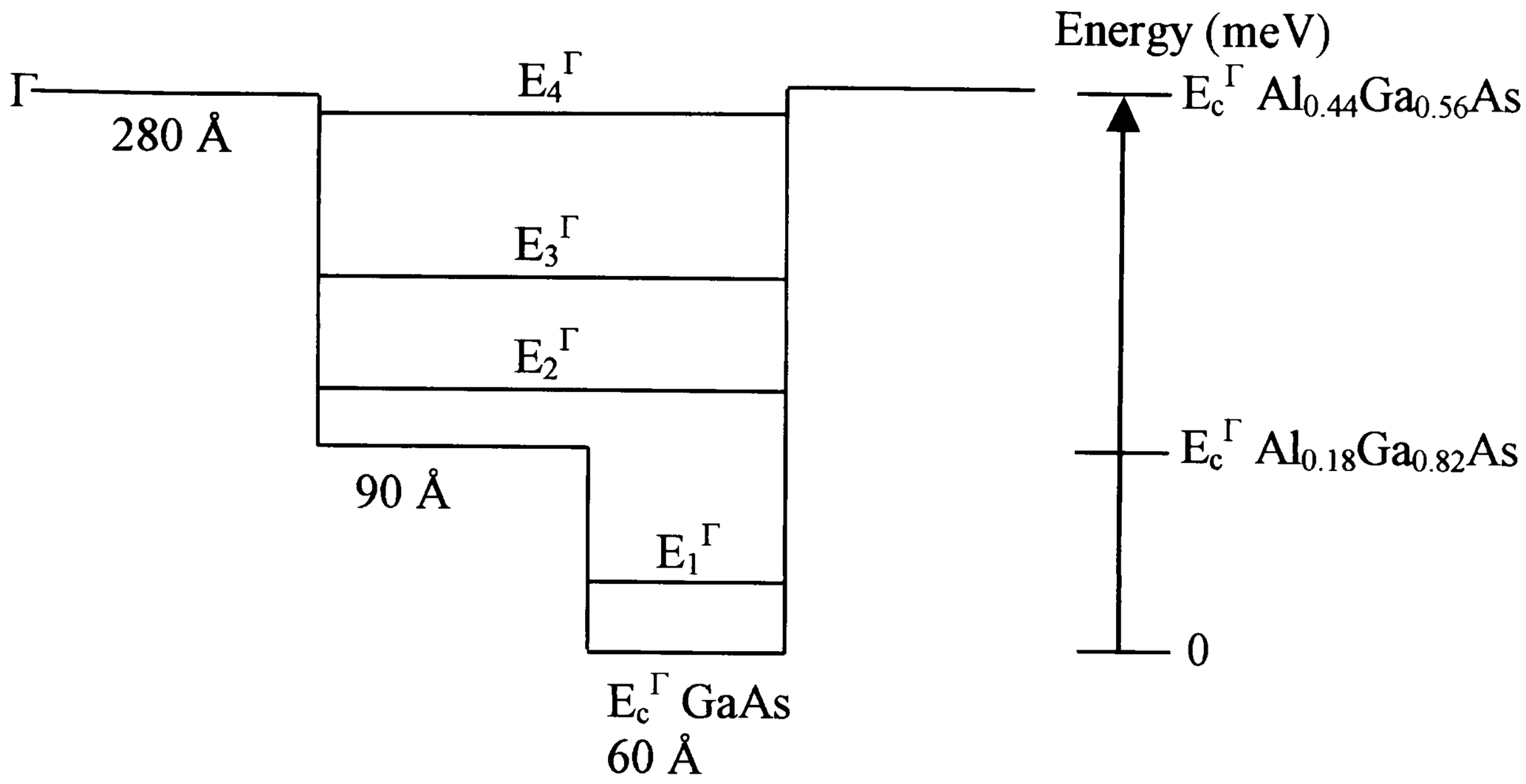

Figure 3.2.3.1: Schematic conduction band profile of the stepped $GaAs/Al_{0.18}Ga_{0.82}As/Al_{0.44}Ga_{0.56}As$ QW reported by Mii *et al.* [15].

	Mii *et al.* [15]	**Our model**
E_1^{Γ} (meV)	54	57
E_2^{Γ} (meV)	162	167
E_3^{Γ} (meV)	216	213
E_4^{Γ} (meV)	305	294
Modelled $E_1^{\Gamma} \rightarrow E_2^{\Gamma}$ transition energy (meV)	108	110
Measured $E_1^{\Gamma} \rightarrow E_2^{\Gamma}$ transition energy (meV)	112	
Modelled $E_1^{\Gamma} \rightarrow E_3^{\Gamma}$ transition energy (meV)	162	156
Measured $E_1^{\Gamma} \rightarrow E_3^{\Gamma}$ transition energy (meV)	150	

Table 3.2.3.1: Comparsion of the subbands energies obtained by Mii *et al.* [15] and our model. The measured and calculated transition energies are also shown.

From Table 3.2.3.1, our calculated values are in good agreement with the values obtained by Mii *et al.* [15]. This again clearly shows that the model can deal with this type of structure.

3.2.4 P-type quantum wells

Figure 3.2.4.1 shows the schematic valence band profile of the p-doped $In_{0.15}Ga_{0.85}As/Al_{0.45}Ga_{0.55}As$ QW reported by Zhang *et al.* [16]. This structure was chosen to test the ability of our model to accurately determined the valence band edge potential as well as the heavy and light holes subband energies. The subband energies of the QWs were calculated using envelope function theory. Table 3.2.4.1 list the values of the valence band edge potential, subbands energies, measured and calculated transition energies obtained by Zhang *et al.* [16] and our model.

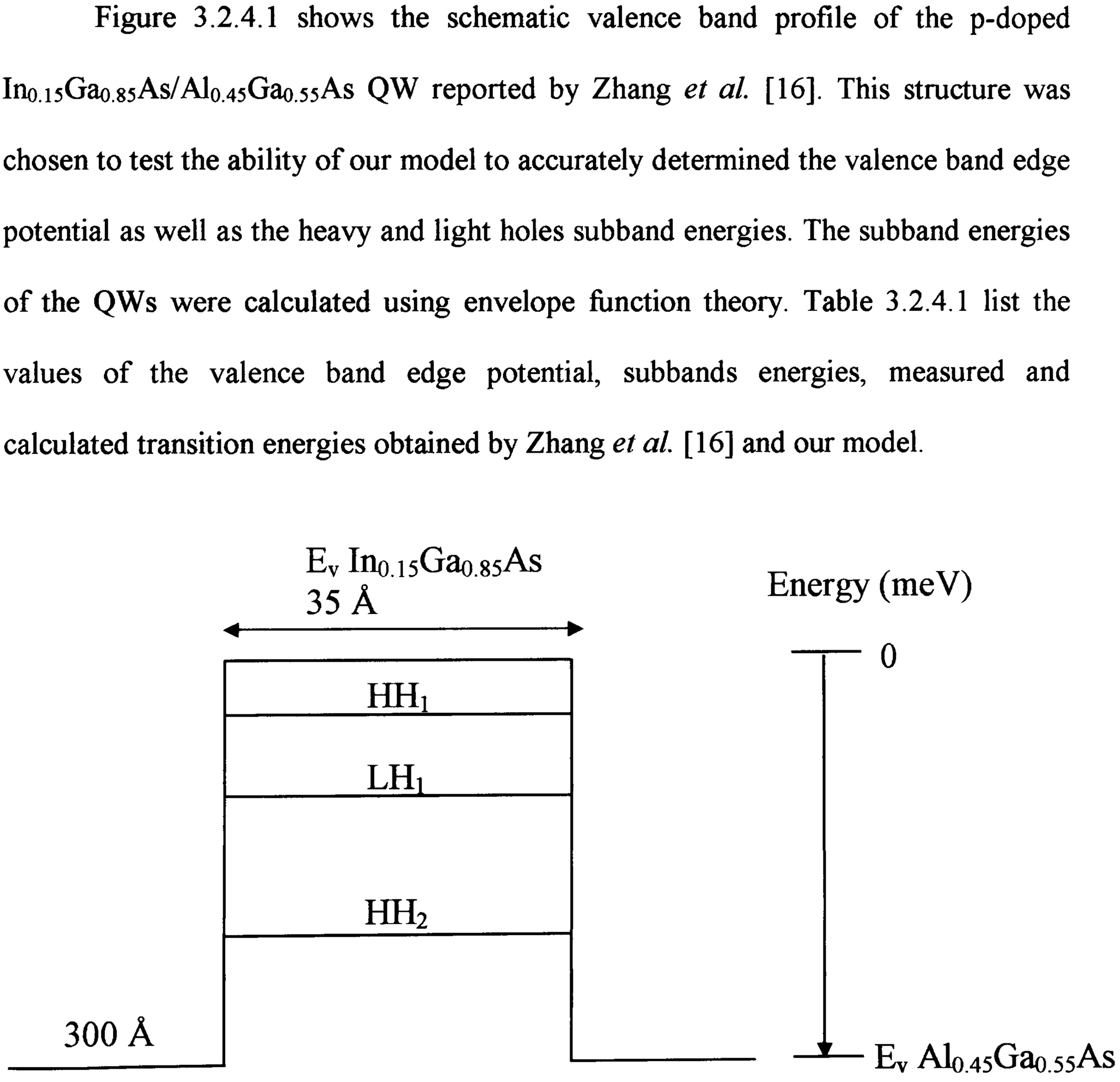

Figure 3.2.4.1: Schematic conduction band profile of the p-doped $In_{0.15}Ga_{0.85}As/Al_{0.45}Ga_{0.55}As$ QW reported by Zhang *et al.* [16].

	Zhang *et al.* [16]	Our model
HH_1 (meV)	41	42
HH_2 (meV)	161	161
LH_1 (meV)	92	129
E_v $Al_{0.45}Ga_{0.55}As$ (meV)	251	253
Modelled $HH_1 \rightarrow HH_2$ transition energy (meV)	119	118
Measured $HH_1 \rightarrow HH_2$ transition energy (meV)	116	

Table 3.2.4.1: Comparsion of the modelled valence band edge potential, subbands energies of the QW structure obtained by Zhang *et al.* [16] and our model. The measured and calculated transition energies are also shown.

It can be seen that the values obtained from our model are in excellent agreement with the results obtained by Zhang *et al.* [16].

3.2.5 Summary

	Schneider *et al.* [12]	**Liu *et al.* [13]**	**Katz *et al.* [14]**	**Mii *et al.* [15]**	**Zhang *et al.* [16]**
QW structure	Lattice-matched DBQWs	Lattice-mismatched DBQWs	Lattice-Matched *X* valley QWs	Lattice-matched Stepped QWs	Lattice-mismatched p-doped QWs
Method	TMM using two-band approximation	One band effective mass approximation	TMM	TMM	Envelope function theory
Modelled Transition energy (meV)	$E_1^{\Gamma}\rightarrow E_2^{\Gamma}$ (296)	$E_1^{\Gamma}\rightarrow E_2^{\Gamma}$ (610) $E_1^{X}\rightarrow X$ continuum (140)	$E_1^{X}\rightarrow E_2^{X}$ (68) $E_1^{X}\rightarrow X$ continuum (177)	$E_1^{\Gamma}\rightarrow E_2^{\Gamma}$ (108) $E_1^{\Gamma}\rightarrow E_3^{\Gamma}$ (162)	$HH_1\rightarrow HH_2$ (119)
Measured Transition energy (meV)	$E_1^{\Gamma}\rightarrow E_2^{\Gamma}$ (293)	$E_1^{\Gamma}\rightarrow E_2^{\Gamma}$ (680) $E_1^{X}\rightarrow X$ continuum (155)	$E_1^{X}\rightarrow E_2^{X}$ (73) $E_1^{X}\rightarrow X$ continuum (177)	$E_1^{\Gamma}\rightarrow E_2^{\Gamma}$ (112) $E_1^{\Gamma}\rightarrow E_3^{\Gamma}$ (150)	$HH_1\rightarrow HH_2$ (116)
Our model Transition energy (meV)	$E_1^{\Gamma}\rightarrow E_2^{\Gamma}$ (283)	$E_1^{\Gamma}\rightarrow E_2^{\Gamma}$ (590) $E_1^{X}\rightarrow X$ continuum (139)	$E_1^{X}\rightarrow E_2^{X}$ (62) $E_1^{X}\rightarrow X$ continuum (169)	$E_1^{\Gamma}\rightarrow E_2^{\Gamma}$ (110) $E_1^{\Gamma}\rightarrow E_3^{\Gamma}$ (156)	$HH_1\rightarrow HH_2$ (118)

Table 3.2.5.1: Comparison between values obtained from our model with respect to different QWs structures reported in the literature.

The table above shows a summary of the comparison between our model and the literature data. One can see that the results obtained from our model are in good agreement with the measured values. The sensitivity check on our model shows that a 1 monolayer (ML) thickness change and 5 percent alloy composition deviation from the intended growth parameters give a variation of about 25 meV and about 1 meV change in the transition energy, respectively while a 5 percent deviation from the chosen ΔE_C:ΔE_V gives a variation of about 6 meV. This indicates that the main discrepancy between the observed and measured values is probably due to the

uncertainty in the layer thickness. Hence, we are able to design new QW structures using this model and to have confidence in our ability to engineer precisely the desired transition energy/peak detection wavelength (λ_p) using this model.

3.3 Modelling of GaAs based DBQWs samples

The objective in this section and 3.4 is to investigate device designs grown at UMIST on GaAs and InP substrates, respectively. First we look at the effect of incorporating a stepped well into a DBQW structure on the selection rules for the intersubband transitions and on the conduction band offset ΔE_C (between the wide outer barrier and well). In addition, the position of subband energy levels was investigated in relation to our goal of achieving short wavelength detection.

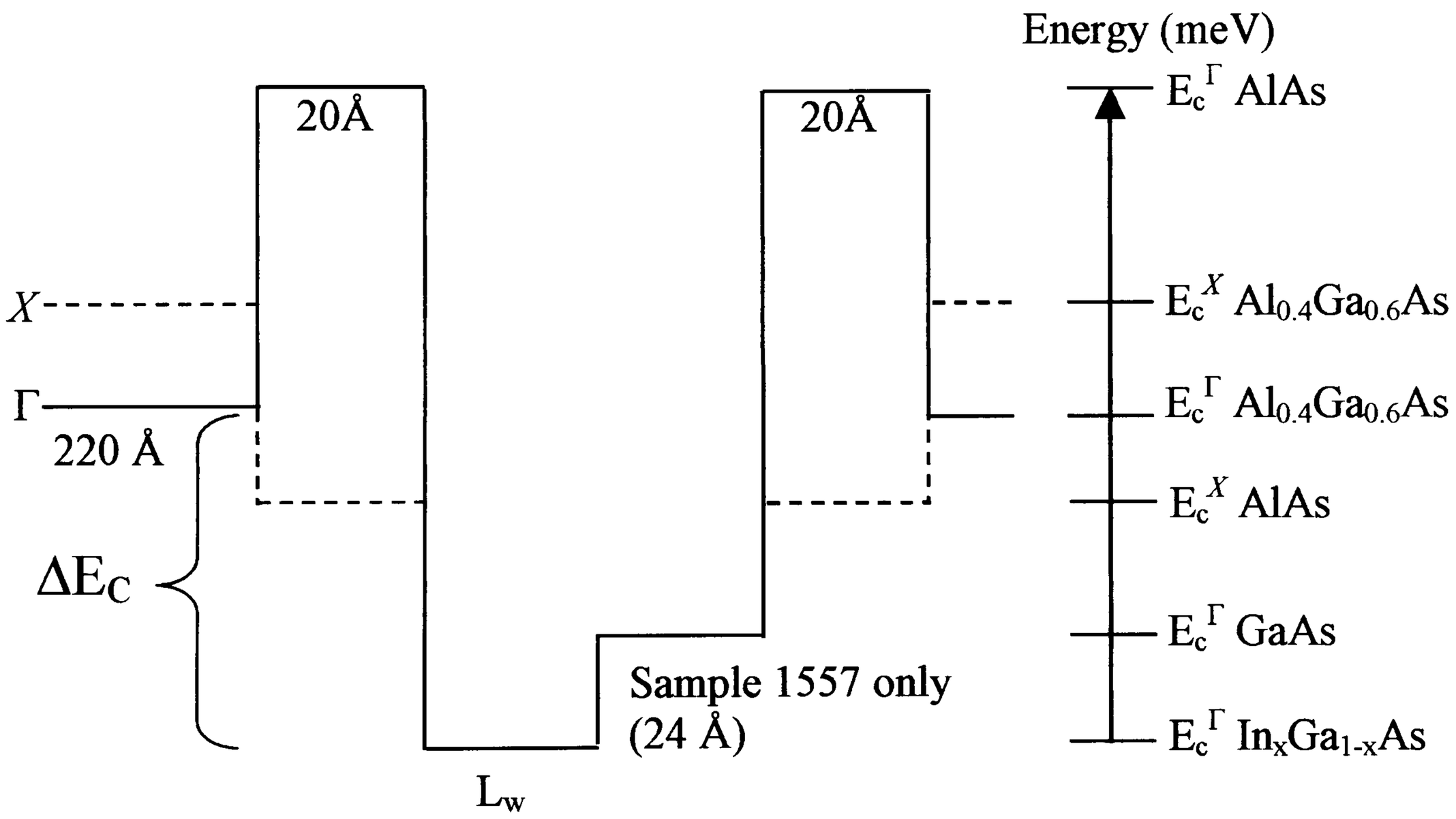

Figure 3.3.1: Modelled generic Γ (thick line) and *X* (dashed line) conduction band edge profile of the GaAs based DBQWs samples.

Energy/conduction band potential levels (meV)	Sample No. 1546	1547	1551	1557
E_1^{Γ}	131	134	131	194
E_2^{Γ}	452	462	452	517
E_3^{Γ}	849	868	849	886
E_1^{X}	242	379	242	413
E_2^{X}	362	499	362	533
$E_1^{\Gamma} + E_F$	163	171	259	276
E_c^{Γ} $Al_{0.4}Ga_{0.6}As$	320	460	320	490
E_c^{X} $Al_{0.4}Ga_{0.6}As$	370	510	370	540
E_c^{Γ} AlAs	1030	1170	1030	1210
E_c^{X} AlAs	180	320	180	360
E_c^{Γ} GaAs	0	0	0	170

Table 3.3.1: Modelled conduction band potentials and subband energy levels in the Γ and *X* band for sample 1546, 1547, 1551, and 1557. All the energy levels are relative to the bottom of the Γ conduction band edge of the $In_xGa_{1-x}As$ QW layer.

Figure 3.3.1 shows the generic conduction band edge of the GaAs based DBQWs samples and Table 3.3.1 lists the modelled conduction band potentials and subband energy levels in the Γ and *X* band. The samples parameters are listed in Table 2.1.1.

3.4 Modelling of InP based DBQWs samples

The advantage of this structure over those in Sec. 3.3 is the still higher ΔE_C compared to the GaAs based DBQWs. This ΔE_C is also larger than in the InP based DBQWs reported in ref. 17 where the operating temperature is around 205 K.

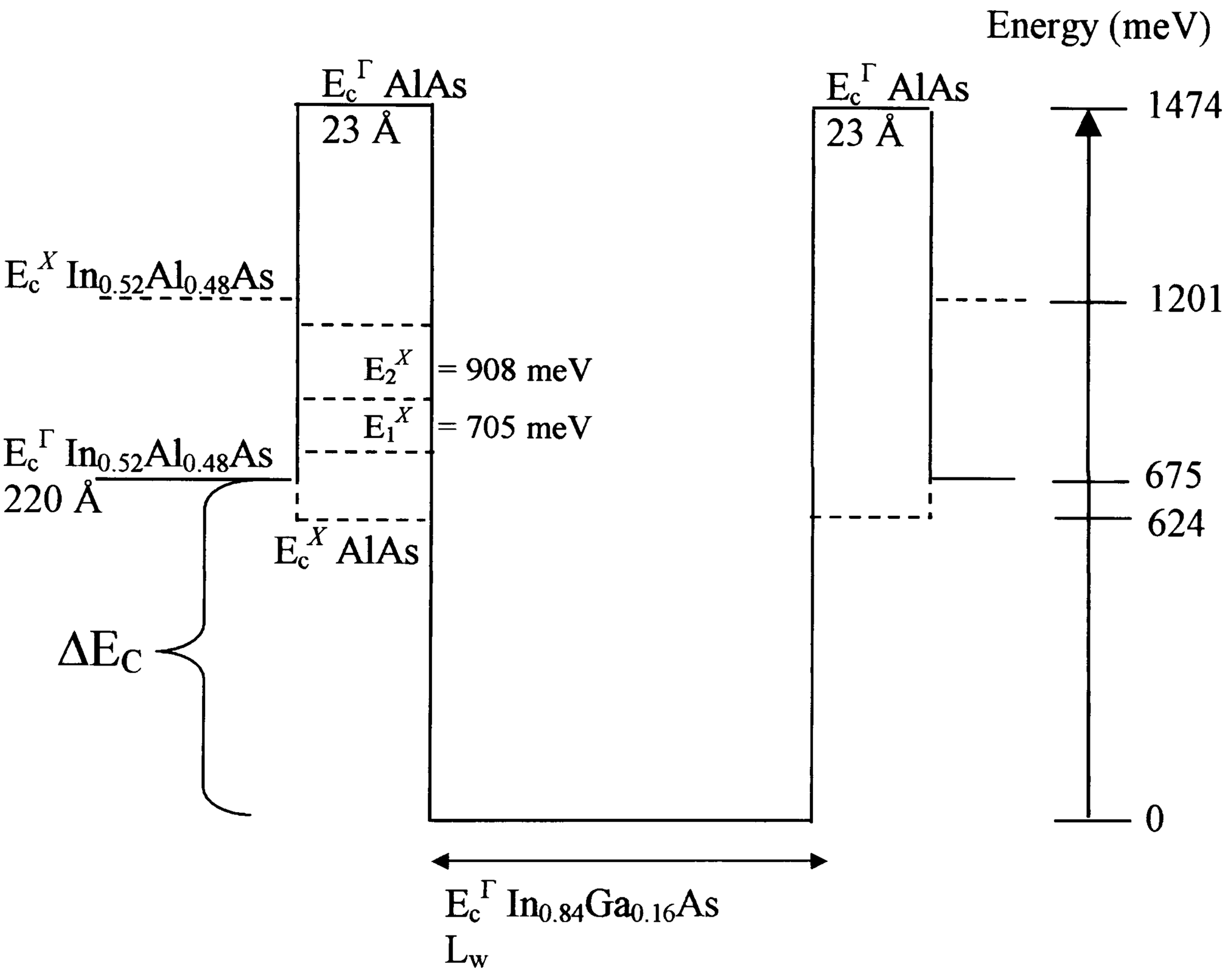

Figure 3.4.1: Modelled generic Γ (thick line) and *X* (dashed line) conduction band edge profile of the InP based DBQWs samples. Energy levels E_1^X and E_2^X confined in the AlAs *X* QW are also shown.

	Sample No.		
Energy levels (meV)	**1554**	**1563**	**1561**
E_1^{Γ}	82	183	301
E_2^{Γ}	276	566	873
E_3^{Γ}	521	1000	1434
E_4^{Γ}	786	1416	
$E_1^{\Gamma} + E_F$	564	627	631

Table 3.4.1: Modelled subband energy levels in the Γ band for the samples. All the energy levels are relative to the bottom of the Γ conduction band of the $In_{0.84}Ga_{0.16}As$ QW layer.

Figure 3.4.1 shows the generic conduction band edge potentials of the InP based DBQWs samples and Table 3.4.1 lists the modelled conduction band subband energy levels in the Γ band. The samples parameters are listed in Table 2.1.2.

References

1) Paul Nicholas Stavrinou, "*A Study of InP Based Strained Layer Heterostructures*", Ph.D. thesis, University of College London, 1994.

2) G. Bastard, and J. A. Brum, "*Electronic States in Semiconductor Heterostructures*", IEEE Journal of Quantum Electronics, 1986, vol. QE-22, p. 1625-1644.

3) M. Ramsteiner, J. D. Ralston, P. Koidl, B. Dischier, H. Biebl, J. Wagner, and H. Ennen, "*Doping Density Dependence of Intersubband Transitions in $GaAs/Al_xGa_{1-x}As$ Quantum-well Structures*", Journal of Applied Physics, 1990, vol. 67, p.3900-3903.

4) K. M. S. V. Bandara , D. D. Coon, Byungsung O, Y. F. Lin and M. H. Francombe, "*Exchange Interactions in Quantum Well Subbands*", Applied Physics Letters, 1988, vol. 53, p. 1931-1933; erratum vol. 55, p. 206 (1989).

5) R. Gupta, private communications.

6) K. L. Tsai, C. P. Lee, P. C. Chen, J .S. Tsang, C. M. Tsai, and J. C. Fan, "*The Effect of Barrier Structure On The Performance of Double Barrier Quantum Well Infra-red Photodetectors*", Solid-State Electronics, 1996, vol. 39, p. 201-204.

7) G. Neu, Y. Chen, C. Deparis, and J. Massies, "*Improvement of the Carrier Confinement by Double-barrier GaAs/AlAs/(Al,Ga)As Quantum Well Structures*", Applied Physics Letters, 1991, vol. 58, p. 2111-2113.

8) H. S. Li, Y. W. Chen, K. L. Wang, and D. Y. C. Lie, "*Intersubband Transitions in Pseudomorphic InGaAs/GaAs/AlGaAs Multiple Step Quantum Wells*", Journal of Vacuum Science Technology B, 1993, vol. 11, p. 1840-1843.

9) J. Y. Andersson, and G. Landgren, "*Intersubband Transitions in Single AlGaAs/GaAs Quantum Wells Studied by Fourier Transform Infrared Spectroscopy*", Journal of Applied Physics, 1988, vol. 64, p. 4123-4127.

10) X. Zhou, P. K. Bhattacharya, G. Hugo, S. C. Hong, and E. Gulari, "*Intersubband Absorption in Strained $In_xGa_{1-x}As/Al_{0.4}Ga_{0.6}As$ ($0 \leq x \leq 0.15$) Multiquantum Wells*", Applied Physics Letters, 1989, vol. 54, p. 855-856.

11) H. Asai, and Y. Kawamura, "*Intersubband absorption in Highly Strained InGaAs/InAlAs Multiquantum Wells*", Applied Physics Letters, 1990, vol. 56, p. 746-748.

12) H. Schneider, F. Fuchs, B. Dischler, J. D. Ralston, and P. Koidl, "*Intersubband Absorption and Infrared Photodetection at 3.5 and 4.2 μm in GaAs Quantum Wells*", Applied Physics Letters, 1991, vol. 58, p. 2234-2236.

13) H. C. Liu, M. Buchanan, and Z. R. Wasilewski, "*Short Wavelength (1-4 μm) Infrared Detectors using Intersubband Transitions in GaAs-based Quantum Wells*", Journal of Applied Physics, 1998, vol. 83, p. 6178-6181; erratum vol. 91, p. 10230 (2002).

14) J. Katz, Y. Zhang, and W. I. Wang, "*Normal Incidence Infrared Absorption in AlAs/AlGaAs X-valley Multiquantum Wells*", Applied Physics Letters, 1992, vol. 61, p. 1697-1699.

15) Y. J. Mii, K. L. Wang, R. P.G. Karunasiri, and P. F. Yuh, "*Observation of Large Oscillator Strengths for Both 1-2 and 1-3 Intersubband Transitions of Step Quantum Well*", Applied Physics Letters, 1990, vol. 56, p. 1046-1048.

16) D. H. Zhang, and W. Shi, "*Dark Current and Infrared Absorption of P-doped InGaAs/AlGaAs Strained Quantum Wells*", Applied Physics Letters, 1998, vol. 73, p. 1095-1097.

17) J. H. Lee, J. C. Chiang, S. S. Li, and P. J. Kannam, "*An AlAs/InGaAs/AlAs/InAlAs Double-barrier Quantum Well Infrared Photodetector Operating at 3.4 μm and 205 K*", Applied Physics Letters, 1999, vol. 74, p. 765-767.

Chapter 4 Early Quantum Wells Structure Studies

4.1 Absorption Setup Test

In order to verify the experimental arrangement and polishing technique, two square quantum wells, samples 960 [1] and 1497 [2], grown at UMIST with known optical properties were used. These have peak detection wavelengths of 10 μm (124 meV) and 4 μm (310 meV), respectively. The modelled conduction band edge profiles of samples 960 and 1497 and their respective 300 K absorption spectral measured at the Brewster angle (73^0) are shown in Figs. 4.1.1 and 4.1.2, respectively.

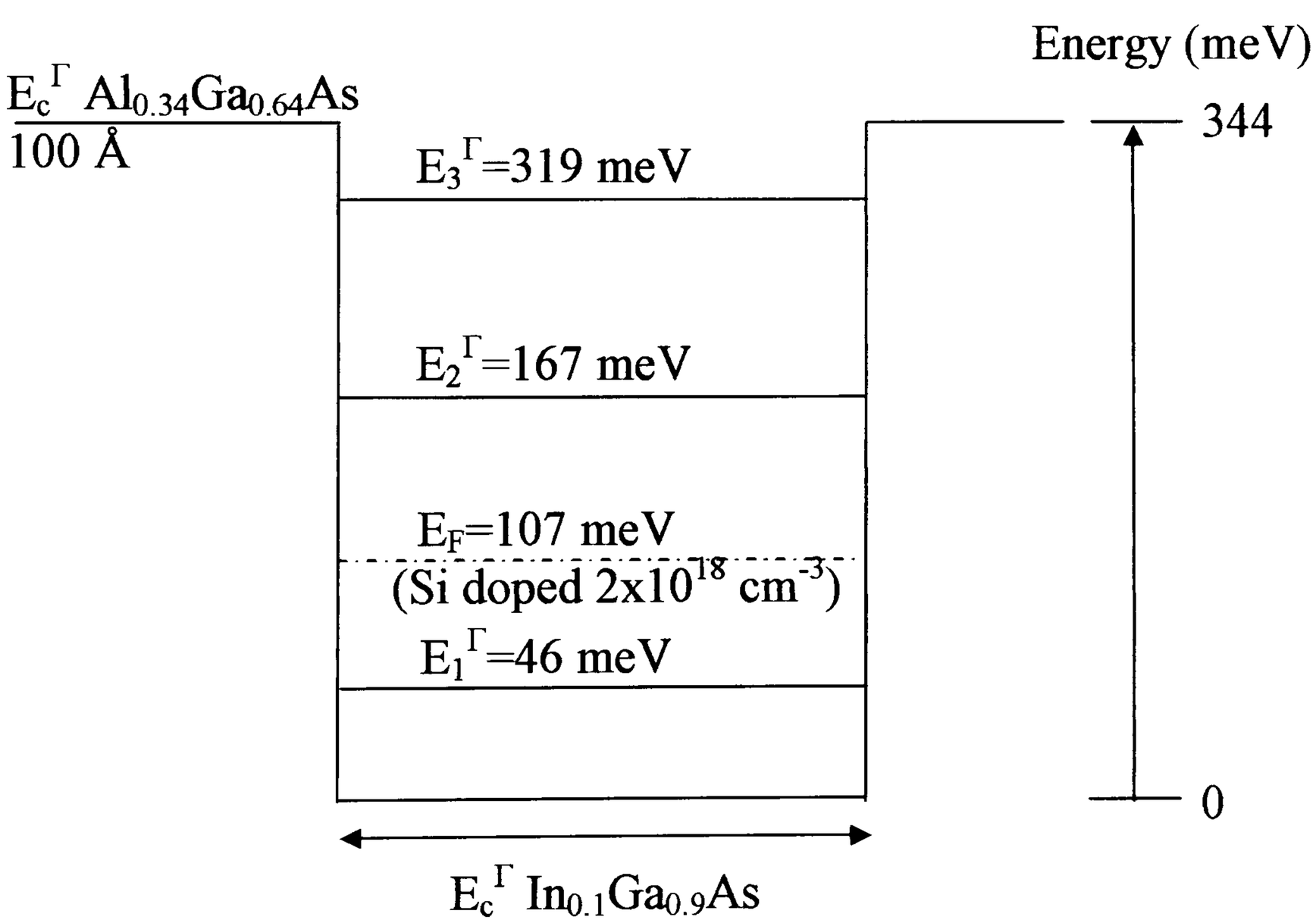

(a)

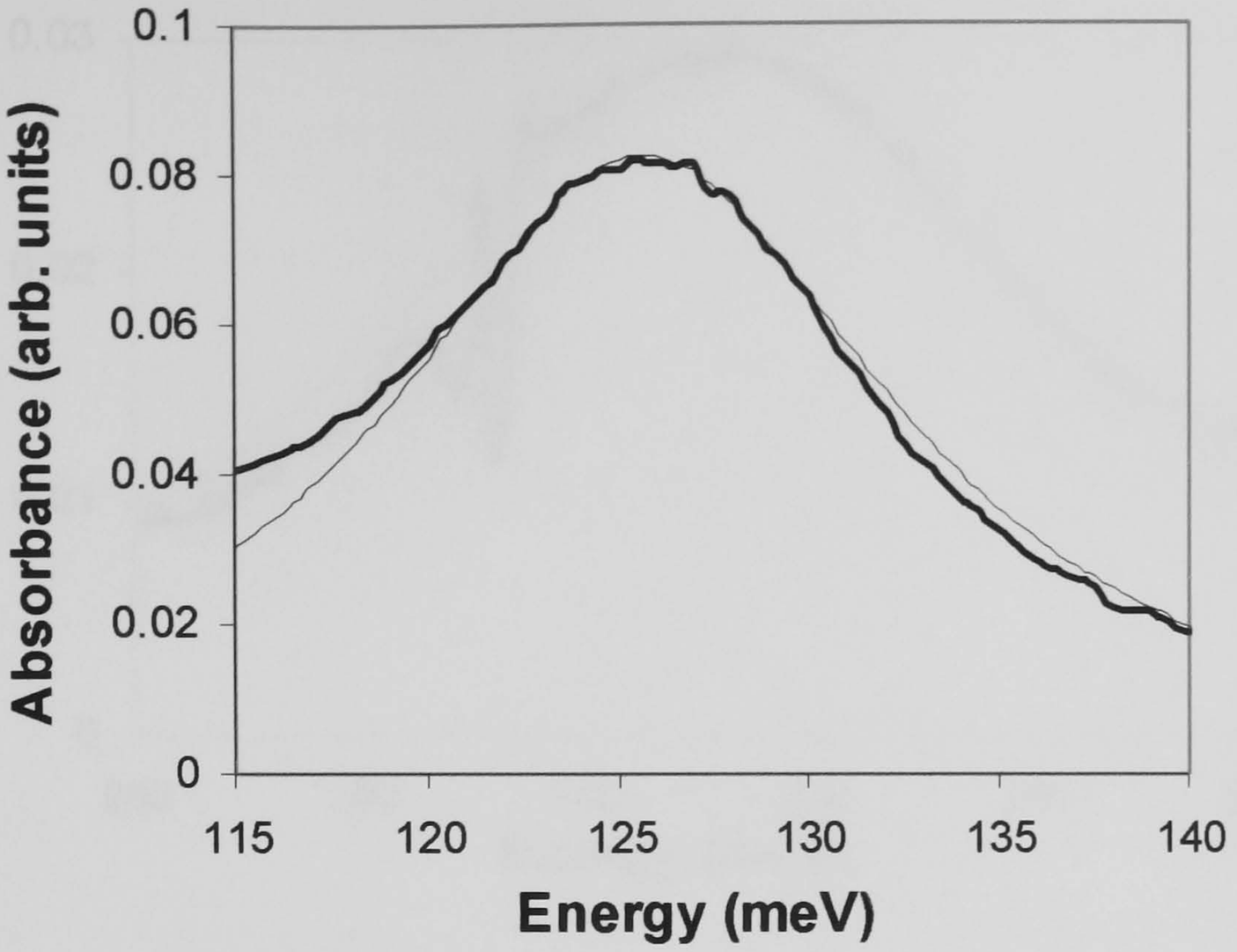

(b)

Figure 4.1.1: Sample 960 (a) modelled conduction band edge profile (b) measured 300 K absorption spectrum (thick line) and Lorentzian curve fit (thin line) at Brewster angle (73^0).

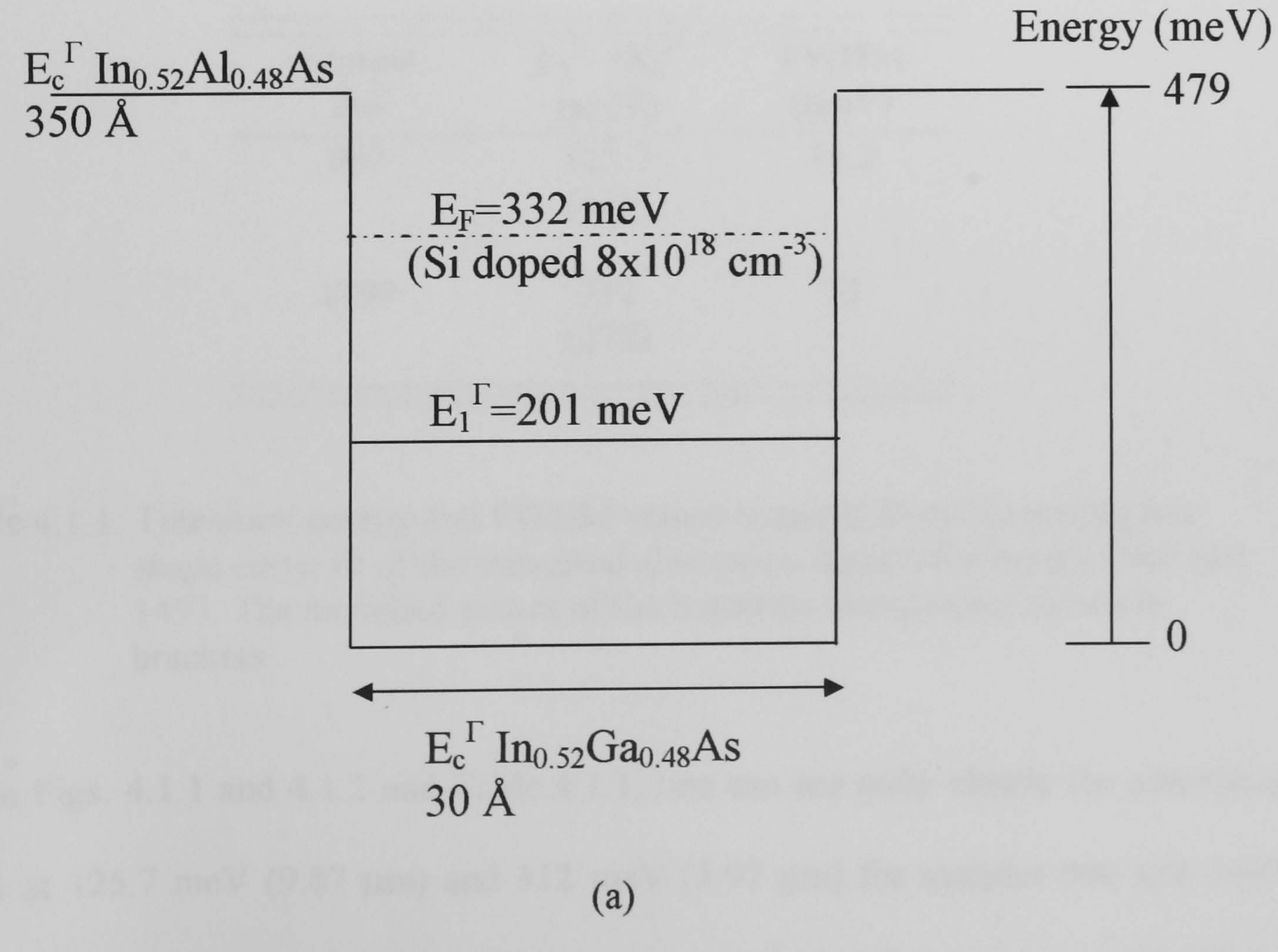

(a)

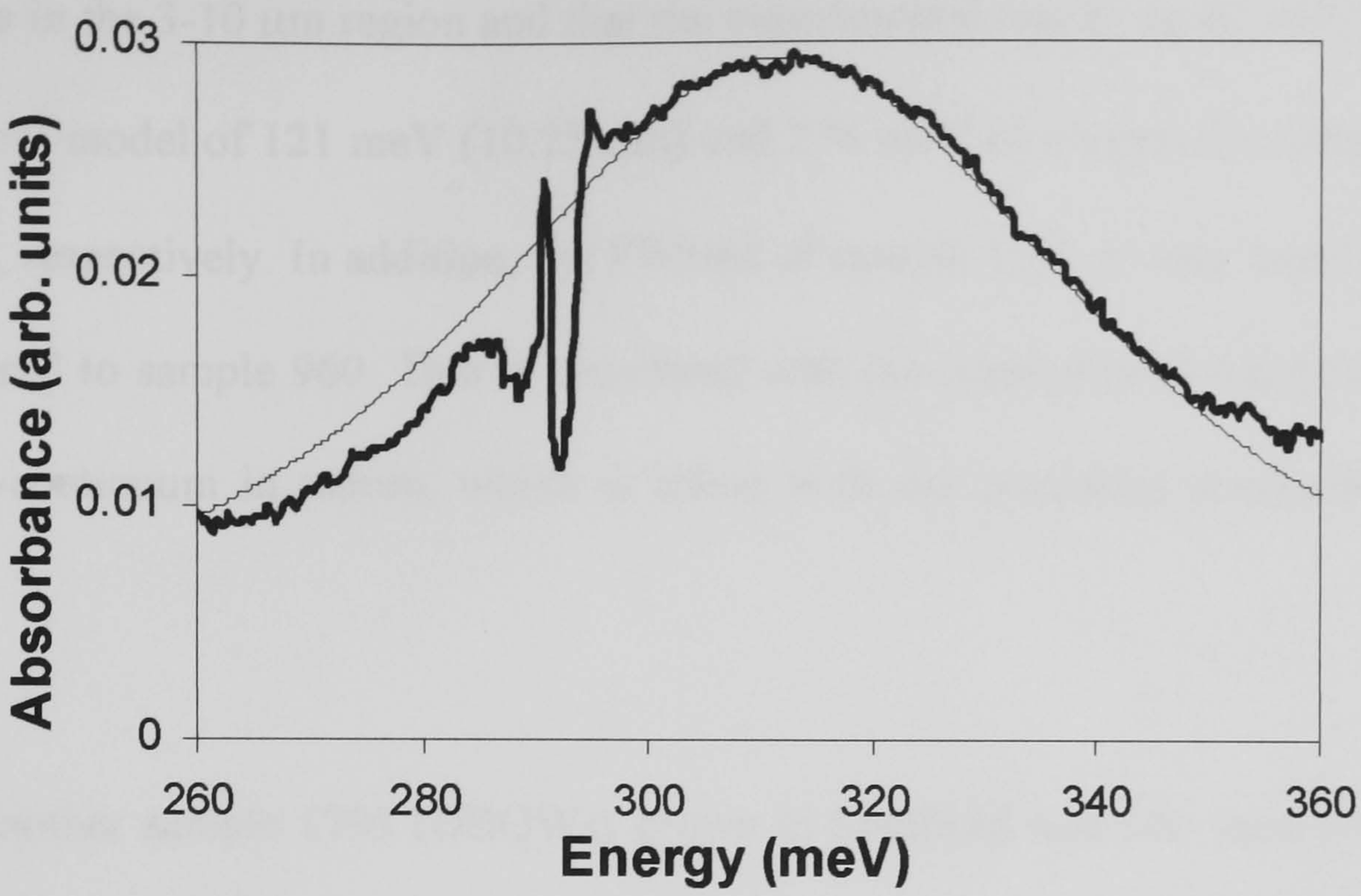

(b)

Figure 4.1.2: Sample 1497 (a) modelled conduction band edge profile (b) measured 300 K absorption spectrum (thick line) and Lorentzian curve fit (thin line) at Brewster angle (73^0). The feature at ~ 285-295 meV is due to atmospheric absorption.

Sample No	$E_1^{\Gamma} \rightarrow E_2^{\Gamma}$ (meV)	FWHM (meV)
960	125.7 (121)	16.2
1497	312 (278)	72

Table 4.1.1: Transition energy and FWHM values obtained from Lorentzian line shape curve fit of the measured absorption spectra for samples 960 and 1497. The modelled values of the transition energies are shown in brackets.

From Figs. 4.1.1 and 4.1.2 and Table 4.1.1, one can see quite clearly the absorption peak at 125.7 meV (9.87 μm) and 312 meV (3.97 μm) for samples 960 and 1497, respectively. Hence, our experimental arrangement is able to detect intersubband

transitions in the 3-10 μm region and that the experimental results agree well with our results from model of 121 meV (10.25 μm) and 278 meV (4.46 μm) for samples 960 and 1497, respectively. In addition, the FWHM of sample 1497 is very much broader as compared to sample 960. This is consistent with the intersubband transition being bound-to-continuum in nature, which is inline with our modelled conduction band profile.

Another sample 1793 (DBQWs) grown in Sheffield was also used to test the setup. Figure 4.1.3 shows the modelled conduction band edge profile and the measured 300 K absorption spectrum using 45^0 waveguide geometry.

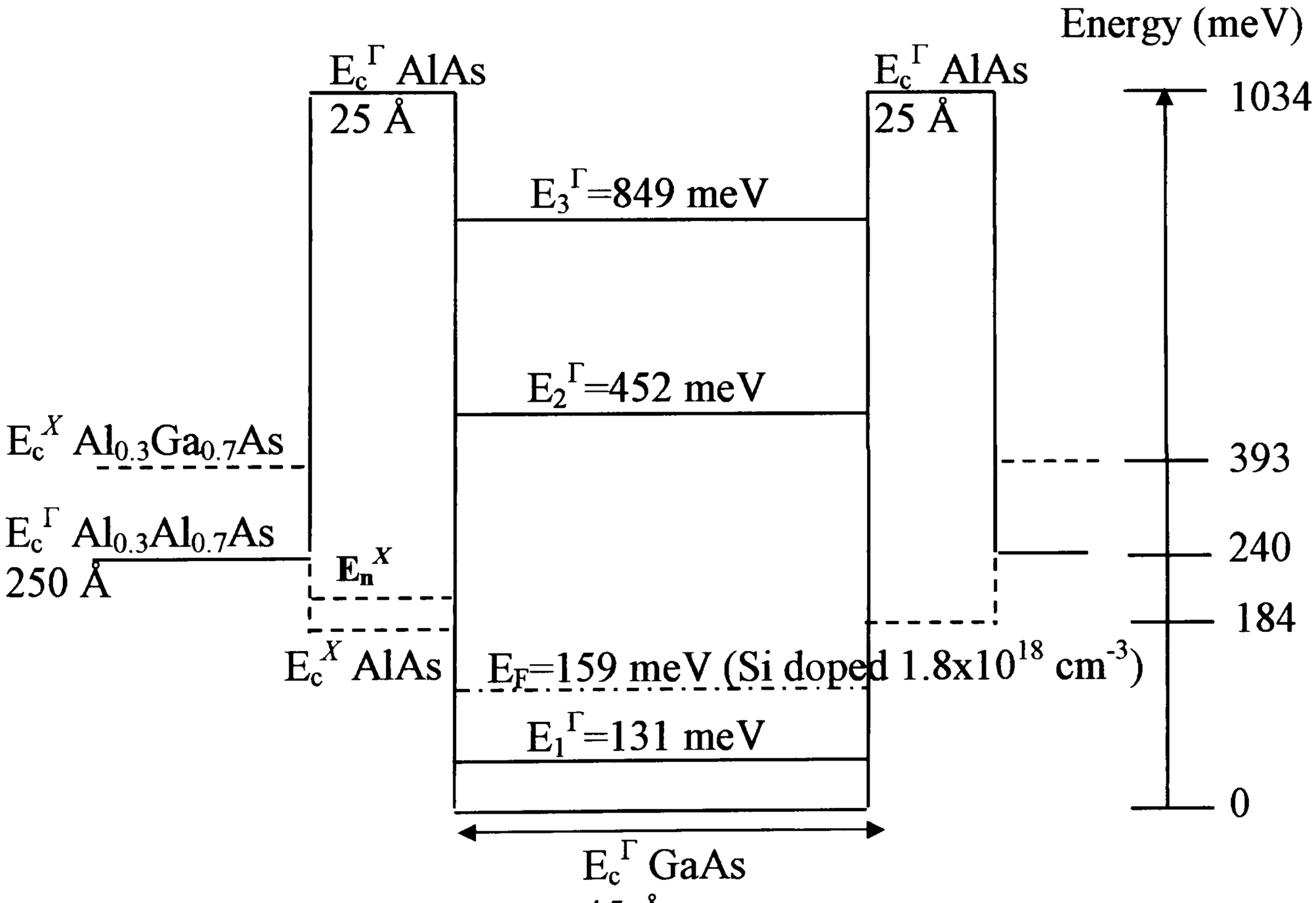

(a)

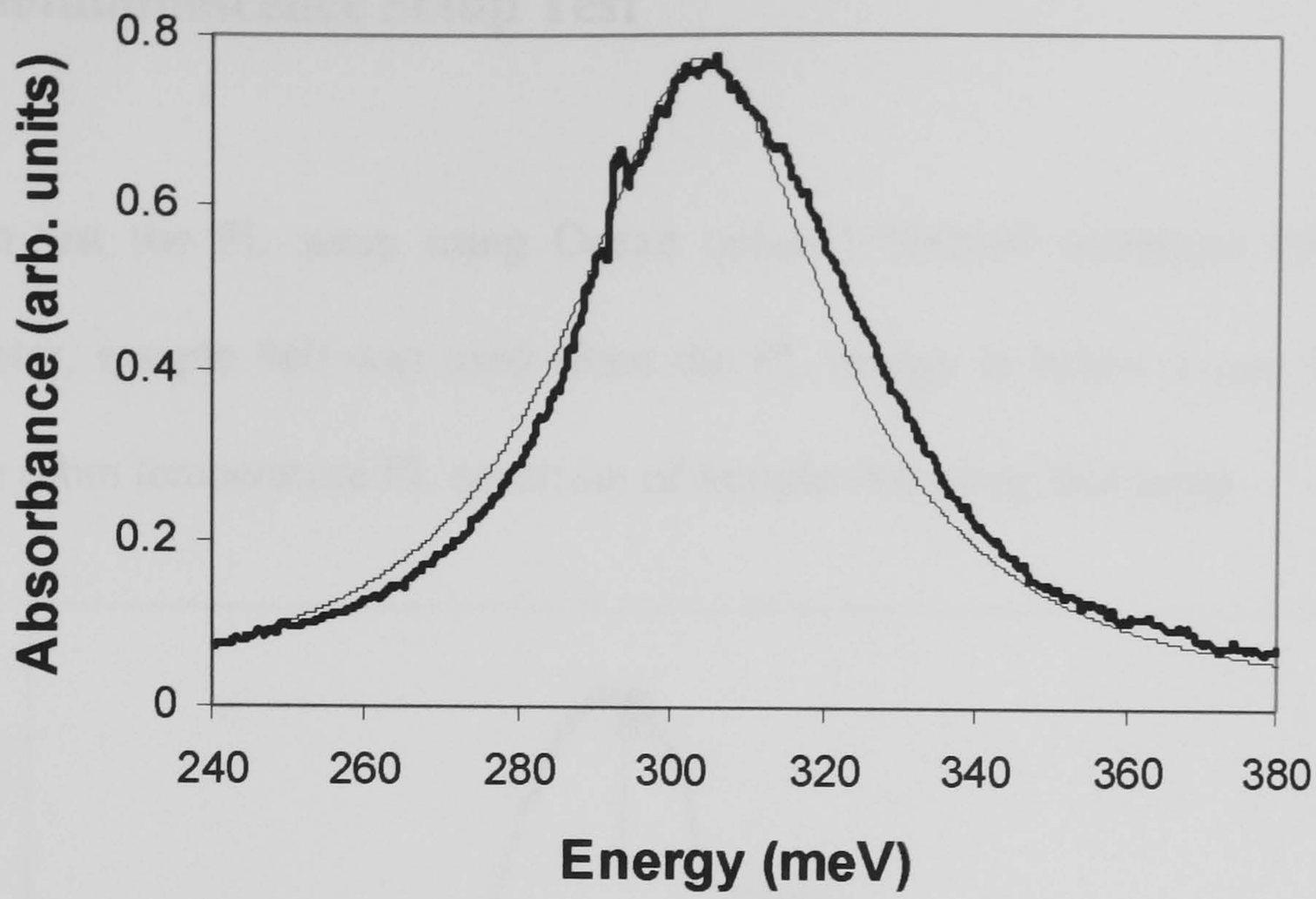

(b)

Figure 4.1.3: Sample 1793 (a) modelled Γ (thick line) and *X* (dashed line) conduction band edge profile (b) measured 300 K absorption spectrum (thick line) and Lorentzian curve fit (thin line) using 45^0 waveguide geometry

From Fig. 4.1.3 (b), a strong clear peak at 304 meV (4.08 μm) is observed which demonstrates the success of our 45^0 edge polishing and also the experimental arrangement for it. The theoretical value of 321 meV (3.86 μm) is in agreement with the measured value. We note that the FWHM of 38 meV is in between the values obtained for sample 960 and 1497. This intermediate value is consistent with the intersubband transition being bound-to-quasicontinuum in nature (see Fig. 1.3.2.4.2), again inline with our modelled conduction band profile.

4.2 Photoluminescence Setup Test

To test the PL setup using Ocean optics USB2000 miniature Fiber Optic spectrometer, sample 960 was used since the PL energy is below 1 μm. Fig. 4.2.1 shows the room temperature PL spectrum of sample 960 using this setup.

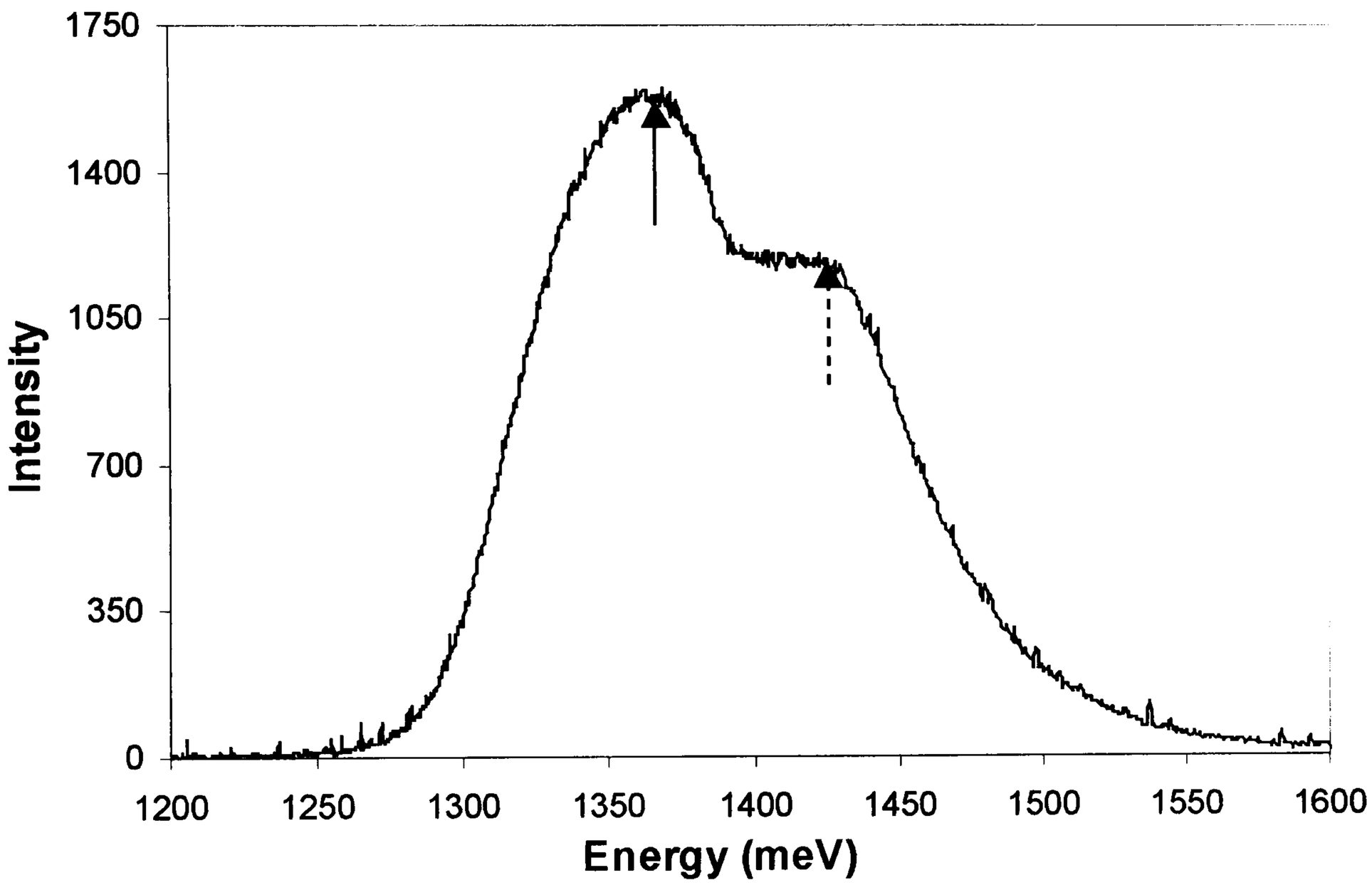

Figure 4.2.1: Photoluminescence spectra at 300K for sample 960. The arrows indicate the transitions of n=1 electron to heavy (↑) and light (⇡) holes.

Two peaks are evident in this spectrum. The dominant peak at 1369 meV and the shoulder peak at 1429 meV are attributed to the n=1 electron to heavy hole and light hole transitions in the well, respectively. These values are in excellent agreement with the modelled values of 1406 meV and 1425 meV, respectively (see modelling using Lorentzian fit to obtain peak positions in Sec. 5.1).

Sample 1497 was used to test the PL setup using Bruker IFS 66/S FTIR since the PL energy is above 1 μm and the result is shown in Fig. 4.2.2.

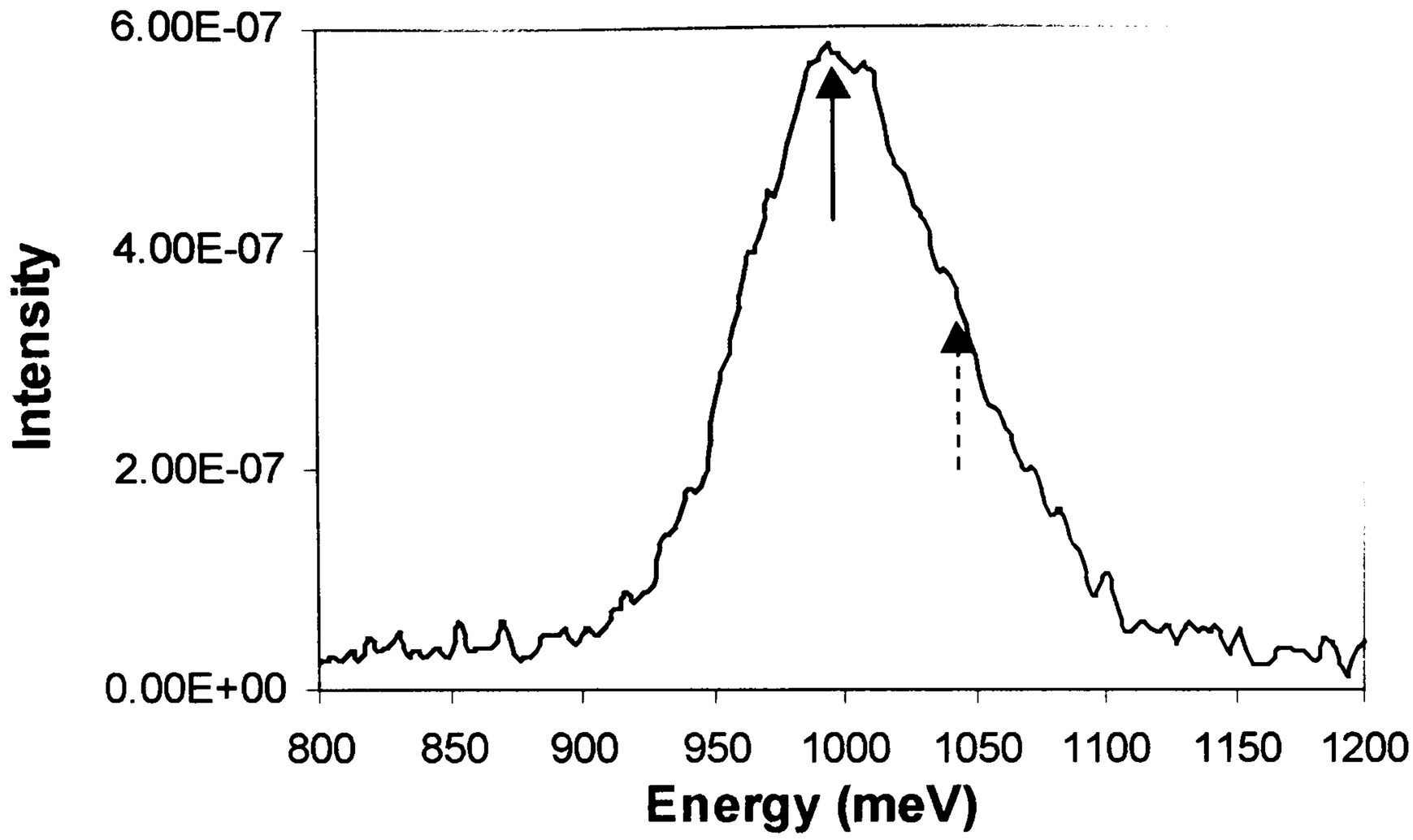

Figure 4.2.2: Photoluminescence spectra at 300K for sample 1497. The arrows indicate the transitions of n=1 electron to heavy (↑) and light (⇡) holes.

The dominant peak at 994 meV is due to the n=1 electron to heavy hole transition while a weaker shoulder peak at 1040 meV (not clearly resolved) is assigned to the n=1 electron to light hole transition in the well. These values are again in excellent agreement with the modelled values of 1005 meV and 1060 meV, respectively.

The observation of these intersubband absorption and PL peaks demonstrates the suitability of our experimental setups and techniques for the characterisation/analysis of mid-IR photodetectors.

4.3 Early Samples

Table 4.3.1 summaries four stepped DBQWs samples grown in Sheffield and Fig. 4.3.1 shows the modelled generic conduction band edge.

Sample	Structure	Doping Method	Modelled Absorption Peaks $E_1^{\Gamma} \rightarrow E_2^{\Gamma}$ (μm)
2067	Outer Barrier (L_{OB}) = $Al_{0.32}Ga_{0.68}As$ at 300 Å Inner Barrier (L_{IB}) = AlAs at 40 Å Well (L_W) = $In_{0.28}Ga_{0.72}As$ at 27 Å Inner Barrier (L_{IB}) = AlAs at 12 Å Step (L_S) = GaAs at 24 Å No. of periods = 20	Doped in the outer barrier (Si doped $2.5x10^{18}$ cm^{-3})	3.95
2066	Outer Barrier (L_{OB}) = $Al_{0.32}Ga_{0.68}As$ at 300 Å Inner Barrier (L_{IB}) = AlAs at 40 Å Well (L_W) = $In_{0.25}Ga_{0.75}As$ at 27 Å Inner Barrier (L_{IB}) = AlAs at 12 Å Step (L_S) = GaAs at 24 Å No. of periods = 20	Doped in the outer barrier (Si doped $2.5x10^{18}$ cm^{-3})	4.03
1618	Outer Barrier (L_{OB}) = $Al_{0.30}Ga_{0.70}As$ at 200 Å Inner Barrier (L_{IB}) = AlAs at 40 Å Well (L_W) = $In_{0.22}Ga_{0.78}As$ at 30 Å Inner Barrier (L_{IB}) = AlAs at 15 Å Step (L_S) = GaAs at 30 Å No. of periods = 20	Doped all the way (Si doped $2.0x10^{17}$ cm^{-3})	4.97
1263	Outer Barrier (L_{OB}) = $Al_{0.32}Ga_{0.68}As$ at 300 Å Inner Barrier (L_{IB}) = AlAs at 26 Å Well (L_W) = $In_{0.22}Ga_{0.78}As$ at 24 Å Inner Barrier (L_{IB}) = AlAs at 26 Å Step (L_S) = GaAs at 24 Å No. of periods = 10	Doped in the well (Si doped $5.0x10^{18}$ cm^{-3})	3.90

Table 4.3.1: Stepped DBQWs samples parameters grown in Sheffield.

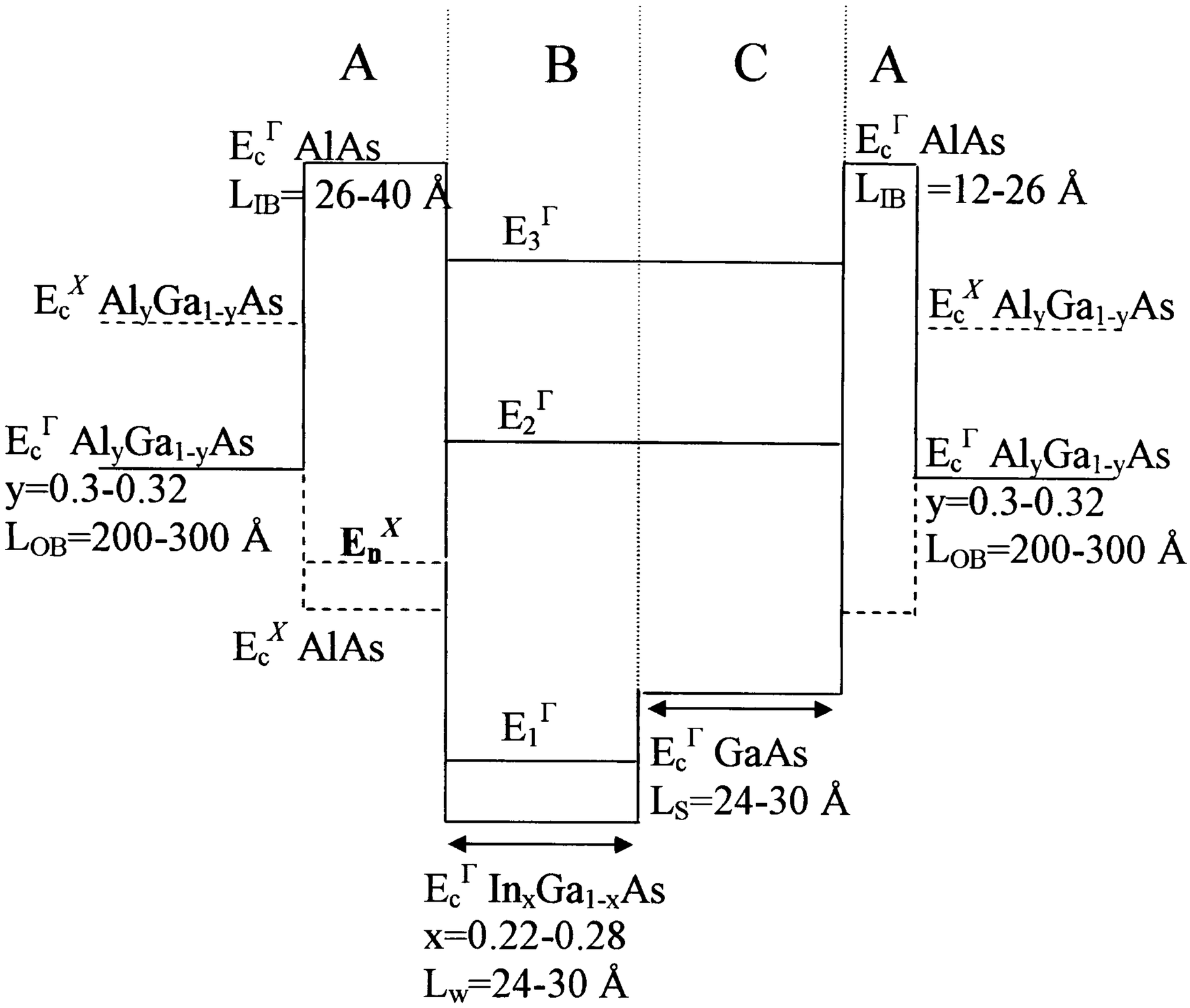

Figure 4.3.1: Modelled generic Γ (thick line) and *X* (dashed line) conduction band edge profile of the stepped DBQWs samples grown in Sheffield.

No absorption peaks are observed for these set of samples. In order to ascertain that there are any carriers in the wells, two Hall samples; one doped in the well (sample 1598) and the other uniformly doped (sample 1599) were grown on undoped GaAs substrates. The modelled conduction band edge profiles of these Hall samples and their respective 300 K absorption spectral measured using 45^0 waveguide geometry are shown in Figs. 4.3.2 and 4.3.3, respectively.

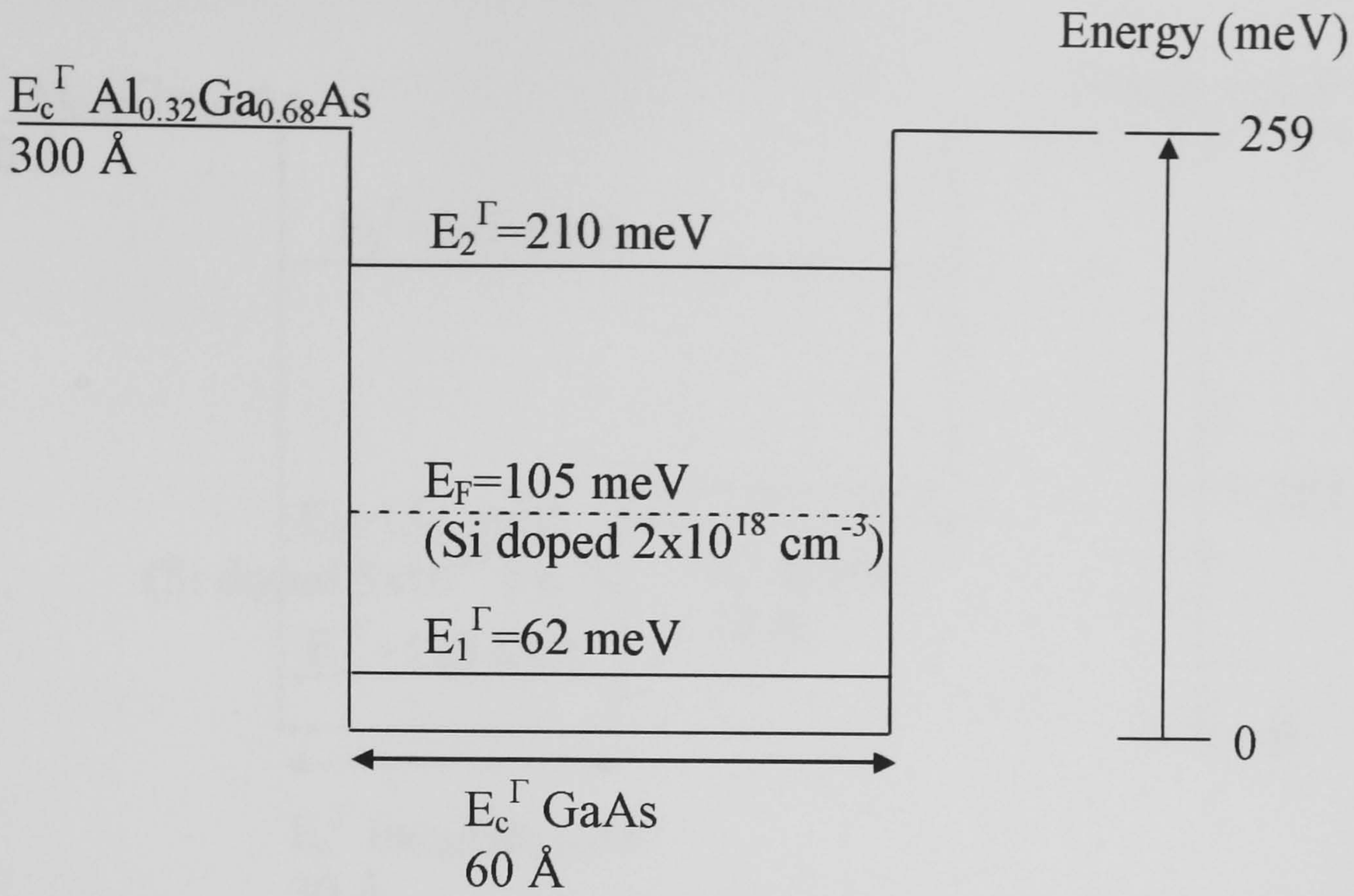

(a)

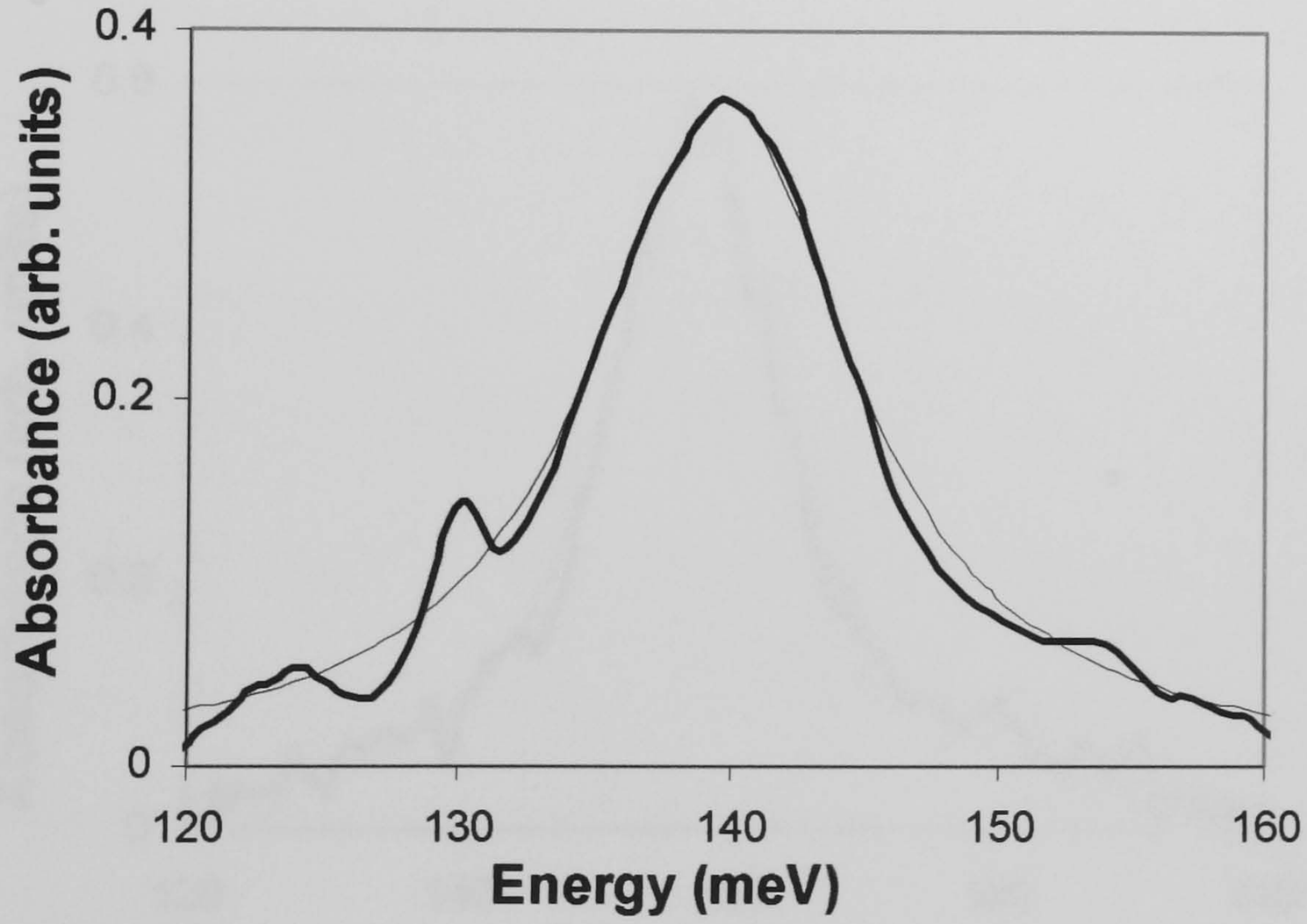

(b)

Figure 4.3.2: Sample 1598 (a) modelled conduction band edge profile (b) measured 300 K absorption spectrum (thick line) and Lorentzian curve fit (thin line) using 45^0 waveguide geometry. The feature at ~ 130 meV and ~ 155 meV are due to atmospheric absorption.

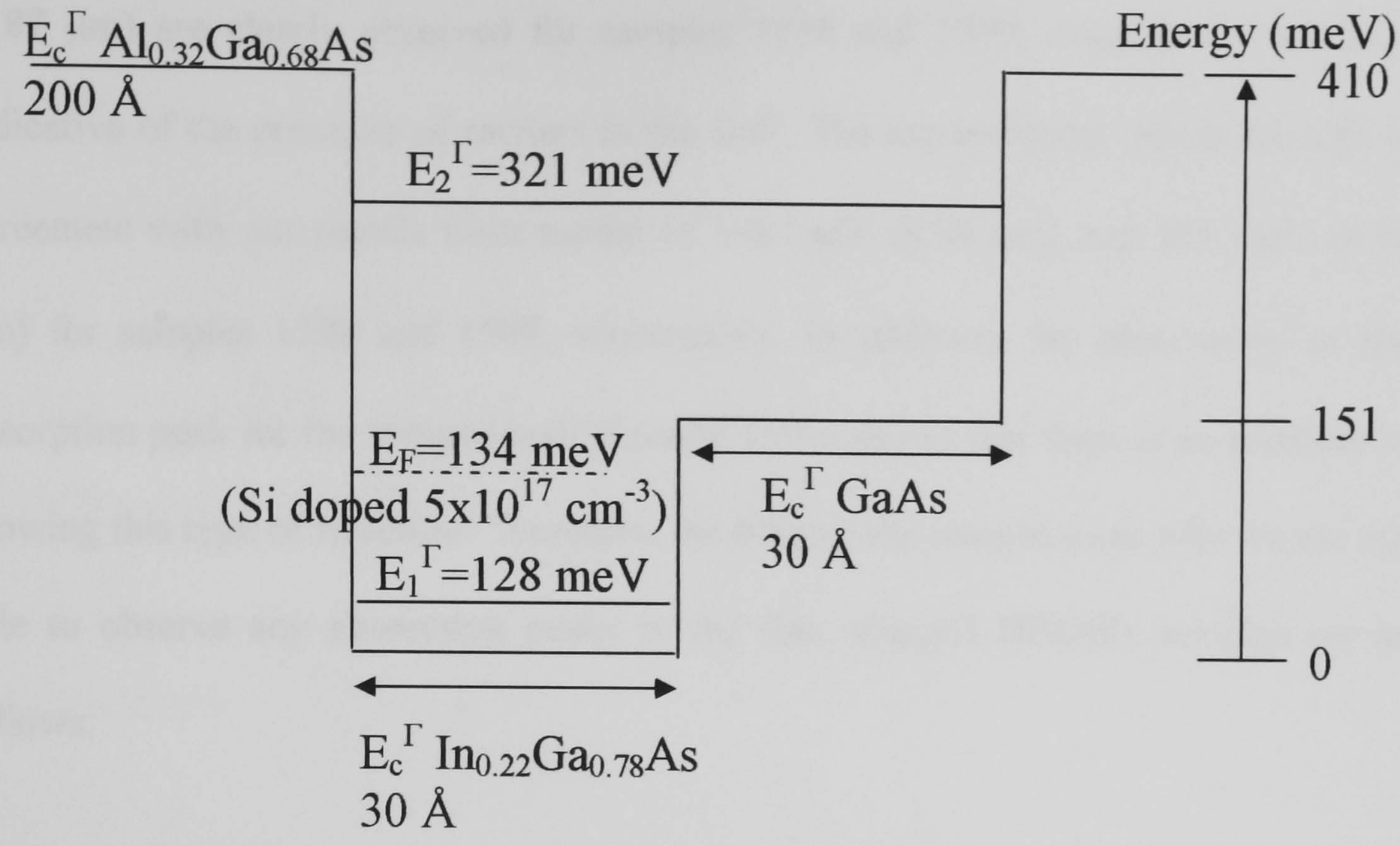

(a)

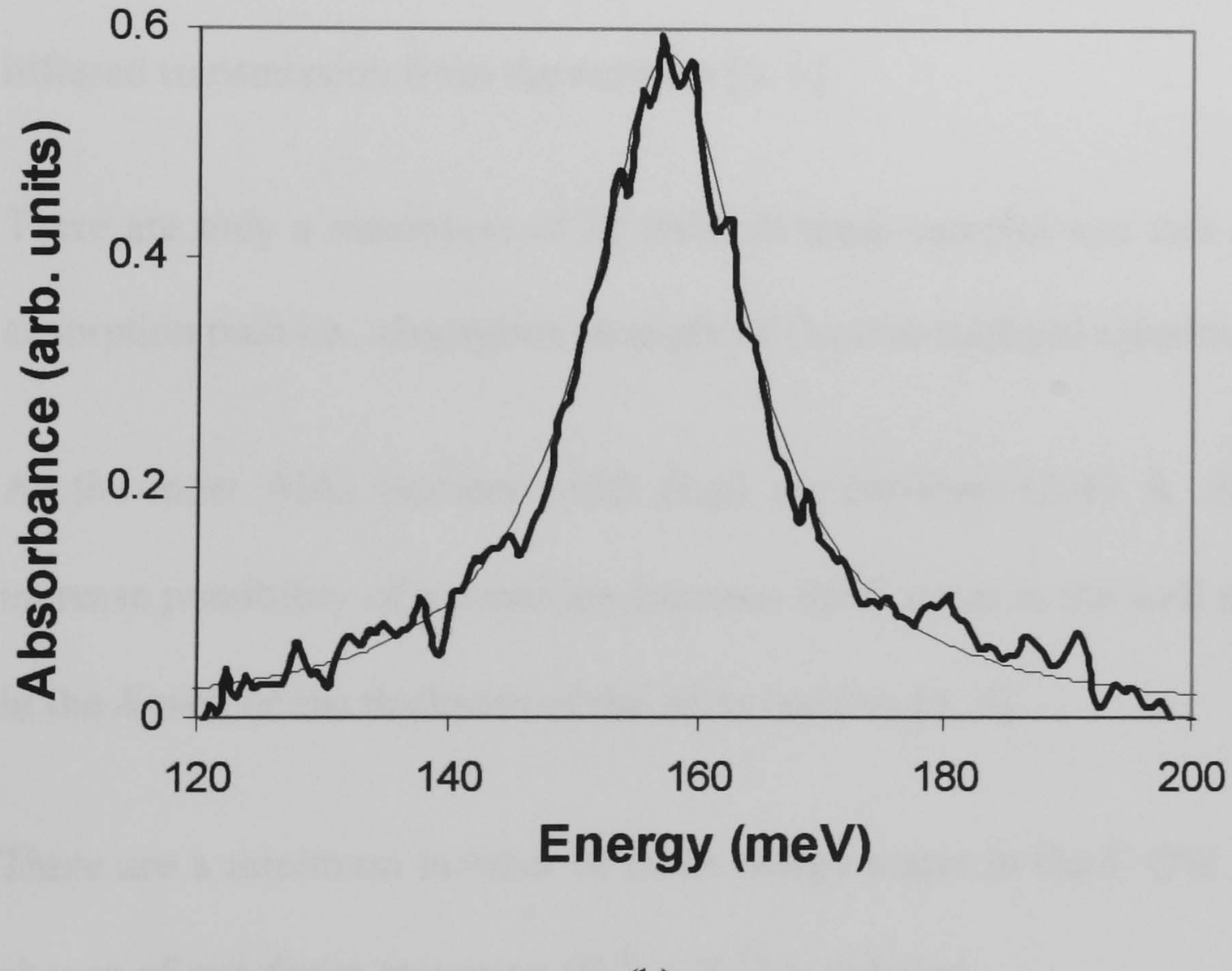

(b)

Figure 4.3.3: Sample 1599 (a) modelled conduction band edge profile (b) measured 300 K absorption spectrum (thick line) and Lorentzian curve fit (thin line) using 45^0 waveguide geometry.

From Figs. 4.3.2 and 4.3.3, absorption peak at 139.7 meV (8.88 μm) and 157.5 meV (7.87 μm) are clearly observed for samples 1598 and 1599, respectively which is indicative of the presence of carriers in the well. The experimental results are also in agreement with our results from model of 148 meV (8.38 μm) and 193 meV (6.42 μm) for samples 1598 and 1599, respectively. In addition, the observation of the absorption peak for the stepped well (sample 1599) shows that there is no problem in growing this type of structure. Therefore, we believe the reasons as to why we are not able to observe any absorption peaks in the four stepped DBQWs samples are as follows:

1) The samples were grown on (100) oriented n^+ doped GaAs substrates where free-carrier absorption in a highly doped substrate would have obscured the infrared transmission from the samples [5, 6].

2) There are only a maximum of 20 wells in these samples and this reduces the absorption path i.e., absorption strength of the intersubband transition.

3) As the inner AlAs barriers width (L_{IB}) are between 12-40 Å, this leads to increase possibility of a transition between the Γ states in the well and *X* states in the *X* well of the thickness of the AlAs barriers [3, 4].

4) There are a minimum number of three energy states in the Γ QW, hence, the chance of our desire transition ($E_1^{\Gamma} \rightarrow E_2^{\Gamma}$) is reduced.

5) Only sample 2067 has the ground state energy E_1^{Γ} confined in the layer B which means that the higher oscillator strength is not achieved.

4.3.1 Conclusions

Although we were not able to observe any absorption peaks in these (stepped DBQWs) samples, these results provided us with some vital information as to what we need to do to observe the intersubband transitions for our future samples such as growing the MQWs on semi-insulating substrates instead of on n^+ doped GaAs substrates, higher doping density and increasing the number of wells.

References

1) Andrew J. Stead, "*Strained InGaAs/AlGaAs quantum well infrared photodetectors for the detection of multiple colour and normal incidence infrared radiation*", Ph.D. thesis, University of Manchester Institute of Science and Technology, 2001.

2) C. J. Mitchell, S. L. Sly, and M. Missous, "*Highly Strained Quantum Cascade Structures for QWIPs and Emission in the Mid to Near Infra-red Region*", The 6th Mid-IR Network Meeting, Imperial College, UK, 9th July 2002.

3) H. C. Liu, P. H. Wilson, M. Lamm, A. G. Steele, Z. R. Wasilewski, J. M. Li, M. Buchanan, and J. G. Simmons, "*Low Dark Current Dual Band Infrared Photodetector using Thin AlAs Barriers and Γ-X Mixed Intersubband Transition in GaAs Quantum Wells*", Applied Physics Letters, 1994, vol. 64, p.475-477.

4) H. C. Liu, M. Buchanan, and Z. R. Wasilewski, "*Short Wavelength (1-4 μm) Infrared Detectors using Intersubband Transitions in GaAs-based Quantum Wells*", Journal of Applied Physics, 1998, vol. 83, p. 6178-6181; erratum vol. 91, p. 10230 (2002).

5) A. Harwit, and J. S. Harris, Jr., "*Observation of Stark Shifts in Quantum Well Intersubband Transitions*", Applied Physics Letters, 1987, vol. 50, p. 685-687.

6) A. Fenigstein, A. Fraenkel, E. Finkman, G. Bahir, and S. E. Schacham, "*Current Induced Intersubband Absorption in GaAs/GaAlAs Quantum Wells*", Applied Physics Letters, 1995, vol. 66, p. 2513-2515.

Chapter 5 GaAs Based Samples

5.1 Initial Characterisation

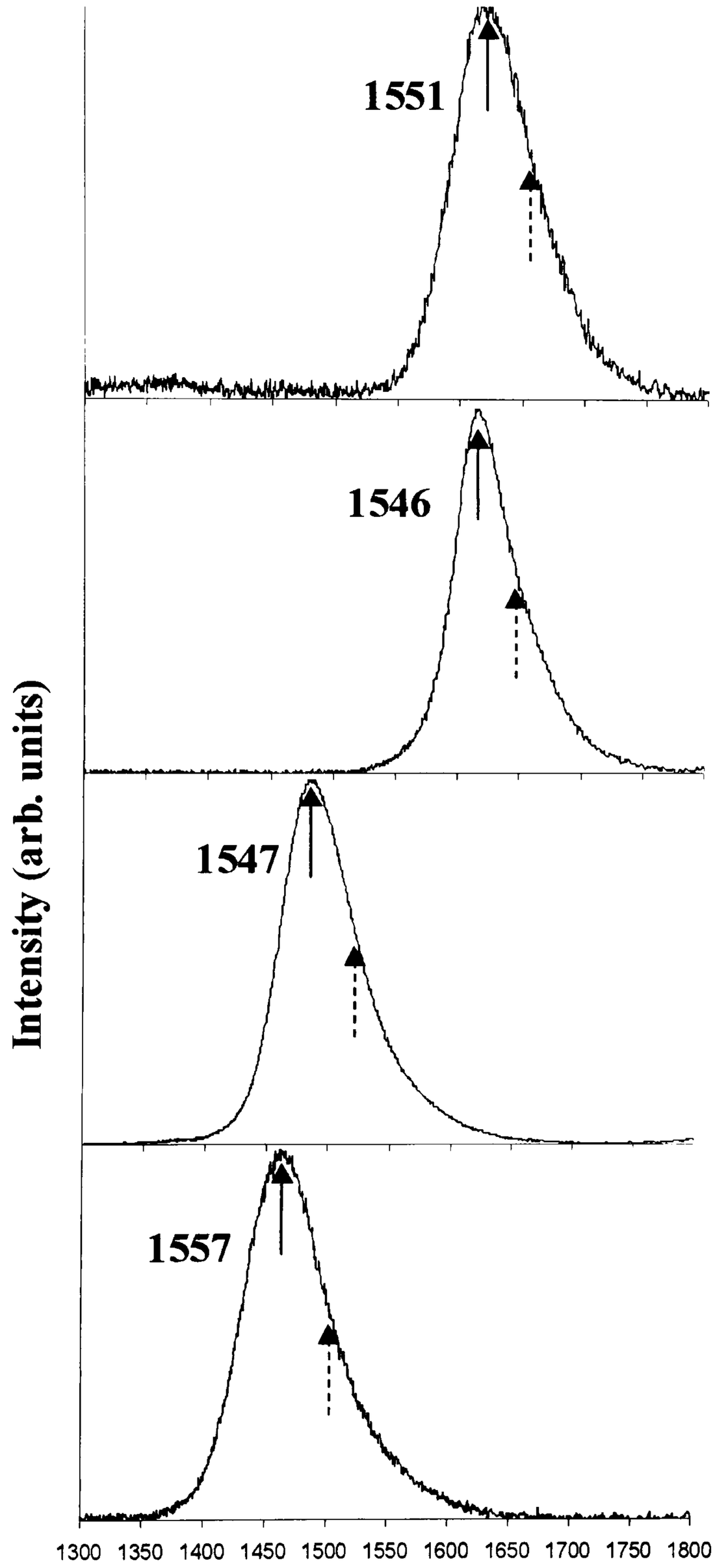

Figure 5.1.1: Photoluminescence spectra at 300K for samples 1546, 1547, 1551, and 1557. The arrows indicate the measured energies for the transitions associated with the n=1 electron to heavy (↑) and light (⇡) holes.

The room temperature Photoluminescence spectra for samples 1546, 1547, 1551, and 1557 are shown in Fig. 5.1.1. The clear and sharp excitonic peaks of these samples confirmed that the samples are of good crystal quality.

No attempt to fit the lineshape of the PL spectral was made as this would require a detailed statistics of the shapes, on which we lack too much information at this point. We have, however, used the Lorentzian lineshape to fit the position of the peaks. Table 5.1.1 shows the fitted and modelled n=1 electron to heavy and light holes transitions in the well.

Sample No	**$E_1 \rightarrow HH_1$ (meV)**	**$E_1 \rightarrow LH_1$ (meV)**
1546	1616 (1588)	1650 (1629)
1547	1483 (1381)	1515 (1489)
1551	1617 (1588)	1650 (1629)
1557	1459 (1417)	1497 (1510)

Table 5.1.1: Room temperature photoluminescence values of samples 1546, 1547, 1551, and 1557. The modelled values are shown in brackets.

As can be seen, the fitted energies are in good agreement with the modelled transition peaks for the two GaAs QWs (1546 and 1551). InGaAs containing structures (1547 and 1557) show a larger discrepancy between fitted and model values. This could be due to deviation from the intended growth parameters. Figure 5.1.2 shows the

experimental and simulated double-crystal X-ray diffraction (DCXRD) spectrum for sample 1557. The simulated DCXRD spectrum for sample 1557 was determined to be 23 Å $In_{0.25}Ga_{0.75}As$, 23 Å GaAs, 24 Å AlAs, and 213 Å $Al_{0.42}Ga_{0.48}As$. These are in close agreement with our intended growth parameters (see Fig. 2.1.2 and Table 2.1.1). Based on these thickness and alloy composition values obtained from the simulated DCXRD spectrum for sample 1557, we obtained n=1 electron to heavy and light holes transitions in the well to be 1425 meV and 1522 meV, respectively, which is in better agreement with the fitted PL values.

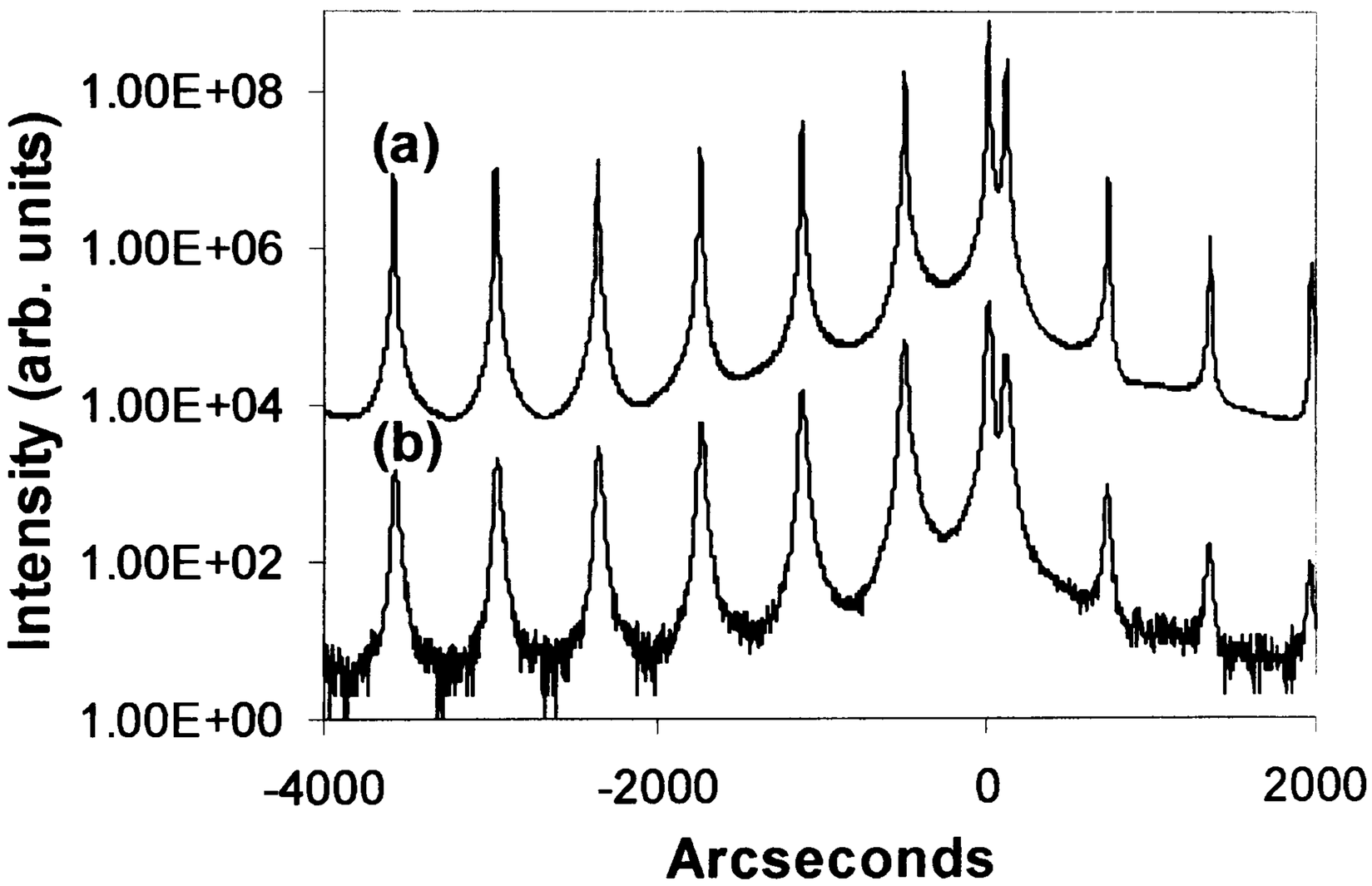

Figure 5.1.2: DCXRD (004) reflection spectrum for sample 1557 (a) simulated curve and (b) experimental data. The spectra are offset for clarity.

Fig. 5.1.3 shows the DCXRD spectra of samples 1547 and 1557. As can be seen, the FWHM of the satellite peaks for sample 1547 is very much broader than sample 1557. We attribute this to some degree of strain relaxation for sample 1547 as it has almost twice the net strain of 1557 (due to the larger well width). It is difficult to simulate the

1547 spectrum due to the relaxation and consequent line broadening. However, the higher discrepancy between the fitted PL and modelled transition energies is likely to be partially due to the relaxation.

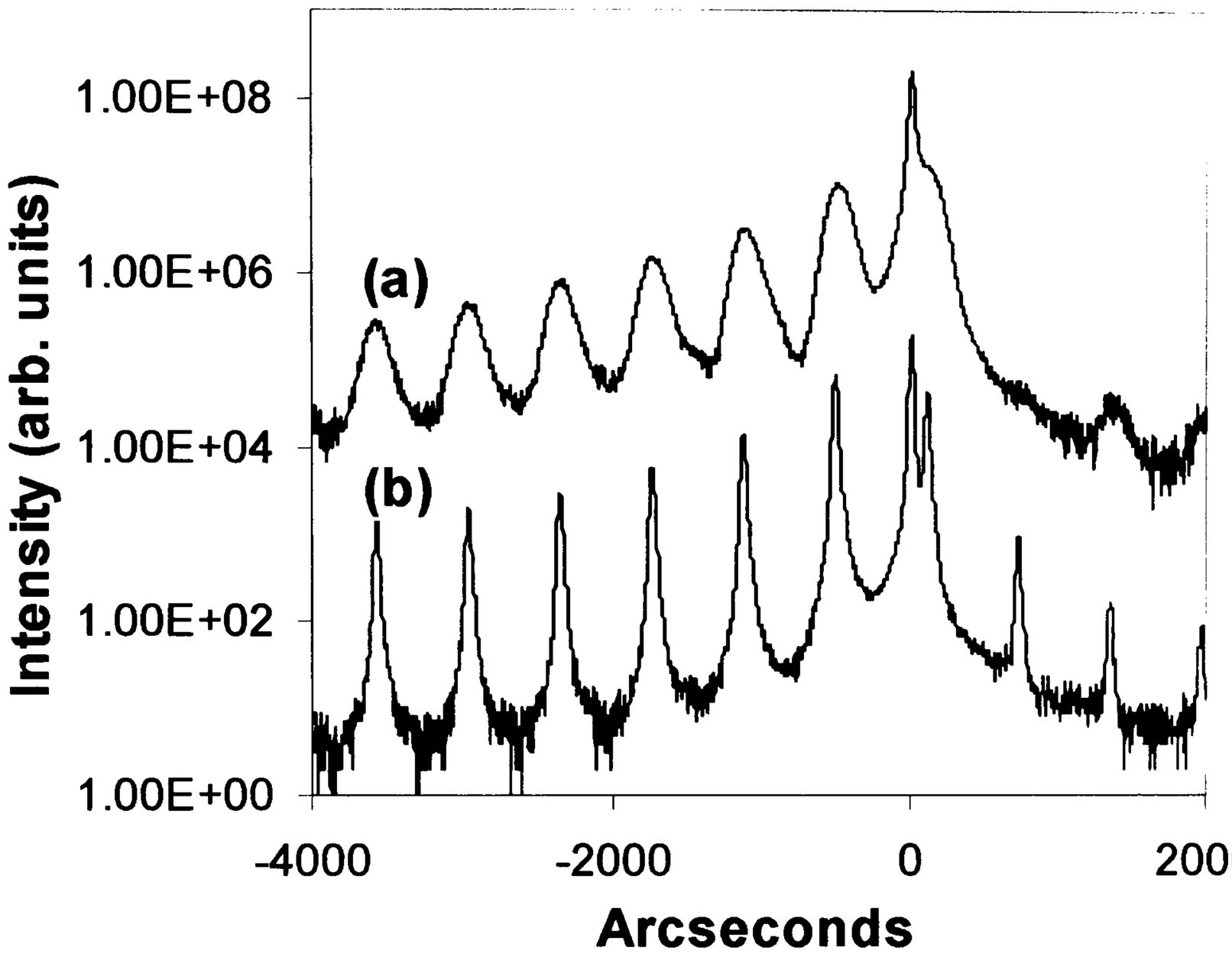

Figure 5.1.3: DCXRD (004) reflection spectrum for sample (a) 1547 and (b) 1557. The spectras are offset for clarity.

5.2 Absorption

Figure 5.2.1 shows the wavelength dependence of the intersubband absorption for the four samples measured in the allowed polarisation. All samples are expected to exhibit $E_1^{\Gamma} \rightarrow E_2^{\Gamma}$ well transitions. The modelled values for these transitions are listed in Table 5.2.1 alongside the measured peak wavelengths. These are in good agreement with each other. A Lorentzian lineshape fit of the absorption spectra gives the full width at half maximum (FWHM) for samples 1546, 1547, 1551, and 1557 as

54 meV, 40 meV, 60 meV and 26 meV respectively. The scattering of electrons from impurities in the well contributes to absorption broadening [1]. Consequently, the more highly doped GaAs sample 1551 shows a larger FWHM than 1546 (see Table 2.1.1). The large values of FWHM for sample 1546 and 1551, relative to 1547 and 1557, may be attributed to interface roughness associated with the lower than optimum GaAs growth temperature for these QWs [2, 3]. Samples 1547 and 1557, on the other hand, are grown at the optimum temperature for the InGaAs layers [3-5] and hence exhibit lower FWHM.

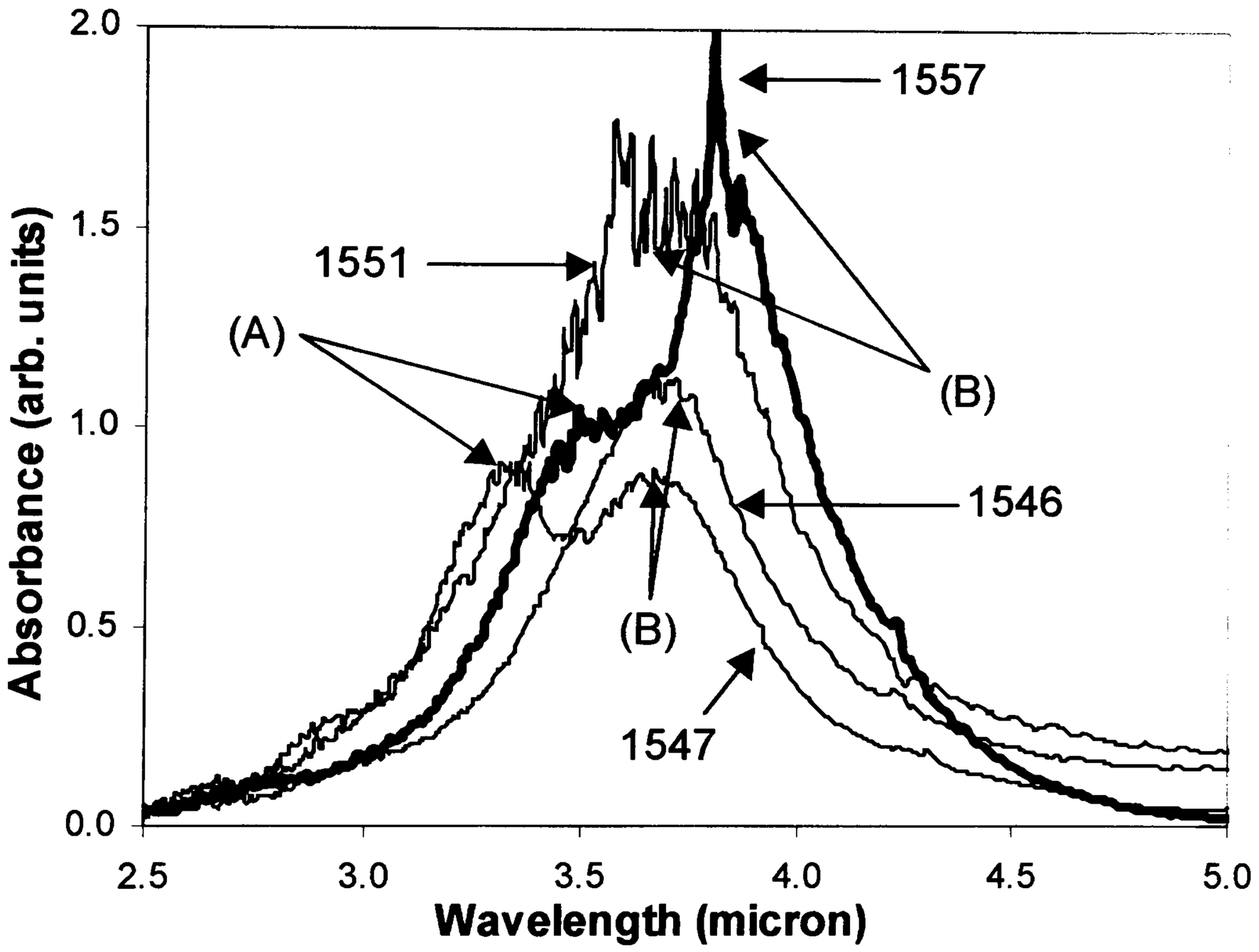

Figure 5.2.1: Absorption spectra at 300K for samples 1546, 1547, 1551, and 1557 in the 45^0 waveguide geometry for which $\Gamma \rightarrow \Gamma$ transitions are allowed. The curves are offset for clarity.

Sample No	$E_1^{\Gamma} \rightarrow E_2^{\Gamma}$ (μm)	FWHM (meV)	$E_1^{\Gamma} \rightarrow E_2^{X}$ (μm)	FWHM (meV)
1546	3.63 (3.85)	54		
1547	3.60 (3.79)	20	3.30 (3.40)	20
1551	3.63 (3.85)	60		
1557	3.70 (3.84)	26	3.37 (3.66)	36

Table 5.2.1: Peak wavelength and FWHM values obtained from a Lorentzian line shape curve fit of the measured absorption spectrum for samples 1546, 1547, 1551, and 1557. The modelled values of the peak wavelengths are shown in brackets.

The ratio of integrated absorption intensities (I_{abs}) of the $\Gamma \rightarrow \Gamma$ transition for samples 1551 and 1557 is 157:64. Since the corresponding carrier densities for the two samples are 38.25×10^{11} cm^{-2} and 20.40×10^{11} cm^{-2} respectively, the ratio I_{abs}/N_S is about the same for both samples. This occurs despite the fact that a *reduction* in the oscillator strength might be expected for this transition in 1557 as other normally forbidden transitions become allowed [5-8]. One possible cause of the increased in absorption in 1557 is a lifting of selection rules by the stepped well. This is explained below.

5.3 Selection rules

In order to explore a possible relaxation of the polarisation selection rules, transmission spectra for three of the samples in Table 5.2.1 were taken in the perpendicular and parallel polarisations; these are presented in Fig. 5.3.1. For our experimental set-up, perpendicular polarisation corresponds to the allowed geometry for $\Gamma \rightarrow \Gamma$ intersubband transitions.

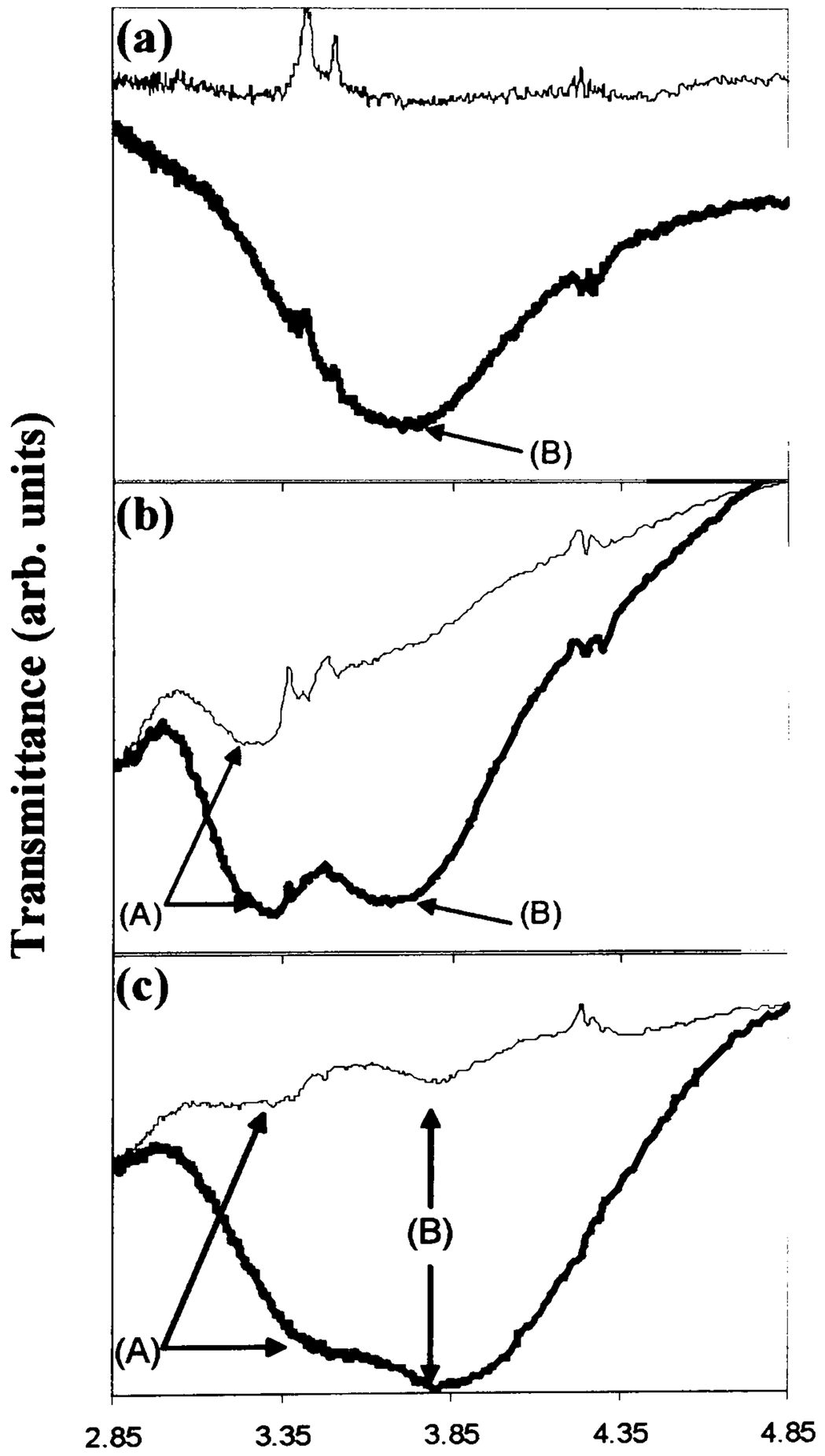

Figure 5.3.1: Transmission spectra of samples: (a) 1546, (b) 1547 and (c) 1557 measured using light polarised with the electric field vector parallel (thin line) or perpendicular (solid line) to the plane of the QWs at 300K. The features at ~ 3.3-3.5 μm and ~ 4.25μm are due to atmospheric absorption.

In Fig. 5.3.1(a) (1546), only one peak, due to the $E_1^{\Gamma} \rightarrow E_2^{\Gamma}$ transition, is observed in the allowed polarisation (peak B). As expected, this is not present in the forbidden geometry. In Fig. 5.3.1(b) (1547), two peaks are observed in the perpendicular polarisation (A and B). Again peak B is not observed in the parallel geometry and it is attributed to $E_1^{\Gamma} \rightarrow E_2^{\Gamma}$. Peak A is seen in both polarisations and we attribute this peak to an $E_1^{\Gamma} \rightarrow E_2^{X}$ transition (Table 4.1.1). In Fig. 5.3.1(c), the stepped well (1557), both peaks A and B are observed at both polarisations. Again from our modelling, we attribute peak A to the $E_1^{\Gamma} \rightarrow E_2^{X}$ transition and peak B to the $E_1^{\Gamma} \rightarrow E_2^{\Gamma}$ transition. The observation of peak B in the parallel polarisation indicates a degree of relaxation of the intersubband selection rules due to the asymmetric QWs [9]. Scattering from the mesa edge [10] is discounted as the reason for observing $\Gamma \rightarrow \Gamma$ absorption at the forbidden polarisation in the stepped well since all the samples were processed in the same manner.

Returning to the assignment of peak A in Figs 5.3.1(b) and 5.3.1(c), the modelled subband energy levels of 1557 (see Table 3.3.2) suggests two possibilities for the origin of this peak. The $E_2^{\Gamma} \rightarrow E_3^{\Gamma}$ and the E_1^{Γ}(well)$\rightarrow E_2^{X}$(AlAs) transitions are both close to the energy of peak A; this is also true for sample 1547. However, observation of the $E_2^{\Gamma} \rightarrow E_3^{\Gamma}$ transition requires population of the E_2^{Γ} level, which in turn would require a carrier concentration much higher than expected (see Table 2.1.1). $\Gamma \rightarrow X$ transitions usually have an oscillator strength considerably smaller than $\Gamma \rightarrow \Gamma$ transitions and hence are not expected to be observed. However it has been suggested that in the growth direction the breaking of translational symmetry leads to $\Gamma \rightarrow X_Z$ mixing and to a lesser extent to $\Gamma \rightarrow X_{xy}$ mixing and hence to enhanced oscillator strength [11, 12]. Observation of peak A in the dipole forbidden geometry

[Fig. 5.3.1(b) and 5.3.1(c)] is also consistent with its attribution to E_1^{Γ}(well)→E_2^{X}(AlAs) transitions [13]. Nevertheless it is surprising that this peak is of comparable strength to the Γ→Γ transitions.

5.4 Conclusions

We have observed absorption in the forbidden polarisation and a narrowing of the linewidth in GaAs-based double-barrier quantum well structures on introduction of an additional InGaAs layer into the well. This occurred despite an expected *reduction* in the oscillator strength for this transition as other normally forbidden transitions become allowed. The observation is attributed to relaxation of the polarization selection rule due to the step in the well. A strong and narrow E_1^{Γ}(well)-E_2^{X}(AlAs). transition was also observed in both the stepped well (1557) and the InGaAs square well (1547), giving the option for dual wavelength operation in these structures. The modelled and measured peak wavelengths for both the Γ-Γ and Γ-*X* intersubband transitions are in good agreement using a band offset ratio ΔE_C:ΔE_V of 0.65:0.35 and an average *X* valley electron effective mass of $m_{e\text{-}x}$(AlAs) = $0.4m_0$.

References

1) E. B. Dupont, D. Delacourt, P. Papillon, J. P. Schnell, and M. Papuchon, "*Influence of Ionized Impurities on the Iinewidth of Intersubband Transitions in GaAs/GaAlAs Quantum Wells*", Applied Physics Letters, 1992, vol. 60, p. 2121-2222.

2) G. Neu, Y. Chen, C. Deparis, and J. Massies, "*Improvement of the Carrier Confinement by Double-Barrier GaAs/AlAs (Al,Ga)As Quantum Well Structures*", Applied Physics Letters, 1991, vol. 58, p. 2111-2113.

3) K. K. Choi, S. V. Bandara, S. D. Gunapala, W. K. Liu, and J. M. Fastenau, "*Detection Wavelength of InGaAs/AlGaAs Quantum Wells and Superlattices*", Journal of Applied Physics, 2002, vol. 91, p. 551-564.

4) D. H. Zhang, and W. Shi, "*Dark Current and Infrared Absorption of P-doped InGaAs/AlGaAs Strained Quantum Wells*", Applied Physics Letters, 1998, vol. 73, p. 1095-1097.

5) H. S. Li, Y. W. Chen, K. L. Wang, and D. Y. C. Lie, "*Intersubband Transitions in Pseudomorphic InGaAs/GaAs/AlGaAs Multiple Step Quantum Wells*", Journal of Vacuum Science Technology B, 1993, vol. 11, p. 1840-1843.

6) Y. J. Mii, K. L. Wang, R. P. G. Karunasiri, and P. F. Yuh, "*Observation of Large Oscillator Strengths for Both 1-2 and 1-3 Intersubband Transitions of Step Quantum Well*", Applied Physics Letters, 1990, vol. 56, p. 1046-1048.

7) R. P. G. Karunasiri, Y. J. Mii, and K. L. Wang, "*Tunable Infrared Modulator and Swtich using Stark Shift in Step Quantum Wells*", IEEE Electron Device Letters, 1990, vol. 11, p. 277-279.

8) T. Mei, G. Karunasiri, and S. L. Chua, "*Two-color Infrared Detection using Intersubband Transitions in Multiple Step Quantum Wells with Superlattice Barriers*", Applied Physics Letters, 1997, vol. 71, p. 2017-2019.

9) Z. Y. Yuan, Z. H. Chen, D. F. Cui, J. W. Ma, Q. Hu, J. M. Zhou, and Y. L. Zhou, "*Normal Incidence Photoresponse in GaAs/AlGaAs Quantum Well Infrared Photodetector*", Applied Physics Letters, 1995, vol. 67, p. 930-931.

10) C. W. Cheah, G. Karunasiri, L. S. Tan, and L. F. Zhou, "*Responsitivity of n-type GaAs/InGaAs/AlGaAs step Multiple-quantum-well Infrared Detectors*", Applied Physics Letters, 2002, vol. 80, p. 145-147.

11) H. C. Liu, P. H. Wilson, M. Lamm, A. G. Steele, Z. R. Wasilewski, and J. M. Li, "*Low Dark Current Dual Band Infrared Photodetector using Thin AlAs Barriers and Γ-X Mixed Intersubband Transitions in GaAs Quantum Wells*", Applied Physics Letters, 1994, vol. 64, p. 475-477.

12) R. Teissier, J. J. Finley, M. S. Skolnick, J. W. Cockburn, J. –L. Pelouard, R. Grey, G. Hill, M. A. Pate, and R. Planel, "*Experimental Determination of Γ-X Intervalley Transfer Mechanisms in GaAs/AlAs Heterostructures*", Physical Review B, 1996, vol. 54, p. R8329-R8332.

13) A. Fenigstein, E. Finkman, G. Bahir, and S. E. Schacham, "*X-Γ Indirect Intersubband Transitions in Type II GaAs/AlAs Superlattices*", Applied Physics Letters, 1996, vol. 69, p. 1758-1760.

Chapter 6 InP Based Samples

6.1 Initial Characterisation

Figure 6.1.1 shows the room temperature PL spectra for samples 1554, 1563, and 1561. Despite the very large lattice mismatch of the two constituent semiconductors (The tensile AlAs layers have a strain of -3.56 % relative to the substrate while the compressively strained $In_{0.84}Ga_{0.16}As$ QWs have a strain of +2.12 %), clear excitonic peaks of these samples confirmed that the samples are of good crystal quality.

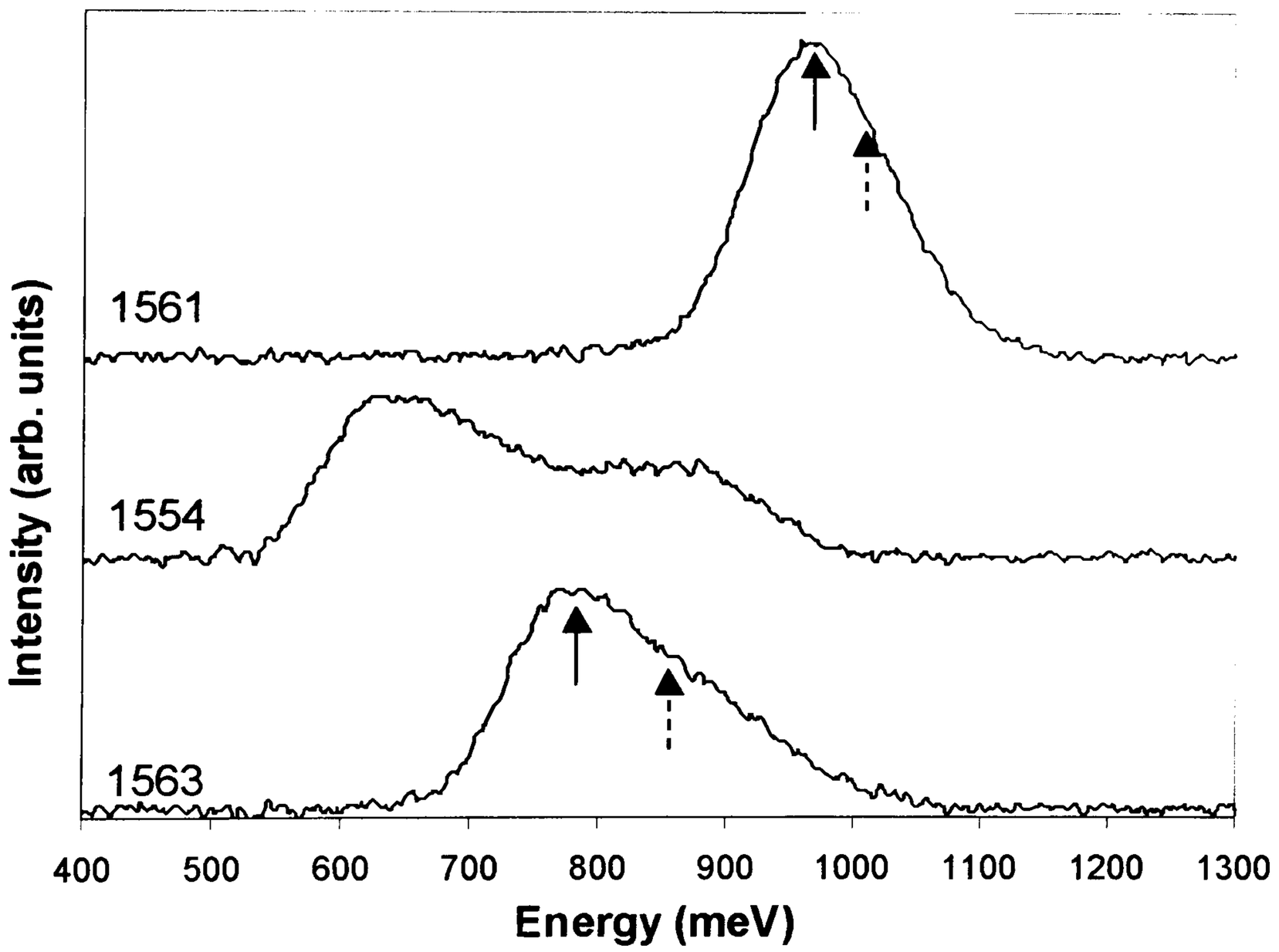

Figure 6.1.1: Photoluminescence spectra at 300K for samples 1554, 1563, and 1561. The spectrums are offset for clarity. The arrows indicate the fitted energies for the transitions associated with the n=1 electron to heavy (↑) and light (⇡) holes.

Again, we have used the Lorentzian lineshape to fit the position of the PL peaks for samples 1563 and 1561. Table 6.1.1 shows the fitted and modelled data. A large discrepancy is observed for sample 1561 which can be attributed to some degree of strain relaxation. This is confirmed by the DCXRD spectrum shown in Fig. 6.1.2. We also find some evidence for variation in well width (see section 6.2.1). For sample 1554, we did not try to fit the spectrum as it is very broad, highly asymmetric and probably the sum of several transitions.

Sample No	**$E_1 \rightarrow HH_1$ (meV)**	**$E_1 \rightarrow LH_1$ (meV)**
1563	779 (718)	872 (854)
1561	950 (871)	990 (991)

Table 6.1.1: Room temperature photoluminescence values of samples 1563, and 1561. The modelled values are also shown in brackets.

Also, from Fig. 6.1.1 and Table 2.1.2, we can see that as the sheet carrier density increases, the number of PL peaks increases and the lineshape becomes more asymmetric. This indicates the population of more than one subband in the QW which is consistent with our intersubband absorption results (see following section) where multiple peaks are observed.

The structural parameters for the individual samples are listed in Table 2.2.1, including data inferred from Hall measurements. The Hall mobility is significantly lower in 1561, the most strained sample, which also has the largest number of wells. Although the effect of interface roughness scattering increases with decreasing well

width and this can reduce electron mobility [1], we attribute the large drop in Hall mobility for 1561 to a degree of strain relaxation. This is seen from the X-ray spectra (see Fig. 6.1.2). A comparison of the satellite peaks reveals that the FWHM is around 70 arc secs for 1561 and 38 arc secs for 1554 which has close to zero net strain (1563 also has FWHM of 38 arc secs).

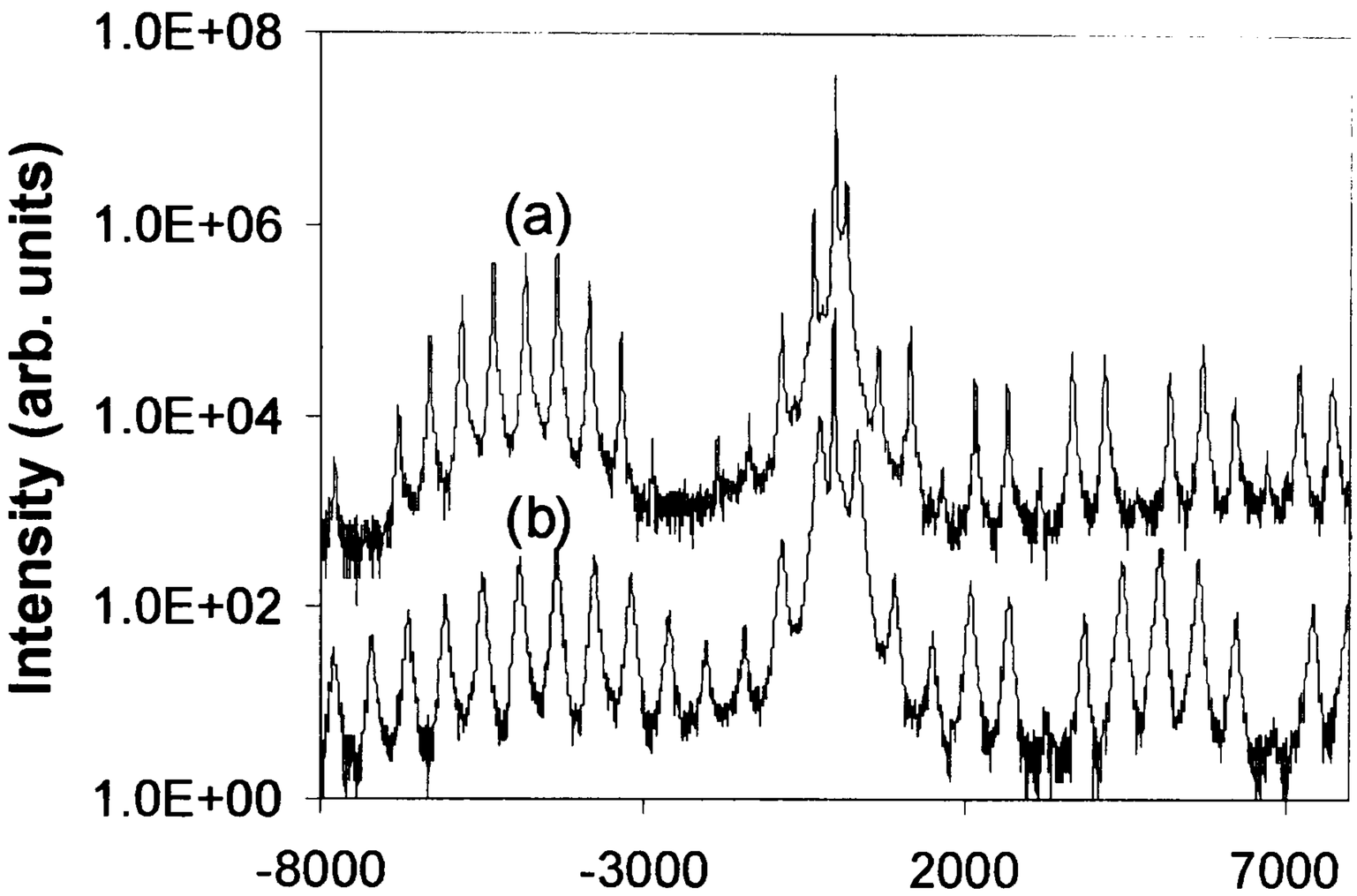

Figure 6.1.2: DCXRD (004) reflection spectrum for sample (a) 1554 and (b) 1561. The FWHM of the satellite peaks for sample 1561 and 1554 are ~ 70 and 38 arc secs, respectively. The spectras are offset for clarity.

6.2 Absorption

Figure 6.2.1 shows the room temperature absorbance of the InP based DBQWs samples. Multiple intersubband transitions, $E_i \rightarrow E_{i+1}$, were observed in the room temperature absorption spectra (where E_i refers to the Γ subband energy level in the well, unless otherwise stated i is the subband index). No peaks were observed in

the parallel (forbidden) polarisation (see Fig. 6.2.2). It can be seen that the peak detection wavelength for these structures can be tuned from 2-7 μm (620-177 meV) by simply varying the InGaAs well width. These spectra were fitted using a Lorentzian lineshape and the resulting peak energies and their corresponding FWHM are summarised in Table 6.2.1.

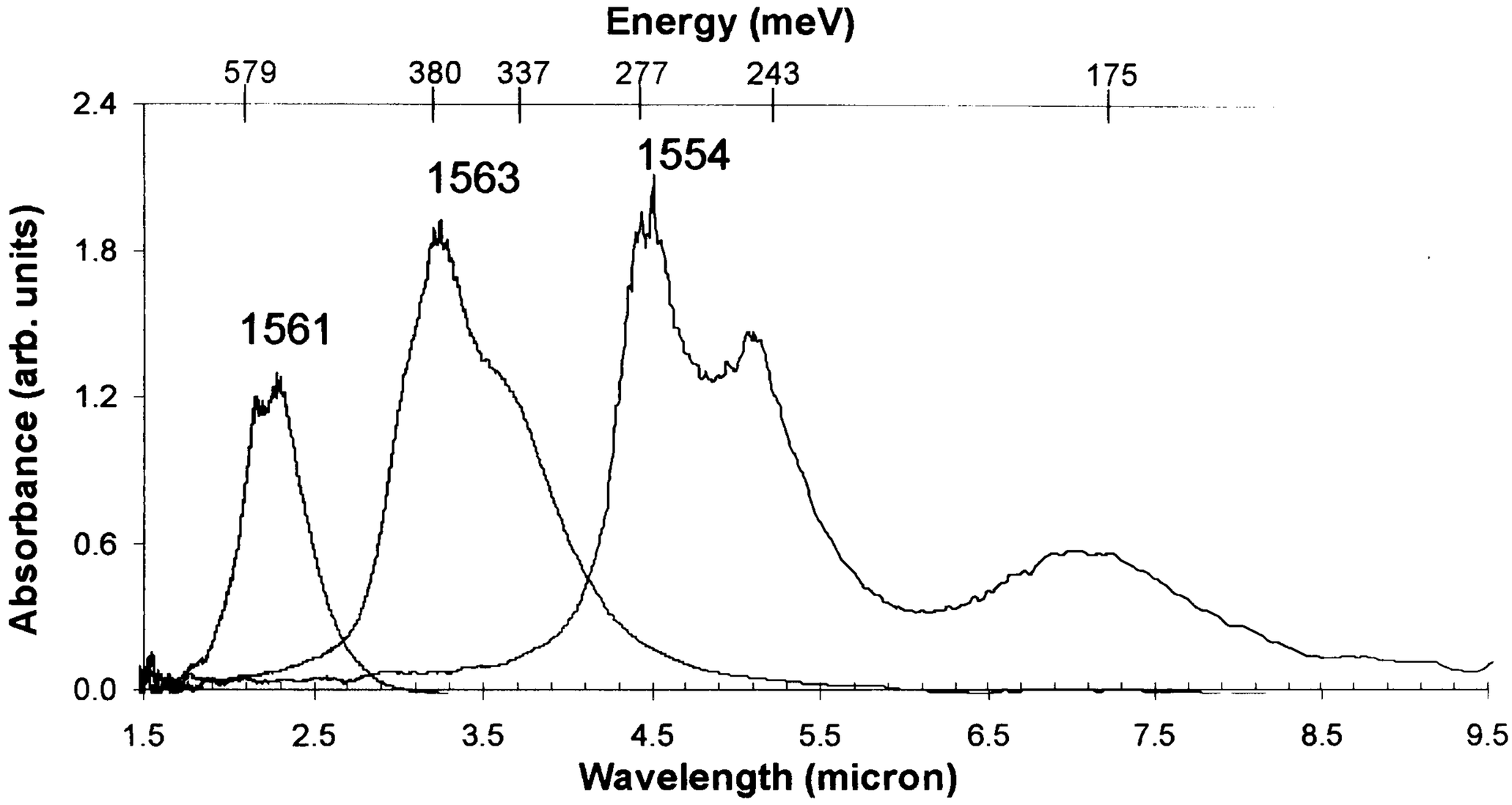

Figure 6.2.1: Measured absorption spectra as a function of wavelength at 300 K for samples 1554, 1563 and 1561 using 45^0 waveguide geometry.

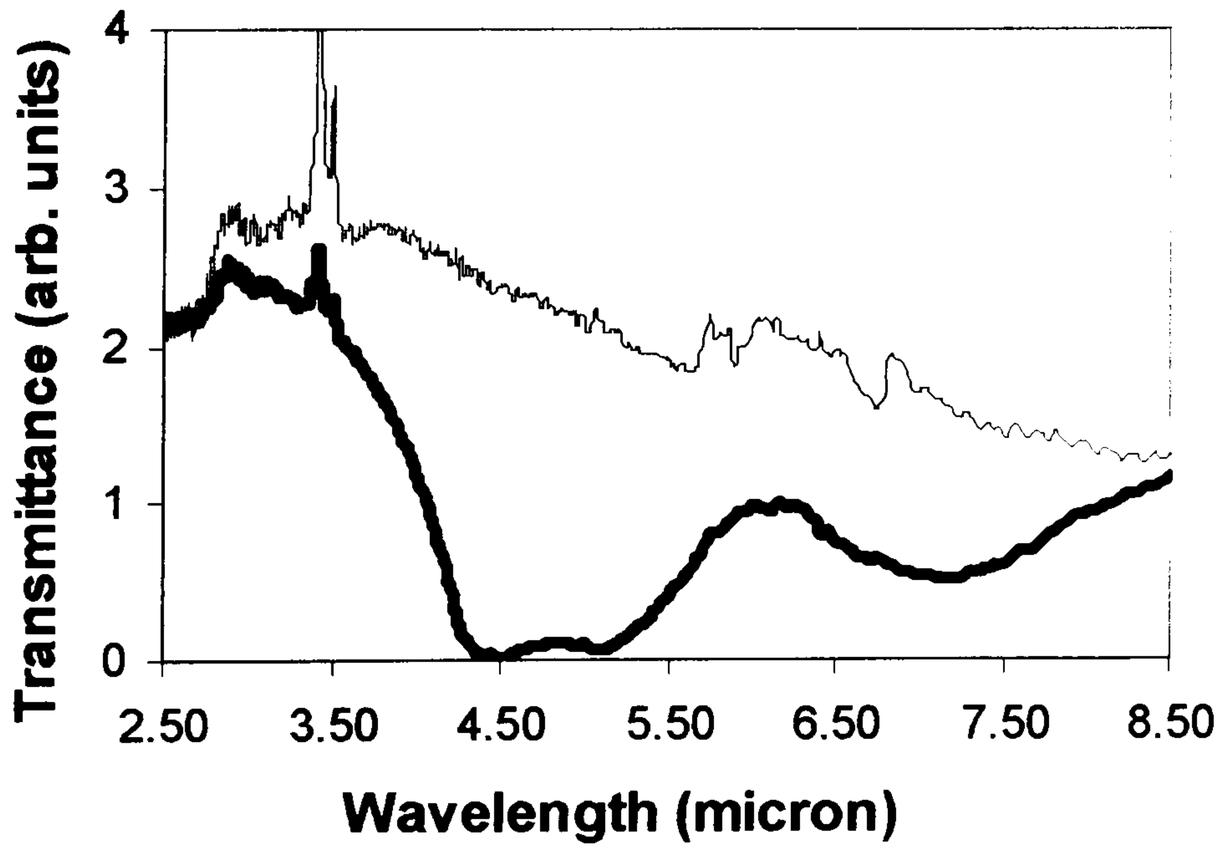

(a)

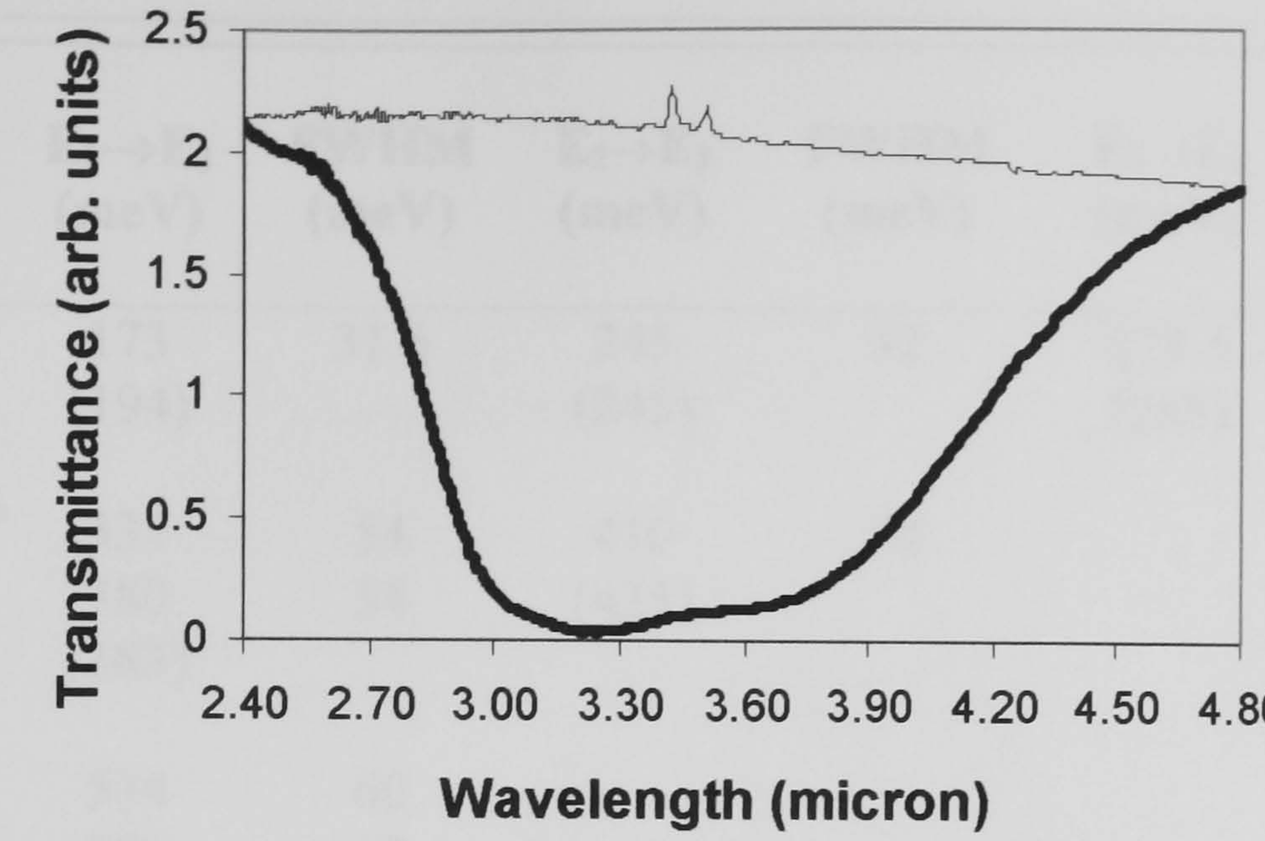

(b)

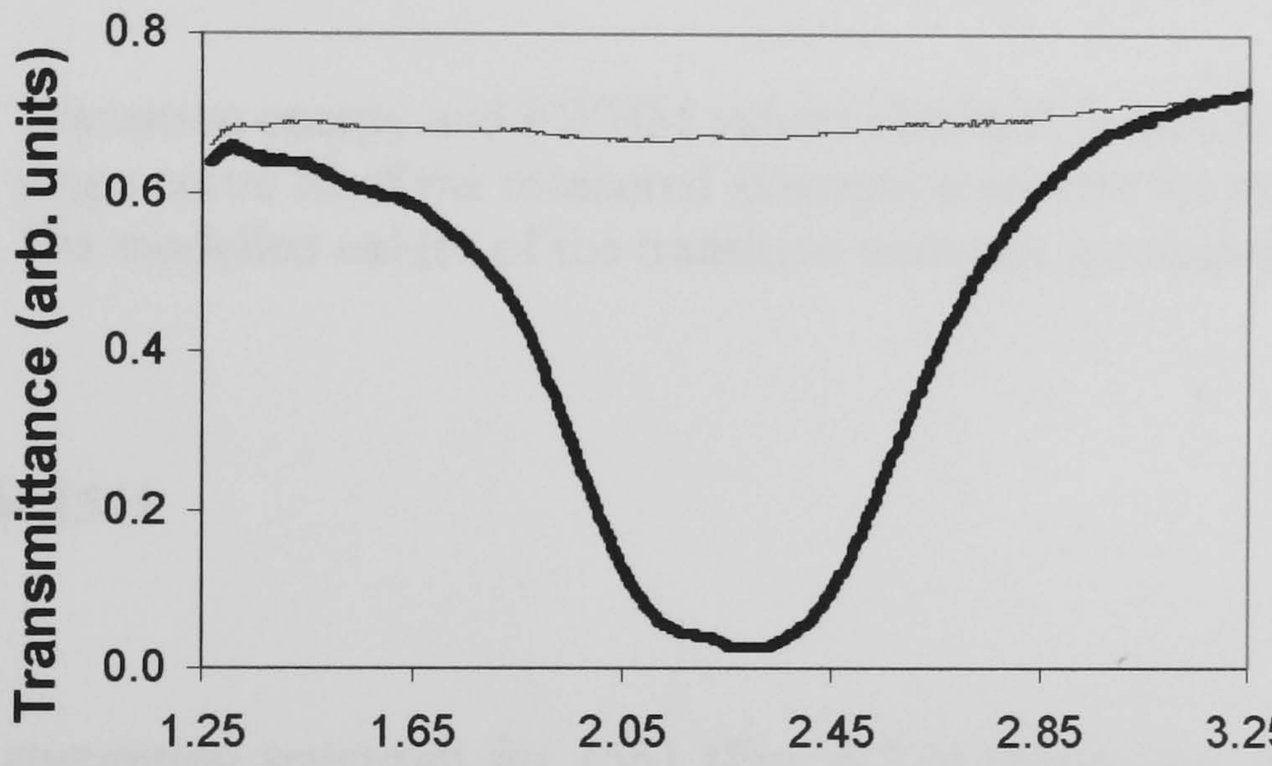

(c)

Figure 6.2.2: Transmission spectra of samples: (a) 1554, (b) 1563 and (c) 1561 measured using light polarised with the electric field vector parallel (thin line) or perpendicular (solid line) to the plane of the QWs at 300K. The features at ~ 3.3-3.5 μm and ~ 5.5-7.25 μm are due to atmospheric absorption.

Sample No	$E_1 \rightarrow E_2$ (meV)	FWHM (meV)	$E_2 \rightarrow E_3$ (meV)	FWHM (meV)	$E_3 \rightarrow E_4$ (meV)	FWHM (meV)
1554	173 (194)	31.6	245 (245)	32	275.5 (265)	23.6
1563	337 380 (383)	54 54	410 (435)	54		
1561	534 579 (572)	60 68				

Table 6.2.1: Transition energy and FWHM values obtained from Lorentzian line shape curve fit of the measured absorption spectra for the three samples. The modelled values of the transition energies are shown in brackets.

6.2.1 Sample 1561

The absorption spectrum for 1561 (Fig. 6.2.1) shows two peaks at 579 meV and 534 meV. From Tables 3.4.1 and 6.2.1, it can be seen that the 579 meV peak is in good agreement with the calculated transition energy of 572 meV for a well width of 30 Å. A better-resolved spectrum of this sample is shown in Fig. 6.2.1.1, where a Lorentzian curve fit is also presented. For 1561 the Fermi energy E_F lies between E_1 and E_2 (Table 3.4.1), so that both the observed peaks are attributed to the transition between E_1 and E_2 in the QW. The separation between the observed peaks is within 50 meV and this can be accounted for by a one ML fluctuation in thickness between different InGaAs wells.

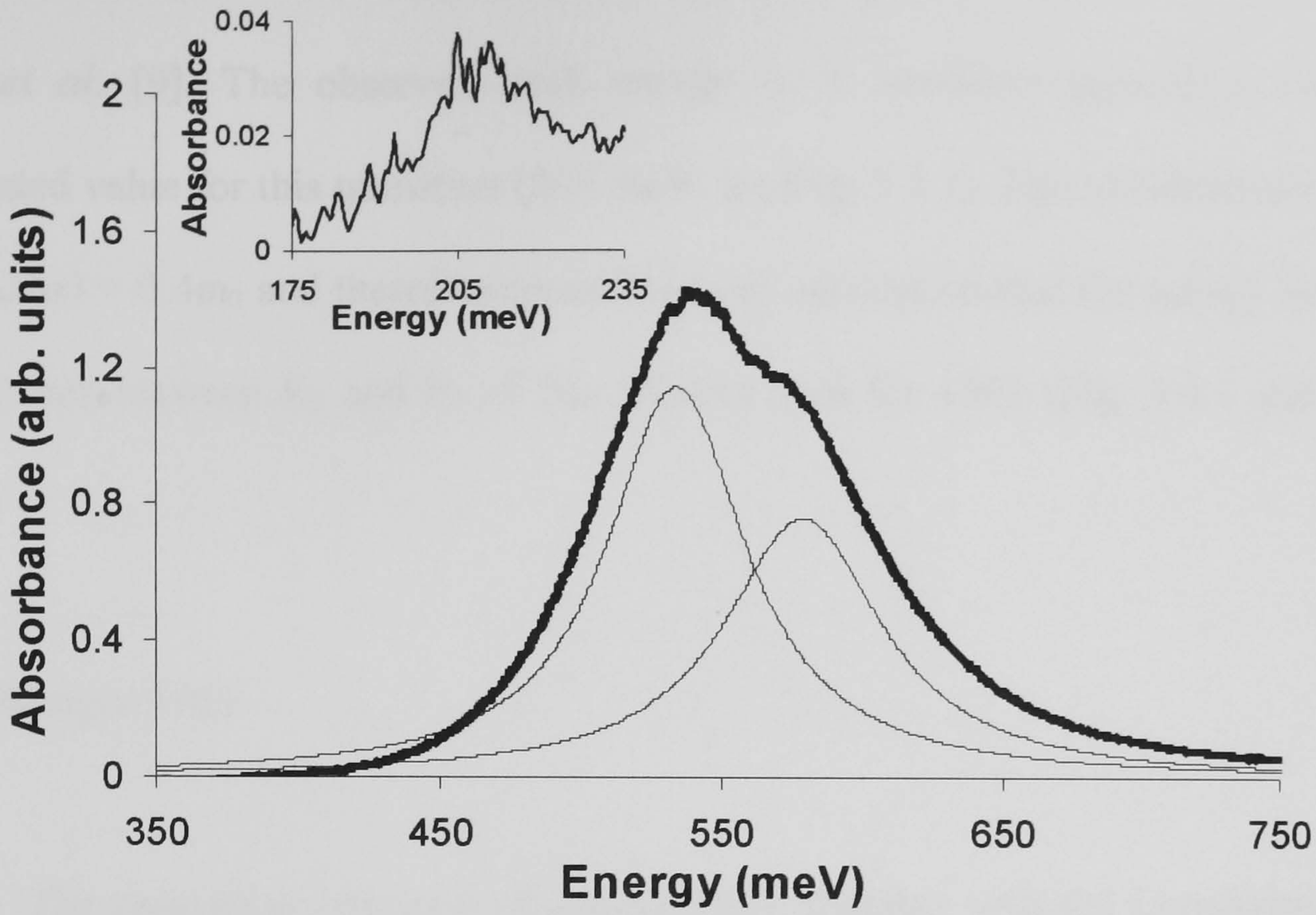

Figure 6.2.1.1: Measured 300 K absorption spectrum for sample 1561 (thick line) and Lorentzian curve fit (thin line) plotted on the energy scale. The inset shows the peak at 207 meV which is attributed to the $E_1^X \rightarrow E_2^X$ transition in the AlAs layer.

Additional evidence for the assignment of both peaks in 1561 to $E_1 \rightarrow E_2$ (rather than assigning one of them to $E_2 \rightarrow E_3$) transition comes from consideration of the position of E_F in relation to the E_1^X (AlAs) energy level. Although there are three subband energy levels in the well, the E_1^X (AlAs) level is below E_2 (Fig. 3.4.1 and Table 3.4.1) and therefore has to be populated with electrons before E_2. However, since the electron mass in the *X* valley in AlAs, is ~ 10 times the effective mass of the electrons in the Γ valley in the $In_{0.84}Ga_{0.16}As$ well, the corresponding density of states is much larger. This implies that the sample doping would have to be impractically high for E_2 to be populated and hence for an $E_2 \rightarrow E_3$ transition to be feasible.

A relatively weak peak at ~ 207 meV is observed and is shown as an inset in Fig. 6.2.1.1. It is seen only in the allowed polarization and is attributed to the E_1^X

$\rightarrow E_2^X$ transition in the AlAs layer. This assignment is in line with the observations of Katz *et al.* [9]. The observed peak energy is in excellent agreement with our calculated value for this transition (203 meV, see Fig. 3.4.1). This validates our use of $m_{e\text{-}x}(AlAs) = 0.4m_0$ and therefore reconfirms our calculation that the energy level E_1^X (AlAs) lies between E_1 and E_2 of the InGaAs well for 1561 (Fig. 3.4.1 and Table 3.4.1).

6.2.2 Sample 1563

The absorption spectrum of sample 1563, together with the Lorentzian curve fit, is shown in Fig. 6.2.2.1.

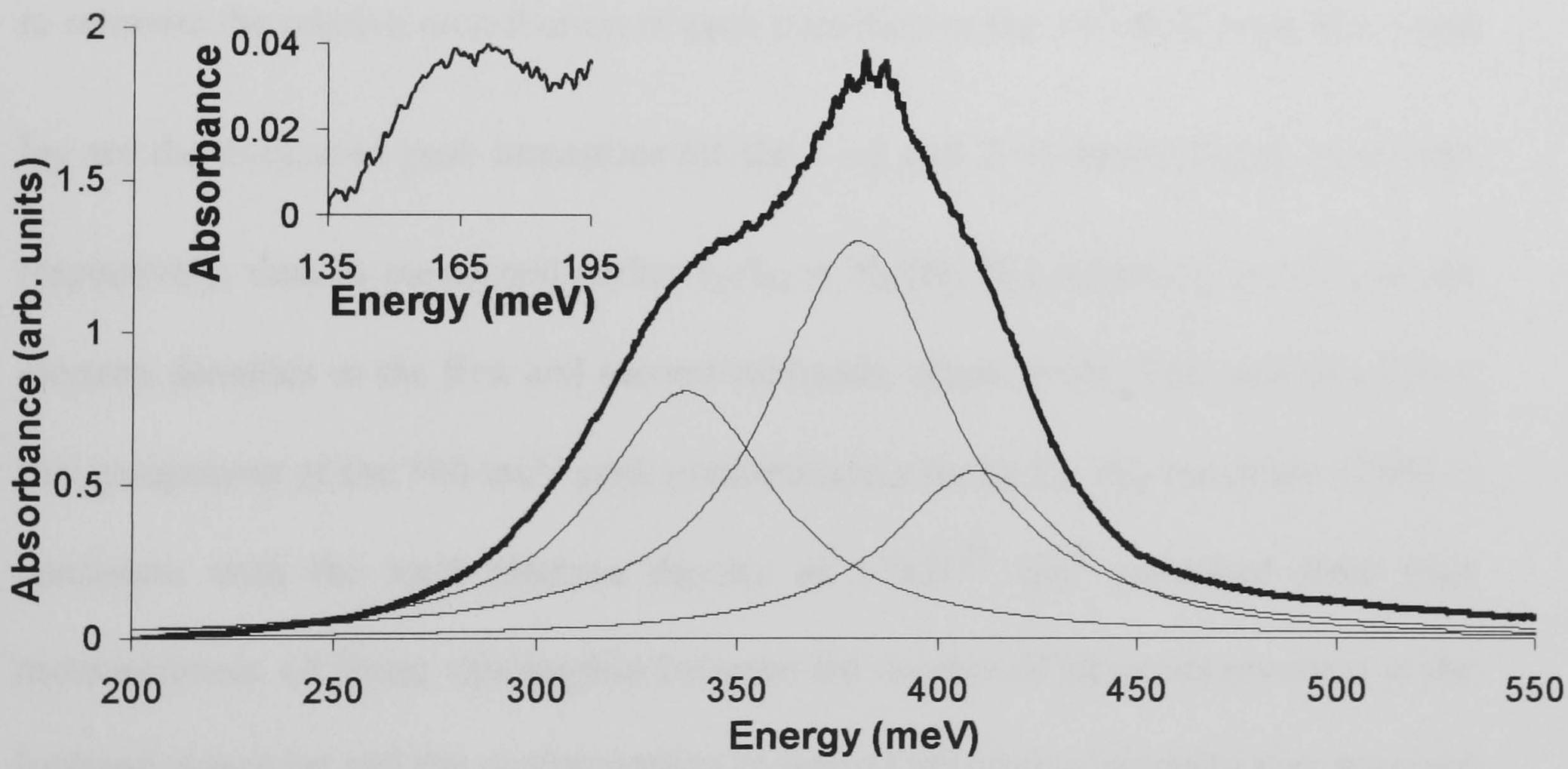

Figure 6.2.2.1: Measured 300 K absorption spectrum for sample 1563 (thick line) and Lorentzian curve fit (thin line) plotted on the energy scale. The inset shows the peak at 170 meV which is attributed to the $E_1^X \rightarrow E_2^X$ transition in the AlAs layer.

Two distinct peaks are observed in this sample; one at 337 meV and the strongest at 380 meV. In addition, there is a weak shoulder at 410 meV. From the

data in Table 3.4.1, it can be seen that the E_F lies between E_2 and E_3 for this sample. Therefore, only two intersubband transitions, $E_1 \rightarrow E_2$ and $E_2 \rightarrow E_3$, are possible for this structure. From our modeling, a variation of 1-2 monolayers (MLs) in thickness between the different InGaAs wells could account for peaks at 337 and 380 mev both arising from the $E_1 \rightarrow E_2$ transition. The shoulder peak at 410 meV must be due to the higher energy $E_2 \rightarrow E_3$ transition (Table 3.4.1). However, if there are two sets of intersubband peaks arising from growth variations within the sample, then we would expect also to see a weaker, lower energy peak from the $E_2 \rightarrow E_3$ transition, possibly also contributing to the peak at 380 meV. Hence we assume that the peak at 380 meV is due to a combination of both the $E_1 \rightarrow E_2$ and $E_2 \rightarrow E_3$ transitions. From the relative intensities of the three observed peaks and the measured carrier density, it is possible to estimate the relative contribution of each transition to the 380 meV peak. If I_{12} and I_{23} are the integrated peak intensities for the $1 \rightarrow 2$ and $2 \rightarrow 3$ intersubband transitions respectively, then as mentioned earlier $I_{23}/I_{12} \propto N_2/(N_1-N_2)$, where N_1 and N_2 are the electron densities in the first and second subbands, respectively. This analysis shows that assignment of the 380 meV peak predominantly to the $E_1 \rightarrow E_2$ transition (90%) is consistent with the total electron density of $\sim 7 \times 10^{12}$ cm^{-2} estimated from Hall measurements. (A linear relationship between the number of electrons involved in the subband transition and the corresponding measured absorption intensity was assumed in the above analysis. However, a similar conclusion is reached if N_1-N_2 and N_2 are weighted with the oscillator strengths for the corresponding intersubband transitions in an infinite quantum well. See discussion on sample 1554.)

We have also observed a weak peak at for sample 1563 at ~ 170 meV in the perpendicular polarization (see inset in Fig 6.2.2.1). This is attributed to the $E_1^X \rightarrow E_2^X$ transition in the AlAs QW layer. The agreement between the observed peak energy (170 meV) and our calculated value for this transition (203 meV, see Fig. 3.4.1) is within the error produced by one ML fluctuation in the AlAs thickness. This again validates our use of $m_{e\text{-}x}(AlAs) = 0.4m_0$ and therefore reconfirms our calculation that the energy level E_1^X (AlAs) lies between E_2 and E_3 of the InGaAs well for sample 1563 (Fig. 3.4.1 and Table 3.4.1). (See argument on the discount of the $E_2 \rightarrow E_3$ transition in sample 1561).

6.2.3 Sample 1554

For sample 1554 (Fig. 6.2.3.1), three peaks are observed at energies between 177 meV and 280 meV (7.5-4.5 μm). These are assigned to $E_1 \rightarrow E_2$=175 meV, $E_2 \rightarrow E_3$= 245 meV and $E_3 \rightarrow E_4$= 275.5 meV Γ transitions in the InGaAs well. The corresponding FWHM are 31.6 meV, 32 meV and 23.6 meV, respectively. The similar FWHM are as expected for transitions within the same electronic band. (On the other hand, the absorption bands for intervalley transitions (e.g. $\Gamma \rightarrow X$) are expected to be broader than $\Gamma \rightarrow \Gamma$ transitions due to the different energy dispersions for Γand *X* electrons [3].)

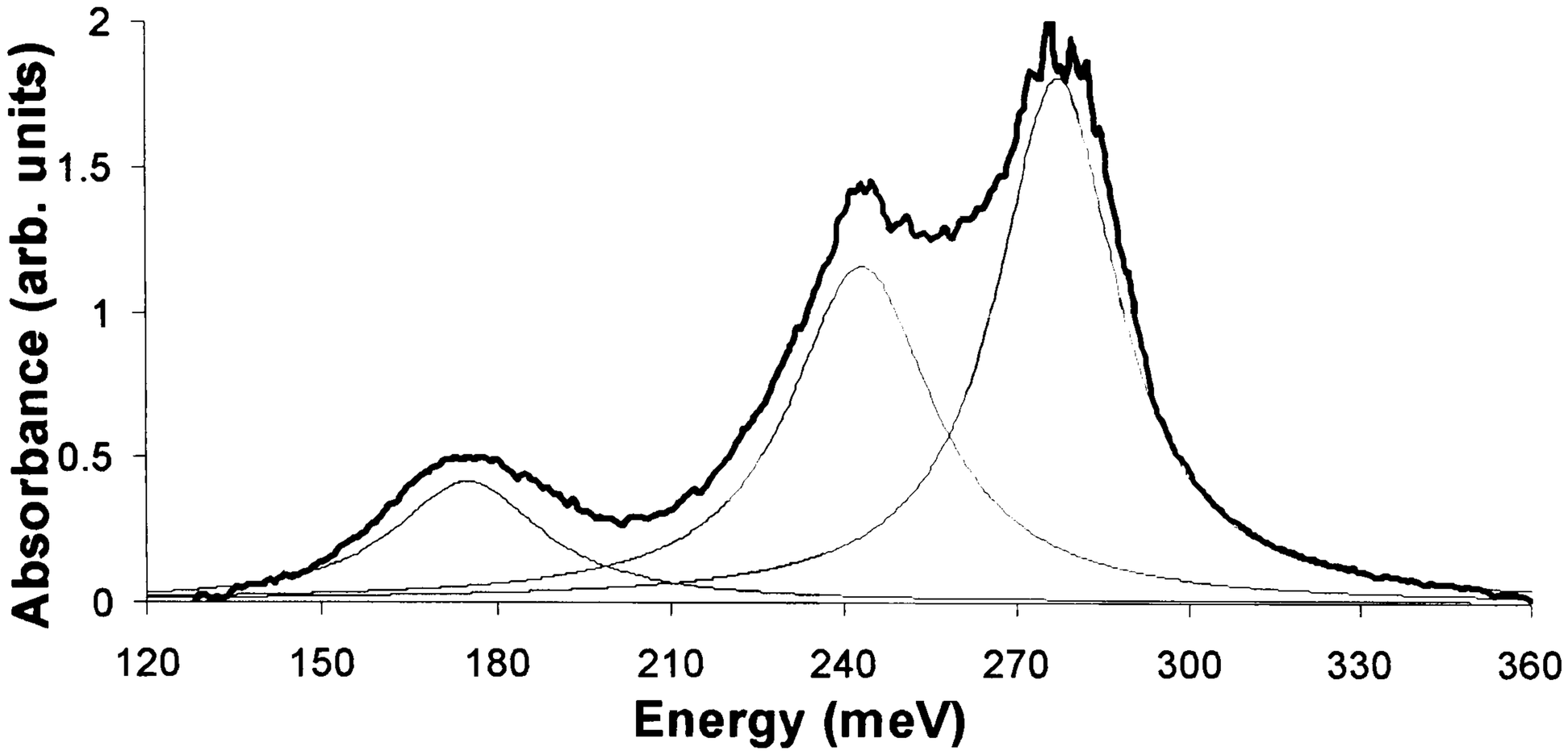

Figure 6.2.3.1: Absorption spectrum measured at 300 K for sample 1554 using 45^0 waveguide geometry (thick line) and Lorentzian curve fit (thin line).

From Table 3.4.1, our model yields four subband energy levels, three of them bound below the $In_{0.52}Al_{0.48}As$ conduction band edge and the fourth quasi-bound by the AlAs alone (see Fig. 3.4.1). For a sheet electron density of 1.1×10^{13} cm^{-2}, the Fermi energy, E_F, is calculated to lie between E_3 and E_4.

Since the E_F is calculated to be between the third and fourth subbands, we expect to observe the three intersubband transitions shown in Fig. 6.2.3.2. Therefore, the electrons taking part in the transitions $E_1 \rightarrow E_2$, $E_2 \rightarrow E_3$ and $E_3 \rightarrow E_4$ correspond to N_1-N_2, N_2-N_3 and N_3, respectively, where N_i is the number of electrons in the i^{th} subband (only for perpendicular polarisation). These transition energies are calculated as $E_1 \rightarrow E_2$=194 meV, $E_2 \rightarrow E_3$=245 meV and $E_3 \rightarrow E_4$=265 meV, which are in close agreement with the measured values.

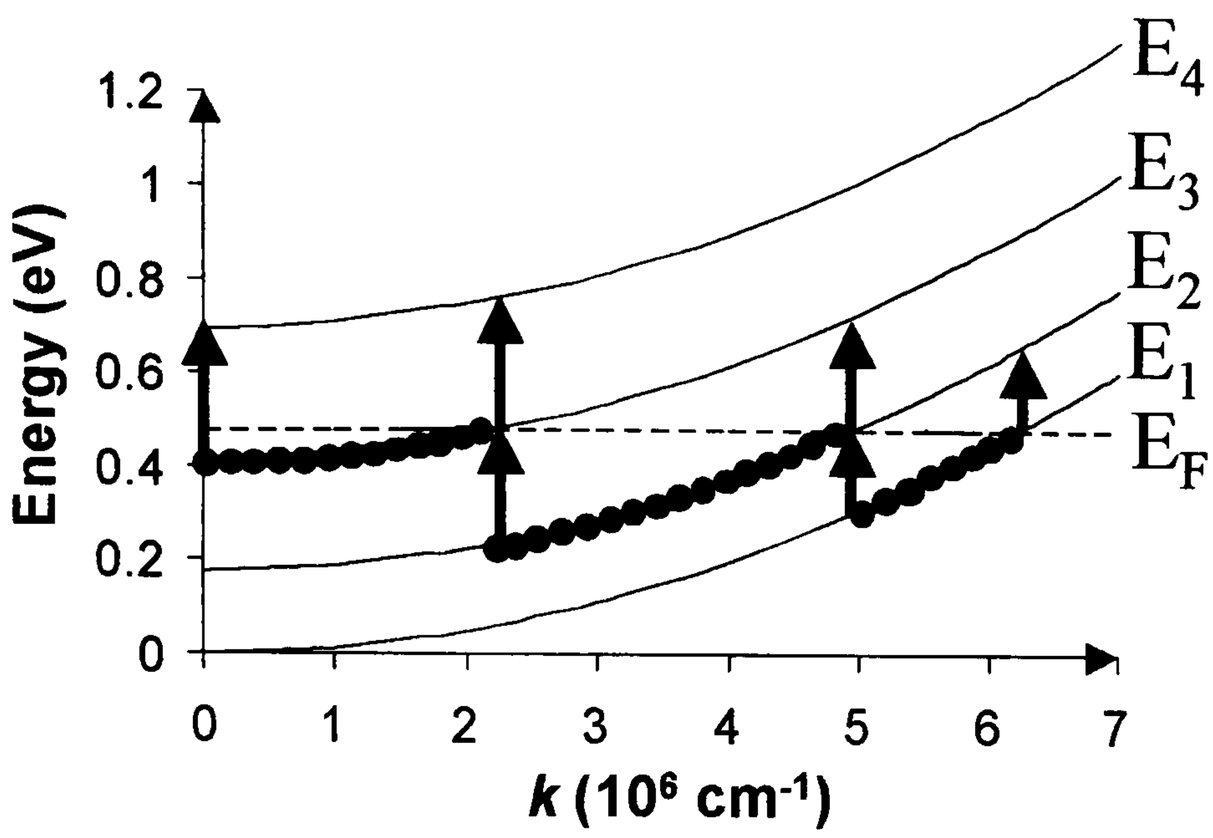

Figure 6.2.3.2: The energy dispersion of the quantized Γ energy levels in the $k_{x,y}$ direction for sample 1554 assuming parallel subbands. The arrows indicate the intersubband transitions and the solid circles show the part of the subband involved in the transition.

From Fig. 6.2.3.1, we observe that $E_3 \rightarrow E_4$ is the strongest of the three absorption peaks with $E_1 \rightarrow E_2$ being the weakest. The normalised integrated absorption intensities are 0.27 : 0.75 : 1 for $E_1 \rightarrow E_2$: $E_2 \rightarrow E_3$: $E_3 \rightarrow E_4$. From Fig. 6.2.3.2, it is apparent that the intensity of the three absorption peaks, is proportional to N_3, N_2–N_3 and N_1–N_2 respectively. (Note that the integrated absorption intensity for a transition is proportional to N_i x f_{osc}, where N_i is the number of electrons participating in the transition and f_{osc} is the oscillator strength for the transition). Neglecting non-parabolicity, the number of electrons in each subband can be calculated from the equation:

$$N_S = N_1 + N_2 + N_3$$

$$= \sum_i \frac{m^* k_B T}{\pi \hbar^2} \ln\left[1 + \exp\left(\frac{E_F - E_i}{k_B T}\right)\right] \qquad (6.2.3.1)$$

where i is the number of subbands.

A calculation of the E_F in 1554 using the electron density obtained from Hall measurements ($N_S = 1.1\times10^{13}$ cm^{-2}), and parabolic bands, yields $N_1 = 5.9\times10^{12}$ cm^{-2}, $N_2 = 3.6\times10^{12}$ cm^{-2} and $N_3 = 0.5\times10^{12}$ cm^{-2}. Hence, the electrons taking part in the transitions: $E_1\rightarrow E_2$, $E_2\rightarrow E_3$ and $E_3\rightarrow E_4$ are N_1-$N_2 = 2.3\times10^{12}$ cm^{-2}, N_2-$N_3 = 3.1\times10^{12}$ cm^{-2}, and $N_3 = 0.5\times10^{12}$ cm^{-2}, respectively. Assuming equal oscillator strengths, this would imply that $E_2\rightarrow E_3$ is the strongest transition. This is clearly not the case experimentally as can be seen from Fig. 6.2.3, where the measured normalized peak intensities for the three transitions, $E_1\rightarrow E_2$, $E_2\rightarrow E_3$ and $E_3\rightarrow E_4$ are 0.27 : 0.75: 1. Closer agreement with experiment is obtained for a total electron density of $N_S = 2\times10^{13}$ cm^{-2}, which gives $N_1 = 9.2\times10^{12}$ cm^{-2}, $N_2 = 7.0\times10^{12}$ cm^{-2} and $N_3 = 3.8\times10^{12}$ cm^{-2} and hence relative transition strengths of 0.6: 0.8: 1.

Weighting N_3, N_2-N_3 and N_1-N_2 with the respective infinite-well oscillator strengths [4] of 2.73, 1.87 and 0.96, also leads us to the conclusion that the Hall measurement underestimates the carrier density in this sample. For $N_S = 2\times10^{13}$ cm^{-2}, we now obtain a ratio of 0:2: 0.58: 1 for the $E_1\rightarrow E_2$, $E_2\rightarrow E_3$ and $E_3\rightarrow E_4$ transitions; which is again inline with experiment. This reinforces our assumption that the total electron density is about 2×10^{13} cm^{-2} giving electrons densities in the three subbands of: N_1=9.2×10^{12} cm^{-2}, N_2=7.0×10^{12} cm^{-2} and N_3=3.8×10^{12} cm^{-2}. Therefore, we assume a total electron density of $N_S = 2\times10^{13}$ cm^{-2}, which implies that the electron densities in the three subbands are similar. The discrepancy between this value of total sheet carrier density and that obtained from Hall measurements may be partly due to depletion of some of the InGaAs wells as a result of the thin cap and buffer layer used

in this structure. This could lead to an underestimation of the sheet carrier density per well by the Hall measurement.

We did not observe any $E_1^X \rightarrow E_2^X$ transition in the AlAs QW for this sample. This is probably to the strong $E_1 \rightarrow E_2$ peak observed at ~ 175 meV which obscured the $E_1^X \rightarrow E_2^X$ transition.

6.2.3.1 Subband Dispersion

Sample 1554 is too highly doped to be useful as a QWIP because its high E_F relative to the outer barriers would lead to a large dark current. However, the ability to observe multiple intersubband transitions and to compare their FWHM offers a valuable insight into the nature of the subband dispersion. Figure 6.2.3.2 shows the energy dispersion in the k_{xy} plane (perpendicular to the growth direction) for this sample. The dispersion has been calculated assuming the same electron effective mass (m*) for all subbands and neglecting the non-parabolicity parameter (α). The electron populations which participate in the various intersubband transitions are also shown.

Many theoretical calculations of m* and α for the first and second subbands have been reported in the literature [5]. For example, von Allmen *et al.* [6] calculate the E - k dispersions using a 14 band model for the first and second Γ subbands in GaAs/AlGaAs MQWs. They found that the second subband has a larger m* and smaller α than the first. The resulting spread of the k-dependent transition energy is expected to contribute to a broadening of the observed $E_1 \rightarrow E_2$ peak. However, Zaluzny [5] has shown that depolarisation effects associated with high electron

doping lead to a reduction of the transition linewidths. (Depolarisation effects are caused by resonant excitation of the free-electron gas in the QWs by the incoming light. This effect is associated with high electron doping and lead to a reduction of the transition linewidths by compensating the line distortion induced by different curvature of the subbands [5].) Hence, for highly-doped GaAs quantum wells, depolarisation effects may cancel the effect of subband non-parabolicity.

From Fig. 6.2.3.2 it can be seen that the $E_1 \rightarrow E_2$, $E_2 \rightarrow E_3$ and $E_3 \rightarrow E_4$ transitions for 1554 occur in different parts of the Brillouin zone and hence these transitions 'sample' different parts of *k* space. The $E_3 \rightarrow E_4$ transition takes place near to the zone center while the $E_1 \rightarrow E_2$ transition involves electrons with the largest *k* values. It is seen from Table 6.2.1 that the FWHM for the $E_3 \rightarrow E_4$ transition is the lowest, and is within the linewidth of 20-30 meV expected for bound-bound transitions in pseudomorphic QWs [7, 8]. This occurs even though the transition is from a bound to a quasi-bound state. As a result, we can neglect nonparabolicity for this transition and assume that subbands E_3 and E_4 are parallel to each other near the zone center. On the other hand, the FWHM for the $E_1 \rightarrow E_2$ and $E_2 \rightarrow E_3$ transitions are both about 8 meV larger than the $E_3 \rightarrow E_4$ transition. Since this comparison of FWHM involves transitions from the same sample, we conclude that any contributions to the peak width from effects, such as interface roughness or impurity scattering, should be the same for all three transitions. Also, as mentioned earlier, for sample 1554 the electron density in the three subbands is very similar and hence the effect of depolarisation on the linewidths of the three transitions is expected to be comparable. Consequently, we attribute the increased FWHM for the $E_1 \rightarrow E_2$ and $E_2 \rightarrow E_3$ transitions to unequal subband m^* and α values.

Using the following equation for the E - k dispersion of an infinite QW [9], unequal effective masses and non-parabolicities can be taken into account:

$$E_n(k) = \frac{E_G}{2}\left[1 + \frac{4E_n^{(0)}}{E_G} + \frac{2\hbar^2 k^2}{m_e E_G}\right]^{1/2} - \frac{E_G}{2} \qquad (6.2.3.1.1)$$

where m_e is the Kane effective mass at the conduction band bottom, E_G is the semiconductor band gap, and $E_n^{(0)} = \pi^2\hbar^2 n^2/(2m_e L_w^2)$ is energy of the nth subband in the parabolic approximation. This equation is used below to calculate the expected spread in $E_i \rightarrow E_{i+1}$ transition energy for various bandgaps and intersubband transitions.

From the position of E_F in Fig. 6.2.3.2, we can see that the two transitions $E_1 \rightarrow E_2$ and $E_2 \rightarrow E_3$ in 1554, mainly sample a region of the Brillioun zone from k = $4.8\text{x}10^6$ cm^{-1} to k = $6.2\text{x}10^6$ cm^{-1} and from k = $2.2\text{x}10^6$ cm^{-1} to k = $4.8\text{x}10^6$ cm^{-1}, respectively. Substituting appropriate values for an 80 Å $In_{0.84}Ga_{0.16}As$ QW into equation (6.2.3.1.1), we obtain $E_1 \rightarrow E_2$ (k=$4.8\text{x}10^6$ cm^{-1}) – $E_1 \rightarrow E_2$ (k= $6.2\text{x}10^6$ cm^{-1}) = 21 meV; $E_2 \rightarrow E_3$ (k = $2.2\text{x}10^6$ cm^{-1}) – $E_2 \rightarrow E_3$ (k = $4.8\text{x}10^6$ cm^{-1}) = 21 meV and $E_3 \rightarrow E_4$ (k= 0) – $E_3 \rightarrow E_4$ (k= $2.2\text{x}10^6$ cm^{-1}) = 3 meV. Hence the calculated contribution of non-parabolicity to the increased linewidth of both the $E_1 \rightarrow E_2$ and the $E_2 \rightarrow E_3$ transitions is 18 meV greater than for $E_3 \rightarrow E_4$. This is consistent with our experimental observation, where the difference in FWHM for the $E_1 \rightarrow E_2$ and $E_2 \rightarrow E_3$ transitions is 8 meV larger than the FWHM for the $E_3 \rightarrow E_4$ transition. (It is coincidental that the calculated spread is the same for $E_1 \rightarrow E_2$ and $E_2 \rightarrow E_3$ in this sample, since, although the non-parabolicity decreases with increasing subband index, electrons from a wider k range participate in the $E_2 \rightarrow E_3$ transitions.)

A similar calculation for an 80 Å GaAs QW gives $E_1 \rightarrow E_2$ (k= 4.8x10^6 cm^{-1}) - $E_1 \rightarrow E_2$ (k = 6.2x10^6 cm^{-1}) = 11 meV, which is about half of the corresponding value obtained for the $In_{0.84}Ga_{0.16}As$ QW. The contribution of depolarisation to linewidth, on the other hand, is expected to be similar in both materials since it depends mainly on the electron density. Therefore the cancelling of the non-parabolicity contribution to linewidth due to depolarisation effects, which is seen in some GaAs QWs, is not anticipated for high indium content InGaAs QWs.

To estimate the electron effective masses and non-parabolicity parameters for the four subbands in the $In_{0.84}Ga_{0.16}As$ QWs, we fitted the E - k dispersion of this sample using equation (6.2.3.1.1) with the following equation in ref. 6:

$$E_i(k_\perp) = E_{0i} + \frac{\hbar^2 k_\perp^2}{2m_i^*} + \alpha_i k_\perp^4 \qquad (6.2.3.1.2)$$

where i is the subband index. Figure 6.2.3.1.1 shows the E - k dispersion obtained using equations (6.2.3.1.1) and (6.2.3.1.2).

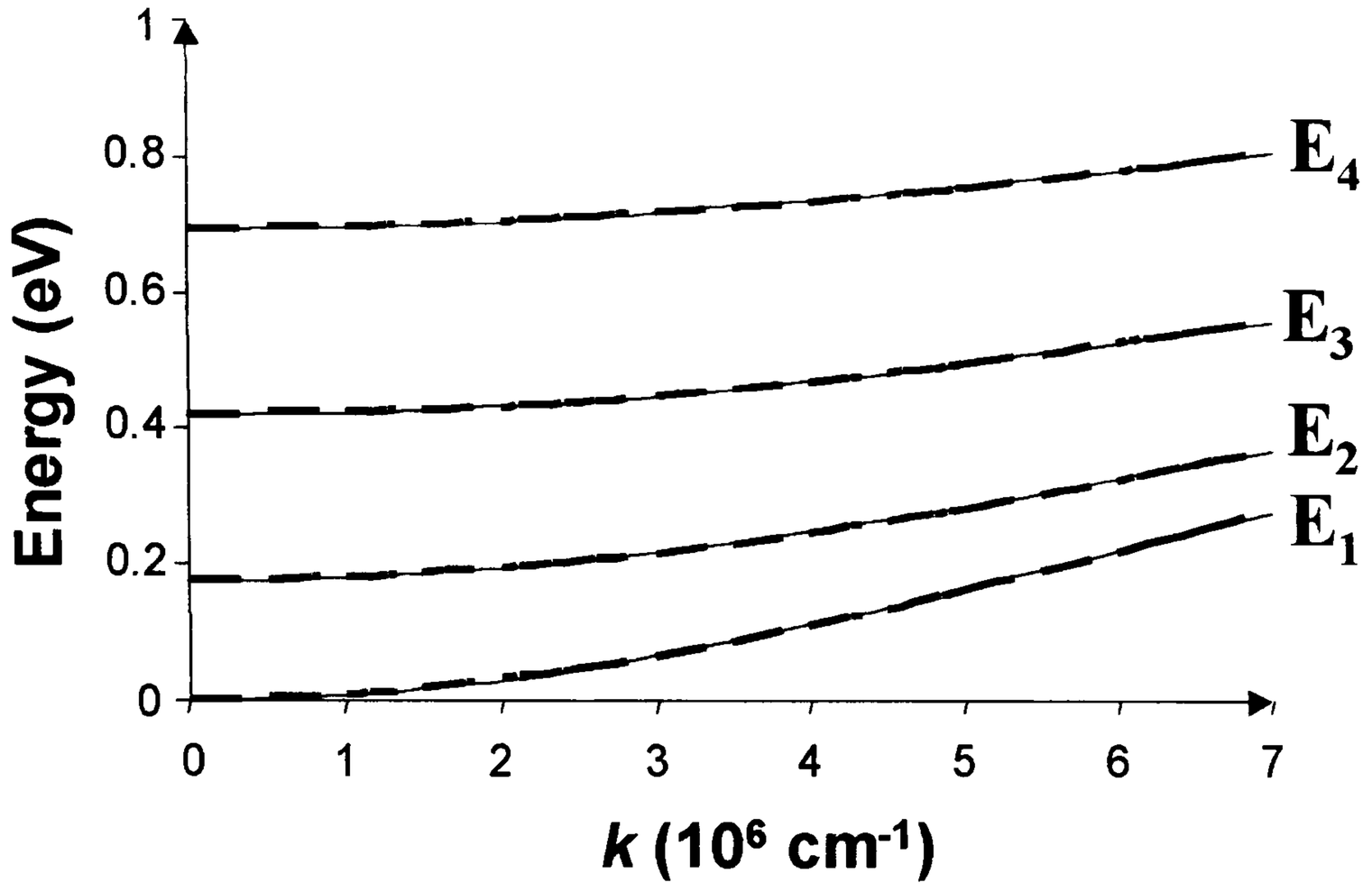

Figure 6.2.3.1.1: The energy dispersion of the quantised Γ energy levels in the $k_{x,y}$ direction for sample 1554 taking into account unequal effective masses and non-parabolicities using equation (6.2.3.1.1) [solid dashed line] and equation (6.2.3.1.2) [thin line].

Table 6.2.3.1.1 lists the estimated electron effective masses and non-parabolicity parameters for the four subbands in the $In_{0.84}Ga_{0.16}As$ QWs from Fig. 6.2.3.1.1.

Subband	**m^*/m_0**	**α (eVÅ^4)**
E_1	0.05	4000
E_2	0.078	1800
E_3	0.11	1100
E_4	0.14	800

Table 6.2.3.1.1: Estimated subband effective masses and non-parabolicities parameters for sample 1554.

It can be seen that the electron effective masses and non-parabolicity parameters of the higher subband m^*_{i+1} and α_{i+1} are larger and smaller, respectively, than the lower

subband. This is due to the larger effective mass and to the smaller non-parabolicity in the barrier than in the well and to the fact that the upper subband is less confined in the well than the lower subband [6]. Note also that the electron effective mass of the lowest subband $m_1^* \approx 0.05m_0$ is higher as compared to the linear interpolated value of $0.03m_0$. This is again due to the penetration of the wavefunction into the barrier.

6.3 Conclusions

In conclusion, we have grown three $In_{0.84}Ga_{0.16}As/AlAs/In_{0.52}Al_{0.48}As$ DBQWs structures on InP substrates with varying degrees of strain compensation due to the different well widths. All three samples show strong intersubband absorption at room temperature. The observed peaks are attributed to $\Gamma \rightarrow \Gamma$ transitions in the well and an $E_1^X \rightarrow E_2^X$ transition in the AlAs layer; peak energies are in good agreement with the calculated values. Both partially strain-compensated samples (1561 and 1563) show evidence of 1-2 monolayer fluctuation in the thickness of the different InGaAs QWs.

In sample 1554, the broad linewidth for the observed $E_1 \rightarrow E_2$ and $E_2 \rightarrow E_3$ transitions as compared to the $E_3 \rightarrow E_4$ transition is attributed to unequal m* and α in the first and second subbands. We suggest that the measurement of multiple intersubband transitions in highly doped QW structures in this way is a simple method to investigate the difference in nonparabolicity between subbands at values of k of interest for practical device applications. Shubnikov de Haas measurements can be used to obtain electron effective masses. However, the method proposed here gives additional information on the E - k dispersion without the need for liquid helium temperatures or extrapolation from high magnetic field conditions. The versatility of

this material system in covering a wide range of the mid infrared spectrum (λ=2-7 μm) has also been demonstrated.

References

1) K. L. Campman, H. Schmidt, A. Imamoglu, and A. C. Gossard, "*Interface Roughness and Alloy-disorder Scattering Contributions to Intersubband Iinewidths*", Applied Physics Letters, 1996, vol. 69, p. 2554-2556.

2) J. Katz, Y. Zhang, and W. I. Wang, "*Normal Incidence Infrared Absorption in AlAs/AlGaAs X-valley Multiquantum Wells*", Applied Physics Letters, 1992, vol. 61, p. 1697-1699.

3) S. R. Schmidt, E. A. Zibik, A. Seilmeier, L. E. Vorobjev, A. E. Zhukov, and U. M. Ustinov, "*Observation of Intersubband Real-space Transfer in GaAs/AlAs Quantum-well Structures Due to Γ-X Mixing*", Applied Physics Letters, 2001, vol. 78, p. 1261-1263.

4) L. C. West, and S. J. Eglash, "*First Observation of an Extremely Large-dipole Infrared Transition within the Conduction Band of a GaAs Quantum Well*", Applied Physics Letters, 1985, vol. 46, p. 1156-1158.

5) M. Zaluzny, "*Intersubband Absorption Line Broadening in Semiconductor Quantum Wells: Nonparabolicity Contribution*", Physical Review B, 1991, vol. 43, p. 4511-4547, and references therein.

6) P. von Allmen, M. Berz, F. -K. Reinhart, and G. Harbeke, "*Intersubband Absorption in GaAs/AlGaAs Quantum Wells Between 4.2K and Room Temperature*", Superlattices and Microstructures, 1989, vol. 5, p. 259-263.

7) L. C. Lenchyshyn, H. C. Liu, M. Buchanan, and Z. R. Wasilewski, "*Mid-wavelength Infrared Detection with $In_xGa_{1-x}As/Al_{0.45}Ga_{0.55}As$ Multiple Quantum Well Structures*", Semiconductor Science Technology, 1995, vol. 10, p. 45-48.

8) H. S. Li, Y. W. Chen, K. L. Wang, and D. Y. C. Lie, "*Intersubband Transitions in Pseudomorphic InGaAs/GaAs/AlGaAs Multiple Step Quantum Wells*", Journal of Vacuum Science Technology B, 1993, vol. 11, p. 1840-1843.

9) B. Gelmont, V. Gorfinkel, and S. Luryi, "*Theory of the Spectral Line Shape and Gain in Quantum Wells with Intersubband Transitions*", Applied Physics Letters, 1996, vol. 68, p. 2171-2173.

Chapter 7 Summary and Future Work

A series of DBQWs structures were grown by MBE (in UMIST) on (100) semi-insulating on GaAs and InP substrates. These samples exhibit clear and strong photoluminescence emissions at room temperature, which is evidence of good crystal quality.

We have observed some component of normal incident absorption in the stepped asymmetric QWs of InGaAs/GaAs/AlAs/AlGaAs DBQWs on GaAs substrates [1, 2]. The step also gives an additional degree of freedom to control the position of the excited states in the QWIP conduction band.

We have also observed strong room temperature intersubband absorption in strain-compensated $In_{0.84}Ga_{0.16}As/AlAs/In_{0.52}Al_{0.48}As$ DBQWs grown on InP substrates [3-6]. Multiple Γ-Γ intersubband transitions have been observed across a wide range of the mid infrared spectrum (2-7 μm) in three structures of differing InGaAs well width (30 Å, 45 Å, and 80 Å) and therefore with a differing net strain. This absorption range is not covered by direct-gap GaAs/AlGaAs structures. In the course of this work, we have also been able to estimate the subband non-parabolicity (m^* and α) from absorption spectra in highly doped quantum wells (QWs).

As mentioned earlier, there has been little work done in improving the operating temperature for detectors based on intersubband transitions. The highest operating temperature reported in the literature with a peak detection wavelength at ~ 3.4 μm is around 205 K [7].

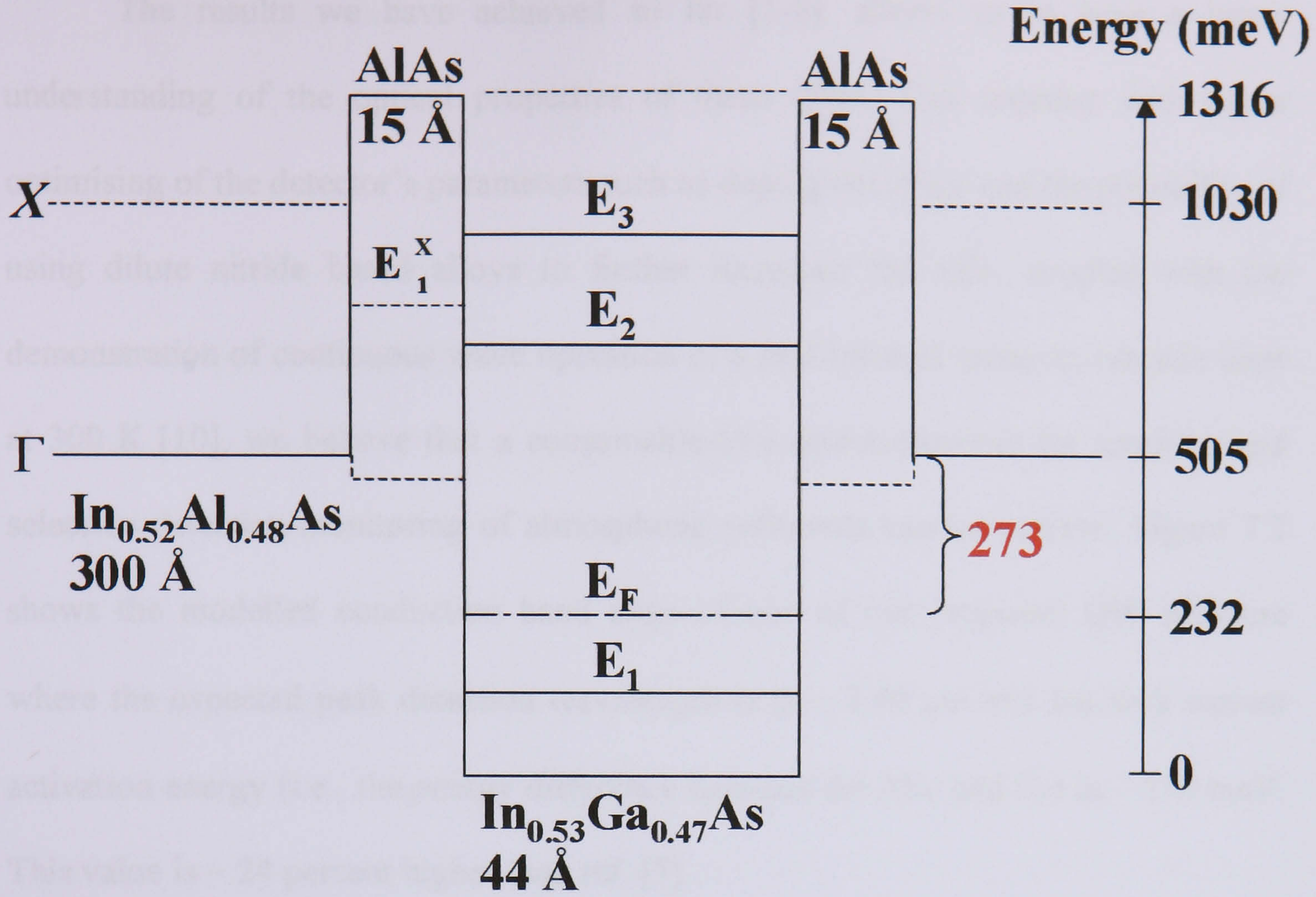

Figure 7.1: Schematic Γ (thick line) and *X* (dashed line) conduction band profile of the DBQW structure reported by Lee *et al.* [7] using our model.

The main obstacle to high temperature operation is the QW low conduction band offset ΔE_C. We have grown QW structures using the strain-compensation technique to tackle this problem [3-6]. Using this technique, we have achieved ~ 175 meV increase in the ΔE_C as compared to QWIPs working at 205 K; our devices show excellent optical and structural properties.

The ΔE_C could be further increased by the incorporation of a small amount of nitrogen (1-3.45 %) in GaAs alloys with little effect on the electronic structure of the valence band [8]. In addition, these alloys can be grown on GaAs substrates with negligible lattice-mismatched. Detection at 1.64 μm has already been reported using AlAs/AlGaAs barriers and symmetric GaAs/GaAsN/GaAs QWs [9].

The results we have achieved so far [1-6], allows us to have a better understanding of the optical properties of these QWs. This together with better optimising of the detector's parameters such as doping densities, and the possibility of using dilute nitride based alloys to further increased the ΔE_C, coupled with the demonstration of continuous wave operation of a mid-infrared quantum cascade laser at 300 K [10], we believe that a consumable-free detector/emitter for sensitive and selective detection/monitoring of atmospheric pollutants can be achieve. Figure 7.2 shows the modelled conduction band edge of one of our proposed QW structure where the expected peak detection wavelength is at ~ 3.49 μm and the dark current activation energy (i.e., the energy difference between the ΔE_C and E_F) is ~ 338 meV. This value is ~ 24 percent higher than ref. [7].

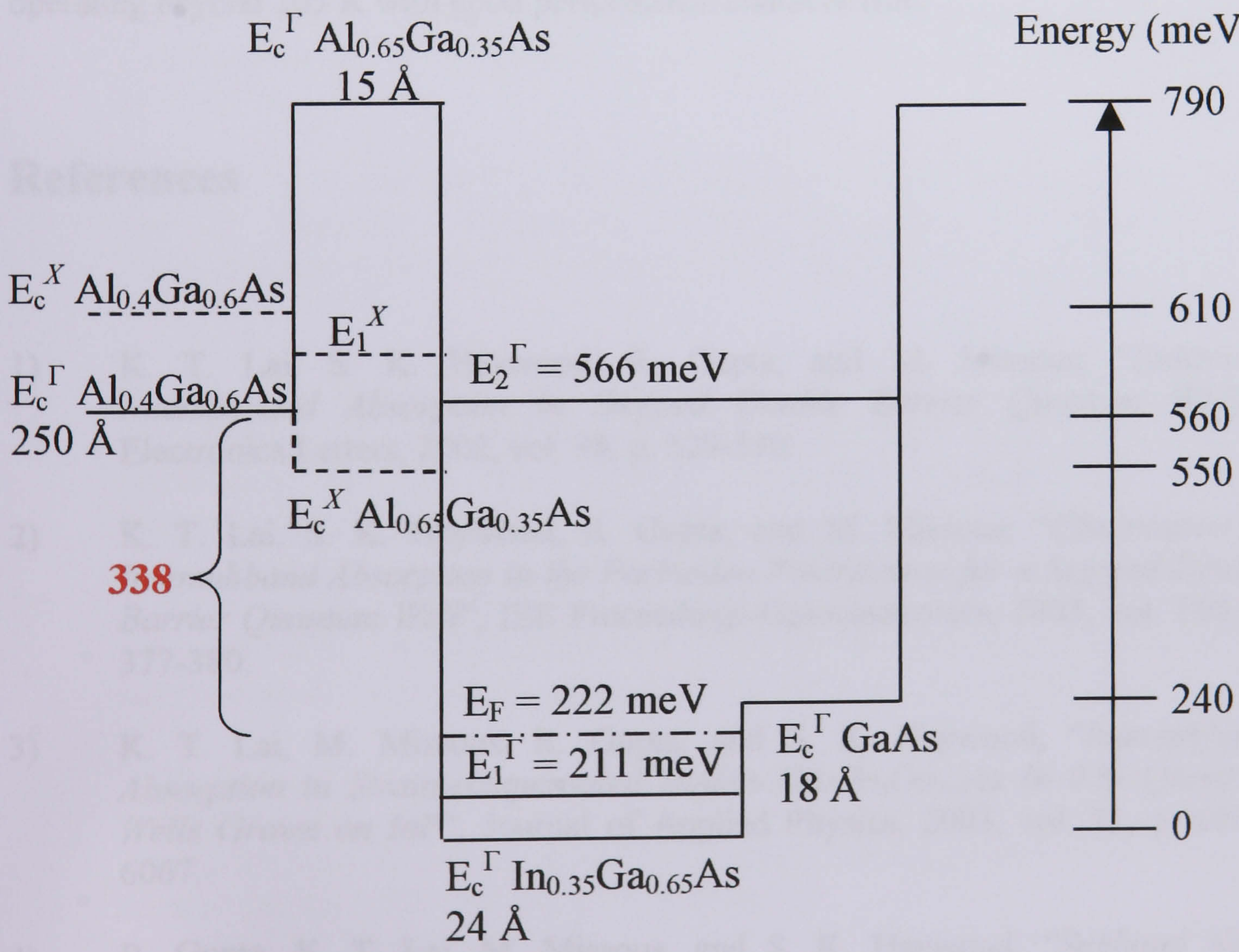

Figure 7.2: Modelled generic Γ (thick line) and *X* (dashed line) conduction band edge profile of our proposed GaAs based DBQWs samples.

Another advantage of the DBQW structure is that it offers significant photovoltaic (PV) mode detection with excellent detection characteristics which are comparable to the photoconductive (PC) mode QWIPs [7, 11-16]. This PV response has been interpreted as due to the doping migration effect [12, 16], with further enhancement by the DBQW structure itself [11]. The PV mode operation is promising for practical applications since the suppression of the dark current improves the noise properties.

Although, we have yet to perform any electrical measurements on these samples as they are not being processed at this moment of time, however, we are hopeful in the not too distant future, we will be able to report a QWIP capable of operating beyond 205 K with good performance characteristic.

References

1) K. T. Lai, S. K. Haywood, R. Gupta, and M. Missous, "*Enhanced Intersubband Absorption in Stepped Double Barrier Quantum Wells*", Electronics Letters, 2002, vol. 38, p. 529-530.

2) K. T. Lai, S. K. Haywood, R. Gupta, and M. Missous, "*Observation of Intersubband Absorption in the Forbidden Polarisation for a Stepped Double Barrier Quantum Well*", IEE Proceedings-Optoelectronics, 2003, vol. 150, p. 377-380.

3) K. T. Lai, M. Missous, R. Gupta, and S. K. Haywood, "*Intersubband Absorption in Strain-compensated InAlAs/AlAs/$In_xGa_{1-x}As$ (x~0.8) Quantum Wells Grown on InP*", Journal of Applied Physics, 2003, vol. 93, p. 6065-6067.

4) R. Gupta, K. T. Lai, M. Missous, and S. K. Haywood, "*Subband Non-parabolicity Estimated from Multiple Intersubband Absorption in Highly Doped Multiple Quantum Wells*", Physical Review B, 2004, vol. 69, p. 033303(1)-033303(4).

5) M. Missous, C. J. Mitchell, S. L. Sly, K. T. Lai, R. Gupta, and S. K. Haywood, "*Highly Strain $In_xGa_{(1-x)}As$- $In_yAl_{(1-y)}As$ ($x>0.8$, $y<0.3$) Layers for Short Wavelength QWIP and QCL Structures Grown by MBE*", Physica E, 2004, vol. 20, p. 496-502.

6) K. T. Lai, R. Gupta, M. Missous, and S. K. Haywood, "*Intersubband Absorption from 2 to 7 μm in Strain-compensated Double-barrier $In_xGa_{1-x}As$ Multiquantum Wells*", Semiconductor Science Technology, 2004, vol. 19, p. 1263-1267.

7) J. H. Lee, J. C. Chiang, S. S. Li, and P. J. Kannam, "*An AlAs/InGaAs/AlAs/InAlAs Double-barrier Quantum Well Infrared Photodetector Operating at 3.4 μm and 205 K*", Applied Physics Letters, 1999, vol. 74, p. 765-767.

8) A. Yu. Egorov, V .A. Odnobludov, V. V. Mamutin, A. E. Zhukov, A. F. Tsatsul'nikov, N. V. Kryzhanovskaya, V. M. Ustinov, Y. G. Hong and C. W. Tu, "*Valence Band Structure of GaAsN Compounds and Band-edge Lineup in GaAs/GaAsN/InGaAs Heterostructures*", Journal of Crystal Growth, 2003, vol. 251, p. 417-421.

9) E. Luna, M. Hopkinson, J. M. Ulloa, A. Guzmán, and E. Muñoz, "*Dilute Nitride Based Double-barrier Quantum-well Infrared Photodetector Operating in the Near Infrared*", Applied Physics Letters, 2003, vol. 83, p. 3111-3113.

10) M. Beck, D. Hofstetter,T. Aellen, J. Faist, U. Oesterle, M. Ilegems, E Gini, and H. Melchior, "*Continuous Wave Operation of a Mid-infrared Semiconductor Laser at Room Temperature*", Science, 2002, vol. 295 p. 301-305.

11) H. Schneider, P. Koidl, F. Fuchs, B. Dischier, K. Schwarz, and J. D. Ralston, "*Photovoltaic Intersubband Detectors for 3-5 μm Using GaAs Quantum Wells Sandwiched Between AlAs Tunnel Barriers*", Semiconductor Science Technology, 1991, vol. 6, p. C120-C123.

12) Y. H. Wang, J. C. Chiang, S. S. Li, and P. Ho, "*A GaAs/AlAs/AlGaAs and GaAs/AlGaAs Stacked Quantum Well Infrared Photodetector for 3-5 and 8-14 μm Detection*", Journal of Applied Physics, 1994, vol. 76, p.2538-2540.

13) Y. H. Zhang, D. S. Jiang, J. B. Xia, L .Q. Cui, C. Y. Song, Z. Q. Zhuo and W. K. Ge, "*A Voltage-controlled Tunable Two-color Infrared Photodetector using GaAs/AlAs/GaAlAs and Strained GaAs/GaAlAs Multiquantum Wells*", Applied Physics Letters, 1996, vol. 68, p.2114-2116.

14) K. L. Tsai, C. P. Lee, P. C. Chen, J .S. Tsang, C. M. Tsai, and J. C. Fan, "*The Effect of Barrier Structure On The Performance of Double Barrier Quantum Well Infra-red Photodetectors*", Solid-State Electronics, 1996, vol. 39, p. 201-204.

15) W. G. Wu, D. S. Jiang, L. Q. Cui, C .Y. Song, and Y. Zhuang, "*Structural and Photoelectric Studies on Double Barrier Quantum Well Infrared Detectors*", Solid-State Electronics, 1999, vol. 43, p. 723-727.

16) E. Luna, A. Guzmán, J. L. Sánchez-Rojas, E. Calleja, and E. Muñoz, "*Modulation-doping in 3-5μm GaAs/AlAs/AlGaAs Double-barrier Quantum-well Infrared Photodetectors: An Alternative to Achieve High Photovoltaic Performance and High Temperature Detection*", Infrared Physics & Technology, 2003, vol. 44, p. 383-390.

Appendix A

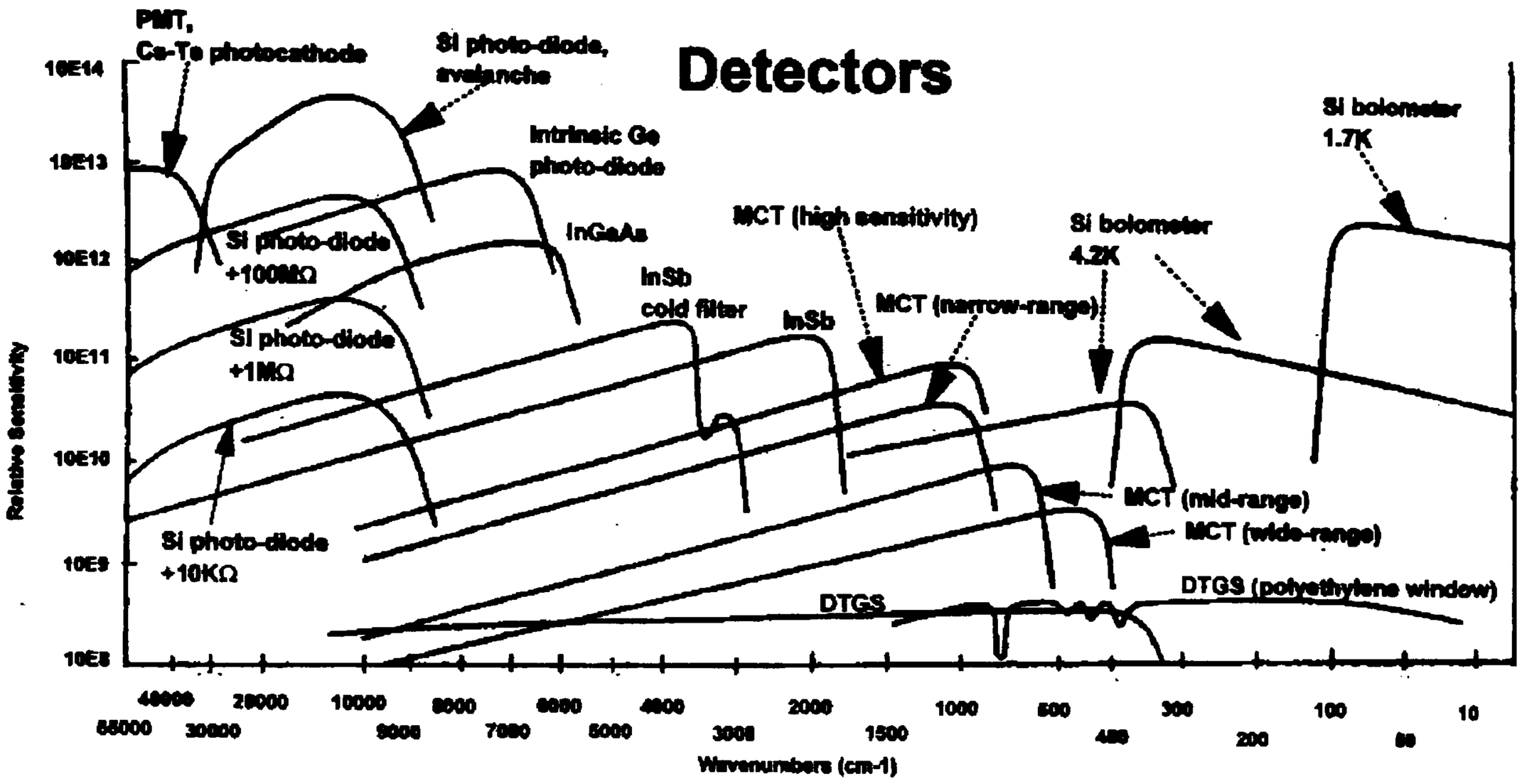

Figure A.1: The relative sensitivities of a range of detectors used with infrared and Raman spectroscopy.

Appendix B

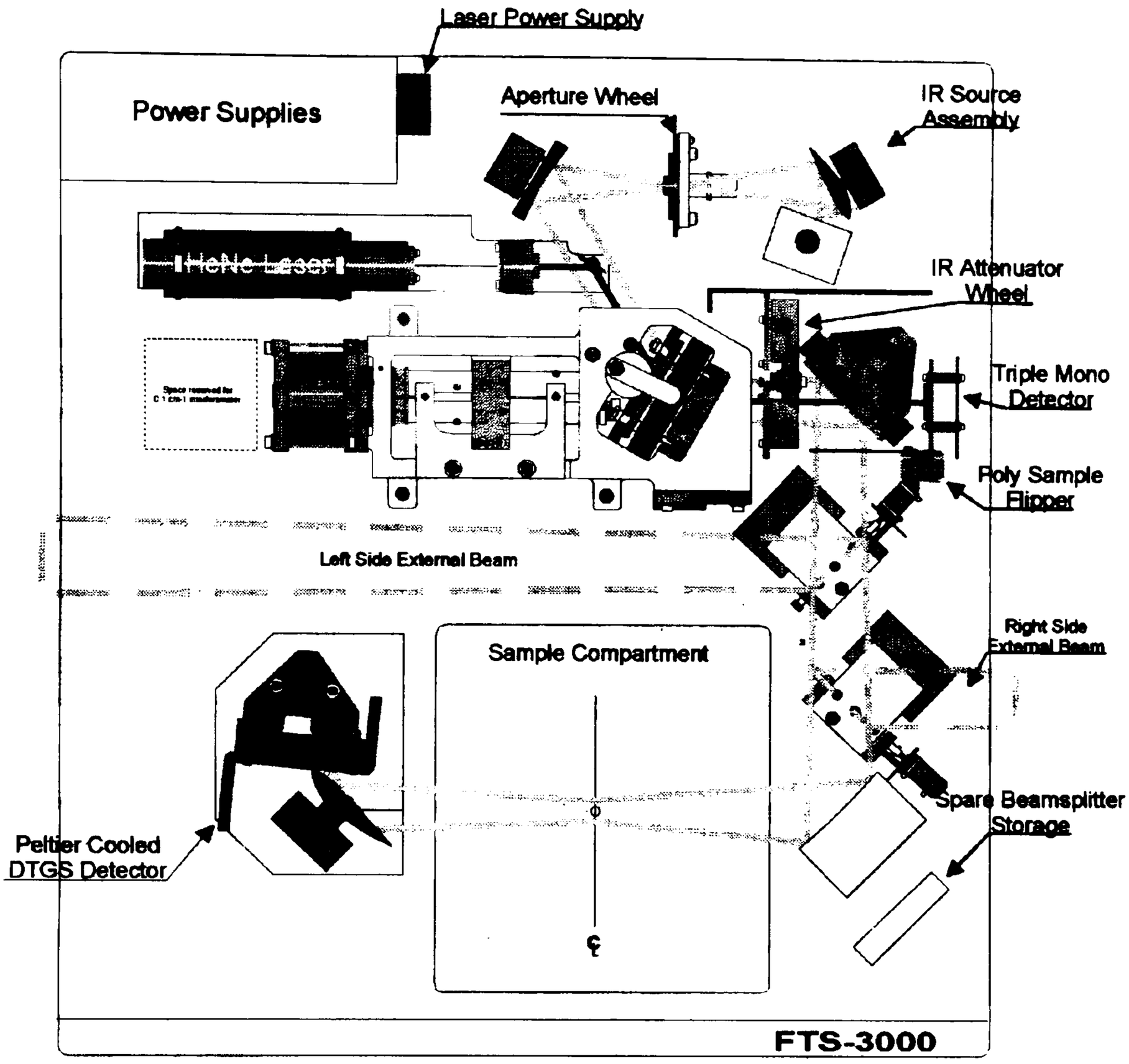

Figure B.1: Schematic diagram of the internal layout of the Bio-rad FTS-3000 FTIR.

Appendix C

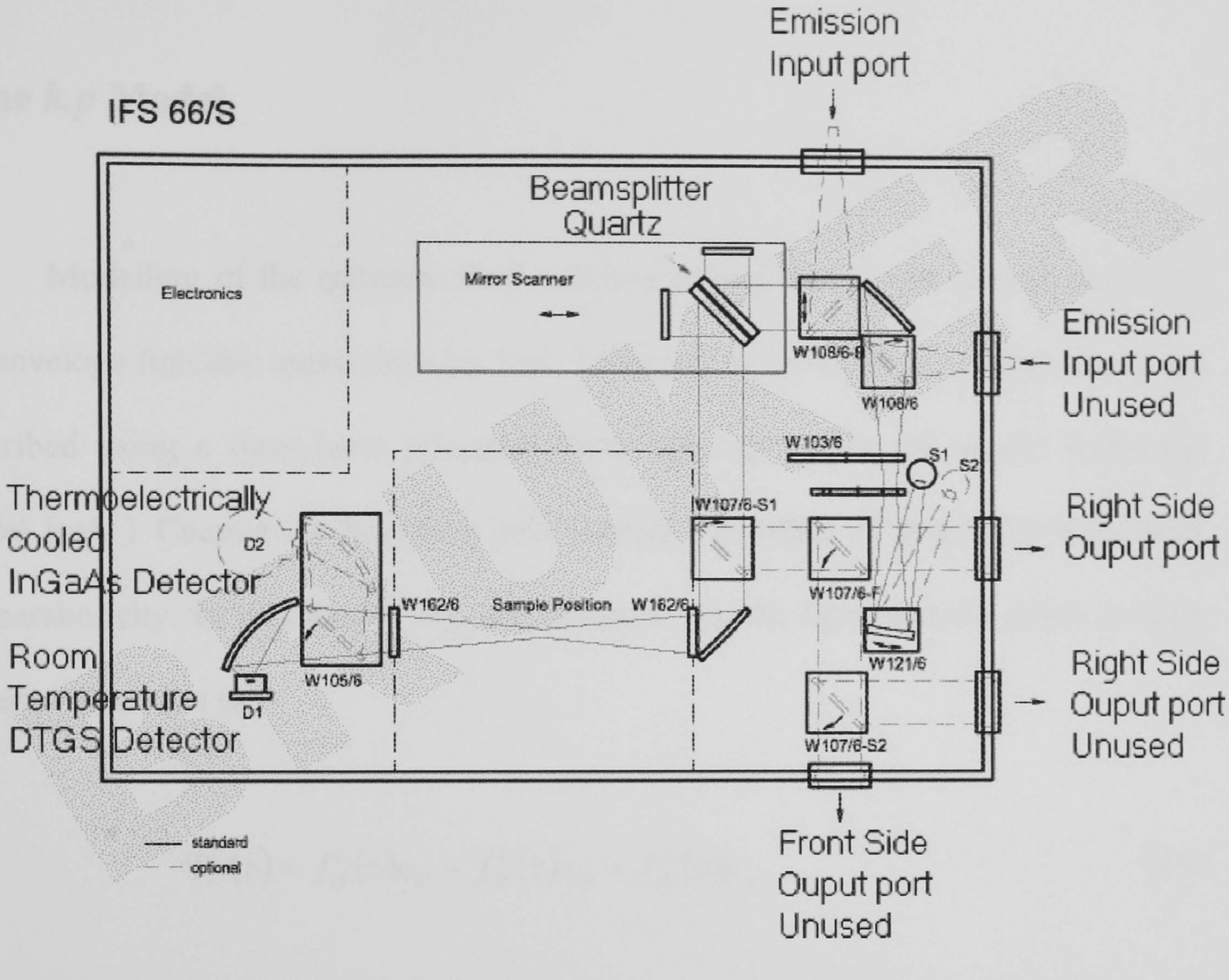

Figure C.1: Schematic diagram of the internal layout of the Bruker IFS 66/S FTIR.

Appendix D

Kane *k.p* Model

Modelling of the quantum well subband energy levels was carried out using the envelope function approximation [ref. 2 Chapter 3] in which the energy states are described using a three-band (electron, light hole, spin split off bands) Kane ***k.p*** model [ref. 1 Chapter 3] that takes into account the effect of strain and bulk band nonparabolicity. In this model, the wavefunction for the light particle states in each material is written as

$$\Psi^{l}(z) = f_{el}^{l}(z)u_{el} + f_{lh}^{l}(z)u_{lh} + f_{so}^{l}(z)u_{so} \tag{D1}$$

where $f_{el}^{l}(z)$, $f_{lh}^{l}(z)$ and $f_{so}^{l}(z)$ are the conduction, light hole, and spin-orbit split-off envelope functions in material l and z is the confinement direction. The basic functions, u_{el}, u_{lh} and u_{so} are the band edge Bloch function which are assumed to be the same in each material. They are:

$$u_{el} = \left|\frac{1}{2},\frac{1}{2}\right\rangle = \left|s\uparrow\right\rangle \tag{D2}$$

$$u_{lh} = \left|\frac{3}{2},\frac{1}{2}\right\rangle = \frac{1}{\sqrt{6}}\left|(X+iY)\downarrow\right\rangle - \sqrt{\frac{2}{3}}\left|iZ\uparrow\right\rangle \tag{D3}$$

$$u_{so} = \left|\frac{1}{2},\frac{1}{2}\right\rangle = \frac{1}{\sqrt{3}}[\left|(X+iY)\downarrow\right\rangle + \left|Z\uparrow\right\rangle] \tag{D4}$$

The Hamiltonian operating on the envelope functions for the light particle states is written as:

$$H^{l}_{total_{3B}} = \begin{bmatrix} E^{l}_{gs} & -i\sqrt{\frac{2}{3}}P_K\hat{k}_z & i\sqrt{\frac{1}{3}}P_K\hat{k}_z \\ i\sqrt{\frac{2}{3}}P^{l}_K\hat{k}_z & E^{l}_{lh}(=\delta E^{l}_s) & -\sqrt{\frac{1}{2}}\delta E^{l}_s \\ -i\sqrt{\frac{1}{3}}P_K\hat{k}_z & -\sqrt{\frac{1}{2}}\delta E^{l}_s & E^{l}_{so} \end{bmatrix} \quad \text{(D5)}$$

where $\hat{k}_z$ stands for -i∂/∂z, P_K is the matrix element, E^{l}_{so} is the energy of the spin orbit splitting, E^{l}_{gs} is the strained band gap between the conduction and heavy hole band edge

$$E^{l}_{so} = -\Delta^{l} + \frac{1}{2}\delta E^{l}_s \quad \text{(D6)}$$

$$E^{l}_{gs} = E^{l}_g + \delta E^{(gap)l}_h + \frac{1}{2}\delta E^{l}_s \quad \text{(D7)}$$

$$\begin{aligned} \delta E^{(gap)l}_h &= \delta E^{(c)l}_h - \delta E^{(v)l}_h \\ &= \left(a^{l}_c - a^{l}_v\right)\left(2e^{l}_{\|} + e^{l}_{zz}\right) \\ &= a^{l}_{gap}\left(2e^{l}_{\|} + e^{l}_{zz}\right) \end{aligned} \quad \text{(D8)}$$

$$\delta E^{l}_s = 2b^{l}\left(e^{l}_{zz} - e^{l}_{\|}\right) \quad \text{(D9)}$$

and

$$\delta E^{(c)l}_h = a^{l}_c\left(2e^{l}_{\|} + e^{l}_{zz}\right) \quad \text{(D10)}$$

$$\delta E^{(v)l}_h = a^{l}_v\left(2e^{l}_{\|} + e^{l}_{zz}\right) \quad \text{(D11)}$$

$$e^{l}_{\|} = \frac{a^{s}_o - a^{l}_o}{a^{l}_o} \quad \text{(D12)}$$

$$e_{zz}^{l} = -\frac{2C_{12}^{l}}{C_{11}^{l}} e_{a}^{l} \qquad \text{(D13)}$$

where Δ^{l} its spin orbit splitting, $E_{h}^{(gap)l}$ is the hydrostatic shift of the conduction band $E_{h}^{(c)l}$ relative to the valence band $E_{h}^{(v)l}$, δE_{s}^{l} is the hydrostatic shift of the spin-orbit split-off band, a_{c}^{l} and a_{v}^{l} are the hydrostatic deformation potentials of the conduction and valence band edges, respectively, b^{l} is the shear deformation potential, a_{o}^{s} and a_{o}^{l} are the substrate and material lattice constants, respectively and the C_{ij} parameters are the bulk elastic coefficients for the material. (See Chapter 3, Table 3.1.1 for material parameters). Since only the confinement motion is considered, the heavy hole state does not coupled to the near bands and is treated separately. The zero of the energy is taken at the top of the valence band edge in the well. Further comprehensive details can be obtained from ref. 1 of Chapter 3.

List of Publications

Fig. 4*a*. Fig. 4*b* and *c* show the waveforms of two input voltages, V_{CG} and V_{SG}, synchronised with V_{CLK}. During four periods of evaluation, four different binary combinations of V_{CG} and V_{SG} are accommodated by two input voltages. Although the voltage levels of input and output are mismatched, the waveform of the output voltage shows full swing XOR operation with respect to the supply voltage, V_{DD}, as shown in Fig. 4*d*.

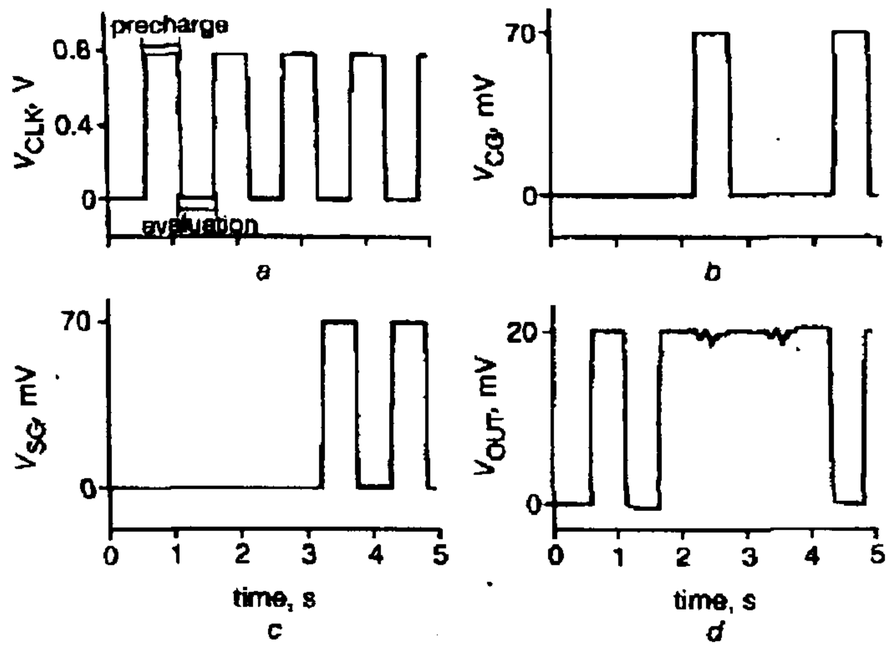

Fig. 4 *Experimental demonstration of basic operation of dynamic XOR logic gate*

$V_{DD} = 20$ mV, $V_{BG} = 14$ V, $T = 10$ K
a Waveform of clock signal V_{CLK} fed to MOSFET gate
b Waveform of control gate voltage V_{CG} synchronised with V_{CLK}
c Waveform of sidewall gate voltage V_{SG} synchronised with V_{CLK}
d Waveform of output voltage V_{OUT}

Conclusion: Basic operation of the dynamic exclusive-OR gate implemented by a MOSFET and a SET based on the gate-induced Si island is experimentally demonstrated at 10 K, for the first time. The logic output voltage shows a full swing operation at the supply voltage of 20 mV. Fabricated SETs are advantageous for implementing a multi-gate single-electron logic circuit and integrating with MOSFETs in that their depletion gates can control the peak position of the Coulomb oscillation and their fabrication method is compatible with the conventional CMOS process technology.

Acknowledgment: This work has been supported by the BK 21 program and the national program for 'Tera-bit Level Nano Device Project' as a part of the 21st Century Frontier Project.

8 January 2002
Electronics Letters Online No: 20020345
DOI: 10.1049/el:20020345

Dae Hwan Kim, Kyung Rok Kim, Suk-Kang Sung, Jong Duk Lee and Byung-Gook Park (*Inter-University Semiconductor Research Center (ISRC) and School of Electrical Engineering, Seoul National University, San 56-1, Shinlim-dong, Kwanak-gu, Seoul 151–742, Republic of Korea*)

E-mail: bgpark@snu.ac.kr

References

1 TORIUMI, A., UCHIDA, K., OHBA, R., and KOGA, J.: 'Challenge and prospects for silicon SET/FET hybrid circuits', *Physica B*, 1999, **272**, pp. 522–526
2 KIM, D.H., SUNG, S.-K., SIM, J.S., KIM, K.R., LEE, J.D., PARK, B.-G., CHOI, B.H., HWANG, S.W., and AHN, D.: 'Single-electron transistor based on a silicon-on-insulator quantum wire fabricated by a side-wall patterning method', *Appl. Phys. Lett.*, 2001, **79**, (23), pp. 3812–3814
3 TAKAHASHI, Y., FUJIWARA, A., YAMAZAKI, K., NAMATSU, H., KURIHARA, K., and MURASE, K.: 'Multigate single-electron transistors and their application to an exclusive-OR gate', *Appl. Phys. Lett.*, 2000, **76**, (5), pp. 637–639
4 TUCKER, J.R.: 'Complementary digital logic based on the Coulomb blockade', *J. Appl. Phys.*, 1992, **72**, (9), pp. 4399–4413
5 UCHIDA, K., MATSUZAWA, K., and TORIUMI, A.: 'A new design scheme for logic circuits with single electron transistors', *Jpn. J. Appl. Phys. Pt. 1*, 1999, **38**, (7A), pp. 4027–4032

Enhanced intersubband absorption in stepped double barrier quantum wells

K.T. Lai, S.K. Haywood, R. Gupta and M. Missous

Intersubband absorption is measured in the conduction band of GaAs and stepped GaAs/$In_xGa_{1-x}As$ multiple-quantum-wells confined by narrow AlAs barriers. Enhanced absorption from $n=1$ to $n=2$ is observed in the stepped wells. This is attributed to relaxation of the intersubband polarisation selection rule.

Introduction: Two windows in the atmospheric absorption spectrum can be exploited for the optical detection of gases. In the long-wavelength window from 8–12 μm, quantum well intersubband photodetectors based on lattice-matched GaAs/$Al_xGa_{1-x}As$ alloys provide high performance detector elements [1]. The choice of detector is less clear for the 3–5 μm window, where gases such as CO, CO_2, and CH_4 exhibit well resolved vibrational absorption bands [2]. To achieve an intersubband transition in GaAs/$Al_xGa_{1-x}As$ quantum wells (QWs) below 5.6 μm requires indirect $Al_xGa_{1-x}As$ barriers i.e. $x>0.45$. Beyond the $\Gamma-X$ crossover the thermal activation energy is reduced and therefore device dark current increases [3]. In addition, the $\Gamma-X$ scattering associated with $x>0.45$ together with GaAs X-barrier trapping can result in inefficient carrier collection and thus a decrease in photocurrent. Nevertheless, the mature epitaxial growth and processing technology of GaAs-based materials leads to high growth uniformity and excellent reproducibility. Thus despite the problems associated with indirect barriers, it may still be desirable to use GaAs/$Al_xGa_{1-x}As$ intersubband detectors in this wavelength region. Thin indirect AlAs barriers in combination with GaAs or strained InGaAs wells have been shown to be effective in enhancing the responsivity of 3–5 μm intersubband transitions due to improved carrier confinement [4, 5]. Stepped QWs are also known to relax the selection rules for intersubband transitions [6]. In this Letter we present a comparative study of the intersubband absorption of square and stepped wells in a double barrier quantum well (DBQW) structure i.e. the QW is confined by thin AlAs and wide direct $Al_xGa_{1-x}As$ barriers.

Table 1: Sample parameters: N_D, QW doping density; N_S, QW sheet carrier density

Sample No.	InGaAs (% In)	Well width (nm)	N_D (10^{18} cm^{-3})	N_S (10^{11} cm^{-2})	Absorption peak (μm)
1546	0	4.5	1.7	7.7	3.62
1551	0	4.5	8.5	38.3	3.62
1557	25	2.4+2.4	8.5	20.4	3.70

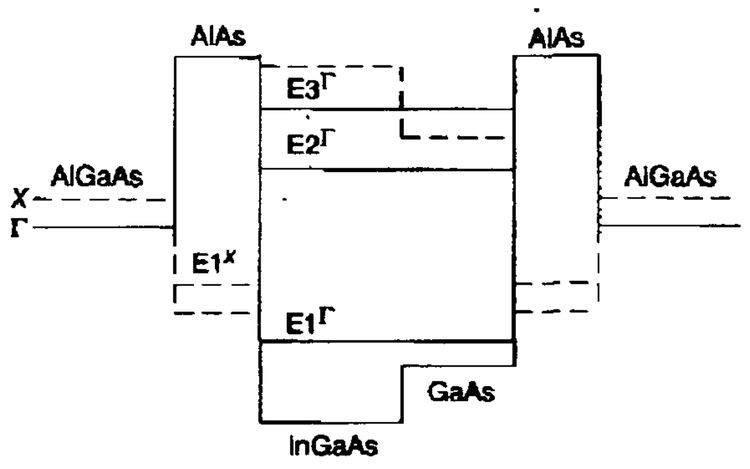

Fig. 1 *Modelled conduction band-edge profile for sample 1557*

Sample details: The samples were grown by molecular beam epitaxy on (100) semi-insulating GaAs substrates in a VG Semicon V90H reactor with 4 in substrate growth capability. We used near stoichiometric growth conditions [7] at low temperatures (~520°C) to achieve the high optical quality evidenced by efficient room temperature photoluminescence from all the samples. Table 1 shows the detailed sample parameters. Each sample has 50 well/barrier periods in the active region sandwiched between a 10 nm undoped GaAs cap layer and a 100 nm undoped GaAs buffer layer. The wells are confined by 2 nm AlAs barriers followed by 22 nm $Al_{0.4}Ga_{0.6}As$. Samples 1546 and 1551 both have 4.5 nm GaAs wells of different silicon doping level. Sample 1557 is a stepped $In_{0.25}Ga_{0.75}As$/GaAs well where only the InGaAs layer is doped. Fig. 1 shows the conduction band-edge

profile of 1557. Modelling of the quantum well subband energy levels was carried out using the envelope function approximation in which the energy states are described using a three-band Kane $k.p$ approximation that takes into account the effect of band nonparabolicity and strain. We used this model to design structures each with an $n=1$ to $n=2$ transition at about 3.6 μm and to ascertain that all the samples have the same number of states in the well (three).

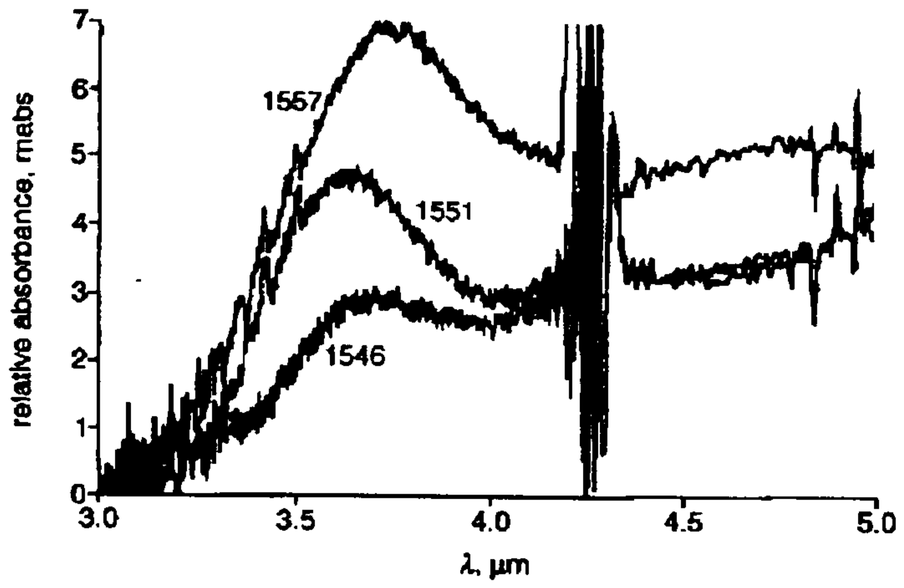

Fig. 2 *Room temperature FTIR absorption spectrum of samples 1546, 1551, and 1557 at Brewster angle using p-polarised light*

Curves are offset for clarity. Dip at 4.25 μm is due to CO_2 absorption in infrared beam path

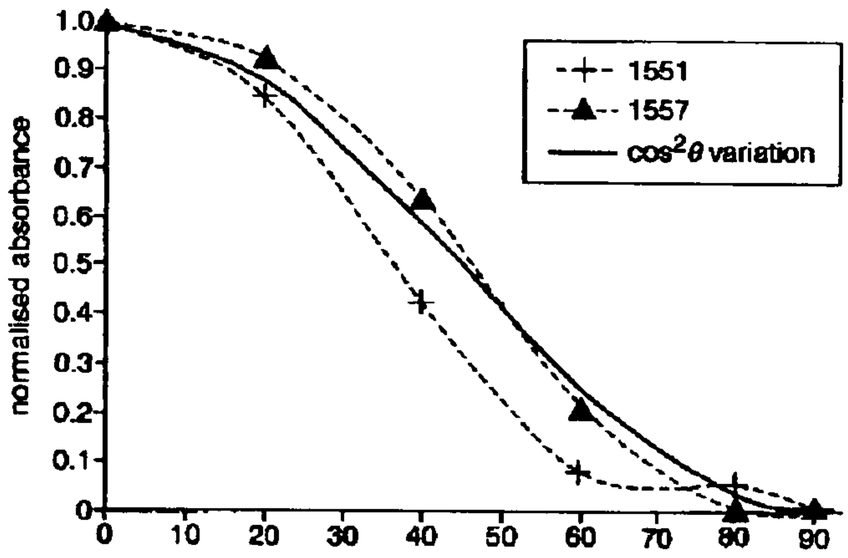

Fig. 3 *Normalised $n=1$ to $n=2$ peak intensity against polariser angle, θ, for samples 1551 and 1557*

Results: The room temperature intersubband absorption was measured in a Bio-Rad FT-3000 Fourier transform infrared spectrometer with a ZnSe wire grid polariser. Since the polarisation selection rule allows only radiation with its electric field vector perpendicular to the plane of the QW to stimulate an intersubband transition [1], the samples were oriented at the Brewster angle. The absorption spectrum was then measured using light p-polarised with respect to the plane of incidence. Fig. 2 shows the $n=1$ to $n=2$ intersubband absorption for the three samples studied. As expected there is an increase in the magnitude of absorption with carrier concentration for the two GaAs well samples (1546 and 1551). Significantly increased absorption is observed for the stepped well sample (1557) compared to 1551, even though it has a lower sheet carrier density (see Table 1). To investigate further the increased absorption in the stepped DBQW, the angle of the polariser was varied from $\theta=0$ to 90° thus varying the fraction of p-polarised light in the incident beam. The normalised peak intensities for the stepped well (1557) and the higher-doped GaAs well (1551) are shown in Fig. 3. According to the selection rule for light induced intersubband transitions in QWs the absorption should decrease as $\cos^2\theta$ under these conditions. The solid line in Fig. 3 indicates this theoretical curve. The stepped well shows a greater than $\cos^2\theta$ dependence of the peak intensity whereas the square well peak intensity drops off much more rapidly with polariser angle. The enhanced absorption in the stepped well and the persistence of the absorption to greater polariser angles indicates a degree of relaxation of the selection rule forbidding normal incidence absorption. Since all the samples have three levels in the well and incorporation of the step is known to increase the oscillator strength of the normally forbidden $n=1$ to $n=3$ transition [6], the increase in the $n=1$ to $n=2$ transition in sample 1557 cannot be due to an increase in oscillator strength for this transition. It has previously been proposed that reduction in the well bandgap partially relaxes the electric field vector selection rule [8]. Alternatively the step itself may have a similar effect due to the contribution to the energy states from two different materials. Relaxation of the selection rule in a conventional stepped well has been theoretically analysed in [9]. (It is interesting to note that here we observe absorption enhancement despite the $n=1$ level not being confined with the InGaAs alone.)

Conclusion: We have demonstrated an enhancement in the strength of the $n=1$ to $n=2$ intersubband absorption in GaAs DBQWs by introduction of an InGaAs layer. This occurs despite an expected reduction in the oscillator strength for this transition due to other normally forbidden transitions becoming allowed. The enhanced absorption is attributed to relaxation of the electric field vector selection rule.

13 December 2001
Electronics Letters Online No: 20020261
DOI: 10.1049/el:20020261

K.T. Lai, S.K. Haywood and R. Gupta (*Department of Engineering, University of Hull, Cottingham Road, Hull HU6 7RX, United Kingdom*)

E-mail: s.k.haywood@hull.ac.uk

M. Missous (*Department of Electrical Engineering and Electronics, UMIST, P.O. Box 88, Manchester M60 1QD, United Kingdom*)

References

1 LEVINE, B.F.: 'Quantum-well infrared photodetectors', *J. Appl. Phys.*, 1993, **74**, pp. R1–R81
2 LENCHYSHYN, L.C., LIU, H.C., BUCHANAN, M., and WASILEWSKI, Z.R.: 'Mid-wavelength infrared detection with $In_xGa_{1-x}As$ aAs/$Al_{0.45}Ga_{0.55}As$ multiple quantum well structures', *Semicond. Sci. Technol.*, 1995, **10**, pp. 45–48
3 LEVINE, B.F., GUNAPALA, S.D., and KOPF, R.F.: 'Photovoltaic GaAs quantum well infrared detectors at 4.2 μm using indirect $Al_xGa_{1-x}As$ barrier', *Appl. Phys. Lett.*, 1991, **58**, pp. 1551–1553
4 LIU, H.C., BUCHANAN, M., and WASILEWSKI, Z.R.: 'Short wavelength (1–4 μm) infrared detectors using intersubband transitions in GaAs-based quantum wells', *Appl. Phys. Lett.*, 1998, **83**, pp. 6178–6181
5 NEU, G., CHEN, Y., DEPARIS, C., and MASSIES, J.: 'Improvement of the carrier confinement by double-barrier GaAs/AlAs/(Al,Ga)As quantum well structures', *Appl. Phys. Lett.*, 1991, **58**, pp. 2111–2113
6 MII, Y.J., WANG, K.L., KARUNASIRI, R.P.G., and YUH, P.F.: 'Observation of large oscillator strengths for both 1–2 and 1–3 intersubband transitions of step quantum well', *Appl. Phys. Lett.*, 1990, **56**, pp. 1046–1048
7 MISSOUS, M.: 'Stoichiometric low-temperture GaAs and AlGaAs: a reflection high-energy electron-diffraction study', *J. Appl. Phys.*, 1995, **78**, pp. 4467–4471
8 LIU, H.C., BUCHANAN, M., and WASILEWSKI, Z.R.: 'How good is the polarization selection rule for intersubband transitions', *Appl. Phys. Lett.*, 1998, **72**, pp. 1682–1684
9 YUH, P.F., and WANG, K.L.: 'Optical transitions in a step quantum well', *J. Appl. Phys.*, 1989, **65**, pp. 4377–4381

Well-driven floating gate transistors

A.F. Mondragón-Torres, M.C. Schneider and E. Sánchez-Sinencio

A new layout structure for floating gate MOS devices on top of an isolating n-well is proposed. The well provides the floating device with noise isolation from the substrate and can also be used as an additional input for threshold voltage control or signal modulation.

Introduction: Floating gate (FG) transistors are used in both digital and analogue circuits. In digital circuits they are the core of flash memories [1, 2]. For analogue circuits, multiple input (MI) FGMOS devices are used in low voltage applications [3], as analogue memories [4] or as translinear computing elements [5].

Observation of intersubband absorption in the forbidden polarisation for a stepped double barrier quantum well

K.T. Lai, S.K. Haywood, R. Gupta and M. Missous

Abstract: Intersubband absorption in the conduction band of a series of double barrier multiple quantum wells has been studied. Absorption in the forbidden polarisation was observed for a $GaAs/In_xGa_{(1-x)}As/AlAs/Al_yGa_{(1-y)}As$ stepped well using 45° waveguide geometry. This is attributed to the relaxation of the polarisation selection rule. This corroborates the authors' previous observation of enhanced absorption at the Brewster angle in these structures. In 45° waveguide geometry, it is possible to resolve Γ(well)–X(AlAs) transitions in some samples. The observed energies of both Γ–Γand Γ–X transitions are in good agreement with the proposed theoretical model using an X-band effective mass of $0.4\,m_o$.

1 Introduction

High-performance quantum well infrared photodetectors (QWIPs) based on $GaAs/Al_yGa_{(1-y)}As$ grown on GaAs substrates have been exploited to operate in the long-wavelength atmospheric window at 8–12 μm [1, 2]. Another atmospheric window of great interest for the detection of gases such as CO, CO_2 and CH_4 is 3–5 μm. Here many gases exhibit well-resolved vibrational absorption bands [3]. However, the detection wavelength for $GaAs/Al_yGa_{(1-y)}As$ materials has a lower limit of 5.6 μm [4] due to the need to keep the $Al_yGa_{(1-y)}As$ barriers direct. This short-wavelength limit is imposed by the (Γ–X) band-crossing in $Al_yGa_{(1-y)}As$ at $y > 0.45$ [5]. Beyond this band-crossing, the minimum energy for thermal emission from the well decreases, which can lead to an increase in the device dark current [4]. In addition, the Γ–X scattering in the $Al_yGa_{(1-y)}As$ barrier can trap photoexcited electrons in the X-band thereby resulting in inefficient carrier collection and degradation of the detector efficiency. Nevertheless, the mature epitaxial growth and processing technology of GaAs-based materials leads to high growth uniformity and excellent reproducibility. Thus despite the problems associated with indirect barriers, it may still be desirable to use $GaAs/Al_yGa_{(1-y)}As$ intersubband detectors in this wavelength region. Thin indirect AlAs barriers (with thicker outer barriers of direct AlGaAs) in combination with GaAs or strained InGaAs wells have been shown to be effective in enhancing the responsivity of 3–5 μm intersubband transitions (ISBTs) [6, 7]. The AlAs barriers offer strong carrier confinement and if they are kept below about 3 nm the effects of Γ–X scattering can be avoided [6]. Dark current is determined predominantly by the wider direct AlGaAs barriers.

In n-type square QWs, quantum mechanical selection rules imply that ISBT can only be induced when the incident radiation has a component of the electric field vector perpendicular to the plane of the wells. Therefore, they are unable to detect normal incidence radiation. On the other hand, stepped QWs have been shown to relax this polarisation rule [8, 9]. Stepped wells also offer the option of greater wavelength tunability due to the larger quantum confined Stark effect than found for square wells [10].

We have previously reported the enhancement of intersubband absorption in the conduction band of a $GaAs/In_xGa_{(1-x)}As$ double barrier stepped quantum well structure at the Brewster angle [11]. Here, we present a comparative study of the intersubband absorption in several DBQW structures: (*a*) square GaAs QWs (1546 and 1551), (*b*) a strained $In_{0.2}Ga_{0.8}As$ QW (1547), and (*c*) a stepped $In_{0.25}Ga_{0.75}As/GaAs$ QW (1557). All samples were measured in the 45° waveguide geometry.

2 *k.p* model

Modelling of the quantum well subband energy levels was carried out using the envelope function approximation [12] in which the energy states are described using a three-band Kane ***k.p*** model [13] that takes into account the effect of band non-parabolicity and strain. The band offset ratio $\Delta E_C/\Delta E_V$ was taken as 0.65:0.35 [7]. The input material parameters to the model are listed in Table 1. The model was used to design a series of structures, each with an $n = 1$ to $n = 2$ transition at about 3.6 μm, and to ascertain that all the samples have the same number of states in the well (three). As an example, Fig. 1 shows the modelled conduction band edge potential profile of the stepped well (1557). The X-energy levels shown in this diagram were calculated using an average X-valley electron effective mass of $0.4\,m_o$. This value was chosen as it consistently gave the best fit to experimentally observed transitions reported in the literature involving *X*-states in AlAs layers of similar

IEE Proceedings online no. 20030409

doi: 10.1049/ip-opt:20030409

Paper first received 15th October 2002 and in revised form 5th February 2003

K.T. Lai, S.K. Haywood and R. Gupta are with the Department of Engineering, University of Hull, Cottingham Road, Hull HU6 7RX, UK

M. Missous is with the Department of Electronic & Electrical Engineering, UMIST, PO Box 88, Manchester M60 1QD, UK

Table 1: Parameters used for modelling

Parameters	Symbol	Unit	GaAs	InAs	AlAs
Lattice constant	a_0	Å	5.6533 [14]	6.0584 [15]	5.6611 [14]
Elastic stiffness constant	C_{11}	10^{11} dyn/cm^2	11.88 [14]	8.329 [15]	12.02 [14]
Elastic stiffness constant	C_{12}	10^{11} dyn/cm^2	5.38 [14]	4.526 [15]	5.70 [14]
Spin orbit splitting	*Delta*	eV	0.34 [17]	0.38 [17]	0.28 [17]
Shear deformation potential	*b*	eV	−1.7 [14]	−1.8 [15]	−1.5 [14]
Hydrostatic deformation potential	*agap*	eV	−8.233 [17]	−6.08 [17]	−8.11 [17]
Luttinger parameter	*g*1		6.95 [16]	20.40 [16]	3.45 [16]
Luttinger parameter	*g*2		2.25 [16]	8.30 [16]	0.68 [16]
Electron effective mass	m_e/m_o		0.067 [16]	0.0239 [16]	0.15 [16]
Static dielectric constants	*eperm*		13.18 [14]	14.6 [15]	10.06 [14]

Parameter	Symbol	Unit	$Al_YGa_{1-Y}As$	$In_{1-x}Ga_xAs$
Bandgap energy (300 K)	E_g	eV	$1.424 + 1.247y$ $(0 < y < 0.45)$ [19] $1.424 + 1.247y + 1.147(y - 0.45)^2$ $(0.45 < y < 1.0)$ [19]	$(0.324 + 0.7x + 0.4x^2)$ [18]

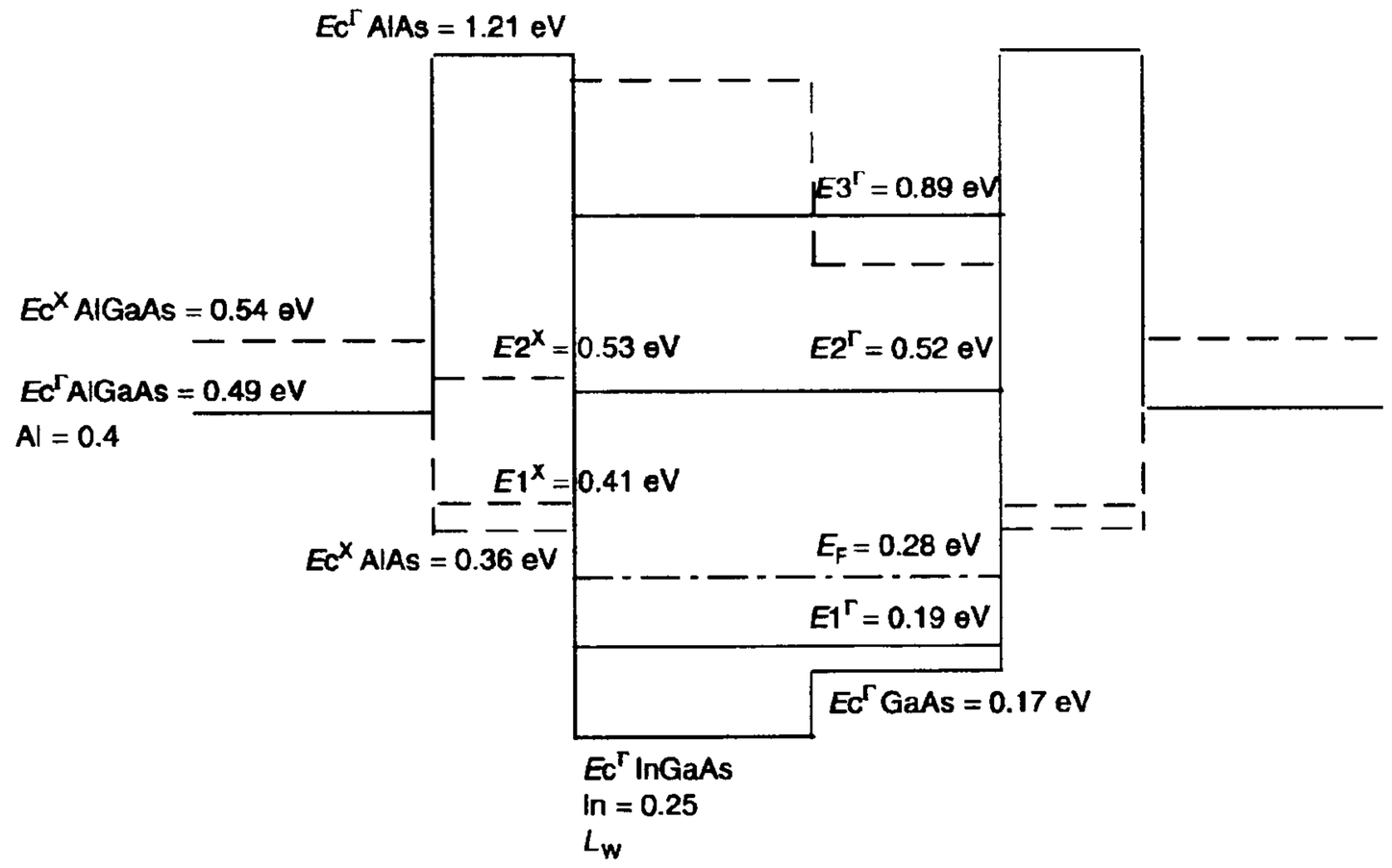

Fig. 1 *Modelled conduction band edge profile for Γ (solid line) and X (dashed line) of sample 1557*

thickness to those used in our structures [20, 21]. Table 2 shows $E1^\Gamma - E2^\Gamma$ and $E1^\Gamma - E2^X$ transition energies modelled for all four samples discussed in this paper.

3 Experiment

The samples were grown by molecular beam epitaxy on (100) semi-insulating GaAs substrates in a VG Semicon V90H reactor with four inch substrate growth capability. We used near stoichiometric growth conditions [22] at low temperatures (~520 °C) to achieve the high optical quality evidenced by efficient room temperature photoluminescence from all the samples. Figure 2 shows the generic growth sequence for the four samples and Table 2 contains the individual sample growth parameters.

The sample end faces were polished at 45° to facilitate the coupling of light in and out of the waveguide. The room temperature intersubband absorption was measured using a Bio-Rad FTS-3000 Fourier transform infrared spectrometer with a cooled mercury cadmium telluride detector.

Table 2: Sample parameters, measured and modelled transition energies

Sample	Indium content (*x*)	QW thickness (L_W), Å	QW sheet carrier density (N_S), $\times 10^{11}$ cm^{-2}	Measured absorption peaks $E1^\Gamma - E2^\Gamma$ [$E1^\Gamma - E2^X$], μm	Modelled absorption peaks $E1^\Gamma - E2^\Gamma$ [$E1^\Gamma - E2^X$], μm
1546	0	45	7.65	3.63	3.85 [5.37]
1547	0.2	45	7.65	3.60 [3.30]	3.79 [3.40]
1551	0	45	38.25	3.63	3.85 [5.37]
1557	0.25	24 + 24 (stepped)	20.40	3.70 [3.37]	3.84 [3.66]

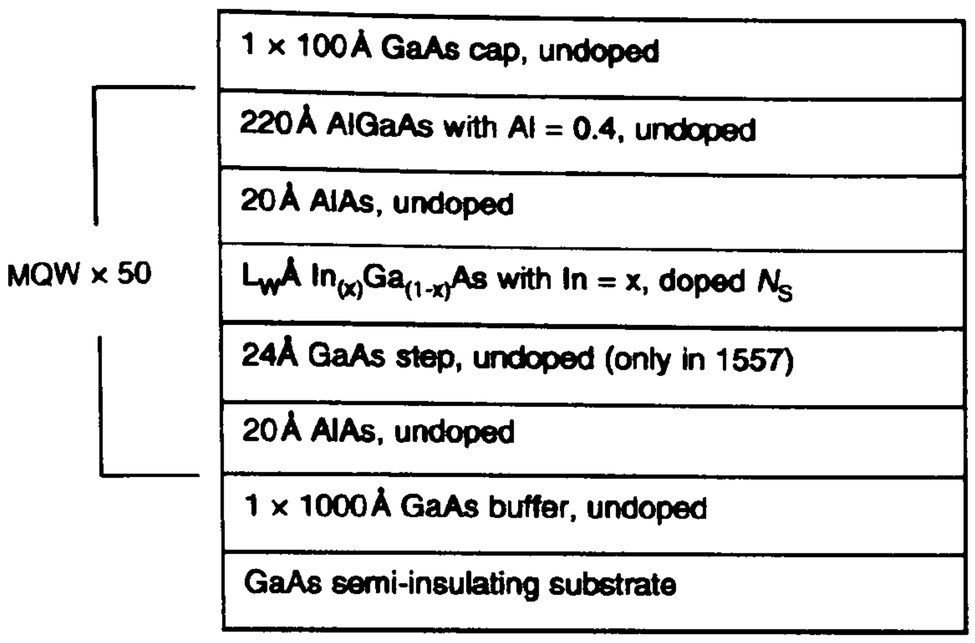

Fig. 2 *Generic sample structure*

Values of L_W and N_S for each sample are as shown in Table 2

The resolution was chosen to be $8\,cm^{-1}$. A ZnSe wire grid polariser was used to resolve the incident infrared light into components with electric field vector perpendicular (intersubband allowed) or parallel (intersubband forbidden) to the plane of the QWs.

4 Results and discussion

Figure 3 shows the wavelength dependence of the intersubband absorption for the four samples measured in the allowed polarisation. All samples are expected to exhibit $E1^{\Gamma}-E2^{\Gamma}$ well transitions. The modelled values for these transitions are listed in Table 2 alongside the measured peak wavelengths. These are in good agreement with each other. A Lorentzian lineshape fit of the absorption spectra gives the full width at half maximum (FWHM) for samples 1546, 1547, 1551, and 1557 as 54 meV, 40 meV, 60 meV and 26 meV respectively. The scattering of electrons from impurities in the well contributes to absorption broadening. Consequently, the more highly doped GaAs sample 1551 shows a larger FWHM than 1546 (see Table 2). The large values of FWHM for sample 1546 and 1551, relative to 1547 and 1557, may be attributed to interface roughness associated with the lower than optimum GaAs growth temperature for these QWs [7, 23]. Samples 1547 and 1557, on the other hand, are grown at the optimum temperature for the InGaAs layers and hence exhibit lower FWHM [23].

The ratio of integrated absorption intensities (I_{abs}) of the $\Gamma-\Gamma$ transition for samples 1551 and 1557 is 157:64. Since the corresponding carrier densities for the two samples are $38.25\times10^{11}\,cm^{-2}$ and $20.40\times10^{11}\,cm^{-2}$ respectively, the ratio I_{abs}/N_S is about the same for both samples. This occurs despite the fact that a reduction in the oscillator strength might be expected for this transition in 1557 as other normally forbidden transitions become allowed [8, 9].

In order to explore a possible relaxation of the polarisation selection rules, transmission spectra for three of the samples in Table 2 were taken in the perpendicular and parallel polarisations; these are presented in Fig. 4. For our experimental set-up, perpendicular polarisation corresponds to the allowed geometry for $\Gamma-\Gamma$ ISBTs. In Fig. 4*a* (1546), only one peak, due to the $E1^{\Gamma}-E2^{\Gamma}$ transition, is observed in the allowed polarisation (peak B). As expected, this is not present in the forbidden geometry. In Fig. 4*b* (1547), two peaks are observed in the perpendicular polarisation (A and B). Again peak B is not observed in the parallel geometry and it is attributed to $E1^{\Gamma}-E2^{\Gamma}$.

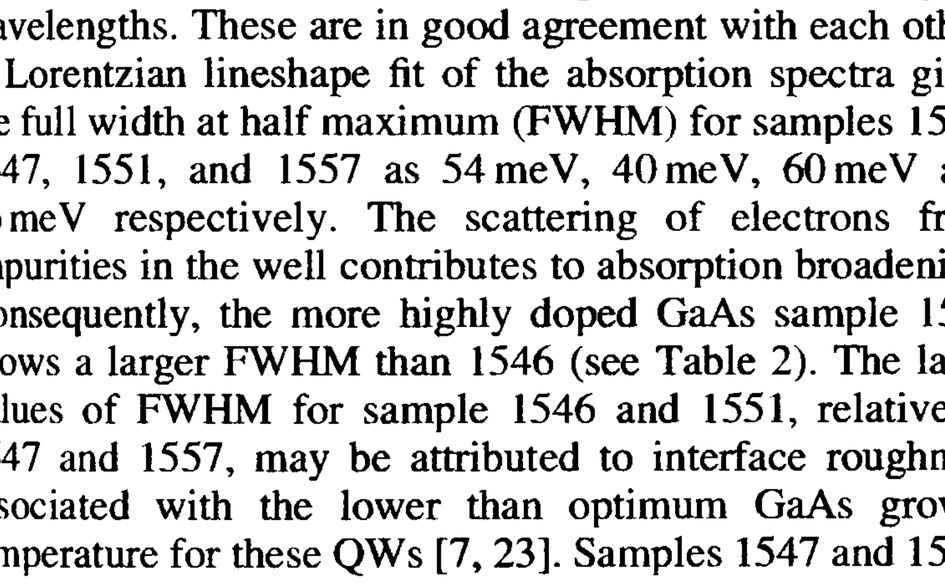

Fig. 3 *Absorption spectra at 300 K for samples 1546, 1547, 1551, and 1557 in the 45° waveguide geometry for which $\Gamma-\Gamma$ transitions are allowed*

The curves are offset for clarity

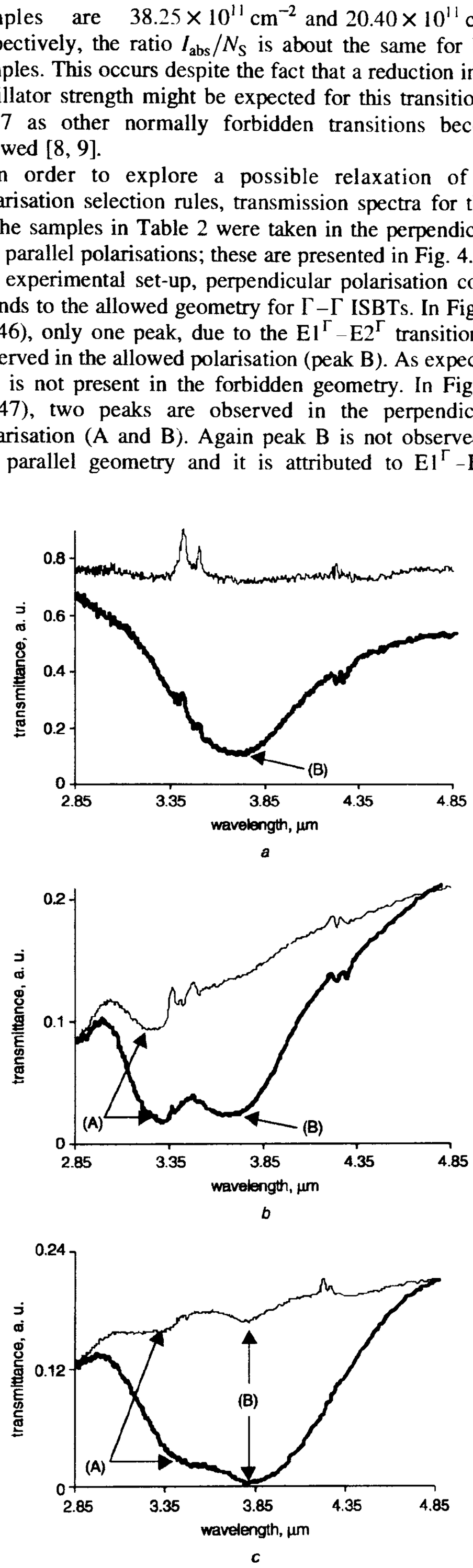

Fig. 4 *Transmission spectra of samples 1546, 1547 and 1557 measured using light polarised with the electric field vector parallel (fine line) or perpendicular (dark line) to the plane of the QWs at 300 K*

The features at ~3.35 μm and ~4.25 μm are due to atmospheric absorption

Peak A is seen in both polarisations and we attribute this peak to an $E1^{\Gamma}-E2^{X}$ transition (Table 2). In Fig. 4*c*, the stepped well (1557), both peaks A and B are observed at both polarisations. Again from our modelling, we attribute peak A to the $E1^{\Gamma}-E2^{X}$ transition and peak B to the $E1^{\Gamma}-E2^{\Gamma}$ transition. The observation of peak B in the parallel polarisation indicates a degree of relaxation of the intersubband selection rules due to the asymmetric QWs. Scattering from the mesa edge [24] is discounted as the reason for observing $\Gamma-\Gamma$ absorption at the forbidden polarisation in the stepped well, since all the samples were processed in the same manner.

Returning to the assignment of peak A in Figs. 4*b* and 4*c*, the band diagram of 1557 (Fig. 1) suggests two possibilities for the origin of this peak. The $E2^{\Gamma}-E3^{\Gamma}$ and the $E1^{\Gamma}$ (well)$-E2^{X}$(AlAs) transitions are both close to the energy of peak A; this is also true for sample 1547. However, observation of the $E2^{\Gamma}-E3^{\Gamma}$ transition requires population of the $E2^{\Gamma}$ level, which in turn would require a carrier concentration much higher than expected (see Table 2). $\Gamma-X$ transitions usually have an oscillator strength considerably smaller than $\Gamma-\Gamma$ transitions and hence are not expected to be observed. However, it has been suggested that in the growth direction the breaking of translational symmetry leads to $\Gamma-X_z$ mixing and to a lesser extent to $\Gamma-X_{xy}$ mixing and hence to enhanced oscillator strength [21, 25]. Observation of peak A in the dipole forbidden geometry (Figs. 4*b* and 4*c*) is also consistent with its attribution to $E1^{\Gamma}$ (well)$-E2^{X}$(AlAs) transitions [26]. Nevertheless it is surprising that this peak is of comparable strength to the $\Gamma-\Gamma$ transitions.

5 Conclusions

We have observed absorption in the forbidden polarisation and a narrowing of the linewidth in GaAs-based double-barrier quantum well structures upon introduction of an additional InGaAs layer into the well. This occurred despite an expected reduction in the oscillator strength for this transition as other normally forbidden transitions become allowed. The observation is attributed to relaxation of the polarisation selection rule due to the step in the well. A strong and narrow $E1^{\Gamma}$(well)$-E2^{X}$(AlAs). transition was also observed in both the stepped well (1557) and the InGaAs square well (1547), giving the option for dual wavelength operation in these structures. The modelled and measured peak wavelengths for both the $\Gamma-\Gamma$ and $\Gamma-X$ ISBTs are in good agreement using a band offset ratio $\Delta E_C/\Delta E_V$ of 0.65:0.35 and an average X-valley electron effective mass of $0.4\,m_o$.

6 References

1 Manasreh, M.O.: 'Semiconductor quantum wells and superlattices for long wavelength infrared detections' (Artech House, Boston, 1993)
2 Levine, B.F.: 'Quantum-well infrared photodetectors', *J. Appl. Phys.*, 1993, **74**, (8), pp. R1–R81
3 Lenchyshyn, L.C., Liu, H.C., Buchanan, M., and Wasilewski, Z.R.: 'Mid-wavelength infrared detection with $In_xGa_{1-x}As/Al_{0.45}Ga_{0.55}As$ multiple quantum well structures', *Semicond. Sci. Technol.*, 1995, **10**, (1), pp. 45–48
4 Levine, B.F., Gunapala, S.D., and Kopf, R.F.: 'Photovoltaic GaAs quantum well infrared detectors at 4.2 μm using indirect Al_xGa_{1-x} barrier', *Appl. Phys. Lett.*, 1991, **58**, (14), pp. 1551–1553
5 Adachi, S.: 'Properties of aluminum gallium arsenide', EMIS Dalare-views series (INSPEC, London, 1993)
6 Liu, H.C., Buchanan, M., and Wasilewski, Z.R.: 'Short wavelength (1–4 μm) infrared detectors using intersubband transitions in GaAs-based quantum wells', *J. Appl. Phys.*, 1998, **83**, (11), pp. 6178–6181
7 Neu, G., Chen, Y., Deparis, C., and Massies, J.: 'Improvement of the carrier confinement by double-barrier GaAs/AlAs/(Al,Ga)As quantum well structures', *Appl. Phys. Lett.*, 1991, **58**, (19), pp. 2111–2113
8 Yuan, Z.Y., Chen, Z.H., Cui, D.F., Ma, J.W., Hu, Q., Zhou, J.M., and Zhou, Y.L.: 'Normal incidence photoresponse in GaAs/AlGaAs quantum well infrared photodetector', *Appl. Phys. Lett.*, 1995, **67**, (7), pp. 930–931
9 Mii, Y.J., Wang, K.L., Karunasiri, R.P.G., and Yuh, P.F.: 'Observation of large oscillator strengths for both 1-2 and 1-3 intersubband transitions of step quantum well', *Appl. Phys. Lett.*, 1990, **56**, (11), pp. 1046–1048
10 Martinet, E., Luc, F., Rosencher, E., Bois, P.H., and Delaitre, S.: 'Electrical tunability of infrared detectors using compositionally asymmetric GaAs/AlGaAs multiquantum wells', *Appl. Phys. Lett.*, 1992, **60**, (7), pp. 895–897
11 Lai, K.T., Haywood, S.K., Gupta, R., and Missous, M.: 'Enhanced intersubband absorption in stepped double barrier quantum wells', *Electron. Lett.*, 2002, **38**, (11), pp. 529–530
12 Bastard, G., and Brum, J.A.: 'Electronic states in semiconductor heterostructures', *IEEE J. Quantum Electron.*, 1986, **QE-22**, (9), pp. 1625–1644
13 Stavrinou, P.N.: 'A study of InP based strained layer heterostructures', PhD dissertation, Department of Electronic and Electrical Engineering, University of College London, 1994
14 Adachi, S.: 'GaAs, AlAs and $Al_xGa_{1-x}As$: material parameters for use in research and device applications', *J. Appl. Phys.*, 1985, **58**, (3), pp. R1–R29
15 Adachi, S.: 'Material parameters of $In_{1-x}Ga_xAs_yP_{1-y}$ and related binaries', *J. Appl. Phys.*, 1982, **53**, (12), pp. 8775–8792
16 Ishikawa, T., and Bowers, J.E.: 'Band lineup and in-plane effective mass of InGaAsP on InP strained-layer quantum well', *IEEE J. Quantum Electron.*, 1994, **30**, (2), pp. 562–569
17 Jensen, J.R., Hvam, J.M., and Langbein, W.: 'Optical properties of InAlGaAs quantum wells: influence of segregation and band bowing', *J. Appl. Phys.*, 1999, **86**, (5), pp. 2584–2589
18 Madelung, O., Schulz, M., Von Der Osten, W., and Rössler, U.: 'Landort-Bornstein, numerical data and functional relationships in science and technology (New Series III)', vol. 22a, Semiconductors (Springer, Berlin, 1987)
19 Hiroshima, T., and Nishi, K.: 'Quantum-confined stark effect in graded-gap quantum wells', *J. Appl. Phys.*, 1987, **62**, (5), pp. 3360–3364
20 Katz, J., Zhang, Y., and Wang, W.I.: 'Normal incidence infrared absorption in AlAs/AlGaAs x-valley multiquantum wells', *Appl. Phys. Lett.*, 1992, **61**, (14), pp. 1697–1699
21 Liu, H.C., Wilson, P.H., Lamm, M., Steele, A.G., Wasilewski, Z.R., and Li, J.M.: 'Low dark current dual band infrared photodetector using thin AlAs barriers and Γ-X mixed intersubband transitions in GaAs quantum wells', *Appl. Phys. Lett.*, 1994, **64**, (4), pp. 475–477
22 Missous, M.: 'Stoichiometric low-temperature GaAs and AlGaAs: A reflection high-energy electron-diffraction study', *J. Appl. Phys.*, 1995, **78**, (7), pp. 4467–4471
23 Zhang, D.H., and Shi, W.: 'Dark current and infrared absorption of p-doped InGaAs/AlGaAs strained quantum wells', *Appl. Phys. Lett.*, 1998, **73**, (8), pp. 1095–1097
24 Cheah, C.W., Karunasiri, G., Tan, L.S., and Zhou, L.F.: 'Responsitivities of n-type GaAs/InGaAs/AlGaAs step multiple-quantum-well infrared detectors', *Appl. Phys. Lett.*, 2002, **80**, (1), pp. 145–147
25 Teissier, R., Finley, J.J., Skolnick, M.S., Cockburn, J.W., Pelouard, J.-L., Grey, R., Hill, G., Pate, M.A., and Planel, R.: 'Experimental determination of Γ-X intervalley transfer mechanisms in GaAs/AlAs heterostructures', *Phys. Rev. B.*, 1996, **54**, (12), pp. R8329–R8332
26 Fenigstein, A., Finkman, E., Bahir, G., and Schacham, S.E.: 'X–Γ indirect intersubband transitions in type II GaAs/AlAs superlattices', *Appl. Phys. Lett.*, 1996, **69**, (12), pp. 1758–1760

Intersubband absorption in strain-compensated InAlAs/AlAs/$In_xGa_{(1-x)}As$ ($x\sim0.8$) quantum wells grown on InP

K. T. Lai[a)]
Department of Engineering, University of Hull, Cottingham Road, Hull, HU6 7RX, United Kingdom

M. Missous
Department of Electrical Engineering & Electronics, UMIST, Sackville Street, Manchester M60 1QD, United Kingdom

R. Gupta and S. K. Haywood
Department of Engineering, University of Hull, Cottingham Road, Hull, HU6 7RX, United Kingdom

(Received 17 October 2002; accepted 17 February 2003)

We report the observation of strong room temperature absorption peaks between 4 and 7 μm in strain-compensated $In_{0.84}Ga_{0.16}As/AlAs/In_{0.52}Al_{0.48}As$ double-barrier multiple-quantum-well structures. The observed peaks at 4.4, 5.0, and 7.2 μm are attributed to $E_3\rightarrow E_4$, $E_2\rightarrow E_3$, and $E_1\rightarrow E_2$ Γ-Γ electron intersubband transitions, respectively, the transition energies are in good agreement with our theoretical model. The large conduction band offset and low effective mass in this material system, as well as the possibility for strain compensation between wells and barriers, make this a promising route to efficient room temperature quantum well infrared photodetectors. © *2003 American Institute of Physics.* [DOI: 10.1063/1.1565688]

Quantum well infrared photodetectors (QWIPs) based on lattice-matched GaAs/AlGaAs multiple quantum wells (MQW's) have been widely used for detection of 8–14 μm infrared radiation.[1] However, it would be difficult to obtain wavelengths shorter than 6 μm for this material system since the maximum direct conduction band offset[2] for GaAs/$Al_xGa_{1-x}As$ ($x=0.45$) is $\Delta E_C\approx350$ meV. When $Al_xGa_{1-x}As$ becomes indirect,[3] the energy for thermally activated emission of carriers from the well is reduced, and this can result in a higher dark current leading to poor temperature performance of the photodetector.[4] In order to design QWIPs operating at wavelengths shorter than 6 μm, it is necessary to choose material systems having a larger ΔE_c. Several routes have been used to achieve an increased ΔE_c and thus operation at shorter wavelengths. Incorporating indium in the GaAs well while retaining AlGaAs barriers and GaAs substrates can take ΔE_c to about 500 meV (for InGaAs with 20% In).[5] However, the resultant compressive strain introduced into the well limits the indium content and the number of periods that can be used with this approach. The heterostructure $In_{0.53}Ga_{0.47}As/In_{0.52}Al_{0.48}As$, lattice-matched to InP, also has a $\Delta E_C=500$ meV, making it suitable for detection below 6 μm.[6] A 3.4 μm photodetector operating at 205 K has been demonstrated in this material system.[7] Reference 7 illustrates a further advantage of large ΔE_C, i.e., that the energy levels involved in the optical transition can be positioned to minimize the dark current and therefore maximize the operating temperature.

Using InGaAs/AlInAs, still larger ΔE_C may be achieved by increasing the In and Al mole fractions in the well and barrier, respectively. However, again this will result in internal strain in the MQW system due to the lattice mismatch. To avoid dislocations and degradation of crystal quality, the total strain must be kept below a critical value. In this article, we demonstrate a method of achieving this using strain compensation. The compressively strained $In_xGa_{1-x}As$ wells ($x\sim0.84$) are placed between thin tensile-strained AlAs inner barriers followed by thicker outer $In_{0.52}Al_{0.48}As$ barriers lattice-matched to the InP substrate. The widths of the well and the AlAs barriers are chosen so that the opposing strain in these layers approximately cancels out (strain compensation). The conduction band discontinuity between $In_{0.52}AsAl_{0.48}As$ and $In_{0.84}Ga_{0.16}As$ is calculated to be 0.675 eV (using a band offset ratio[6] $\Delta E_C/\Delta E_V$ of 0.70:0.30), which should offer the possibility of excellent high temperature performance. Room temperature absorption spectra showed several peaks which were shown to originate from intersubband transitions in the conduction band of the InGaAs well.

The sample used in this study (1554) was grown by molecular beam epitaxy on an InP substrate at a growth temperature of ~420 °C, using conditions of exact stoichiometry.[8] This condition leads to high quality Al containing compounds even at low temperatures. The structure of 1554 is depicted in Fig. 1. It consists of 15 QW periods, where each period is made up of a 2.3 nm AlAs barrier (undoped), an 8.0 nm $In_{0.84}Ga_{0.16}As$ well (doped with Si to 8.0×10^{18} cm^{-3}), another 2.3 nm undoped AlAs barrier, and a 22 nm undoped $In_{0.52}Al_{0.48}As$ thick outer barrier. The MQW structure was capped with 10 nm undoped $In_{0.53}Ga_{0.47}As$ and grown on a 50 nm buffer layer of undoped $In_{0.52}Al_{0.48}As$. The tensile AlAs layers have a strain of −3.56% relative to the substrate, while the compressively strained $In_{0.84}Ga_{0.16}As$ QWs have a strain of +2.12%. The "strain number" [defined here as relative strain (%) × thickness (nm)] is then 0.0584, i.e., slightly tensile but close to

a)Electronic mail: k.t.lai@hull.ac.uk

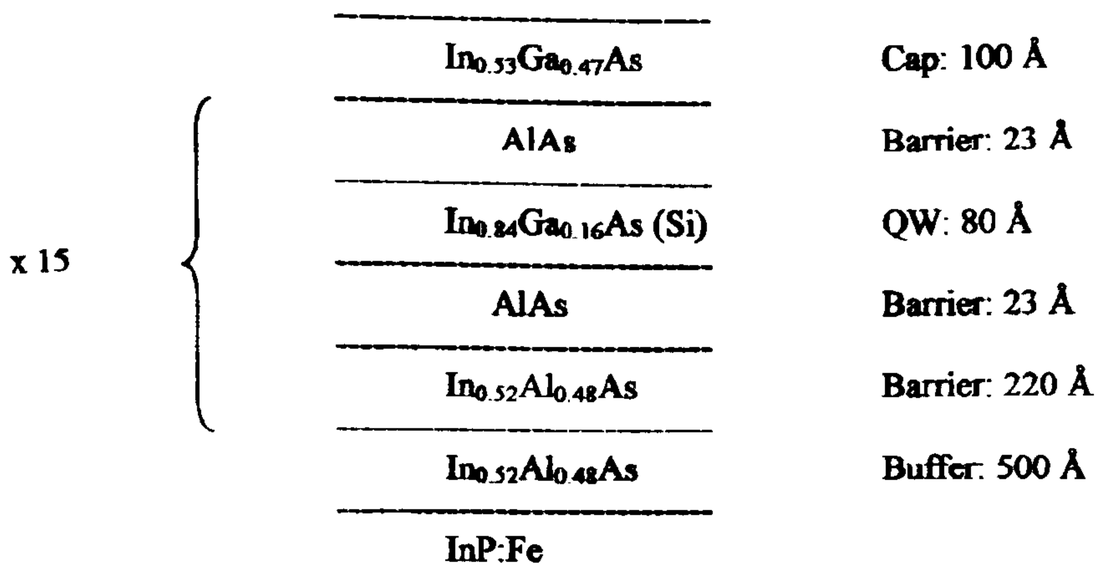

FIG. 1. Growth profile for sample 1554.

achieving strain balance. The thickness and alloy composition values of the sample were confirmed by double-crystal x-ray diffraction as can be seen from the experimental and simulated diffraction spectra shown in Fig. 2. The high structural integrity of the sample is also demonstrated by the sharp and intense satellite peaks. An electron mobility of 2000 $cm^2/V\,s$ was obtained from room temperature Hall measurements indicative of high quality interfaces between well and barrier layers. From the Hall measurement, the sheet electron density was inferred to be 1.1×10^{13} cm^{-2} per well.

The room temperature absorption measurements were performed in a Bio-Rad FTS-3000 Fourier transform infrared spectrometer using a cooled mercury cadmium telluride detector. A resolution of 8 cm^{-1} was chosen and the number of scans was set to 1000. A ZnSe wire grid polarizer was used to resolve the incident IR light into components with the electric field vector either perpendicular (intersubband absorption allowed) or parallel (intersubband absorption forbidden) to the plane of the QWs. The sample was processed into a waveguide structure with the edges polished at 45° to enhance coupling of light into the sample.

Figure 3 shows the conduction band profile of one unit of the MQW: $In_{0.52}Al_{0.48}As/AlAs/In_{0.84}Ga_{0.16}As/AlAs/In_{0.52}Al_{0.48}As$. The subband energy levels in the $In_{0.84}Ga_{0.16}As$ well (Γ valley) were obtained by solving a three-band Kane $k\cdot p$ model in the envelope function approximation.[9] The model takes account of band nonparabolicity and strain due to lattice mismatch. The model yields four subband levels, three of them bound below the $Al_{0.48}In_{0.52}As$ conduction band edge and the fourth quasi-bound by the AlAs alone, as shown in Fig. 3. For a sheet electron density of 1.1×10^{13} cm^{-2}, the Fermi energy E_F is calculated to lie between E_3 and E_4.

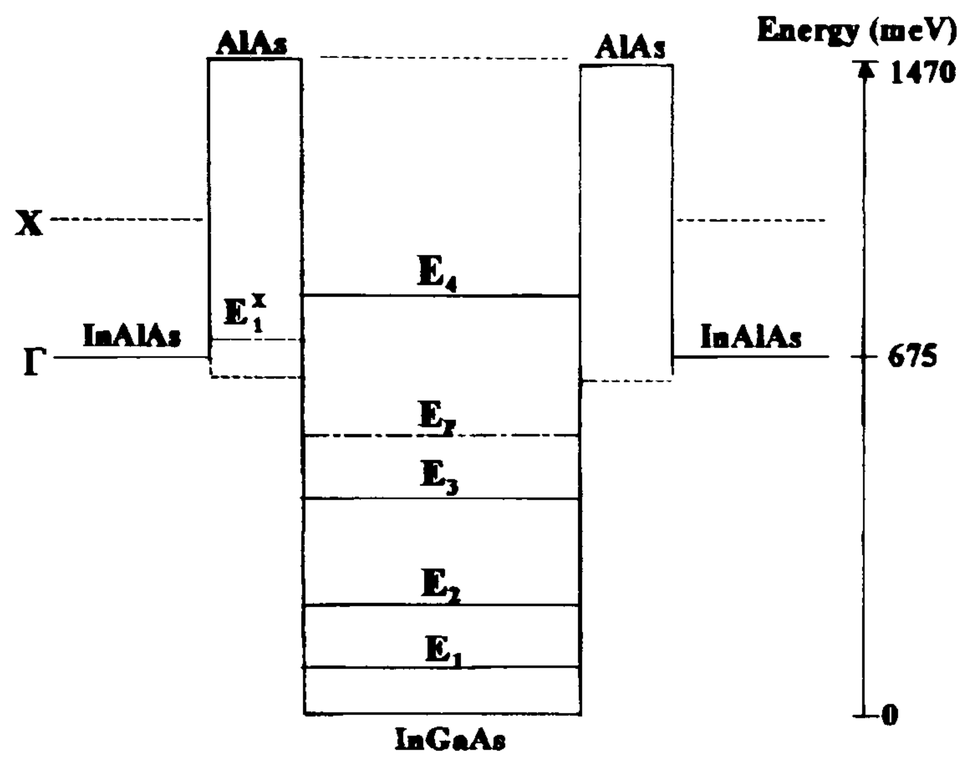

FIG. 3. Modeled conduction band profile of a single period of sample 1554 showing the relative positions of subband energy levels and the Fermi level (not to scale).

Figure 4 shows the transmission spectra of this sample, measured at room temperature, for both incident polarizations. The spectrum for parallel polarization is almost flat apart from the features at ~3.3–3.5 μm and between ~5.5 and 7.5 μm, which are attributed to atmospheric absorption. The spectrum for perpendicular polarization, on the other hand, exhibits three distinct peaks, which are attributed to intersubband transitions in the conduction band of the quantum well. The corresponding absorption spectrum of the sample in the perpendicular polarization is shown in Fig. 5(a). A Lorentzian curve fit is also shown and this has been used to determine the energy and half-widths of the three peaks. The values obtained are $E_{12}=175$ meV, $E_{23}=243$ meV and $E_{34}=277$ meV, with corresponding half-widths of $\Gamma_{12}=15.5$ meV, $\Gamma_{23}=15.2$ meV and $\Gamma_{34}=13.0$ meV. The similar half-widths are as expected for transitions within the

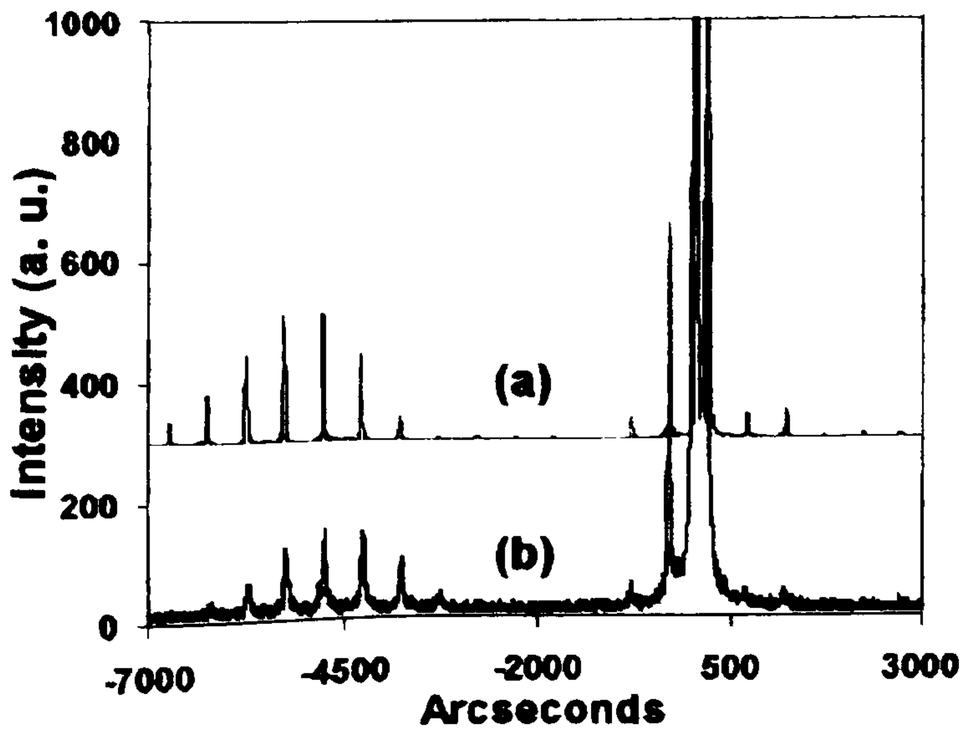

FIG. 2. Double-crystal x-ray diffraction spectra: (a) simulated curve and (b) experimental data.

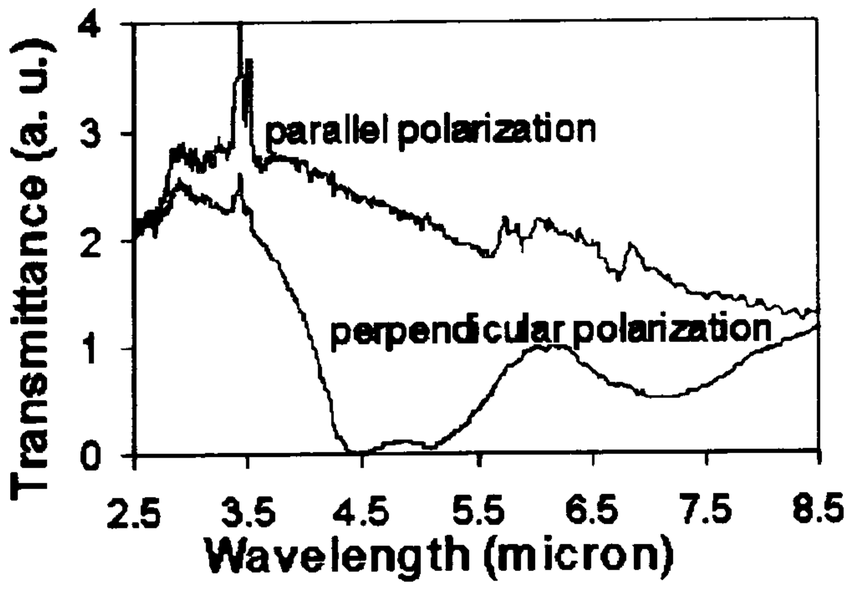

FIG. 4. Measured transmission spectra (ratioed against substrate) at room temperature as a function of wavelength using a 45° waveguide structure. The features at ~3.3–3.5 and ~5.5–7.5 μm are due to atmospheric absorption.

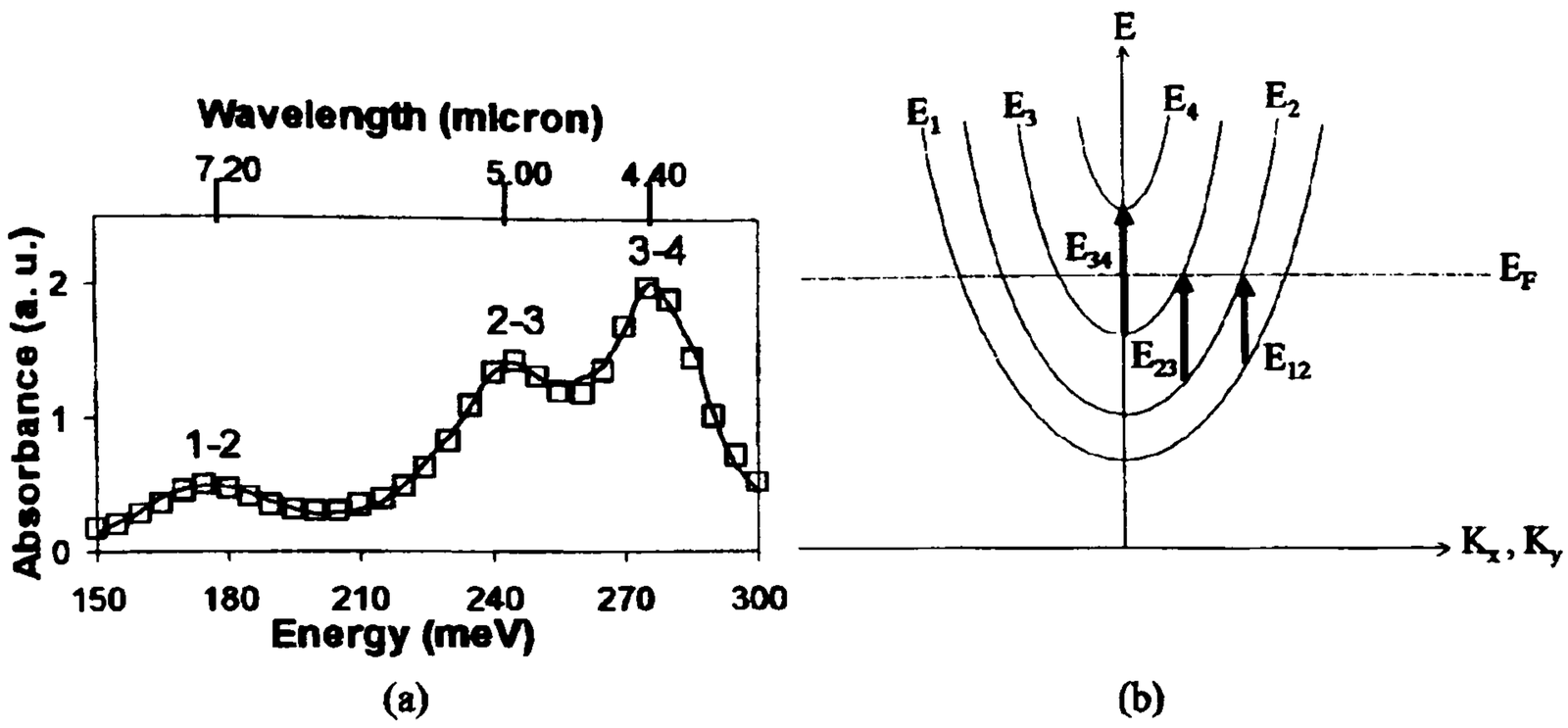

FIG. 5. (a) Measured room temperature absorption spectrum (solid line) and Lorentzian curve fit to the data (-□-). (b) The energy dispersion of the quantized energy levels in the $K_{x,y}$ direction. Arrows indicate the three intersubband energy transitions.

same electronic band. [On the other hand, the absorption bands for intervalley transitions (e.g., Γ-X) are expected to be broader than Γ-Γ transitions due to the different energy dispersions for Γ and X electrons].[10]

Since the E_F is calculated to be between the third and fourth subbands, we expect to observe the three intersubband transitions shown in Fig. 5(b), $E_3 \rightarrow E_4$, $E_2 \rightarrow E_3$, and $E_1 \rightarrow E_2$, only for perpendicular polarization. These transition energies are calculated as $E_3 \rightarrow E_4 = 265$ meV, $E_2 \rightarrow E_3 = 246$ meV, and $E_1 \rightarrow E_2 = 195$ meV, which are in close agreement with the measured values. The sample shows strong absorption comparable to that measured from GaAs double-barrier MQWs (DBMQW's) of similar two-dimensional carrier density and dimensions.[11]

From Fig. 5(a), we observe that $E_3 \rightarrow E_4$ is the strongest of the three absorption peaks with $E_1 \rightarrow E_2$ being the weakest. The normalized transition strengths are 1:0.75:0.27 for $E_3 \rightarrow E_4 : E_2 \rightarrow E_3 : E_1 \rightarrow E_2$. From Fig. 5(b), it is apparent that the intensities of the three absorption peaks are proportional to N_3, $N_2 - N_3$, and $N_1 - N_2$, respectively. Neglecting nonparabolicity, the number of electrons in each subband can be calculated from the equation

$$N_S = N_1 + N_2 + N_3 = \sum_i \frac{m^* k_B T}{\pi \hbar^2} \ln\left[1 + \exp\left(\frac{E_F - E_i}{k_B T}\right)\right] \tag{1}$$

where i is the number of subbands. From this equation and using the total sheet carrier density of 1.1×10^{13} cm^{-2} taken from the Hall measurement, we obtain $N_1 = 5.9 \times 10^{12}$ cm^{-2}, $N_2 = 3.6 \times 10^{12}$ cm^{-2}, and $N_3 = 0.5 \times 10^{12}$ cm^{-2}. Hence, $N_1 - N_2 = 2.3 \times 10^{12}$ cm^{-2}, $N_2 - N_3 = 3.1 \times 10^{12}$ cm^{-2}, and $N_3 = 0.5 \times 10^{12}$ cm^{-2}, which implies that the $E_2 \rightarrow E_3$ transition should be the strongest and $E_3 \rightarrow E_4$ the weakest. This is in contradiction to the experimental observation. To account for the relative intensities of the peaks in the measured absorption spectrum, a higher total sheet carrier density must be assumed. If $N_S = 2 \times 10^{13}$ cm^{-2}, then $N_1 = 9.2 \times 10^{12}$ cm^{-2}, $N_2 = 7.0 \times 10^{12}$ cm^{-2}, and $N_3 = 3.8 \times 10^{12}$ cm^{-2} giving the relative transition strengths of $E_3 \rightarrow E_4 : E_2 \rightarrow E_3 : E_1 \rightarrow E_2$ of 1:0.8:0.6. This at least reproduces the experimentally observed trend. The discrepancy between this value of total sheet carrier density and that obtained from Hall measurements may be partly due to depletion of some of the InGaAs wells as a result of the thin cap and buffer layer used in this structure. This could lead to an underestimation of the sheet carrier density per well by the Hall measurement.

In conclusion, we have observed intense room temperature intersubband absorption in a highly strained (but also strain-compensated) DBMQW structure. The observed peak energies agree well with calculated values for Γ-Γ intersubband transitions in the well, and the similar half-widths confirm this assignment. In order to account for the experimentally observed transition strengths, it was necessary to assume a slightly higher value of sheet carrier concentration ($N_S = 2 \times 10^{13}$ cm^{-2}) than was inferred from the Hall data. The highly favorable band offsets and low effective mass in this material system combined with the inherent strain compensation between wells and barriers make it extremely promising as a route to efficient room temperature short wavelength QWIPs.

[1] B. F. Levine, C. G. Bethea, K. G. Glogovsky, J. W. Stayt, and R. E. Lelbenguth, Semicond. Sci. Technol. **6**, C114 (1991).
[2] R. C. Miller, D. A. Kleinman, and A. C. Gossard, Phys. Rev. B **29**, 7085 (1984).
[3] S. Adachi, J. Appl. Phys. **58**, R1 (1985).
[4] A. Fiore, E. Rosencher, P. Bois, J. Nagle, and N. Laurent, Appl. Phys. Lett. **64**, 478 (1994).
[5] L. C. Lenchyshyn, H. C. Liu, M. Buchanan, and Z. R. Wasilewski, Semicond. Sci. Technol. **10**, 45 (1995).
[6] H. Asai and Y. Kawamura, Appl. Phys. Lett. **56**, 746 (1990).
[7] J. H. Lee, J. C. Chiang, S. S. Li, and P. J. Kannam, Appl. Phys. Lett. **74**, 765 (1999).
[8] M. Missous, J. Appl. Phys. **78**, 4467 (1995).
[9] P. N. Stavrinou, Ph.D. thesis, University College, London, 1994.
[10] S. R. Schmidt, E. A. Zibik, A. Seilmeier, L. E. Vorobjev, A. E. Zhukov, and U. M. Ustinov, Appl. Phys. Lett. **78**, 1261 (2001).
[11] K. T. Lai, S. K. Haywood, R. Gupta, and M. Missous, IEE Proc. Optoelectron. (to be published).

Available online at www.sciencedirect.com
SCIENCE DIRECT®
Physica E 20 (2004) 496–502
PHYSICA E
www.elsevier.com/locate/physe

Highly strained $In_xGa_{(1-x)}As-In_yAl_{(1-y)}As$ ($x > 0.8$, $y < 0.3$) layers for short wavelength QWIP and QCL structures grown by MBE

M. Missous[a,*], C. Mitchell[a], J. Sly[a], K.T. Lai[b], R. Gupta[b], S.K. Haywood[b]

[a] *Department of Electrical Engineering and Electronics, UMIST, Centre for Electronic Materials, P.O. Box 88, Sackville Street, Manchester M60 1QD, England, UK*
[b] *Department of Engineering, University of Hull, Cottingham Road, Hull, HU6 7RX, UK*

Abstract

Highly strained quantum cascade laser (QCL) and quantum well infrared photodetector (QWIPs) structures based on $In_xGa_{(1-x)}As-In_yAl_{(1-y)}As$ ($x > 0.8, y < 0.3$) layers have been grown by molecular beam epitaxy. Conditions of exact stoichiometric growth were used at a temperature of ~420°C to produce structures that are suitable for both emission and detection in the 2–5 μm mid-infrared regime. High structural integrity, as assessed by double crystal X-ray diffraction, room temperature photoluminescence and electrical characteristics were observed. Strong room temperature intersubband absorption in highly tensile strained and strain-compensated $In_{0.84}Ga_{0.16}As/AlAs/In_{0.52}Al_{0.48}As$ double barrier quantum wells grown on InP substrates is demonstrated. Γ–Γ intersubband transitions have been observed across a wide range of the mid-infrared spectrum (2–7 μm) in three structures of differing $In_{0.84}Ga_{0.16}As$ well width (30, 45, and 80 Å). We demonstrate short-wavelength IR, intersubband operation in both detection and emission for application in QC and QWIP structures. By pushing the InGaAs–InAlAs system to its ultimate limit, we have obtained the highest band offsets that are theoretically possible in this system both for the Γ–Γ bands and the Γ–X bands, thereby opening up the way for both high power and high efficiency coupled with short-wavelength operation at *room temperature*. The versatility of this material system and technique in covering a wide range of the infrared spectrum is thus demonstrated.

PACS: 42.72.Ai; 73.40.c; 81.15Hi; 85.35.Be

Keywords: Strained epitaxy; Quantum cascade lasers (QCL); Quantum well infrared photodetectors (QWIP)

1. Introduction

The use of quantum wells (QWs) as infrared detectors and emitters (quantum well infrared photodetectors (QWIP) and quantum cascade laser (QCL) structures) is well documented and has permitted the use of mature technologies such as GaAs and InP to access wavelengths that have traditionally been associated with much smaller band gap semiconductors [1–5]. Indeed, intersubband optical transitions between the quantised energy levels in the QW now forms the basis for a new class of high-speed devices because of the inherent picosecond relaxation times

* Corresponding author. Tel.: +44-161-2004797; fax: +44-161-2004770.
E-mail address: missous@umist.ac.uk (M. Missous).

1386-9477/$ - see front matter © 2003 Elsevier B.V. All rights reserved.
doi:10.1016/j.physe.2003.08.066

associated with the intersubband electronic levels. The accessible wavelength range (both in emission and detection) is dictated by the difference in energies that are available in the QW and most of the applications, by far, have concentrated on GaAs–$Al_xGa_{(1-x)}As$ or lattice matched $In_{0.53}Ga_{0.47}As$–$In_{0.52}Al_{0.48}As$ technologies because of their highly sophisticated growth and processing status. However, this has the disadvantage of limiting the wavelength range from ~5 to 87 μm. The very interesting 2–5 μm range, where both free space optical communications and thermal imaging applications are possible, has been largely left untouched. Suitable detector and source devices that are inexpensive, efficient and compact, as well as tunable and multicolour are not readily available yet. Intersubband transitions in the 2–5 μm region calls for very high band offsets in the conduction band (for electrons), which can only be achieved, in theory, through the use of highly strained $In_xGa_{(1-x)}As$–$In_yAl_{(1-y)}As$ ($x>0.8, y<0.3$) structures [6–8]. When grown on InP, it is possible to tailor the In and Al compositions x and y in such a way that compressive and tensile strain are generated in the well and barrier regions, respectively, and thus strain compensation is possible, especially in QWIP structures. Both QWIP and QCL structures rely on the growth of ultra-thin layers in the build up of their active regions, with the thickness of individual layers rarely exceeding 8 nm and most commonly ranging from 2 to 5 nm. This feature that makes the growth of strained layers a possibility since the critical thickness of even the most highly mismatched pair in the $In_xGa_{(1-x)}As$–$In_yAl_{(1-y)}As$ ($x\sim0.8, y\sim0$) system would still be safely above the 8 nm upper limit. The $In_xGa_{(1-x)}As$–$In_yAl_{(1-y)}As$ ($x\sim0.8, y\sim0$) would also allow access to band gap energies ranging from ~0.36 eV (InAs) to ~2.25 eV (AlAs) and conduction band offsets as high as ~1.5 eV. Note that this energy range is still associated with InP technology and all its advantages such as the existence of a mature and well-defined process technology.

In this paper we will demonstrate that the use of highly strained epitaxial layers in the $In_xGa_{(1-x)}As$–$In_yAl_{(1-y)}As$ ($x>0.8, y<0.3$) system (with total strain in the range ± 2%) does indeed lead to great improvements in both emitter and detector structures by allowing high-efficiency photoluminescence (PL) and absorption operation at room temperature . This is due to the much greater carrier confinements brought about by the high band discontinuities.

2. Quantum cascade structures

The fabrication of such highly strained devices faces two fundamental obstacles. First, efficient absorption or amplification requires not only many periods in the structures but also for these periods to be highly uniform. Second, the many interfaces (typically from 50 to over 500) must all have high perfection, since transport across these interfaces is highly sensitive to structural defects. The QCL is a periodic structure alternating between a short-period superlattice (the Bragg reflector and injector region) and a typical double-well active region in which population inversion is established. The epitaxial layer profile of a typical ~2 μm structure as studied here is shown in Fig. 1. Here we have used $In_{0.84}Ga_{0.16}As$ for the QW for which the compressive strain with respect to InP is 2.12% and $In_{0.30}Al_{0.7}As$ for the barrier for which the tensile strain with respect to InP is −1.52%. The respective unstrained band gaps are 0.495 and 2 eV both direct. Under operating bias carriers flow through a superlattice miniband (layers 10–18) and tunnel into the highest E_2 subband of the double-well active region (layers 4 and 6). Tunnelling out of the E_2 subband is impeded by the minigap of the downstream Bragg reflector and injector region, so the carriers relax by radiative and non-radiative processes down to the E_1 and E_0 subbands, which can tunnel out into the downstream Bragg reflector. The active region parameters are chosen to fix the (E_1–E_0) energy separation close to the optical phonon energy, leading to a much shorter lifetime of the E_1 subband and establishing population inversion and laser action at $\Delta E = (E_2 - E_1)$. To retain overall charge neutrality under bias, the injector is doped to avoid charge domain formation. To enhance the optical power and obtain the lowest threshold current, as many periods as possible are required. However, to reduce the threshold voltage and obtain the minimum power dissipation, as few periods as possible are required. So in practice a compromise between the two is used. Typically, this results in approximately 25 periods but as few as three or even one have been used [9]. The key observation

LayerNo		Thickness(nm)
1.	**$In_{0.3}Al_{0.7}As$**	**4**
2.	$In_{0.84}Ga_{0.16}As$	1
3.	**$In_{0.3}Al_{0.7}As$**	**2.8**
4.	$In_{0.84}Ga_{0.16}As$ QW_1	4.4
5.	**$In_{0.3}Al_{0.7}As$**	**1.9**
6.	$In_{0.84}Ga_{0.16}As$ QW_2	3.8
7.	**$In_{0.3}Al_{0.7}As$**	**1.4**
8.	$In_{0.84}Ga_{0.16}As$	5.06
9.	**$In_{0.3}Al_{0.7}As$**	**.47**
10.	$In_{0.84}Ga_{0.16}As$	2.6
11.	**$In_{0.3}Al_{0.7}As$**	**.53**
12.	$In_{0.84}Ga_{0.16}As$ (doped)	2.5
13.	**$In_{0.3}Al_{0.7}As$**	**.62**
14.	$In_{0.84}Ga_{0.16}As$ (doped)	2.4
15.	**$In_{0.3}Al_{0.7}As$**	.7
16.	$In_{0.84}Ga_{0.16}As$	2.3
17.	**$In_{0.3}Al_{0.7}As$**	.77
18.	$In_{0.84}Ga_{0.16}As$	2.2

Fig. 1. Epitaxial layer profile of a typical 2 μm QCL structure.

to make for such a design is that the sum of all the QW thicknesses is different from the sum of the barrier thicknesses. The "strain number" (defined here as relative strain (%) × thickness (nm)) is 0.356, a net compressive strain per period. This compressive strain will become higher as the number of periods increases. To balance the strain in the system, a decrease in the indium contents to virtually zero would be required. But this would then leave us with indirect band-gap barriers that would have detrimental effects on the QC operation. Thus to keep both well and barrier direct and to access short wavelengths, we have retained these compositions (another way to achieve strain balance is to decrease the indium content in the well, but that would preclude accessing wavelengths $\leqslant 2$ μm). With these constraints in place, a five period $In_{0.84}Ga_{0.16}As-In_{0.3}Al_{0.7}As$ QCL structure was grown by molecular beam epitaxy (MBE) to ascertain the feasibility of fabricating such structures. The MBE growth details have been reported elsewhere [10,11]. As the X-ray diffraction spectrum in Fig. 2(a) shows, there is excellent agreement between the data and the simulated spectrum indicating that it is possible to grow extremely well-defined structures that are able to withstand the large compressive strains.

However, the window for growth is quite limited as Fig. 2(b) demonstrates. Here two identical QCL structure are shown but with the Al contents in the barrier kept at 70% for one and changed to 64% for the other. The X-ray spectrum for the lower Al content sample is very poor. The period can be clearly seen but the crystal integrity is no longer sustained. Concomitant with the X-ray data, very strong PL emission is observed at room temperature from the optimised sample (Fig. 3). A sharp peak at 0.746 eV with a full-width at half-maximum (FWHM) of 42 meV is observed. We assign this transition to the 4.4 nm active QW. No PL signals were observed from the second sample, even at 4 K.

It is clear from the data above that it is possible not only to grow such highly strained structures but also to have both high crystalline integrity and high interface perfection as demonstrated by the strong room temperature photoluminescence (RT PL) emissions. We have also been able to obtain essentially identical data on a 10 period structure with no loss of crystal integrity or RT PL efficiency. Faist et al. [12] and Kohler et al. [13] have reported strained $In_xGa_{(1-x)}As-In_yAl_{(1-y)}As$ QCL structures emitting at 3.4 μm (with $x = 0.7$, $y = 0.4$ and a period of 16) [12] and at 4.6 μm (with $x = 0.62$, $y = 0.4$ and period of 26) [13], respectively. Both structures used designs that are almost strain compensated. However, we believe our structures to be the most strained and thus potentially lead to emission wavelength much shorter than the 3.4 μm reported to date [12].

QC-LED structure with lattice-matched InGaAs spacer and ohmic contacts cladding the highly strained design shown above were then grown and fabricated. A typical IV characteristic at room temperature is shown in Fig. 4. Well-defined IV characteristics are obtained in both forwards and reverse directions. In the latter the observation of strong negative differential resistance (NDR) is evident even at room temperature. Electroluminescence experiments are in

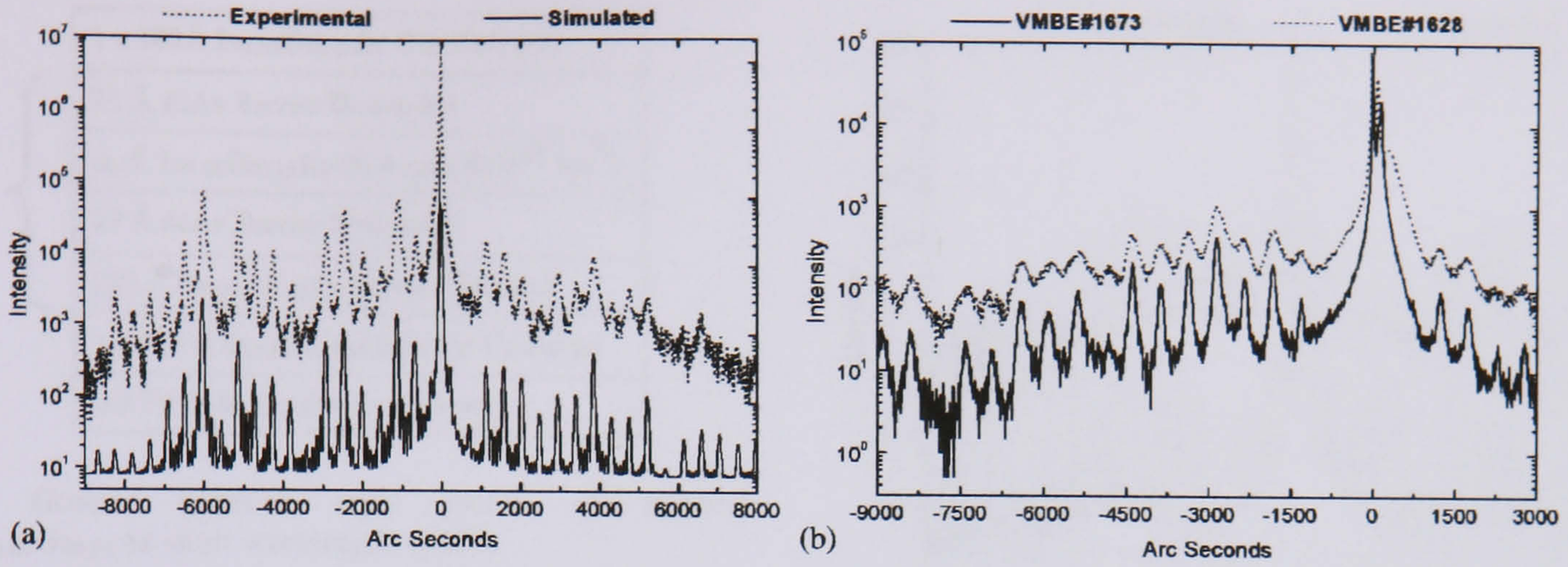

Fig. 2. (a) DCXRD (004) reflection of a five period $In_{0.84}Ga_{0.16}As-In_{0.3}Al_{0.7}As$ QCL structure. Note the excellent fit to the X-ray data. (b) DCXRD (004) reflection of two five period $In_{0.84}Ga_{0.16}As-In_{0.3}Al_{0.7}As$ and $In_{0.84}Ga_{0.16}As-In_{0.35}Al_{0.65}As$ QCL structures. Note the loss of crystal integrity in the second sample.

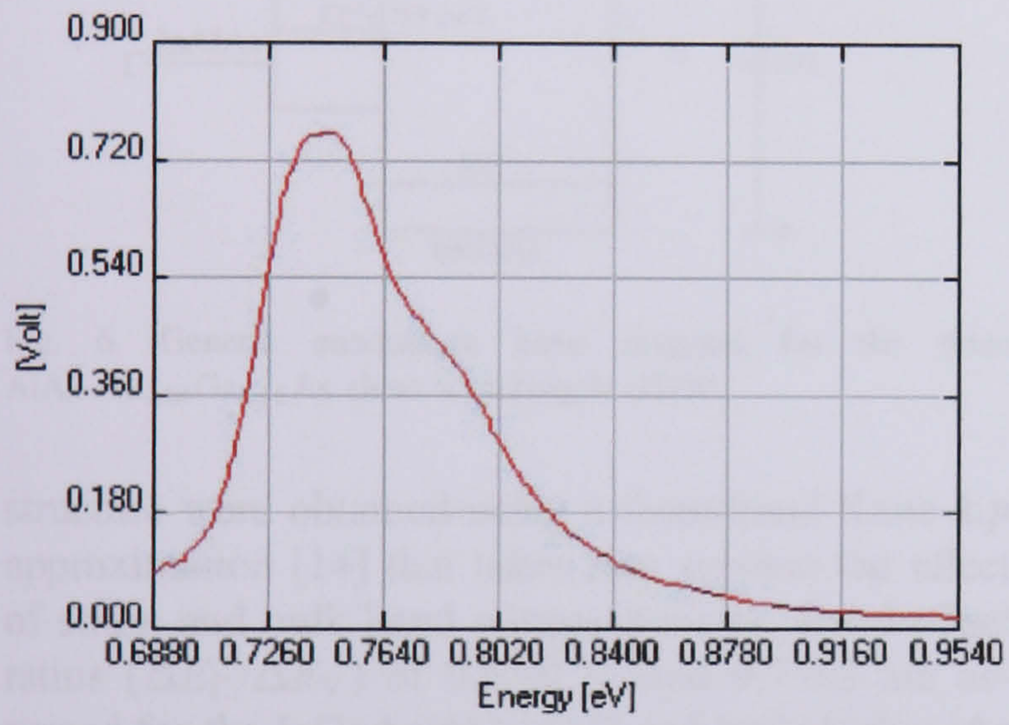

Fig. 3. Room temperature PL of QCL structure shown in Fig. 2(a).

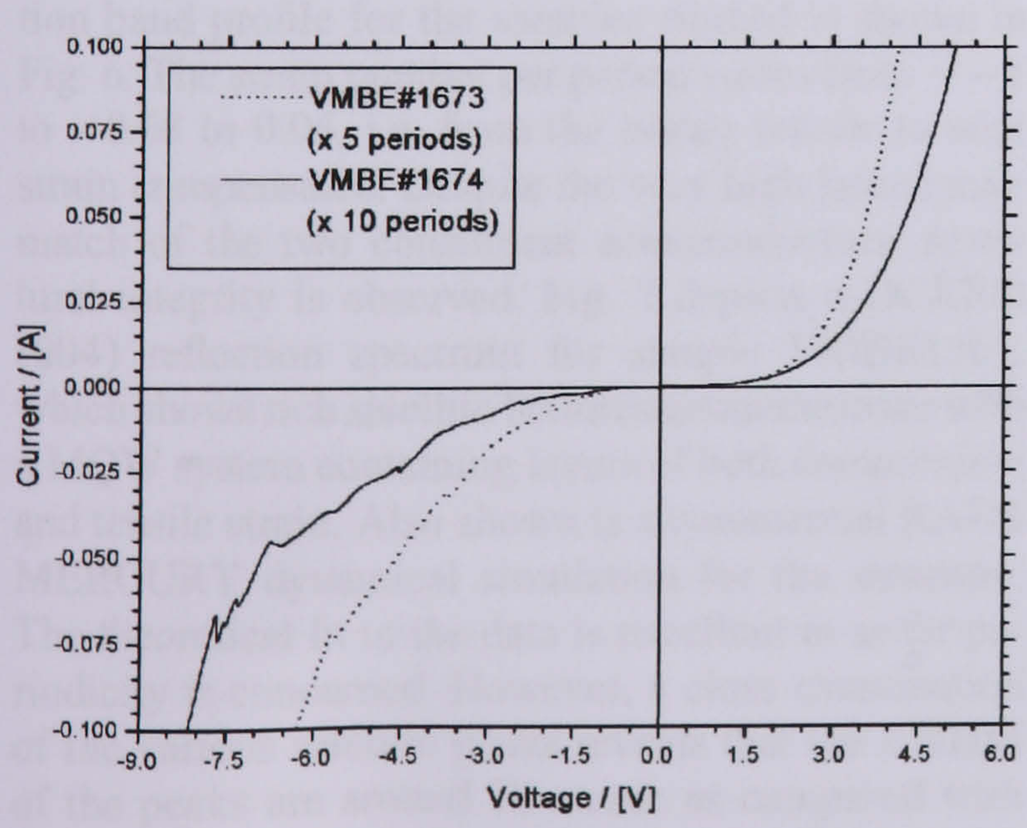

Fig. 4. Room temperature IV characteristics of QC-LED structures with 5 and 10 periods.

progress to determine the emission wavelengths of these structures.

3. Quantum well infrared photodetectors

The main factor limiting high-temperature performance of QWIPs is thermionic emission over the barriers. This can be reduced either by lowering the operating temperature of the detectors (which usually requires fairly bulky and expensive cryo-coolers) or by maximising the barrier height (at the wavelength of operation). As for the QCL structures the large ΔE_C is achieved by increasing the In composition in the InGaAs well to 84% and balancing the high compressive strain with thin tensile-strained AlAs inner barriers [11] followed by a lattice-matched $In_{0.52}Al_{0.48}As$ acting both a strain "relief" layer for the next period and also as the barrier for tunnelling from the QW. With this rationale the structures shown in Fig. 5 were grown. The ΔE_C for these structures is estimated to be ~675 meV with respect to the wide lattice-matched InAlAs barriers and 1.475 eV for the AlAs tensile layers. The samples used in this study were grown by MBE on (100) semi-insulating InP:Fe substrates at a temperature of ~420°C using conditions similar to those reported previously [10,11]. Three structures were studied, which differed only in their well width and therefore the net strain. The well width varied from 3 (Sample VMBE1561) to 4.5 (Sample VMBE1563) to 8 nm (Sample VMBE1554). The conduction band profile and energy levels for the

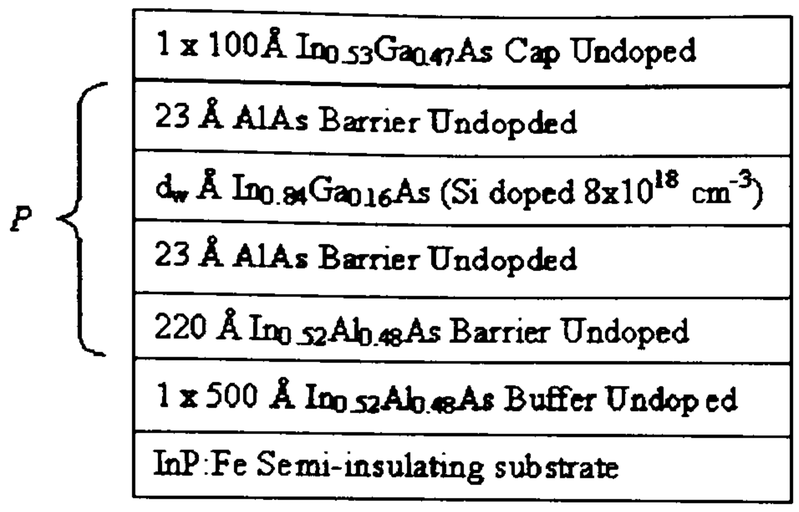

Fig. 5. Generic epitaxial layer profile of strained AlAs–$In_{0.84}Ga_{0.16}As$ short wavelength QWIP.

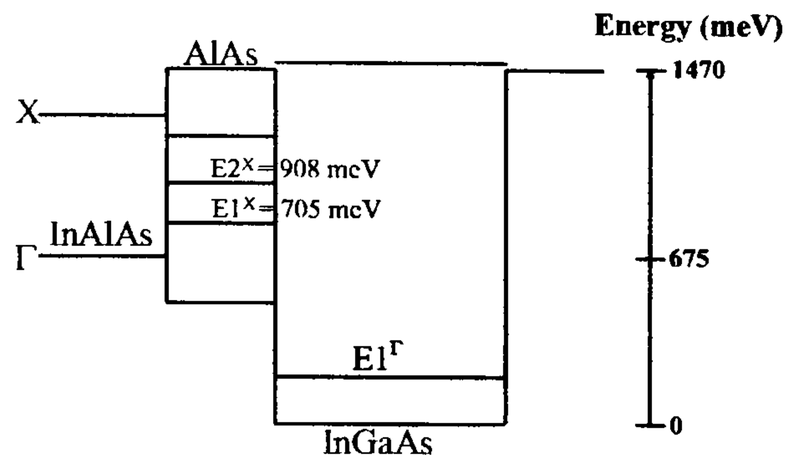

Fig. 6. Generic conduction band diagram for the three AlAs–$In_{0.84}Ga_{0.16}As$ short wavelength QWIP.

structure were obtained using a three-band Kane ***k.p*** approximation [14] that takes into account the effect of strain and bulk band nonparabolicity. Band offset ratios ($\Delta E_C/\Delta E_V$) of 0.65:0.35 and 0.7:0.3 are assumed for the InGaAs/AlAs [15] and InGaAs/InAlAs [16] heterojunctions, respectively. A generic conduction band profile for the samples studied is shown in Fig. 6. The strain number per period varies from ~ -1 to -0.68 to 0.06, i.e. from the highly tensile to near strain compensated. Despite the very high lattice mismatch of the two constituent semiconductors, structural integrity is observed. Fig. 7 depicts a DCXRD (004) reflection spectrum for sample VMBE1561, which shows rich satellite features commensurate with a MQW system containing layers of both compressive and tensile strain. Also shown is a commercial RADS MERCURY dynamical simulation for the structure. The theoretical fit to the data is excellent in as far periodicity is concerned. However, a close examination of the various satellite peaks reveals that the FWHM of the peaks are around 70 arcsec as compared with ~38 arcsec for the strain compensated (VMBE1554) and the less highly tensile wafer (VMBE1563). This

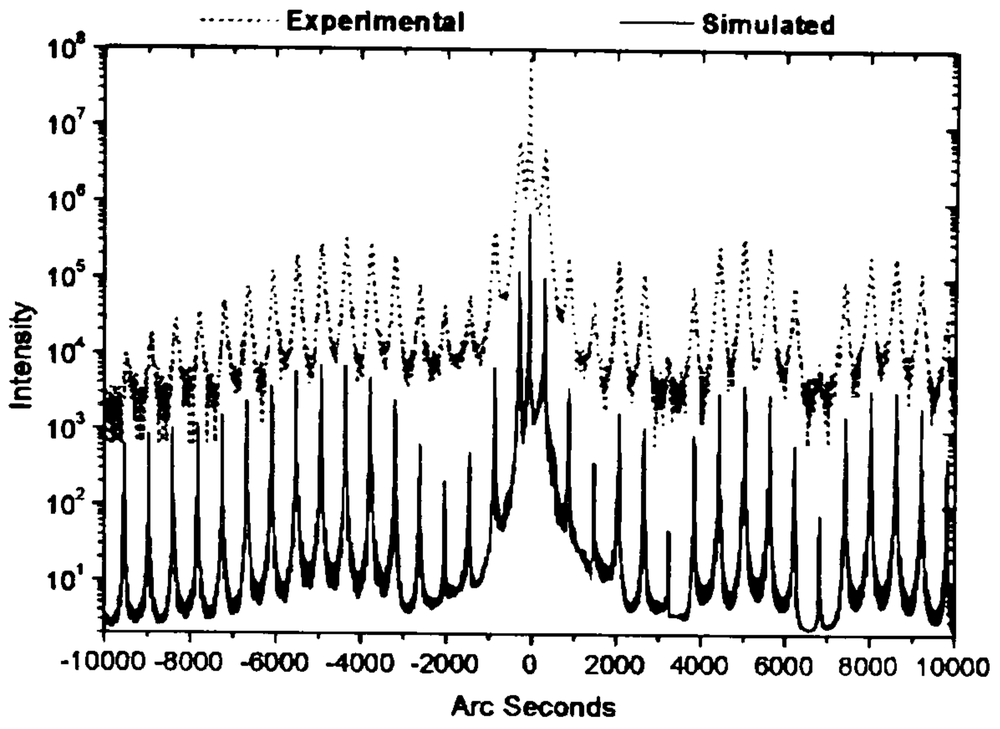

Fig. 7. DCXRD (004) reflection of highly tensile strained AlAs–$In_{0.84}Ga_{0.16}As$ short wavelength QWIP.

Table 1

Parameter	1561	1563	1554
Period (P)	25	15	15
QW thickness (d_w, A)	30	45	80
Strain number	−1	−0.68	0.06
Hall carrier density ($\times 10^{12}/cm^2$)	4.24	7	11
Hall Mobility (cm^2/V s)	269	1832	2000

difference is also reflected in the transport properties since the Hall mobility is seen to decrease quite dramatically as the net tensile strain per period increases (see Table 1). Thus there is a limit to how much net tensile strain can be accommodated.

It is clear from Table 1 that the transport properties of the QWIPs are excellent and the high electron mobilities attest to the abruptness of the various interfaces even though the high tensile sample suffers from the increased net strain.

As far as the optical properties were concerned, the active regions of all three samples showed strong PL emission both at room temperature and at 4 K (see Fig. 8). The interband emission varies from 0.68 eV (0.59 eV) to 1.04 eV (0.96 eV) at 4 K (RT).

Table 2 summarizes the calculated Γ subband energy levels in each of the InGaAs wells. Since the three samples: 1561, 1563 and 1554 differ only in their InGaAs layer thickness, they are all characterized by the same E^X subband levels in the X QW in AlAs. These subband energies were calculated using an X valley

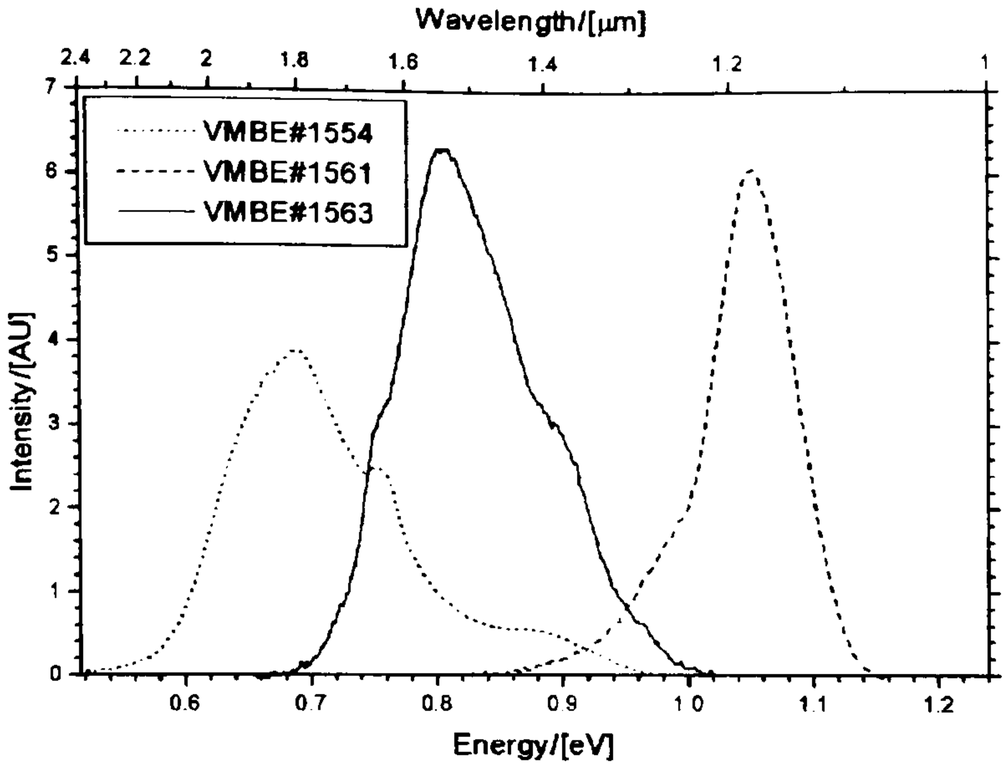

Fig. 8. 4 K PL of the three AlAs–$In_{0.84}Ga_{0.16}As$ short wavelength QWIP.

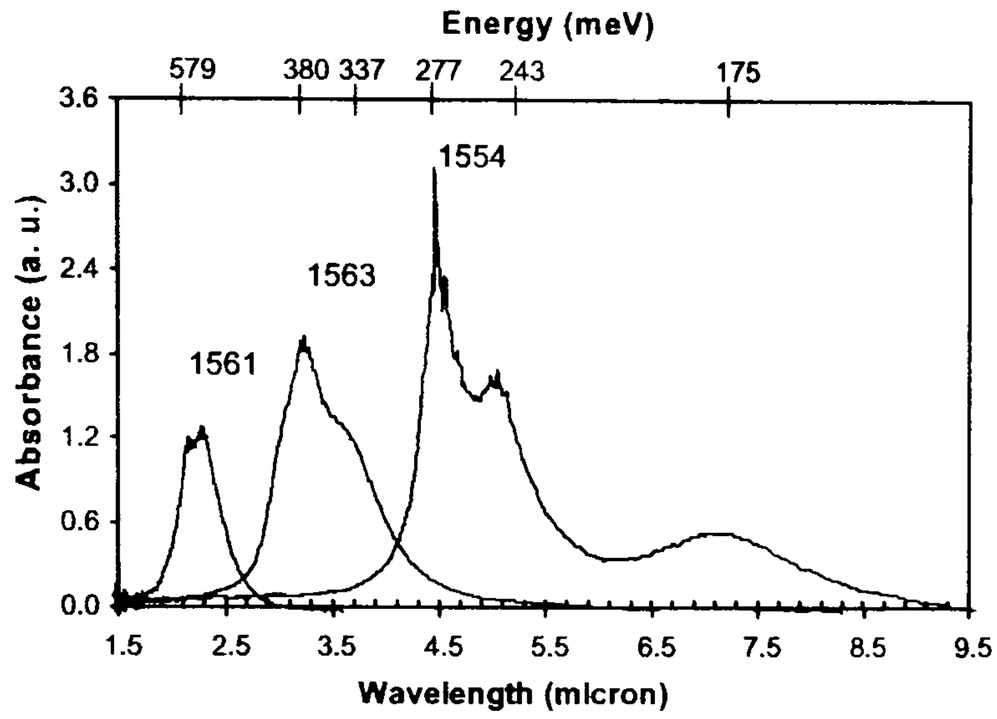

Fig. 9. Room temperature intersubband transitions covering the range 2– 7 μm in the highly strained QWIP structures.

Table 2

Sample No.	Energy levels (meV)			
	E1	E2	E3	E4
1554	82	276	521	786
1563	183	566	1000	1416
1561	301	873	1434	

effective mass of $m_{e-x} = 0.4m_0$ and are also shown in Fig. 6, where the energy levels are with respect to the Γ conduction band edge of the InGaAs QW. From Fig. 6 and Table 2, it can be seen that the energy level E_1^X in the AlAs layer is below E_2^Γ in 1561, between E_2^Γ and E_3^Γ in 1563, and between E_3^Γ and E_4^Γ in 1554.

Multiple intersubband transitions, $E_i \rightarrow E_{i+1}$, were observed in the room temperature absorption spectra due to the high doping in these samples (Fig. 9). Although this makes these particular samples unsuitable for room temperature operation, a comparison of their FWHM has been used (for the first time to our knowledge) to obtain information about the conduction band energy dispersion in QW structures [17].

Intersubband transitions in the strained AlAs–$In_xGa_{(1-x)}As$ system have been observed previously in structure grown on InP [6,7] and on GaAs [8] and with Indium contents of ~0.53 up to 0.4. Smet et al. [7] and Hirayama et al. [6] obtained intersubband transitions as low as 1.55 μm but only in structures having 3 ML (~9 Å) well thickness and even operation at ~1.8–2 μm could only be achieved using well widths of 6 ML (~18 Å). These samples consisted of only one or two periods. With such structures there is a concern with the absorption strength as electron leakage from the first Γ- to the X-subband in the AlAs will cause a dramatic decrease in the electron population in the Γ-branch. This puts a lower limit on how thin the QW must be in order to have fully functional devices. Asano et al. [8] has shown theoretically that at well width below 7 ML, the absorption should be almost completely quenched for $AlAs/In_{0.4}Ga_{0.6}As$ at a wavelength of ~1.9 μm. In our case, because of the much deeper well, intersubband absorption at 2 μm is reached with fairly wide wells (10 ML). The designs achieve both high periodicity and large Γ–X separation leading to devices with strong intersubband absorption magnitude and making the prospect of realising QWIP devices that work near room temperature a real possibility. The key to high temperature operation is maximising the barrier/well discontinuity for the chosen wavelength of operation. For any given wavelength the structure is then designed to place the excited state just above the InAlAs continuum and the ground state at an appropriate level in the well. Using the strained InGaAs structures, we have shown that we can achieve near 0.675 eV conduction band offset. Lee et al. [18] reported 205 K operation for a 0.5 eV band discontinuity (lattice-matched InGaAs/InAlAs on InP) but with a Fermi level ~0.27 eV below the barrier edge. With the much higher band offsets we are able to obtain in our system, better than 205 K

operation should be achievable for 4–5 μm devices with near room temperature operation at shorter wavelengths a real possibility.

4. Conclusion

In conclusion we have demonstrated short wavelength IR, intersubband operation at wavelengths as short as 2 μm for application in QCL and QWIP structures. Our aim is to push the strained $In_xGa_{(1-x)}As-In_yAl_{(1-y)}As$ system to its ultimate limit in an attempt to obtain the highest band offsets that are theoretically possible in this system. Both for the Γ–Γ bands and Γ–X bands, this would open up the way for both high power and high efficiency coupled with short-wavelength operation at *room temperature*. The versatility of this material system and growth techniques in covering a wide range of the infrared spectrum is also demonstrated.

Acknowledgements

This work is supported by the EPSRC, which is gratefully acknowledged.

We thank Prof. A. Shore and Dr. S. Banerjee of the University of Wales at Bangor for providing the design of the QC structure and Prof. A. Krier of the University of Lancaster, UK for the 4K PL measurements of the QWIP structures.

References

[1] B.F. Levine, J. Appl. Phys. 74 (1993) R1.
[2] B.F. Levine, C.G. Bethea, K.G. Glogovsky, J.W. Stayt, R.E. Lelbenguth, Semicond. Sci. Technol. 6 (1991) C114.
[3] H. Asai, Y. Kawamura, Appl. Phys. Lett. 56 (1990) 746.
[4] Q. Zhou, M.O. Manasreh, B.D. Weaver, M. Missous, J. Appl. Phys. 81 (2002) 3374.
[5] G. Gmachl, F. Capasso, D.L. Sivco, A.Y. Cho, Rep. Prog. Phys. 64 (2001) 1533.
[6] Y. Hirayama, J.H. Smet, L.H. Peng, C.G. Fonstad, E.P. Ippen, Appl. Phys. Lett. 63 (1993) 1663.
[7] J.H. Smet, L.H. Peng, Y. Hirayama, C.G. Fonstad, Appl. Phys. Lett. 64 (1994) 986.
[8] T. Asano, S. Noda, T. Abe, A. Sasaki, J. Appl. Phys. 82 (1997) 3385.
[9] C. Gmachl, F. Capasso, A. Tredicucci, D.L. Sivco, R. Kohler, A.L. Hutchinson, A.Y. Cho, IEEE J. Selected Topics Quantum Electron 5 (1999) 808.
[12] J. Faist, F. Capasso, D.L. Sivco, A.L. Hutchinson, S.N.G. Chu, A.Y. Cho, Appl. Phys. Lett. 72 (1998) 680.
[13] R. Kohler, C. Gmachl, A. Tredicucci, F. Capasso, D.L. Sivco, S.N.G. Chu, A.Y. Cho, Appl. Phys. Lett. 76 (2000) 1092.
[10] K.T. Lai, S.K. Haywood, R. Gupta, M. Missous, Electron. Lett. 38 (2002) 529.
[11] K.T. Lai, M. Missous, R. Gupta, S.K. Haywood, J. Appl. Phys. 93 (2003) 6065.
[14] P.N. Stavrinou, Ph.D. Thesis, University College London, 1994.
[15] G. Neu, Y. Chen, C. Deparis, J. Massies, Appl. Phys. Lett. 58 (1991) 2111.
[16] H. Asai, Y. Kawamura, Appl. Phys. Lett. 56 (1990) 746.
[17] R. Gupta, K.T. Lai, M. Missous, S.K. Haywood, Phys. Rev. B, submitted for publication.
[18] J.H. Lee, J.C. Chiang, S.S. Li, P.J. Kannam, Appl. Phys. Lett. 74 (1999) 765.

PHYSICAL REVIEW B **69**, 033303 (2004)

Subband nonparabolicity estimated from multiple intersubband absorption in highly doped multiple quantum wells

R. Gupta,[1] K. T. Lai,[1] M. Missous,[2] and S. K. Haywood[1]
[1]*Department of Engineering, University of Hull, Cottingham Road, Hull, HU6 7RX, United Kingdom*
[2]*Department of Electrical Engineering & Electronics, UMIST, Sackville Street, Manchester M60 1QD, United Kingdom*
(Received 22 April 2003; revised manuscript received 10 October 2003; published 28 January 2004)

We report strong room-temperature intersubband absorption in 80 Å strain-compensated $In_{0.84}Ga_{0.16}As/AlAs/In_{0.52}Al_{0.48}As$ double-barrier quantum wells grown on InP substrates. From the multiple Γ-Γ intersubband transitions observed, it is inferred that the electron effective masses and nonparabolicity parameters for the first two subbands differ significantly from each other. For the range $k \sim 5\times10^6 - 6\times10^6$ cm^{-1}, the difference in subband parameters results in a change in transition energy of about twice the value calculated for the corresponding GaAs/AlGaAs quantum well.

DOI: 10.1103/PhysRevB.69.033303 PACS number(s): 73.21.Fg, 78.67.De, 78.30.Fs, 85.30.De

I. INTRODUCTION

The main factor limiting performance of quantum well intersubband photodetectors (QWIPs) is thermionic emission over the barriers, which may be reduced by lowering the operating temperature of the detectors. However, this cooling requirement makes QWIPs bulky, expensive, and inconvenient to use. For high-temperature operation the barrier height needs to be maximized (for the wavelength of operation) to reduce thermionic emission. The direct-gap materials $GaAs/Al_{0.45}Ga_{0.55}As$ grown on GaAs (Ref. 1) and $In_{0.53}Ga_{0.47}As/In_{0.52}Al_{0.48}As$ lattice-matched to InP (Ref. 2) have conduction-band offsets (ΔE_C) of $\sim$350 meV and $\sim$500 meV, respectively. In order to increase ΔE_C, it becomes necessary to use strained-layer structures.[3] However, one of the major considerations is then the generation of misfit dislocations when a certain critical layer thickness is exceeded.[4] This adversely affects the structural, optical, and electrical properties. One route to overcome this limitation has been demonstrated by Chui *et al.*[5] They used a linearly graded InGaAs buffer layer on a GaAs substrate followed by $In_{0.5}Ga_{0.5}As/Al_{0.45}Ga_{0.55}As$ quantum well (QW) structures to achieve a very large conduction band discontinuity ($\Delta E_C = 800$ meV).

Another means of achieving large ΔE_C is by increasing the indium composition in the InGaAs well and balancing the high compressive strain with thin tensile-strained AlAs inner barriers. We have studied $In_{0.84}Ga_{0.16}As/AlAs/In_{0.52}Al_{0.48}As$ double-barrier QWs (DBQWs), grown on InP substrates, using this strain compensation method. The ΔE_C for these structures (with respect to the wide InAlAs barrier) is estimated to be $\sim$675 meV. This high band offset allows observation of intersubband transitions over a wide spectral range. We have observed strong room-temperature absorption between 2 μm and 7 μm from three structures, of differing well width and, therefore, differing net strain.[6] In the sample with an 8 nm well (strain-compensated), multiple intersubband transitions $E_i \rightarrow E_{i+1}$ were observed (where E_i refers to the Γ subband energy level in the well). In this paper, a comparison of the full width at half maximum (FWHM) of these absorption peaks is used to obtain information about the subband energy dispersion.

The next section contains details of the sample growth and measurement techniques, while the theoretical model to calculate the conduction-band profile and energy levels is presented in Sec. III. The results are discussed in Sec. IV and conclusions are outlined in Sec. V.

II. EXPERIMENT

A. Sample preparation

The samples were grown by molecular beam epitaxy on (100) semi-insulating InP:Fe substrates at a temperature of $\sim$420 °C using conditions similar to those reported previously.[7] The strain-compensated sample (1554) consisted of a 500 Å $In_{0.52}Al_{0.48}As$ buffer layer (undoped) followed by 15 periods of $In_{0.52}Al_{0.48}As$ (220 Å, undoped), AlAs (23 Å, undoped), InGaAs (80 Å, Si doped to 8×10^{18} cm^{-3}), and AlAs (23 Å, undoped). The whole structure is capped with a 100 Å layer of $In_{0.53}Ga_{0.47}As$ (undoped).

B. Measurements

The x-ray diffraction spectrum of sample 1554 could be closely simulated using the intended growth parameters.[7] Narrow satellite peaks (around 35 arc sec) are indicative of pseudomorphic growth, as is the 300 K electron mobility of 2000 cm^2/(V sec) obtained from Hall measurements. The electron density per well also calculated from Hall data was estimated from to be 1.1×10^{13} cm^{-2}, giving a Fermi energy of $E_F = 484$ meV.

A Bio-Rad FTS-3000 Fourier transform infrared spectrometer with a ceramic broadband source, a potassium bromide beam splitter, and a cooled mercury cadmium telluride detector was used to measure the absorbance of the sample at 300 K. A ZnSe wire grid polarizer was used to resolve the incident IR light into components with electric field vector perpendicular (allowed) or parallel (forbidden) to the plane of the QWs. The sample was processed into 45° waveguide structures to enhance the intersubband response. A substrate

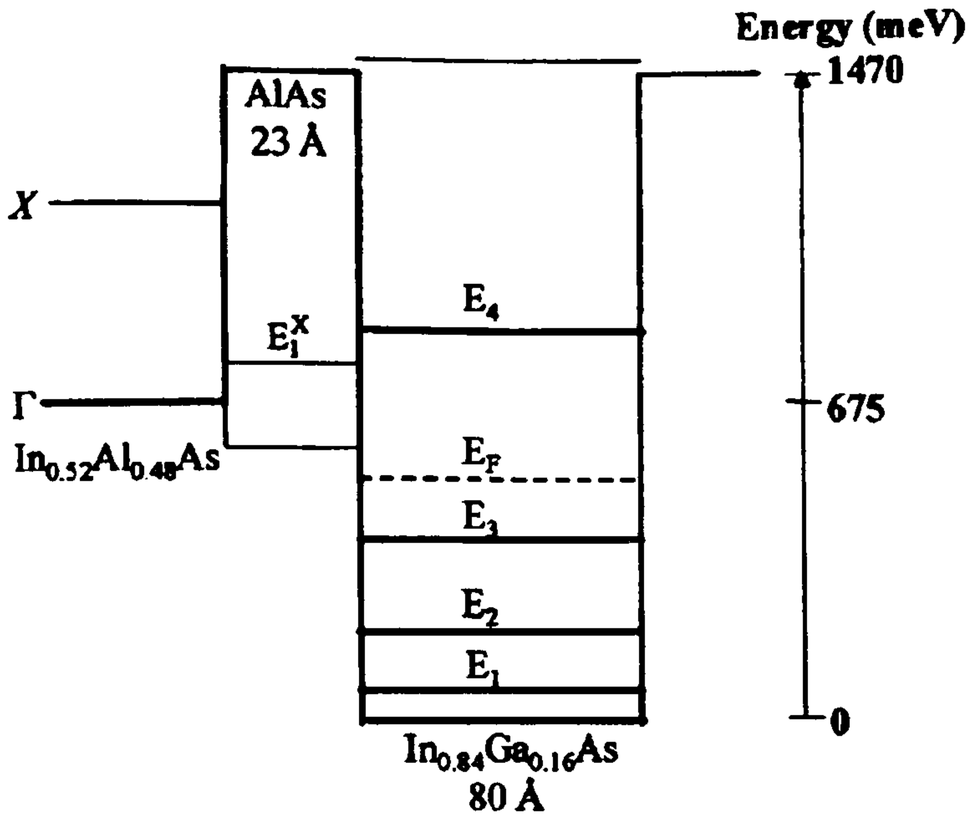

FIG. 1. Modeled Γ (thick line) and X (thin line) conduction band edge profile of sample 1554 showing the relative positions of the calculated Fermi level (dashed line) and the subband energy levels.

spectrum was taken under the same conditions as each sample measurement in order to eliminate any background effects.

III. MODELING

The conduction band profile and energy levels for the structure were obtained using a three-band Kane $k \cdot p$ approximation[8] that takes into account the effect of strain and bulk band nonparabolicity. Band offset ratios (ΔE_C:ΔE_V) of 0.65:0.35 and 0.7:0.3 are assumed for the InGaAs/AlAs (Ref. 9) and InGaAs/InAlAs (Ref. 10) heterojunctions, respectively. This model has been used successfully to determine the peak detection wavelength of a variety of other DBQWs, both strained and unstrained, in the InGaAlAs system.[11] The conduction band profile for the sample studied is shown in Fig. 1. The structure has four energy levels in the well with energies at $E_1 = 82$ meV, $E_2 = 276$ meV, $E_3 = 521$ meV, and $E_4 = 726$ meV. The E^X subband levels in the AlAs X QW were calculated using an average X valley effective mass of $m_{e-x} = 0.4m_0$. These levels are also shown in Fig. 1, where the energy levels are with respect to the Γ conduction band edge of the InGaAs QW. It can be seen that the energy level E_1^X in the AlAs layer is below E_4.

IV. RESULTS AND DISCUSSION

Figure 2 shows the room-temperature absorbance of 1554, where absorbance is equal to $-\log[T_{\text{allowed}}/T_{\text{forbidden}}]$ and T is the transmittance. [No peaks were observed in the parallel (forbidden) polarization.] The spectrum was fitted using Lorentzian line shapes and the resulting peak energies with their corresponding FWHM are summarized in Table I. Three absorption peaks are seen at energies between 177 meV and 280 meV (7.5–4.5 μm). These are assigned to $E_1 \rightarrow E_2$, $E_2 \rightarrow E_3$, and $E_3 \rightarrow E_4$ Γ transitions in the InGaAs well.

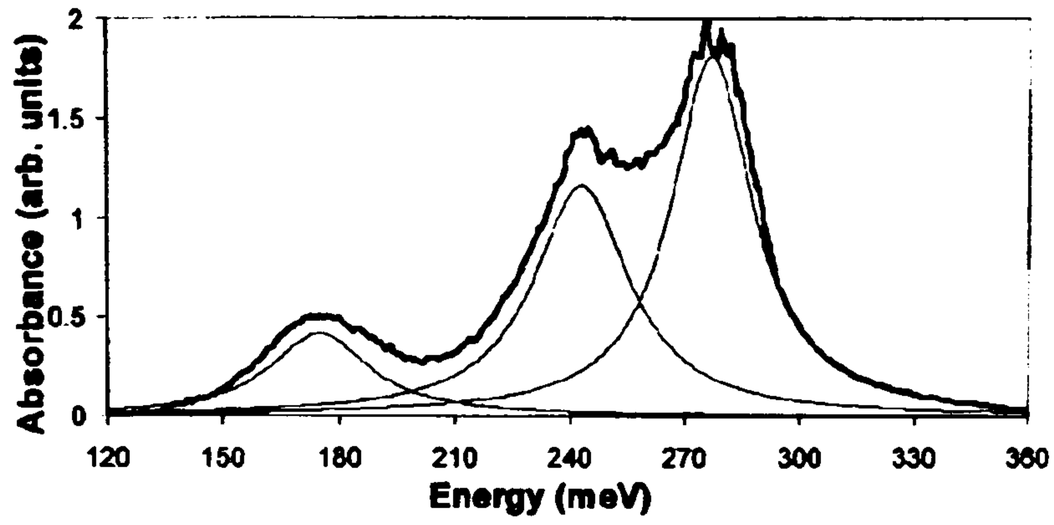

FIG. 2. Absorption spectrum measured at 300 K for sample 1554 using 45° waveguide geometry (thick line) and Lorentzian curve fit (thin line).

Sample 1554 is too highly doped to be useful as a QWIP because its high E_F relative to the outer barriers would lead to a large dark current. However, the ability to observe multiple intersubband transitions and to compare their FWHM offers a valuable insight into the nature of the subband dispersion. Figure 3 shows the energy dispersion in the k_{xy} plane (perpendicular to the growth direction) for this sample. The dispersion has been calculated assuming the same electron effective mass (m^*) for all subbands and neglecting the nonparabolicity parameter (α). The electron populations which participate in the various intersubband transitions are also shown. The electrons taking part in the transitions $E_1 \rightarrow E_2$, $E_2 \rightarrow E_3$, and $E_3 \rightarrow E_4$ correspond to N_1-N_2, N_2-N_3, and N_3, respectively, where N_i is the number of electrons in the ith subband.

Many theoretical calculations of m^* and α for the first and second subbands have been reported in the literature.[12] For example, von Allmen *et al.*[13] calculate the E-k dispersions using a 14-band model for the first and second Γ subbands in GaAs/AlGaAs multiple QWs (MQWs). They found that the second subband has a larger m^* and smaller α than the first. The resulting spread of the k-dependent transition energy is expected to contribute to a broadening of the observed $E_1 \rightarrow E_2$ peak. However, Zaluzny[12] has shown that depolarization effects associated with high electron doping lead to a reduction of the transition linewidths. The effect of depolarization on transition linewidth has been shown to depend on the electron density.[12] Hence, for highly doped GaAs quantum wells, depolarization effects may cancel the effect of subband nonparabolicity.

From Fig. 3 it can be seen that the $E_1 \rightarrow E_2$, $E_2 \rightarrow E_3$, and $E_3 \rightarrow E_4$ transitions for 1554 occur in different parts of the Brillouin zone and hence these transitions "sample" different parts of k space. The $E_3 \rightarrow E_4$ transition takes place near to the zone center while the $E_1 \rightarrow E_2$ transition involves electrons with the largest k values. It is seen from Table I that the FWHM for the $E_3 \rightarrow E_4$ transition is the lowest and is within the linewidth of 20–30 meV expected for bound-bound transitions in pseudomorphic QWs.[14] This occurs even though the transition is from a bound to a quasibound state. As a result, we can neglect nonparabolicity for this transition and assume that subbands E_3 and E_4 are parallel to each other near the zone center. On the other hand, the FWHM for the $E_1 \rightarrow E_2$ and $E_2 \rightarrow E_3$ transitions are both about 8 meV larger

TABLE I. Transition energy and FWHM values obtained from a Lorentzian line shape curve fit of the measured absorption spectrum for sample 1554. The modeled values of the transition energies are shown in brackets.

Sample No.	$E_1 \rightarrow E_2$ (meV)	FWHM (meV)	$E_2 \rightarrow E_3$ (meV)	FWHM (meV)	$E_3 \rightarrow E_4$ (meV)	FWHM (meV)
1554	173 (194)	31.6	245 (245)	32	275.5 (265)	23.6

than the $E_3 \rightarrow E_4$ transition. Since this comparison of FWHM involves transitions from the same sample, we conclude that any contributions to the peak width from effects, such as interface roughness or impurity scattering, should be the same for all three transitions. Also, as shown in the Appendix, for sample 1554 the electron density in the three subbands is very similar and hence the effect of depolarization on the linewidths of the three transitions is expected to be comparable. Consequently, we attribute the increased FWHM for the $E_1 \rightarrow E_2$ and $E_2 \rightarrow E_3$ transitions to unequal subband m^* and α values.

Using the following equation for the E-k dispersion of an infinite QW,[15] unequal effective masses and nonparabolicities can be taken into account:

$$E_n(k) = \frac{E_G}{2}\left[1 + \frac{4E_n^{(0)}}{E_G} + \frac{2\hbar^2 k^2}{m_e E_G}\right]^{1/2} - \frac{E_G}{2}, \qquad (1)$$

where m_e is the Kane effective mass at the conduction band bottom, E_G is the semiconductor band gap, and $E_n^{(0)} = \pi^2\hbar^2 n^2/(2m_e L_w^2)$ is energy of the nth subband in the parabolic approximation. This equation is used below to calculate the expected spread in $E_i \rightarrow E_{i+1}$ transition energy for various band gaps and intersubband transitions.

From the position of E_F in Fig. 1, we can see that the two transitions $E_1 \rightarrow E_2$ and $E_2 \rightarrow E_3$ in 1554 mainly sample a region of the Brillioun zone from $k = 4.8 \times 10^6$ cm^{-1} to $k = 6.2 \times 10^6$ cm^{-1} and from $k = 2.2 \times 10^6$ cm^{-1} to $k = 4.8 \times 10^6$ cm^{-1}, respectively. Substituting appropriate values for an 80 Å $In_{0.84}Ga_{0.16}As$ QW into Eq. (1), we obtain $E_1 \rightarrow E_2$ ($k = 4.8 \times 10^6$ cm^{-1}) $- E_1 \rightarrow E_2$ ($k = 6.2 \times 10^6$ cm^{-1}) $= 21$ meV; $E_2 \rightarrow E_3$ ($k = 2.2 \times 10^6$ cm^{-1}) $- E_2 \rightarrow E_3$ ($k = 4.8 \times 10^6$ cm^{-1}) $= 21$ meV, and $E_3 \rightarrow E_4$ ($k = 0$) $- E_3 \rightarrow E_4$ ($k = 2.2 \times 10^6$ cm^{-1}) $= 3$ meV. Hence the calculated contribution of nonparabolicity to the increased linewidth of both the $E_1 \rightarrow E_2$ and $E_2 \rightarrow E_3$ transitions is 18 meV greater than for $E_3 \rightarrow E_4$. This is consistent with our experimental observation, where the difference in FWHM for the $E_1 \rightarrow E_2$ and $E_2 \rightarrow E_3$ transitions is 8 meV larger than the FWHM for the $E_3 \rightarrow E_4$ transition. (It is coincidental that the calculated spread is the same for $E_1 \rightarrow E_2$ and $E_2 \rightarrow E_3$ in this sample, since, although the nonparabolicity decreases with increasing subband index, electrons from a wider k range participate in the $E_2 \rightarrow E_3$ transitions.)

A similar calculation for an 80 Å GaAs QW gives $E_1 \rightarrow E_2$ ($k = 4.8 \times 10^6$ cm^{-1}) $- E_1 \rightarrow E_2$ ($k = 6.2 \times 10^6$ cm^{-1}) $= 11$ meV, which is about half of the corresponding value obtained for the $In_{0.84}Ga_{0.16}As$ QW. The contribution of depolarization to linewidth, on the other hand, is expected to be similar in both materials since it depends mainly on the electron density. Therefore the canceling of the nonparabolicity contribution to linewidth due to depolarization effects, which is seen in some GaAs QWs, is not anticipated for high indium content InGaAs QWs.

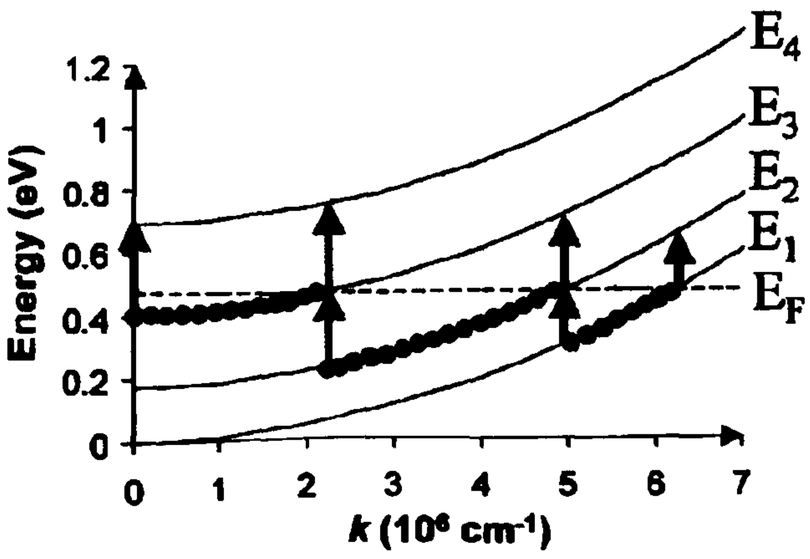

FIG. 3. The energy dispersion of the quantized Γ energy levels in the $k_{x,y}$ direction for sample 1554 assuming parallel subbands. The arrows indicate the intersubband transitions and the solid circles show the part of the subband involved in the transition.

V. CONCLUSION

In conclusion, we have observed multiple $\Gamma \rightarrow \Gamma$ transitions in $In_{0.84}Ga_{0.16}As/AlAs/In_{0.52}Al_{0.48}As$ DBQWs on InP substrates. The peak energies are in good agreement with the calculated values. The broad linewidth for the observed $E_1 \rightarrow E_2$ and $E_2 \rightarrow E_3$ transitions as compared to the $E_3 \rightarrow E_4$ transition is attributed to unequal m^* and α in the first and second subbands. We suggest that the measurement of multiple intersubband transitions in highly doped QW structures in this way is a simple method to investigate the difference in nonparabolicity between subbands at values of k of interest for practical device applications. Shubnikov–de Haas measurements can be used to obtain electron effective masses. However, the method proposed here gives additional information on the E-k dispersion without the need for liquid helium temperatures or extrapolation from high magnetic field conditions.

APPENDIX: ESTIMATION OF THE SUBBAND ELECTRON DENSITY FROM INTEGRATED PEAK INTENSITIES

The integrated absorption strength for a transition is proportional to $N_i \times f_{osc}$, where N_i is the number of electrons

participating in the transition and f_{osc} is the oscillator strength for the transition. A calculation of the Fermi energy in 1554 using the electron density obtained from Hall measurements ($N_S = 1.1 \times 10^{13}$ cm^{-2}) and parabolic bands yields $N_1 = 5.9 \times 10^{12}$ cm^{-2}, $N_2 = 3.6 \times 10^{12}$ cm^{-2}, and $N_3 = 0.5 \times 10^{12}$ cm^{-2}. Hence, the electrons taking part in the transitions $E_1 \rightarrow E_2$, $E_2 \rightarrow E_3$, and $E_3 \rightarrow E_4$ are N_1-$N_2 = 2.3 \times 10^{12}$ cm^{-2}, N_2-$N_3 = 3.1 \times 10^{12}$ cm^{-2}, and $N_3 = 0.5 \times 10^{12}$ cm^{-2}, respectively. Weighting N_1-N_2, N_2-N_3, and N_3 with the respective infinite-well oscillator strengths[16] of 0.96, 1.87, and 2.73 yields the relative integrated intensities for the three transitions as 1.62: 4.25: 1. This is clearly not the case experimentally as can be seen from Fig. 2, where the measured normalized peak intensities for the three transitions $E_1 \rightarrow E_2$, $E_2 \rightarrow E_3$, and $E_3 \rightarrow E_4$ are 0.27: 0.75: 1. A much closer agreement with experiment is obtained for a total electron density of $N_S = 2 \times 10^{13}$ cm^{-2}, which gives $N_1 = 9.2 \times 10^{12}$ cm^{-2}, $N_2 = 7.0 \times 10^{12}$ cm^{-2}, and $N_3 = 3.8 \times 10^{12}$ cm^{-2} and hence relative transition strengths of 0.2: 0.58: 1. Therefore, we assume a total electron density of $N_S = 2 \times 10^{13}$ cm^{-2}, which implies that the electron densities in the three subbands are similar.

[1] R. C. Miller, D. A. Kleinman, and A. C. Gossard, Phys. Rev. B **29**, 7085 (1984).
[2] H. Asai and Y. Kawamura, Phys. Rev. B **43**, 4748 (1991).
[3] J. H. Smet, L. H. Peng, Y. Hirayama, and C. G. Fonstad, Appl. Phys. Lett. **64**, 986 (1994).
[4] J. W. Matthews and A. E. Blakeslee, J. Cryst. Growth **27**, 118 (1974).
[5] H. C. Chui, S. M. Lord, E. Martinet, M. M. Fejer, and J. S. Harris, Jr., Appl. Phys. Lett. **63**, 364 (1993).
[6] R. Gupta, K. T. Lai, M. Missous, and S. K. Haywood (unpublished).
[7] K. T. Lai, M. Missous, R. Gupta, and S. K. Haywood, J. Appl. Phys. **93**, 6065 (2003).
[8] P. N. Stavrinou, Ph.D. thesis, University of College London, 1994.
[9] G. Neu, Y. Chen, C. Deparis, and J. Massies, Appl. Phys. Lett. **58**, 2111 (1991).
[10] H. Asai and Y. Kawamura, Appl. Phys. Lett. **56**, 746 (1990).
[11] K. T. Lai, S. K. Haywood, R. Gupta, and M. Missous, IEE Proc.: Optoelectron. **150**, 377 (2003).
[12] M. Zaluzny, Phys. Rev. B **43**, 4511 (1991), and references therein.
[13] P. von Allmen, M. Berz, F.-K. Reinhart, and G. Harbeke, Superlattices Microstruct. **5**, 259 (1989).
[14] L. C. Lenchyshyn, H. C. Liu, M. Buchanan, and Z. R. Wasilewski, Semicond. Sci. Technol. **10**, 45 (1995).
[15] B. Gelmont, V. Gorfinkel, and S. Luryi, Appl. Phys. Lett. **68**, 2171 (1996).
[16] L. C. West and S. J. Eglash, Appl. Phys. Lett. **46**, 1156 (1985).

INSTITUTE OF PHYSICS PUBLISHING SEMICONDUCTOR SCIENCE AND TECHNOLOGY

Semicond. Sci. Technol. **19** (2004) 1263–1267 PII: S0268-1242(04)76550-5

Intersubband absorption from 2 to 7 μm in strain-compensated double-barrier $In_xGa_{1-x}As$ multiquantum wells

K T Lai[1], R Gupta[1], M Missous[2] and S K Haywood[1]

[1] Department of Engineering, University of Hull, Cottingham Road, Hull, HU6 7RX, UK

[2] Department of Electrical Engineering & Electronics, UMIST, Sackville Street, Manchester M60 1QD, UK

Received 23 February 2004
Published 16 September 2004
Online at stacks.iop.org/SST/19/1263
doi:10.1088/0268-1242/19/11/009

Abstract

We report observations of strong room temperature intersubband absorption in strain-compensated $In_{0.84}Ga_{0.16}As/AlAs/In_{0.52}Al_{0.48}As$ double-barrier quantum wells grown on InP substrates. Multiple $\Gamma \rightarrow \Gamma$ intersubband transitions have been observed across a wide range of the mid infrared spectrum (2–7 μm) in three structures of differing InGaAs well width (30 Å, 45 Å and 80 Å) and therefore with differing net strain. This absorption range is not covered by direct-gap GaAs/AlGaAs structures.

1. Introduction

Infrared photodetectors based on intersubband transitions in quantum well (QW) structures have been widely investigated over the last decade [1]. They exhibit a large oscillator strength and both the peak detection wavelength and spectral lineshape may be controlled by varying the structural parameters of the QW, i.e., well width and barrier height. This gives greater design flexibility compared to interband detectors. In addition, these detectors are fabricated using well-established growth and processing techniques, where high uniformity and reproducibility can be achieved so that large area focal plane arrays become feasible.

The main factor limiting the performance of QW intersubband photodetectors (QWIPs) is thermionic emission over the barriers. This can be reduced by lowering the operating temperature of the detectors. However, this cooling requirement makes QWIPs bulky, expensive and inconvenient to use. For high temperature operation the barrier height needs to be maximized (for the wavelength of operation) to reduce thermionic emission. The direct-gap materials, $GaAs/Al_{0.45}Ga_{0.55}As$, grown on GaAs [2] and $In_{0.53}Ga_{0.47}As/In_{0.52}Al_{0.48}As$ lattice-matched to InP [3], have conduction band offsets (ΔE_C) of ~350 meV and ~500 meV, respectively. In order to increase ΔE_C, it becomes necessary to use strained layer structures [4]. However, one of the major considerations is then the generation of misfit dislocations when a certain critical layer thickness is exceeded [5]. This adversely affects the structural, optical and electrical properties of QWIPs. One route to overcome this limitation has been demonstrated by Chui *et al* [6]. They used a linearly graded InGaAs buffer layer on a GaAs substrate followed by $In_{0.5}Ga_{0.5}As/Al_{0.45}Ga_{0.55}As$ QW structures to achieve a very large conduction band discontinuity (ΔE_C = 800 meV).

We have used an alternative route to achieve a large ΔE_C, by increasing the In composition in the InGaAs well and compensating the high compressive strain with thin AlAs barriers tensile-strained with respect to the InP substrate. For example, ΔE_C for $In_{0.84}Ga_{0.16}As/AlAs/In_{0.52}Al_{0.48}As$ double-barrier QWs (DBQWs), grown on InP substrates, is estimated to be ~675 meV (with respect to the wide InAlAs barrier). Although, only one subband should be occupied for optimum QWIP design, the high AlAs barriers allow observation of multiple Γ–Γ absorption peaks in highly doped, wide wells. These transitions have been used previously to obtain information about the subband energy dispersion [7].

This paper presents intersubband absorption measurements on three structures, of differing well width, and therefore differing net strain. The next section contains details of sample growth and measurement techniques, while the theoretical model to calculate the conduction band profile and energy levels is presented in section 3. The results are discussed in section 4 and the conclusions are outlined in section 5.

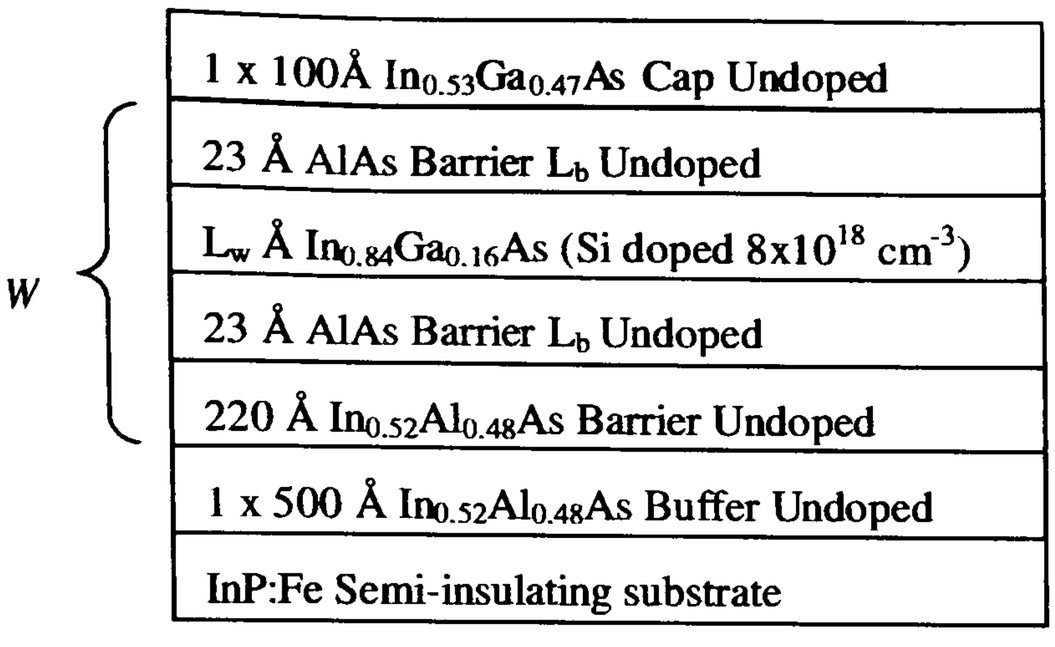

Figure 1. Generic epitaxial layer structure of the samples.

Table 1. Samples parameters.

	1554	1563	1561
QW periods, W	15	15	25
QW thickness, L_w (Å)	80	45	30
Average net strain per QW period (%)	0[a]	−0.74[a]	−1.3[a]
Measured Hall QW sheet carrier density, N_S ($\times 10^{12}$ cm^{-2})	11	7.0	4.24
Hall mobility, μ (cm^2 $(V\ s)^{-1}$)	2000	1832	269
Fermi energy as inferred from Hall measurement, E_F (meV)	482	444	330

[a] These values were obtained using $[(L_w(a_w - a_s)/a_s) + (L_b(a_b - a_s)/a_s)]/(L_w + L_b)$, where a_w, a_b and a_s are the lattice constants for the InGaAs well, AlAs inner barrier and the InP substrate, respectively.

2. Experiment

The samples used in this study were grown by molecular beam epitaxy on (100) semi-insulating InP:Fe substrates at a temperature of ~420 °C using conditions similar to those reported previously [8]. Figure 1 shows the generic layer structure of these samples. The structural parameters for individual samples, including data inferred from Hall measurements, are listed in table 1. The Hall mobility is significantly lower in 1561, the most strained sample, which also has the largest number of wells. Although the effect of interface roughness scattering increases with decreasing well width and this can reduce electron mobility [9], we attribute the large drop in Hall mobility for 1561 to a degree of strain relaxation. This can be seen from the x-ray spectra for samples 1554 and 1561 which are shown in figure 2. X-ray simulations based on the intended growth parameters closely reproduce the peak positions in all the measured spectra (e.g. see [8] for 1554 data). However, comparison of the satellite peaks in figure 2 reveals that the FWHM is around 70 arcsec for 1561 and 38 arcsec for 1554 which has close to zero net strain (1563 also has FWHM of 38 arcsec). A Bio-Rad FTS-3000 Fourier transform infrared spectrometer (FTIR) with a ceramic broadband source, a potassium bromide (KBr) beam splitter and a cooled mercury cadmium telluride (MCT) detector were used to measure the absorbance of the three samples at 300 K. For spectra containing peaks below 3 μm, additional measurements were made using a tungsten halogen source and a quartz beam splitter to achieve higher resolution. A ZnSe wire grid polarizer was used to resolve the incident IR light into

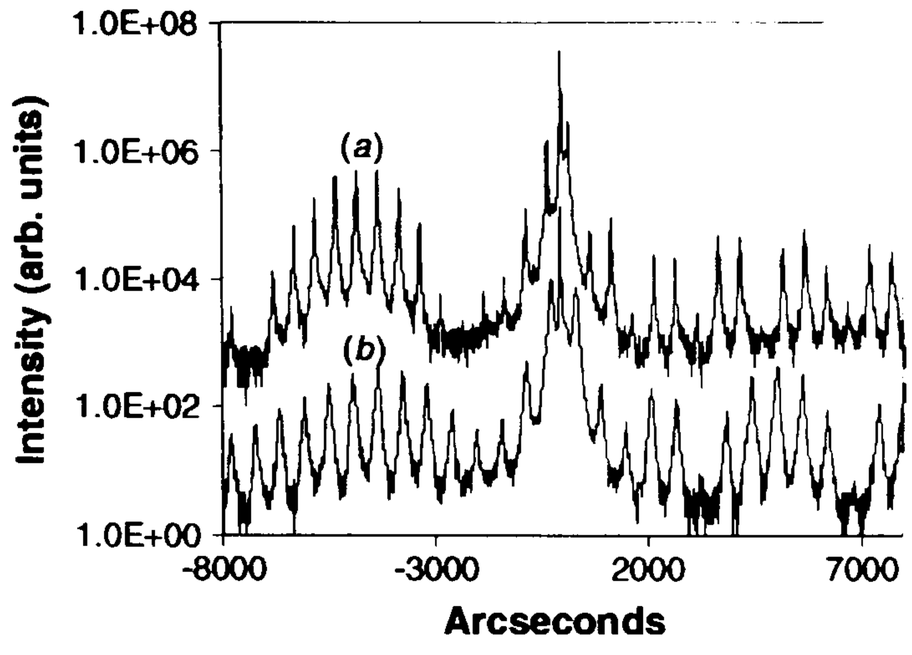

Figure 2. DCXRD (004) reflection spectrum for sample (*a*) 1554 and (*b*) 1561. The FWHM of the satellite peaks for sample 1561 and 1554 are ~70 and 38 arcsec, respectively. The spectra are offset for clarity.

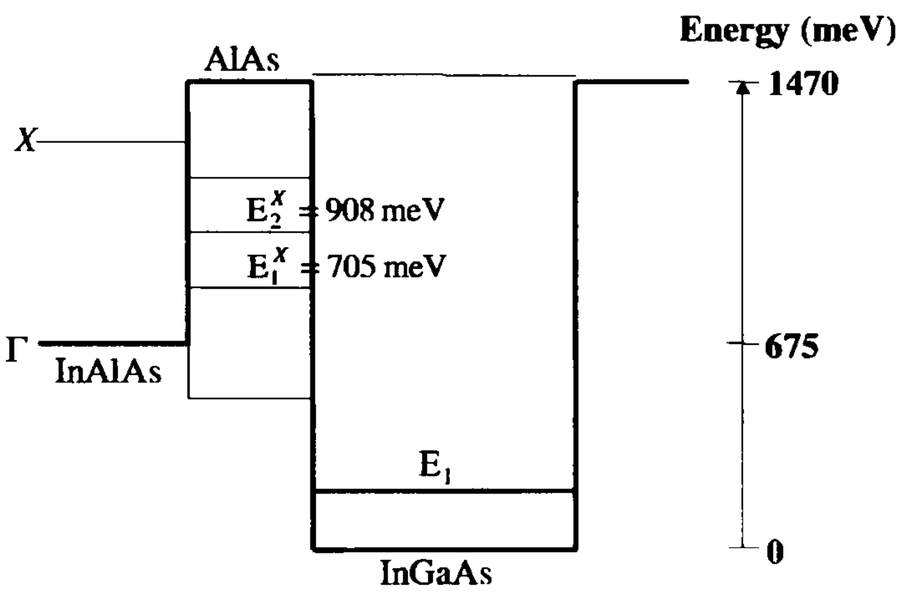

Figure 3. Modelled generic Γ (thick line) and X (thin line) conduction band edge profile of the samples. Energy levels E_1^X and E_2^X confined in the AlAs X QW are also shown.

Table 2. Modelled subband energy levels in the Γ band for the samples. All the energy levels are relative to the bottom of the Γ conduction band of the InGaAs QW layer.

	Energy levels (meV)				
Sample number	E_1	E_2	E_3	E_4	$E_1 + E_F$
1554	82	276	521	786	564
1563	183	566	1000	1416	627
1561	301	873	1434		631

components with electric field vector perpendicular (allowed) or parallel (forbidden) to the plane of the QWs. To facilitate coupling of light with the intersubband transition, samples were processed in a 45° waveguide geometry. A substrate spectrum was taken under the same conditions as each sample measurement in order to eliminate any background effects.

3. Modelling

The conduction band profile and energy levels for the structure were obtained using a three-band Kane $\boldsymbol{k} \cdot \boldsymbol{p}$ approximation [10] that takes into account the effect of strain and bulk band nonparabolicity. Band offset ratios ($\Delta E_C : \Delta E_V$) of 0.65 : 0.35 and 0.7 : 0.3 are assumed for the InGaAs/AlAs [11] and InGaAs/InAlAs [12] heterojunctions, respectively. This model has been used successfully to determine the peak

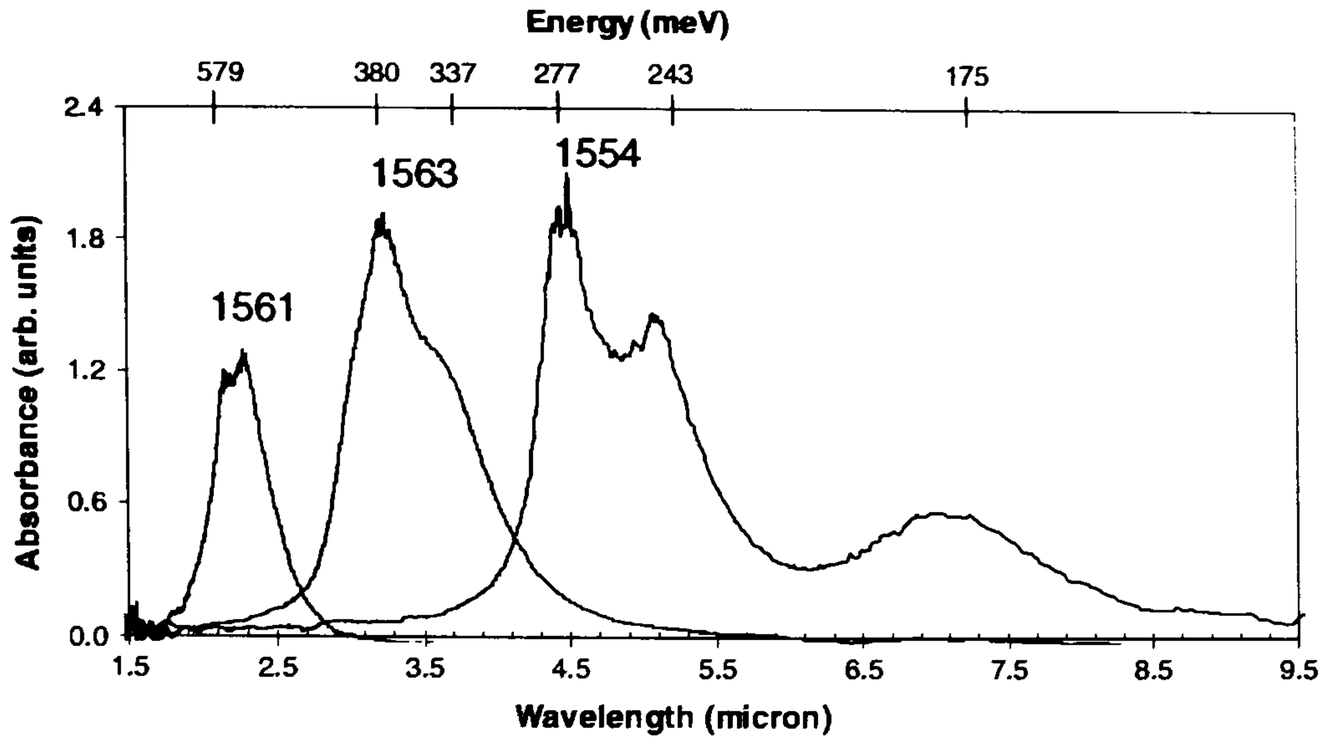

Figure 4. Measured absorption spectra as a function of wavelength at 300 K for samples 1554, 1563 and 1561 using 45° waveguide geometry.

Table 3. Transition energy and FWHM values obtained from Lorentzian line shape curve fit of the measured absorption spectra for the three samples.

Sample number	$E_1 \rightarrow E_2$ (meV)	FWHM (meV)	$E_2 \rightarrow E_3$ (meV)	FWHM (meV)	$E_3 \rightarrow E_4$ (meV)	FWHM (meV)
1554	173	31.6	245	32	275.5	23.6
1563	337	54	410	54		
	380	54				
1561	534	60				
	579	68				

detection wavelength of a variety of other double-barrier quantum wells (DBQWs), both strained and unstrained, in the InGaAlAs system [8, 13]. A generic conduction band profile for the samples studied is shown in figure 3. Table 2 summarizes the calculated Γ subband energy levels in each of the InGaAs wells. Since the three samples: 1561, 1563 and 1554 differ only in their InGaAs layer thickness, they are all characterized by the same E^X subband levels in the X QW in AlAs. X valley subband energies were calculated using an effective mass, m_{e-x}, of $0.4m_0$. They are also shown in figure 3, where the energy levels are with respect to the Γ conduction band edge of the InGaAs QW. From figure 3 and table 2, it can be seen that the energy level E_1^X in the AlAs layer is below E_2 in 1561, between E_2 and E_3 in 1563, and between E_3 and E_4 in 1554.

4. Results and discussion

Figure 4 shows the room temperature absorbance of the three samples (where absorbance is equal to $-\log[T_{\text{allowed}}/T_{\text{forbidden}}]$ and T is the transmittance). No peaks were observed in the parallel (forbidden) polarization. It can be seen that the peak detection wavelength for these structures can be tuned from 2 to 7 μm (620–177 meV) by simply varying the InGaAs well width. These spectra were fitted using a Lorentzian lineshape and the resulting peak energies and the corresponding full width at half maximum (FWHM) are summarized in table 3. For sample 1554, three peaks are observed and these are assigned to $E_1 \rightarrow E_2$, $E_2 \rightarrow E_3$ and $E_3 \rightarrow E_4$ transitions in the InGaAs well. A detailed analysis of this sample including the Lorentzian fit was previously reported [7, 8].

The absorption spectrum of sample 1563, together with the Lorentzian curve fit, is shown in figure 5 plotted on the energy scale. Two distinct peaks are observed in this sample: one at 337 meV and the strongest at 380 meV. In addition, there is a weak shoulder at 410 meV. From the data in table 2, it can be seen that the Fermi energy, E_F, lies between E_2 and E_3 for this sample. Therefore, only two intersubband transitions, $E_1 \rightarrow E_2$ and $E_2 \rightarrow E_3$, are possible. From our modelling, a variation of 1–2 monolayers (MLs) in thickness between the different InGaAs wells could account for peaks at 337 and 380 meV both arising from the $E_1 \rightarrow E_2$ transition. The shoulder peak at 410 meV must be due to the higher energy $E_2 \rightarrow E_3$ transition (table 2). However, if there are two sets of intersubband peaks arising from growth variations within the sample, then we would expect also to see a weaker, lower energy peak from the $E_2 \rightarrow E_3$ transition, possibly also contributing to the peak at 380 meV. Hence, we assume that the peak at 380 meV is due to a combination of both the $E_1 \rightarrow E_2$ and $E_2 \rightarrow E_3$ transitions. From the relative intensities of the three observed peaks and the measured carrier density, it is possible to estimate the relative contribution of each transition to the 380 meV peak. If I_{12} and I_{23} are the integrated peak intensities for the $1 \rightarrow 2$ and $2 \rightarrow 3$ intersubband transitions, respectively, then (as in [7]) $I_{23}/I_{12} \propto N_2/(N_1 - N_2)$ N_1 and N_2 are the electron densities in the first and second subbands, respectively. This analysis shows that the assignment of the 380 meV peak predominantly to the $E_1 \rightarrow E_2$ transition (90%) is consistent with the total electron density of $\sim 7 \times 10^{12}$ cm^{-2} estimated from Hall measurements.

A relatively weak peak at 170 meV is also observed and is shown as an inset in figure 5. It is seen only in the allowed

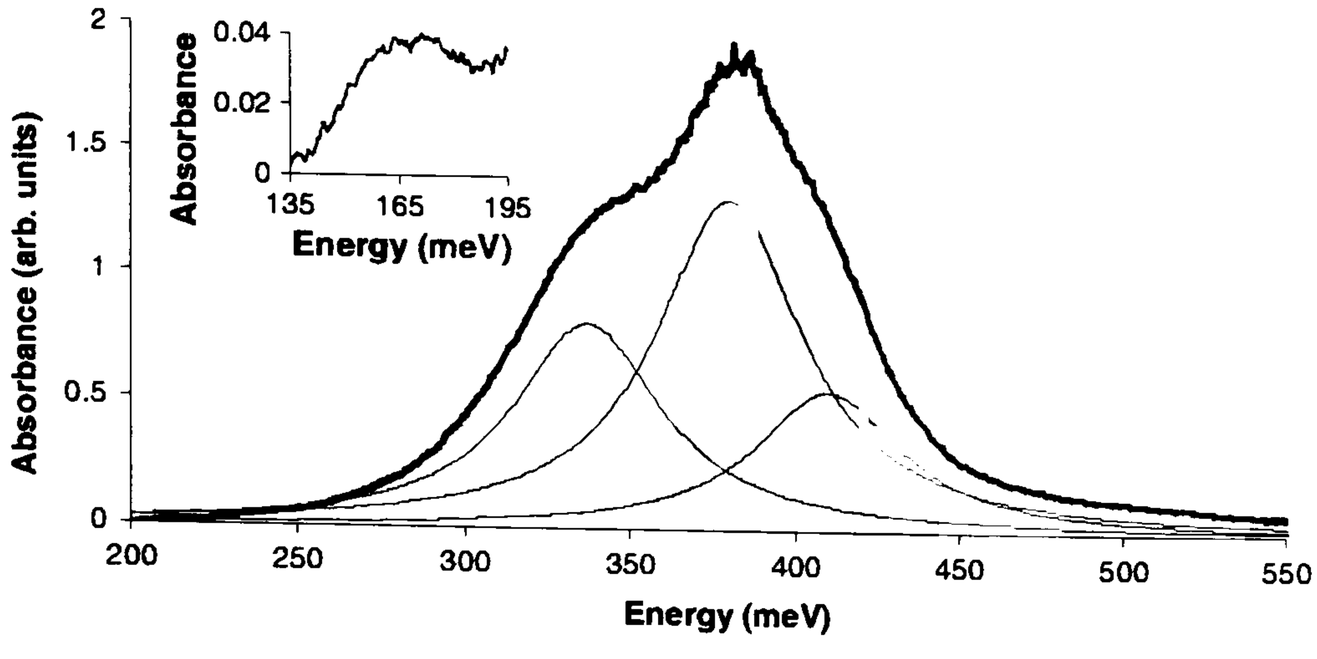

Figure 5. Measured 300 K absorption spectrum for sample 1563 (thick curve) and Lorentzian curve fit (thin curve) plotted on the energy scale. The inset shows the peak at 170 meV which is attributed to the $E_1^X \rightarrow E_2^X$ transition in the AlAs layer.

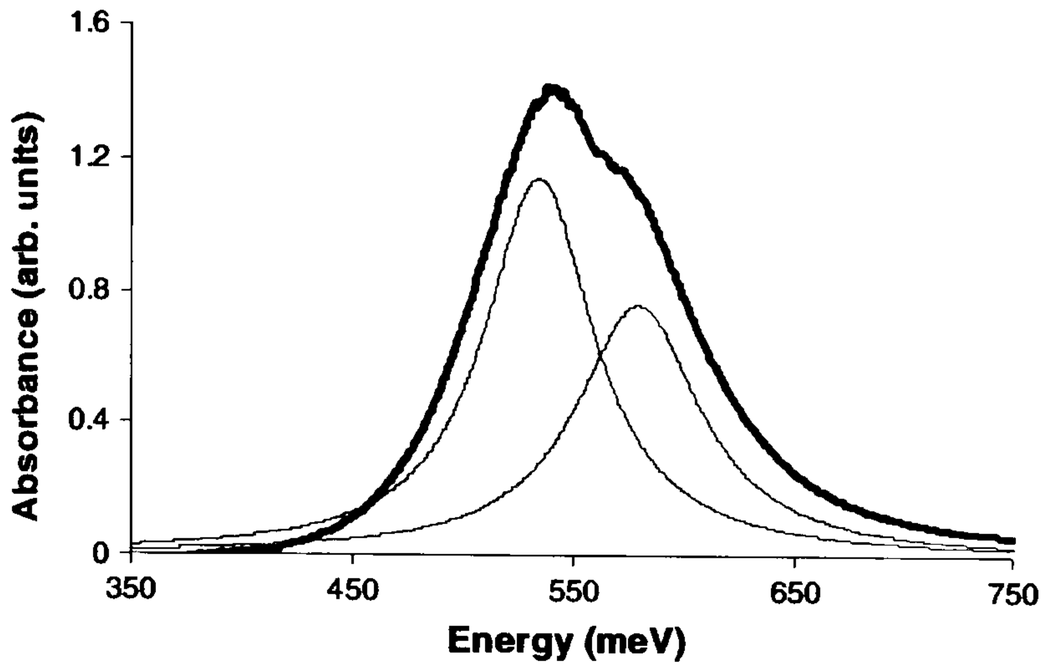

Figure 6. Measured 300 K absorption spectrum for sample 1561 (thick curve) and Lorentzian curve fit (thin curve) plotted on the energy scale.

polarization and is attributed to the $E_1^X \rightarrow E_2^X$ transition in the AlAs layer. This assignment is in line with the observations of Katz *et al* [14]. The agreement between the observed peak energy (170 meV) and our calculated value for this transition (203 meV, see figure 3) is within the error produced by one ML fluctuation in the AlAs thickness. This corroborates our use of $m_{e-x}(\mathrm{AlAs}) = 0.4m_0$ and therefore reconfirms our calculation that the energy level $E_1^X(\mathrm{AlAs})$ lies between E_2 and E_3 of the InGaAs well for 1563 (figure 3 and table 2).

The absorption spectrum for 1561 (figure 4) shows two peaks at 579 meV and 534 meV. From tables 2 and 3, it can be seen that the 579 meV peak is in good agreement with the calculated transition energy of 572 meV for a well width of 30 Å. A better resolved spectrum of this sample is shown in figure 6, where a Lorentzian curve fit is also presented. For 1561, the Fermi energy E_F lies between E_1 and E_2 (table 2), so that both the observed peaks are attributed to the transition between E_1 and E_2 in the QW. The separation between the observed peaks is within 50 meV and this can be accounted for by a one ML variation in thickness of the InGaAs wells.

Additional evidence for the assignment of both peaks in 1561 to $E_1 \rightarrow E_2$ (rather than assigning one of them to $E_2 \rightarrow E_3$) transition comes from consideration of the position of E_F in relation to the $E_1^X(\mathrm{AlAs})$ energy level. Although there are three subband energy levels in the well, the $E_1^X(\mathrm{AlAs})$ level is below E_2 (figure 3 and table 2) and therefore has to be populated with electrons before E_2. However, since the electron mass in the X valley in AlAs is ~10 times the effective mass of the electrons in the Γ valley in the $In_{0.84}Ga_{0.16}As$ well, the corresponding density of states is much larger. This implies that the sample doping would have to be impractically high for E_2 to be populated and hence for an $E_2 \rightarrow E_3$ transition to be possible. (A similar argument allows us discount the $E_3 \rightarrow E_4$ transition 1563.)

We have also observed a weak peak for 1561 at ~207 meV in the perpendicular polarization (not shown). This peak is attributed to the $E_1^X \rightarrow E_2^X$ transition in the AlAs QW layer and is in excellent agreement with our calculated $E_1^X \rightarrow E_2^X(\mathrm{AlAs})$ transition energy (203 meV). For sample 1554, the $E_1^X \rightarrow E_2^X$ transition is possibly obscured by the strong $E_1 \rightarrow E_2$ peak observed at ~175 meV.

5. Conclusion

In conclusion, we have grown three $In_{0.84}Ga_{0.16}As/AlAs/In_{0.52}Al_{0.48}As$ DBQWs, on InP substrates, with varying degrees of net strain due to the different well widths. All three samples show strong intersubband absorption at room temperature. The observed peaks are attributed to $\Gamma \rightarrow \Gamma$ transitions in the well and an $E_1^X \rightarrow E_2^X$ transition in the AlAs layer; peak energies are in good agreement with the calculated values. Both partially strain-compensated samples (1561 and 1563) show evidence of 1–2 monolayer variation in the InGaAs well thicknesses. The use of strain compensation in this versatile material system leads to coverage of a wide range of the mid infrared spectrum ($\lambda = 2$–$7\ \mu$m). The large conduction band offset also allows the potential development of QWIPs operating at room temperature.

References

[1] Levine B F 1993 *J. Appl. Phys.* **74** R1
[2] Miller R C, Kleinman D A and Gossard A C 1984 *Phys. Rev.* B **29** 7085
[3] Asai H and Kawamura Y 1991 *Phys. Rev.* B **43** 4748
[4] Smet J H, Peng L H, Hirayama Y and Fonstad C G 1994 *Appl. Phys. Lett.* **64** 986
[5] Matthews J W and Blakeslee A E 1974 *J. Cryst. Growth* **27** 118
[6] Chui H C, Lord S M, Martinet E, Fejer M M and Harris J S Jr 1993 *Appl. Phys. Lett.* **63** 364

[7] Gupta R, Lai K T, Missous M and Haywood S K 2004 *Phys. Rev.* B **69** 033303
[8] Lai K T, Missous M, Gupta R and Haywood S K 2003 *J. Appl. Phys.* **93** 6065
[9] Campman K L, Schmidt H, Imamoglu A and Gossard A C 1996 *Appl. Phys. Lett.* **69** 2554
[10] Stavrinou P N 1994 *PhD Thesis* University College London
[11] Neu G, Chen Y, Deparis C and Massies J 1991 *Appl. Phys. Lett.* **58** 2111
[12] Asai H and Kawamura Y 1990 *Appl. Phys. Lett.* **56** 746
[13] Lai K T, Haywood S K, Gupta R and Missous M 2003 *IEE Proc. Opto.* **150** 377
[14] Katz J, Zhang Y and Wang W I 1992 *Appl. Phys. Lett.* **61** 1697